Universität Potsdam
Institut für Erd- und Umweltwissenschaften
und
Helmholtz-Zentrum Potsdam – Deutsches GeoForschungsZentrum GFZ
Sektion 4.4 Sedimentbeckenanalyse

Influence of faults on the 3D coupled fluid and heat transport

Kumulative Dissertation

zur Erlangung des akademischen Grades
"doctor rerum naturalium"
(Dr. rer. nat.)
in der Wissenschaftsdisziplin "Geologie"

eingereicht an der
Mathematisch-Naturwissenschaftlichen Fakultät
der Universität Potsdam

von
Yvonne Cherubini

Potsdam, Juli 2013

Published online at the
Institutional Repository of the University of Potsdam:
URL http://opus.kobv.de/ubp/volltexte/2014/6975/
URN urn:nbn:de:kobv:517-opus-69755
http://nbn-resolving.de/urn:nbn:de:kobv:517-opus-69755

Table of contents

List of figures IV
List of tables IX
Abstract X
Zusammenfassung XIII
1 Introduction 1
1.1 Objective 3
1.2 Thesis outline 3
1.3 Synopsis of the chapters 4
2 Impact of single inclined faults on the fluid flow and heat transport: results from 3D finite element simulations 7
2.1 Introduction 8
2.2 Methodology 10
2.2.1 Mathematical and physical principles 10
2.2.2 Model set-up 13
2.2.3 Simulations 14
2.2.4 Initial and boundary conditions 15
2.2.5 Time discretization 17
2.3 Results 17
2.3.1 Background model 17
Fluid pressure, fluid velocity and temperature fields 17
2.3.2 Fault model 18
Early stage pressure, fluid velocity and temperature evolution 18
Final stage 21
2.3.3 Sensitivity analysis for fault transmissivities 26
Sensitivity analysis: width of the fault zone (WFZ) 26
Sensitivity analysis: permeability 30
2.4 Discussion 33
2.5 Conclusions 35
3 Controls on the deep thermal field – implications from 3D numerical simulations for the geothermal research site Groß Schönebeck 38
3.1 Introduction 39
3.2 Geological setting and model setup 42
3.2.1 Fault system 45
3.3 Method 46
3.3.1 FEM model construction: Spatial discretization and parametrization 46

3.3.2 Simulations ... 49
3.3.3 Time discretization ... 50
3.3.4 Boundary and initial conditions ... 50
3.4 Results ... 51
3.4.1 Conductive model 1 ... 51
Comparison between modelled and measured temperatures ... 53
3.4.2 Coupled fluid and heat transport model 2 ... 55
Comparison between modelled and measured temperatures ... 56
3.4.3 Fault model 3 ... 57
Vertical cross section ... 57
Horizontal temperature distribution ... 61
Comparison between modelled and measured temperatures ... 63
Pressure ... 63
3.5 Discussion and conclusions ... 64
4 Influence of major fault zones on the 3D coupled fluid and heat transport for the area of Brandenburg (NE German Basin) ... 74
4.1 Introduction ... 75
4.2 Data and method ... 78
4.2.1 Hydrogeological model ... 78
4.2.2 Fault system ... 81
4.2.3 Set-up of the numerical model ... 82
4.2.4 FEM model construction ... 82
4.2.5 Time discretization ... 85
4.2.6 Boundary and initial conditions ... 85
4.3 Modelling results ... 86
4.3.1 Regional thermal field ... 86
4.3.2 Horizontal temperature distribution: -1,000 m depth ... 87
4.3.3 Horizontal temperature distribution: -3,000 m depth ... 88
4.3.4 Temperature distribution in the fault zones ... 90
4.3.5 Interaction between fault zones and surrounding sediments ... 92
Recharge area – Gardelegen fault zone ... 92
Discharge area – Lausitz fault zone ... 96
3D sections ... 99
4.4 Discussion and conclusions ... 101
5 Discussion, outlook and conclusions ... 106
5.1 Discussion ... 106
5.1.1 Numerical approach ... 106
5.1.2 Heat transfer mechanisms ... 109

5.1.3 Controlling factors ... 112
5.2 Outlook for future studies ... 115
5.3 Conclusions ... 117
References ... 118
Appendix A: Governing equations ... 132
Appendix B: Assessment of the present-day thermal field (NE German Basin) – inferences from 3D modelling ... 136
B.1 Introduction ... 138
B.2 The 3D structural model of Brandenburg ... 140
B.2.1 Database ... 140
B.2.2 Model construction ... 141
B.2.3 Structural setting ... 143
B.3 The 3D conductive thermal model of Brandenburg ... 149
B.3.1 Modelled temperatures ... 150
B.3.2 Comparison with published data ... 154
B.4 The geothermal in-situ laboratory Groß Schönebeck ... 154
B.4.1 Method ... 156
B.4.2 Results from simulations of coupled heat and fluid transfer ... 159
B.5 Conclusions ... 162
Danksagung ... 164
Erklärung ... 166

List of figures

Figure 2.1 Wireframe of the 3D mesh (geological layer + inclined fault) with location the three observation points and pressure (a) as well as temperature (b) boundary conditions applied in all simulations. 16

Figure 2.2 3D pressure field (a) and distribution of discrete 3D isotherms (b) for the background model with location of a horizontal cutting plane at -60 m. 18

Figure 2.3 Fluid pressure evolution through time at the three observation points (a), fluid velocity evolution for observation point 3 (b) and temperature evolution along the three observation points (c), see Figures 2.1a and 2.1b for their respective location. 19

Figure 2.4 Fluid velocity vectors along the whole fault plane as well as along a horizontal plane cutting the model approximately in the central part during (a) the initial stage and (b) after 0.4 days (~0.01 month) of simulation. Non-scaled vectors represent the velocity direction and the background colours map their magnitudes. 21

Figure 2.5 Final pressure field for the reference model showing the stable 3D pressure distribution and location of a horizontal cutting plane at -60 m (a), the pressure isobars on the horizontal cutting plane (b) and pressure contours presenting the pressure differences between background model and reference model (c). 22

Figure 2.6 Fluid velocity vectors along the fault plane as well as along the horizontal cutting plane of the reference model. Non-scaled vectors represent the velocity direction and the background colours map their magnitudes. 24

Figure 2.7 Distribution of discrete 3D isotherms as obtained for the reference model (a) and iso-contours of the temperature differences between background model and reference model (b). 25

Figure 2.8 Fluid velocity vectors along the fault plane as well as along the horizontal cutting plane for model with minimum WFZ (a) and model with maximum WFZ (b). Non-scaled vectors represent the velocity direction and the background colours map their magnitudes. 28

Figure 2.9 Fault zone width vs. fluid velocity (black dots) for all model simulations within the sensitivity study for the WFZ in observation point 2, located in the central part of the fault plane. 28

Figure 2.10 Distribution of discrete 3D isotherms of the temperature differences between model with minimum WFZ and model with maximum WFZ. 29

Figure 2.11 Steady-state fluid velocity vectors along the fault plane as well as along the horizontal cutting plane for model with maximum permeability (a) and model with minimum permeability (b). Non-scaled vectors represent the velocity direction and the background colours map their magnitudes. 31

Figure 2.12 Distribution of discrete 3D isotherms for model with maximum permeability (a) and model with minimum permeability (b). 32

Figure 2.13 Distribution of isobars of the pressure differences between a model with a dipping fault of 60° and a model with a vertical fault on a horizontal cutting plane at -90 m. 35

Figure 3.1 a: Map of Germany showing the location the Groß Schönebeck test site. The study area (red rectangle) covers a surface of 50 km in N-S and of 55 km in E-W direction; b: Topography map of the model area in UTM zone 33N with main rivers and lakes (thin black lines) (ETOPO1, after

Amante and Eakins, 2009). The well GrSk3/90 (black dot) indicates the position of the hydrothermal EGS research site Groß Schönebeck. 40

Figure 3.2 a: Thickness map of Permian Zechstein salt which is characterized by two NE and NW trending salt ridges in the centre and NE; b: 3D hydrotectonic model for the Rotliegend reservoir indicating the hydraulic conductivity of the faults with respect to their kinematic behavior within the current in situ stress field (from Moeck et al. 2005). Red faults: acting as seals; Blue faults: serving as conduits; Yellow tube: location of the well GrSk 3/90; c and d: Simplified subsalt fault system representing the major faults in the area Groß Schönebeck at (c) the Top Rotliegend depth map corresponding to the uppermost surface cut by the faults and (d) the implemented faults in the subsalt layers of the 3D finite element model. According to Figure 3.2b, in both subfigures the red NW-SE oriented faults are supposed to act as barriers, the blue NE-SW trending fault as a conduit to fluid flow. 41

Figure 3.3 a: 3D geological model of Groß Schönebeck with the stratigraphic layers (vertical exaggeration: 7:1). Black points on top indicate the location of the wells in the area Groß Schönebeck for which temperature measurements are available. The dotted black line delineates the location of the vertical cross section from N to S through the research well GrSk3/90 used to illustrate results in Figs. 3.5, 3.7, 3.8. The frontal view displays a vertical profile from W to E through well Tuchen 1. Note the Quaternary channel cutting the Upper Cretaceous layer at shallow depth (up to ~ 200 m) in the SE. 44

Figure 3.4 Spatially varying heat flux used as lower thermal boundary condition extracted from a lithosphere-scale conductive thermal model of Brandenburg (Noack et al. 2012). 50

Figure 3.5 a: Vertical geological cross section from N to S through GrSk 3/90 for which the results in subfigures 3.5b, c, d and Figure 3.7 are shown. Position of the well is displayed by the black solid line. The location of the cross section is delineated in Fig. 3.3a by the dotted black line. The location of the permeable fault cutting the central part of the cross section below the salt rim syncline is indicated by the red solid line. The positions of the two fault barriers dissecting the profile in the N and S parts are displayed by black solid lines. The outlines of the impermeable basement, Zechstein and Muschelkalk layers are grey-shaded and Ruplian is white-shaded in the background of the temperature profiles of Figs. 3.5b, c and 3.7a. In Figs. 3.5d and 3.7c these four layers are black-shaded. Vertical exaggeration: 7:1 for all sections; b: Temperature distribution of the conductive model 1. The conductive thermal field is generally characterized by flat isotherms, which are locally bent in response to the highly conductive Zechstein salt. c: Temperature distribution of the coupled fluid and heat transport model 2. Fluid flow processes alter the thermal regime as displayed by the convex up- and downward shaped isotherms. The development of the coupled fluid system and thermal field is closely related to the distribution of permeable and impermeable sedimentary layers. d: Combination plot of the fluid velocity vectors (length non-scaled) and temperature distribution with reduced intensity in the background. The vectors illustrate the different fluid flow characteristics and changing velocities in the four aquifer systems decoupled from each other. 51

Figure 3.6 Map of the surface topography (defining the hydraulic upper boundary condition) with the locations of the different wells. V1 and V2 display the positions of two virtual wells for which calculated temperatures-depth gradients are plotted in Fig. 3.11. In sub-figures 3.6 a-g, the observed temperature values available for the different wells are plotted against depth in comparison with the modeled temperature gradients for the respective well. Observed temperatures are displayed by black rhombs. The modeled temperatures for conductive model 1 are represented by solid red lines, for the coupled model 2 by dotted orange lines and for the fault model 3 by solid grey lines. The depth position of the Rupelian, the Muschelkalk and the Zechstein layers are outlined by grey lines in the background in each figure. 54

Figure 3.7 a: Temperature distribution of the fault model 3 on the same vertical cross section as Fig. 3.5a. The location of the permeable fault cutting the central part of the cross section below the salt rim syncline is framed by the black rectangle. The locations where the two fault barriers dissect the profile are framed by a dotted black rectangle; b: Zoom on the temperature distribution around the permeable fault as indicated by the black rectangle in Fig. 3.7a. Convex upward shaped isotherms at the faults upper tip and convex downward shaped isotherms at the lower tip form a thermal anomaly induced by the permeable fault; c: Fluid velocity vectors (length non-scaled) and temperature distribution with reduced intensity in the background. The fluid flow in the subsalt sequence is influenced by the three faults dissecting this profile for which d-e display zooms into the fault areas for (d and f) the impermeable faults and for (e) the permeable fault. 58

Figure 3.8 Temperature distribution along the entire permeable fault with fluid vectors (length non-scaled). Alternating hotter (140-148°C) and colder domains (132-140°C) with corresponding convex upward and downward shaped isotherms indicate convective heat transport and vigorous fluid flow within the permeable fault. 60

Figure 3.9 Temperature distribution on a horizontal slice in -4000 m depth cutting (a) the no fault model 2 and (b) the fault model 3 whereas (c) displays the corresponding temperature difference map in which the no fault model 2 is subtracted from fault model 3. Positive values indicate higher temperatures in the fault model and vice versa. The temperature differences are up to 15°C higher in the NE-SW trending permeable fault than in the no fault model 2. Note the area influenced by the latter encompasses ~ 4.8 km at the NE tip of the fault (red arrow); (d-e) Temperature distribution on a horizontal slice in -4400 m depth cutting (d) the no fault model 2 and (e) the fault model 3. Fig. 3.9f shows the temperature difference map in which the no fault model 2 is subtracted from fault model 3. Positive values indicate higher temperatures in the fault model and vice versa. In contrast to -4000 depth, the temperatures in the permeable fault are up to -12 °C cooler than in the no fault model 2. 61

Figure 3.10 Pressure differences between no fault model 2 and fault model 3 (a) at -4000 m depth and (b) at -4400 m depth. Positive values indicate a lower pressure in the fault model whereas negative values correspond to a higher pressure in the fault model. Pressure offsets are visible and most prominent around the NW-SE oriented impermeable faults..... 64

Figure 3.11 Calculated temperatures-depth gradients for two virtual wells in the (a) SW and (b) NE parts of the NE-SW oriented permeable fault. Their locations are displayed in Fig. 3.6 in V1 and V2, respectively. The modeled temperatures for the no fault model 2 are represented by solid orange lines and for the fault model 3 by black solid lines. The depth position of the Rupelian, the Muschelkalk and the Zechstein layers are outlined by grey lines in the background in both figures. Below the Zechstein layer significant temperature differences demonstrate the local impact of the permeable fault on the thermal field. 72

Figure 4.1 (a) Map of Germany showing the outlines of the study area located in the federal state of Brandenburg. The study area (red rectangle) covers a surface of 180 km in N-S and of 200 km in E-W direction. 76

Figure 4.2 (a) 3D geological model of the study area with the stratigraphic layers resolved (vertical exaggeration: 7:1). Note the exposed Pre-Permian basement coming close to the surface at the southwestern margin and the Permian Zechstein diapirs controlling the structural configuration of the overburden sediments. At the southern basin margin, the Gardelegen and Lausitz Escarpments vertically offset the Pre-Permian basement against the Permian to Cenozoic basin fill by several km. 78

Figure 4.3 (a) Thickness map of the Tertiary Rupelian aquitard revealing large geological windows where this clay-rich layer was not deposited or has been eroded. Location of the Gardelegen and Lausitzer Escarpments are given by the solid black lines (also in the following subfigures). 80

Figure 4.4 Laterally variable temperature distribution at -8,000 m depth used as lower thermal boundary condition for all numerical simulations presented in the manuscript. It has been extracted from a lithosphere-scale conductive thermal model of Brandenburg by Noack et al. (2012)..... 86

Figure 4.5 (a-c) Temperature distribution along a horizontal slice at -1,000 m depth cutting the (a) no fault model (model 1), (b) impermeable fault model (model 2) and (c) permeable fault model (model 3)..... 88

Figure 4.6 (a) Temperature distribution along the fault planes in strike direction of the permeable Gardelegen (GF) and Lausitz faults (LF). Alternating hotter and colder domains characterize the thermal state within both fault zones. The red arrows indicate the location of two vertical cross sections shown in Figs. 4.7 and 4.8. The cross sections cut through the faults zones parallel to the N-S-axis. The red circle shows the location of the zoom of Fig. 4.9 (vertical exaggeration: 7:1). 91

Figure 4.7 N-S cross-section through the southwestern part of the Gardelegen fault (GF) plane (the location of the cross section is outlined in Fig. 4.6a by the red arrow on the right-hand side). In the combination plots of temperature distribution and fluid velocity vectors (subfigures 4.7b, d, f), the lengths of the fluid velocity vectors are non-scaled and the temperature distribution is shown with reduced intensity in the background. (a) Temperature distribution for model 1 in which no faults are integrated. The almost flat character of the isotherms reflects the diffusive nature of conductive heat transfer throughout the impermeable Pre-Permian basement. Isotherm deflection is only present where the conductive Zechstein salt is thick. (b) Fluid velocity vectors and temperature distribution for the no fault model 1 indicating horizontal flow in the upper aquifers. Predominantly upward directed flow only occurs where a hydraulic connection exists between the shallow and the deep Rotliegend aquifer. 93

Figure 4.8 N-S cross-section through the southeastern part of the Lausitz fault (LF) plane (the location of the cross section is outlined in Fig. 4.6a by the red arrow on the left-hand side). 97

Figure 4.9 (a) Zoom into the 3D flow field around the permeable fault zone (model 3) above the Permian Zechstein layer (grey-shaded). The temperature distribution along the strike of the Gardelegen fault zone is displayed in the background. Location of the zoom is delineated in Fig. 4.6a by the red circle. The velocity vectors clearly indicate flow from the surrounding aquifers towards the permeable fault zone. The lengths of the fluid velocity vectors are non-scaled. 100

Figure B.1 Location of study area in the south-eastern part of the Central European Basin System; depth to top pre-Permian (modified after Scheck-Wenderoth and Lamarche, 2005). Large rectangle encloses the area covered by the 3D structural and thermal model of Brandenburg, small rectangle indicates the location of the model of the geothermal in situ laboratory Groß Schönebeck, blue line – border of Brandenburg..... 139

Figure B.2 a: 3D view on the structural model of Brandenburg with colour key for the stratigraphic units differentiated in the model. The model is based on Gauss Krüger zone 4 coordinates. b: present topography of the area; black line – border of Brandenburg, blue line – rivers. 142

Figure B.3 Isopachs and depths to the base of successive stratigraphic units in the 3D model: a: base of Permo-Carboniferous volcanics; b: isopachs of Permo-Carboniferous volcanics; c: base of Permian Sedimentary Rotliegend; d: isopachs of Permian Sedimentary Rotliegend; e: base of Permian Zechstein salt; f: isopachs of Permian Zechstein salt. 144

Figure B.4 Isopachs and depths to the base of successive stratigraphic units in the 3D model: a: base of Triassic Buntsandstein; b: isopachs of Triassic Buntsandstein; c: base of Triassic Muschelkalk; d: isopachs of Triassic Muschelkalk; e: base of Triassic Keuper; f: isopach of Triassic Keuper; g: base of Jurassic; h: isopachs of Jurassic. 146

Figure B.5 a: Base of Lower Cretaceous; b: isopachs of Lower Cretaceous; c: base of Upper Cretaceous; d: isopachs of Upper Cretaceous; e: base of Tertiary; f: isopachs of Tertiary; g: base of Quaternary; h: isopachs of Quaternary. 148

Figure B.6 a: Cross section of the 3D structural model; b: cross section of the 3D thermal model, vertical exaggeration 1:10; c-f: Predicted temperature in °C extracted from the 3D conductive thermal model at the depth of c: 2000 m; d: 4000 m; e: 5000 m; f: 8000 m. 152

Figure B.7 a: 3D geological model of the Groß Schönebeck site consisting of 18 layers from the Carboniferous to the Quaternary. The solid and dotted lines indicate the location of a representative cross-section which cuts the model from north to south. b: Relief of the Top Zechstein salt. ... 155

Figure B.8 N-S cross-section illustrating simulation results, vertical exaggeration 1:7. a: Representative cross-section cutting the model from north to south with focus on the Zechstein Salt structure. b-d: Temperature distributions along the cross-section (a) after 250000 years of simulation time: for b: the purely conductive model, c: model in which the fluid density with a constant thermal expansion coefficient is included, d: model in which the fluid viscosity taken as function of temperature is considered in addition to fluid density effects with a non-linear variable thermal expansion. 160

List of tables

Table 2.1 Hydraulic and thermal properties used in the modelling, after Blöcher et al. 2010a. 14

Table 2.2 Fluid properties used for modelling. 14

Table 2.3 List of all numerical models described in this manuscript. The values of the width of the fault zone (WFZ) and permeability adopted in each of the respective models are also presented. 15

Table 3.1 Stratigraphic units with predominant lithologies and corresponding physical properties used for the numerical simulations of the geothermal field for the Groß Schönebeck area. Hydrogeological barriers separating the stratigraphic succession into different aquifer systems are highlighted (bold). 47

Table 3.2 Table with physical properties assigned for the faults. Porosity, heat capacity, thermal conductivity, radiogenic heat production values for the conduit represent average values of the geological layers (adopted from Bächler et al. 2003; Clauser and Villinger, 1990), whereas for the barriers the same values as for the Sedimentary Rotliegend are used. 49

Table 3.3 List of all simulations presented. 49

Table 3.4 Observed temperatures in wells used for the comparison with modeled temperatures of the conductive model 1, the coupled fluid and heat transport model 2 and an additional simulation in which the permeability of the Rupelian clay is decreased to k=1e-18 m² (s. chapter 3.5): Temperature (T) at total depth (TD) of temperature log and corrected temperature (Tcorr.) at TD of log for perturbed logs after Förster (2001). 53

Table 3.5 Observed temperatures in wells after Norden et al. (2008), used for the comparison with modeled temperatures of the conductive model 1, the coupled model 2 and an additional model in which the permeability of the Rupelian aquitard is decreased to k=1e-18 m² (s. chapter 3.5). 53

Table 4.1 Stratigraphic units with predominant lithologies and corresponding physical properties used for the numerical simulations. Hydrogeological barriers separating the stratigraphic succession into different aquifer systems are highlighted (bold). 84

Table 4.2 Thermal and hydraulic properties used for the fault modeling. 85

Table B.1 Input data for 3D structural modelling of Brandenburg: NEGB: 3D structural model of the Northeast German Basin (Scheck and Bayer, 1999); CEBS1: 3D structural model of the Central European Basin System (Scheck-Wenderoth and Lamarche, 2005); CEBS2: 3D structural model of the Central European Basin System (Maystrenko et al. 2010). 141

Table B.2 Input thermal properties for geothermal modelling after Bayer et al. (1997). 150

Table B.3 Thermal conductivities and radiogenic heat production used for the numerical simulations of the geothermal field for the Groß Schönebeck site; Thermal conductivities and radiogenic heat production for the Cenozoic to Upper Permian Zechstein after Norden and Förster (2006) and Norden et al. (2008); Data used for the Upper Rotliegend Formation to Late Carboniferous for thermal conductivities after Blöcher et al. 2010b, for Carboniferous after Ollinger et al. (2010); Values for the radiogenic heat production of the Upper Rotliegend Formation to Carboniferous after Ollinger et al. (2010). 157

Abstract

Faults can act as conduits, barriers or mixed conduit/barrier systems to fluid flow. Therefore, faults may significantly influence fluid flow regimes operating in the subsurface, possibly resulting in distinct variations of the deep thermal field. Both, flow dynamics and temperature changes are in turn crucial factors that need to be taken into account for geothermal energy exploration. In spite of the importance to understand the hydrothermal behavior of faults, studies that quantify the impact of faults on the deep geothermal field in 3D are, however, still sparse,- due to very limited information on physical fault property distribution, on in situ flow patterns in and around active faults as well as due to the methodological challenge to incorporate and simulate faults in 3D numerical models.

This study investigated the influence of faults on the subsurface fluid system and thermal field and explored the processes controlling fluid behavior and thermal distribution both within host rocks and faults as well as the dynamical interaction between both components. For this purpose, 3D finite element simulations of coupled fluid and heat transport have been carried out, both for synthetic and real-case model scenarios on different scales.

A small-scale synthetic model (200 m x 200 m x 120 m) was developed to systematically assess the impact of an inclined fault by changing gradually two main fault characteristics,- its hydraulic width and its permeability within the simulations. The results showed that fault-induced effects on the pressure and temperature are enhanced by increasing the width of a permeable fault due to the larger volume of fluid, which can be guided through the fault. An observed linear inverse relationship revealed that changing the fault width by one order of magnitude results in a fluid velocity decrease (~1e-01 m/s) within the fault. A high permeability contrast between fault and matrix ($\left[\frac{K_{fault}}{K_{layer}}\right]$ = 1e+06) favors fluid advection into the fault and leads to pronounced pressure and temperature changes in and around the same domain. When the permeability contrast between fault domain and host rock is low ($\left[\frac{K_{fault}}{K_{layer}}\right]$ = 1e+02), however, no fluid flow is observed in the fault, thus resulting in undisturbed hydrostatic pressure and temperature fields.

On the basis of these synthetic fault modelling results, the influence of faults on a larger scale have been analyzed within a more complex (real-case) geological setting,- a 3D model of the

geothermal research site Groß Schönebeck (50 km x 55 km x 5 km), located ~40 km north of Berlin. With respect to the hydrogeological setting, the relative impact of different heat transfer mechanisms on the temperature distribution was assessed, first for a reference case where no faults have been integrated. The results suggested that advection and convection are important heat transport processes in the shallow hydrothermal system (up to ~ -3000 m depth) whereas conduction is the predominant heat transport mechanism at greater depths (below ~ -3000 m). The integration of one permeable and three impermeable major faults, which dissect the target reservoir, resulted in distinct changes observed in the local fluid circulation, thermal and pressure field. Modelled convective circulation within the permeable fault decisively modifies the thermal field. This manifests as up to 15° higher temperatures at the upper tip and around 12 °C lower temperatures at the lower tip of the fault, compared to reference case. Within the low permeable faults, heat is transferred only by diffusion, inducing no thermal imprint but local deviations of the hydrostatic pressure field.

To investigate the impact of major fault zones on the basin-scale geothermal field, coupled fluid and heat transport simulations have been conducted for a 3D structural model for the area of Brandenburg (Noack et al. 2010; 2013). The fault zones vertically offset sedimentary sequences by several km. Moreover, the hydrodynamic interaction between fault zones and adjacent aquifer/aquitard systems was analyzed. Two end-member models, which represent different stress-states, comprising a case where the faults are modelled as tight zones and a model with integrated highly permeable fault zones, were chosen to compare to the reference model without fault zones.

The results showed that tight fault zones affect the flow field locally. Acting as hydraulic barriers, fluid flow is deviated with very low velocities along them within a range of ~ 1 km on either sides. The modelled local changes in the groundwater circulation system have no observable effect on the temperature field. Outside this range, flow direction and magnitudes of fluid velocities within the surrounding sediments are unaffected by the presence of tight fault zones. By contrast, permeable fault zones induce a pronounced signature on the thermal field extending over a distance of ~ 2.4-8.8 km at -1000 m depth and ~6-12 km at -3000 m depth. This thermal signature, characterized by alternating cooler and hotter temperature domains, is controlled by up- and downward directed flow within the fault domain, principally driven by existing hydraulic head gradients. Additionally, buoyancy forces may locally play a secondary effect on both the hydrodynamics and thermal field. When the fault zones are modelled as permeable structures, dynamic interaction between fault zones and surrounding sediments

could be observed. This interaction results in changes of the fluid circulation and thermal field within the sediments around the fault zones. These changes are reflected by fluid outflow from faults into the surrounding sediments and fluid inflow from sediments into the faults due to existing hydraulic head gradients.

All studies demonstrated that faults have a considerable impact on the computed fluid and heat flow. The permeability in faults and surrounding geological layers as well as the specific geological setting turned out to be crucial factors in controlling the different kinds of heat transfer mechanisms that may evolve in faults. In addition, the respective influence of faults on the geothermal field depends on the temperature distribution within the surrounding sediments and the fault width. Temperature variations caused by permeable faults may be local but significant as well as changes in fluid dynamics by both conduits and barriers. Thus, the results demonstrated the importance to consider faults in geothermal energy exploration.
In the final analysis, the simulations for the small-, regional- and basin-scale models showed that the outcomes cannot be transferred by upscaling and that it is necessary to consider each geological setting separately with respect to its configuration and scale dimension.

In summary, this study demonstrated that the consideration of faults in 3D finite element models for coupled fluid and heat transport simulations on different scales is feasible. As these type of numerical simulations integrate both, the structural setting of the subsurface and the physical processes controlling subsurface transport, the outcomes of this thesis may provide positive contributions in that they valuably complement field- and laboratory-based investigations.

Zusammenfassung

Geologische Störungen können als Grundwasserleiter, -Barrieren oder als gemischte leitende /stauende Fluidsysteme wirken. Aufgrund dessen können Störungen maßgeblich den Grundwasserfluss im Untergrund beeinflussen, welcher deutliche Veränderungen des tiefen thermischen Feldes bewirken kann. Grundwasserdynamik und Temperaturveränderungen sind wiederum entscheidende Faktoren für die Exploration geothermischer Energie. Trotz der Notwendigkeit, das hydrothermale Verhalten von Störungen zu verstehen, sind Untersuchungen, welche den Einfluss von Störungen auf das tiefe geothermische Feld im dreidimensionalen Raum quantifizieren noch immer rar,- aufgrund stark begrenzter Informationen zur Verteilung physikalischer Störungseigenschaften, in situ Fließwegen des Grundwassers in und um aktive Störungen sowie der methodischen Herausforderung, Störungen in 3D numerische Modelle zu integrieren und zu simulieren.

Diese Studie untersuchte den Einfluss von Störungen auf das Fluidsystem und das thermische Feld im Untergrund. Sie erforschte die physikalischen Prozesse, welche das Fluidverhalten und die Temperaturverteilung in Störungen und in den umgebenden Gesteinen kontrollieren und erkundete auch die dynamische Interaktion zwischen diesen beiden Komponenten. Dazu wurden 3D Finite Elemente Simulationen des gekoppelten Fluid und Wärmetransports für synthetische sowie reale Modelszenarien auf unterschiedlichen Skalen durchgeführt.

Um den Einfluss einer schräg einfallenden Störung systematisch durch die schrittweise Veränderung zweier Haupteigenschaften von Störungen, - deren hydraulische Öffnungsweite und Permeabilität, zu untersuchen, wurde ein klein-skaliges synthetisches Modell (200 m x 200 m x 120 m) entwickelt. Die Ergebnisse zeigten, dass sich die von einer permeablen Störung erzeugten Effekte auf Druck und Temperatur verstärken, wenn die Öffnungsweite der Störung vergrößert wird. Dies geschieht aufgrund des größeren Fluidvolumens, das durch die Störung geleitet werden kann. Ein inverser linearer Zusammenhang wurde festgestellt, welcher zeigt, dass sich die Fluidgeschwindigkeit in der Störung jeweils um ~1e-01 m/s verringert, wenn die Öffnungsweite der Störung um jeweils eine Magnitude vergrößert wird. Ein hoher Permeabilitätskontrast ($\left[\frac{K_{Störung}}{K_{Schicht}}\right]$ = 1e+06) zwischen Störung und umgebender Matrix begünstigt die Fluidadvektion hin zur Störung und führt zu ausgeprägten Druck- und Temperaturveränderungen innerhalb und um die Störung herum. Bei geringem

Permeabilitätskontrast zwischen Störung und umgebendem Gestein ($\left[\frac{K_{Störung}}{K_{Schicht}}\right]$ = 1e+02) findet hingegen kein Fluidfluss in der Störung statt, wobei das hydrostatische Druck- sowie das Temperaturfeld unverändert bleiben.

Auf Grundlage der synthetischen Modellierungsergebnisse wurde der Einfluss von Störungen auf einer größeren Skala anhand eines komplexeren (realen) geologischen Systems analysiert. Dabei handelt es sich um ein 3D Modell des Geothermie-Forschungsstandortes Groß Schönebeck (50 km x 55 km x 5 km), der ca. 40 km nördlich von Berlin liegt. Unter Berücksichtigung der regionalen Hydrogeologie wurde der relative Einfluss verschiedener Wärmetransportmechanismen auf die Temperaturverteilung abgeschätzt,- zunächst für ein Referenzmodell, in welches keine Störungen integriert wurden. Die Ergebnisse deuteten darauf hin, dass advektiver sowie konvektiver Wärmetransport vorwiegend das flache hydrothermale System (bis in etwa -3000 m Tiefe) steuern, während überwiegend konduktiver Wärmetransport das tiefe thermische Feld (unterhalb ~ -3000 m) kontrolliert. Die Integration von einer permeablen und drei impermeablen Hauptstörungen, welche das Reservoir durchschneiden, zeigte unterschiedlich starke Einflüsse auf Fluidzirkulation, Temperatur – und Druckfeld. Die modellierte konvektive Zirkulation in der permeablen Störung verändert das thermische Feld stark. Im Vergleich zu dem Referenzmodell äußert sich dies in bis zu 15°C höheren Temperaturen am oberen Rand und etwa 12°C niedrigeren Temperaturen am unteren Rand der Störung. In den gering durchlässigen Störungen wird die Wärme ausschließlich durch Diffusion geleitet. Der konduktive Wärmetransport beeinflusst das thermische Feld nicht, bewirkt jedoch lokale Veränderungen des hydrostatischen Druckfeldes.

Um den Einfluss großer Störungszonen mit kilometerweitem vertikalen Versatz auf das geothermische Feld der Beckenskala zu untersuchen, wurden gekoppelte Fluid- und Wärmetransportsimulationen für ein 3D Strukturmodell des Gebietes Brandenburg durchgeführt (Noack et al. 2010; 2013). Dabei wurde auch die hydrodynamische Interaktion zwischen Störungszonen und umgebenden Aquifer/Aquitardsystemen analysiert. Zwei Endgliedermodelle, welche verschiedene Spannungszustände repräsentieren und in welchen die Störungen einmal als hydraulisch undurchlässig und einmal als durchlässige Störungszonen integriert sind, wurden für den Vergleich mit einem Referenzmodell ohne Störungszonen ausgewählt.

Die Ergebnisse zeigten, dass die undurchlässigen Störungen den Fluidfluss nur lokal beeinflussen. Da sie als hydraulische Barrieren wirken, wird der Fluidfluss mir sehr geringen Geschwindigkeiten entlang der Störungen innerhalb eines Bereichs von ~ 1 km auf jeder Seite umgelenkt. Die modellierten lokalen Veränderungen des Grundwasserzirkulationssystems haben keinen beobachtbaren Effekt auf das Temperaturfeld. Außerhalb des lokalen Einflussbereichs der Störung werden weder Richtung des Fluidflusses noch Geschwindigkeiten innerhalb der umgebenden Sedimente durch die impermeablen Störungszonen beeinflusst. Hingegen erzeugen permeable Störungszonen eine ausgeprägte thermische Signatur innerhalb eines Einflussbereichs von ~ 2.4-8.8 km in -1000 m Tiefe und ~6-12 km in -3000 m Tiefe. Diese thermische Signatur, in der sich kältere und wärmere Temperaturbereiche abwechseln, wird durch auf- und abwärts gerichteten Fluidfluss innerhalb der Störung verursacht, der grundsätzlich durch existierende Gradienten in der hydraulischen Druckhöhe angetrieben wird. Zusätzlich können lokal Auftriebskräfte als Sekundäreffekt auf die Hydrodynamik und das thermische Feld wirken. Eine dynamische Interaktion zwischen Störungszonen und umgebenden Sedimenten konnte beobachtet werden, wenn die Störungen als permeable Strukturen modelliert wurden. Diese Interaktion resultiert in Veränderungen der Fluidzirkulation und des thermischen Feldes in den Sedimenten, welche die Störungszonen umgeben. Angezeigt werden diese Veränderungen durch Fluidausfluss von den Störungen in die umgebenden Sedimente sowie durch lateralen Zufluss von den Sedimenten in die Störungszonen aufgrund existierender Gradienten in der hydraulischen Druckhöhe.

Alle Studien haben gezeigt, dass Störungen einen beachtlichen Einfluss auf den berechneten Fluid-, und Wärmefluss haben. Es stellte sich heraus, dass die Permeabilität in der Störung und in den umgebenden geologischen Schichten so wie der spezifische geologische Rahmen entscheidende Faktoren in der Ausbildung verschiedener Wärmetransportmechanismen sind, die sich in Störungen entwickeln können. Zusätzlich hängt der jeweilige Einfluss von Störungen auf das geothermische Feld von der Temperaturverteilung in den umgebenden Sedimenten sowie von der Öffnungsweite der Störungen ab. Die von permeablen Störungen verursachten Temperaturveränderungen können lokal, jedoch groß sein, genauso wie die durch hydraulisch leitende und nichtleitende Störungen hervorgerufenen Veränderungen des Fluidystems.
Letztlich haben die Simulationen für die unterschiedlich skalierten Modelle gezeigt, dass die Ergebnisse sich nicht aufeinander übertragen lassen und dass es notwendig ist, jeden geologischen Rahmen hinsichtlich Konfiguration und Größenskala gesondert zu betrachten.

Abschließend hat diese Studie demonstriert, dass die Betrachtung von Störungen in 3D Finiten Elementen Modellen für die Simulation von gekoppeltem Fluid- und Wärmetransport auf unterschiedlichen Skalen möglich ist. Da diese Art von numerischen Simulationen sowohl die geologische Struktur des Untergrunds sowie die im Erdinnern ablaufenden physikalischen Prozesse integriert, können sie einen wertvollen Beitrag leisten, indem sie Feld- und Laborgestützte Untersuchungen vervollständigen.

1 Introduction

Faults and fractures are common in all types of rocks and occur at a variety of scales, from microscopic to continental (National Research Council, 1996). Faults may play a significant role in influencing physical and chemical processes in the subsurface (eg. Faulkner et al. 2010; Gudmundsson, 2011; Smith et al. 1990). More specifically, they act as barriers, conduits, or mixed conduit/barrier systems to fluid flow and as such form important components of fluid flow regimes in the upper crust (Smith et al. 1990; Antonellini and Aydin, 1994; Caine et al. 1996). Therefore, faults can change the flow dynamics of potential reservoirs which may result in distinct variations in temperature,- both crucial factors that need to be taken into account for geothermal exploration and related applications. Besides of geothermal research, the investigation of fault behavior and the way faults transport fluids is important also in many other fields of earth sciences, such as petroleum geology, volcanology, seismology, and hydrogeology (Gudmundsson, 2011).

However, understanding of fluid flow behavior in faults is still limited (Aydin, 2000). One reason for the difficulty in understanding fractures and faults behavior is their complexity (Aydin, 2000). Faults are dynamic systems and their mechanical, geochemical, and hydraulic properties may vary with such factors as lithology, temperature, pressure, and deformation rate over time and space (e.g. Knipe, 1993; Sibson, 1990). At the same time, in situ observations in active fault zones are generally difficult (Fairley, 2009). Only few quantitative data sets are available to provide geologically plausible physical properties for faults, because technology does not allow the acquisition of detailed property distributions from within active faults (Evans et al. 1997; Fairley, 2009). Information on fault property distributions can be derived from exhumed paleofaults (e.g. Antonellini and Aydin, 1994; Caine et al. 1996; Rawling et al. 2001; Reyer et al. 2012), borehole or/and laboratory measurements (e.g. Barton et al. 1995; Caine et al. 1996; Evans et al. 1997; Nativ et al. 1999) or modelling (e.g. Barton et al. 1995; Cappa, 2009). Insights of fluid flow in fault zones may be provided by geochemical and/or geophysical examinations (e.g. Bedrosian et al. 2004; Gébelin et al. 2011; Gottardi et al. 2013; Mulch et al. 2007; Pili et al 2002; Siniscalchi et al. 2010).

In general, such information on fault property distributions and on estimates of origin and fluxes of fluids are fundamental to investigate fault behavior. Based on these information, numerical models may be used to additionally investigate and quantify the interaction of active transport processes in faults and host rocks. Because such models can represent geological processes that occur at very slow rates and over (continental) length scales, they complement field- and

laboratory-based investigations (Person et al. 1996). Therefore, they allow an integrated evaluation of the main physical processes driving the system within the correct time and spatial scale and with regard to its three-dimensional geological architecture (Cacace et al. 2010).
Indeed, numerical models of coupled fluid and heat transport have been increasingly used beforehand to examine the thermo-hydrodynamic behavior of faults in a variety of geological systems. These investigations show that faults may significantly influence the hydrothermal field and therefore might have a high geothermal potential. 2D coupled fluid and heat transport simulations form the majority of these studies, and have been applied to various geological settings in Australia (Garven et al. 2001; Yang, 2004a,b), Ghana (Harcouët-Menou et al. 2009), the North Sea Central Graben (Fleming et al. 1998), the Rhine-Graben (Bense et al. 2008; Clauser and Villinger, 1990; Lampe and Person, 2002), Turkey (Magri et al. 2010) and the USA (McKenna and Blackwell, 2004; Wisian and Blackwell, 2004). However, due to the intrinsic methodological challenge to incorporate and simulate faults in 3D numerical models, such models are still sparse. Commonly, faults are modelled as idealized structures in 3D synthetic models (e.g. Alt-Epping and Zhao, 2010; López and Smith, 1995, 1996). Coupled fluid and heat transport simulations using different numerical approaches like finite differences or finite volumes have been applied to real-case geological systems. As an example, Bächler et al. 2003, showed that observed small-scale temperature anomalies can be explained only by convection systems within steeply dipping fault zones in the Rhine-Graben. Simulation results by Kühn et al. 2006 demonstrated that free convection in hydrothermal systems (Mount Isa in Australia) is highly sensitive to the 3D permeability distribution in the geological architecture. Within 3D finite element based simulations, however, fault implementation is still restricted to simplified orthogonal systems consisting of vertical and horizontal fracture elements. Such models comprise modelled study areas on specific scales in Australia (Schilling et al. 2013; Yang, 2006) and Italy (Baietto et al. 2008).

The aim of this thesis is to improve the knowledge on the influence that faults have on the fluid flow and thermal field. This is achieved by means of 3D finite element simulations of coupled fluid and heat transport. With regard to the numerical implementation, the questions whether and how it is possible to integrate and model inclined faults in 3D numerical models are addressed. The thesis focuses on the main research question on how faults may influence the coupled fluid and heat transport on different scales, including local-scale synthetic, regional- and basin-scale models. For the regional- and basin-scale models, the study areas of the hydrothermal research site of Groß Schönebeck (40 km north of Berlin) and Brandenburg are

chosen. Both study areas are located within the Northeast German Basin (NEGB) and combine natural fault systems with a complex geological setting. Moreover, the NEGB is a well-investigated sedimentary basin owing to over 40 years of hydrocarbon exploration and different large research projects (e.g. DEKORP-BASIN Research Group, 1999) (Scheck, 1997). Since then, a huge amount of data have been collected, including a dense net of industrial seismic lines and some hundreds of wells (Scheck and Bayer, 1999). Much of these data have been published (e.g. Hoth et al. 1993), and an excellent base of knowledge has been established over decades (Bayer et al. 1999 and references therein, e.g. Benek et al. 1996; McCann, 1996; McCann, 1998; Schneider and Gebhardt, 1993). Based on well data and depth maps, a detailed 3D structural model of the basin has been constructed by Scheck, 1997. Furthermore, the NEGB is subject of geological storage of CO_2 (e.g. Kühn et al. 2012; Liebscher et al. 2012) and of geothermal research and utilization (Seibt and Kellner, 2003). The basin hosts several of the centralized geothermal plants in Germany (Schellschmidt et al. 2000) and represents a good example for a low-enthalpy natural geothermal system (e.g. Hebig et al. 2012).

1.1 Objective

The objective of this thesis is to assess the influence of faults on the 3D coupled fluid and heat transport on different scales. In line with this objective, the following main research questions are addressed:

1. Is it possible to integrate and model inclined faults in 3D numerical models? If yes, what is the best method?
2. Which kind of heat transport processes may evolve in faults of different permeabilities?
3. Which are the main controlling factors for the development of different kinds of heat transport mechanisms and their resulting influence on the geothermal field?
4. What are the implications for geothermal energy exploration?

1.2 Thesis outline

Chapters 2, 3 and 4 are based on two manuscripts, accepted for publication in peer-reviewed scientific journals and one submitted manuscript, which is currently under review. Chapter 5 provides a final discussion and general conclusions resulting from the evaluation of the work at large. In the Appendix A, the governing equations of density coupled fluid and heat transport

in saturated porous media are given. Appendix B represents a complementary scientific paper, published in a peer-reviewed scientific journal which addresses questions of fluid and heat transport and has been additionally emerged during the time of this thesis.

1.3 Synopsis of the chapters

Chapter 2 Impact of single inclined faults on the fluid flow and heat transport: results from 3D finite element simulations

This chapter focuses on the question how a dipping fault influences the 3D hydrogeothermal field with respect to its permeability and its geometrical width. On that account, a sensitivity analysis for these two important fault parameters is carried out. To systematically assess the respective influence of the inclined fault on the fluid pressure, velocity and temperature, 3D simulations of coupled fluid and heat transport are carried out based on a small-scale and structurally simplified synthetic model, which includes one geological layer and one dipping fault. The synthetic finite element model is constructed by means of a recently developed and fully automated open-source pre-processor that enables implementing inclined fault planes in a three dimensional finite element model (Cacace et al. 2013). The numerical simulations are conducted by the open-source simulator "OpenGeoSys" (Kolditz et al. 2012a). By applying this new combined approach, the reliability of the method is tested by providing necessary fundamental information for simulations of more complex (real case) settings.

As a first author, I was the main contributing author for this manuscript. I constructed the model and conducted the numerical simulations, prepared the figures and wrote the text with minor contributions from the three co-authors.

Chapter 3 Controls on the deep thermal field – implications from 3D numerical simulations for the geothermal research site Groß Schönebeck

Based on the knowledge gained during the study leading to chapter 2, this chapter examines the influence of faults on a larger scale for the specific real-case geothermal site of Groß Schönebeck. First, the relative impact of different heat transport mechanisms on the regional-scale geothermal field is studied with respect to the specific regional hydrogeological setting. For this purpose, an existing 3D model of Groß Schönebeck based on an earlier structural model (Moeck et al. 2005), is structurally refined in order to differentiate major hydraulically active layers. Based on this improved model, conductive and coupled fluid and heat transport simulations are carried out by means of the commercial software FFEFLOW®. In a next step,

the influence of faults dissecting the target reservoir is assessed. Therefore, the respective faults are implemented as vertical faults in the geothermal reservoir zone and the model outcomes are compared with results from the model setting without faults. Finally, the simulated temperatures of all models are validated against temperature measurements from wells located in the study area. The discussion includes a detailed analysis of observed deviations between modelled and measured temperatures and discusses the choice of reasonable permeability values for both, faults and adjacent sedimentary layers, representing an important factor in influencing the fluid and thermal system.

For this manuscript, I was the main contributing author. I structurally refined the model and conducted the numerical simulations, prepared all figures and wrote the text with minor contributions from the co-authors Magdalena Scheck-Wenderoth and Mauro Cacace.

Chapter 4 Influence of major fault zones on the 3D coupled fluid and heat transport for the area of Brandenburg (NE German Basin)

Within this chapter, the impact of major fault zones, characterized by several km of vertical offset, is analysed on the 3D basin-scale fluid and heat system for the larger Brandenburg area. By means of this upscaling, it is verified whether the outcomes obtained from the previous regional-scale Groß Schönebeck study (chapter 3) are transferable to the basin-scale Brandenburg model. Furthermore, the hydrodynamic interaction between fault zones and adjacent sedimentary layers is considered. Therefore, two major fault zones are integrated into an existing structural model of Brandenburg (Noack et al. 2010, Appendix B). Coupled fluid and heat transport simulations are performed by using the commercial software FFEFLOW®. As the stated present-day stress field is a matter of debate, the fault zones could act as preferential pathways or as barriers for fluid flow. Therefore, different geological scenarios are tested by systemically changing the permeability of the fault zones. Two end-member models, including a model with tight fault zones and a model with highly permeable faults are compared to a setting where no faults are considered. The results provide new insights on hydraulic and thermal behavior of fault zones. By quantifying the heat transport mechanisms occurring in both fault zones and surrounding sediments, the dynamic interaction between these two domains is identified.

For this paper, I was the main author. Based on the existing structural model, I carried out the numerical simulations and prepared all figures. The text was written by myself with minor contributions from the co-authors Mauro Cacace and Magdalena-Scheck-Wenderoth.

Appendix B Assessment of the present-day thermal field (NE-German Basin) – inferences from 3D modelling

This complementary paper is devoted to the characterization of the thermal field for the Brandenburg area and the geothermal research site of Groß Schönebeck. The first part of this publication describes the model construction and the resulting structural setting of a refined 3D structural model of Brandenburg in northeast Germany. To assess the regional thermal field, the steady-state conductive thermal distribution is calculated and compared with published heat flow and temperature data. The second part of this paper zooms on a specific location of Brandenburg by representing results from numerical simulations for a 3D model of the geothermal site of Groß Schönebeck. Conductive as well as coupled fluid and heat transport simulations are carried out by stepwise increasing the degree of coupling between the governing equations to assess the impact of each heat transport mechanism on the geothermal field. The simulations for the Groß Schönebeck model are performed by means of the commercial software FFEFLOW®. By investigating the dominant heat transport mechanisms, this study provides first insights of the controls of the deep thermal field of Groß Schönebeck. The results served as a basis for the detailed analyses of the regional fluid system and thermal field and subsequent integration of faults (chapter 3).

The first part of the related manuscript covering the results of the Brandenburg model has been written by the first author Vera Noack, while I was responsible for the second part of the manuscript dealing with the coupled simulations of the Groß Schönebeck model. Therefore, I have evaluated and summarized the results of the coupled simulations and prepared the last two figures of the paper. I contributed in minor parts to the abstract, introduction and conclusions by addressing the Groß Schönebeck case study.

2 Impact of single inclined faults on the fluid flow and heat transport: results from 3D finite element simulations

Abstract

The impact of inclined faults on the hydrothermal field is assessed by adding simplified structural settings to synthetic models. This study is innovative in carrying out numerical simulations because it integrates the real 3D nature of flow influenced by a fault in a porous medium, thereby providing a useful tool for complex geothermal modelling. The 3D simulations for the coupled fluid flow and heat transport processes are based on the finite element method. In the model, one geological layer is dissected by a dipping fault. Sensitivity analyses are conducted to quantify the effects of the fault`s transmissivity on the fluid flow and thermal field. Different fault models are compared with a model where no fault is present to evaluate the effect of varying fault transmissivity.

The results show that faults have a significant impact on the hydrothermal field. Varying either the fault zone width or the fault permeability will result in relevant differences in the pressure, velocity and temperature field. A linear relationship between fault zone width and fluid velocity is found, indicating that velocities increase with decreasing widths. The faults act as preferential pathways for advective heat transport in case of highly transmissive faults, whereas almost no fluid may be transported through poorly transmissive faults.

Published as:
Cherubini Y, Cacace M, Blöcher M, Scheck-Wenderoth M (2013) Impact of single faults on the fluid and heat transport: results from 3D finite element simulations. Environmental Earth Science 70(8): 3603-3618, http://link.springer.com/article/10.1007%2Fs12665-012-2212-z. The final publication is available at link.springer.com.

2.1 Introduction

Faults and fractures occur throughout the entire crust in scales ranging from millimetres to several kilometres (Press and Siever, 1995). They have a significant impact on physical processes controlling heat transfer and fluid motion in the subsurface as they disturb the conformal succession of geological layers.

Depending on their hydraulic properties, faults can act as preferential pathways or as barriers to fluid flow (Barton et al. 1995). Therefore, it is important to understand the role of faults and their impact on the fluid and heat transport in order to predict geothermal energy reserves. Important fault parameters are their physical properties (e.g. fault permeability), their orientation with respect to the recent and paleo stress fields and their geometrical configuration, comprising their dipping angle and width.

Numerical simulations provide a useful and increasingly common tool for geothermal applications as they consider both, the structural setting of the subsurface and the physical processes controlling the fluid and heat transport. As such, numerical simulations can provide essential information on the fluid motion and temperature variations in the subsurface. It is, however, still a methodological challenge to incorporate faults in 3D numerical simulations of the thermal field.

In this paper, the impact of faults on the geothermal field is studied by 3D modeling of varying scenarios with an inclined fault. This approach represents an improvement, as previous modelling studies have been mainly restricted to 2D simulations or to simplified orthogonal systems that only consists of vertical and horizontal fracture elements. The latter, however, evidenced that faults may decisively influence the thermal field.

2D flow and heat transport simulations reveal that hot basinal fluids may be guided in faults from the basement to the surface (Magri et al. 2010). Accordingly, large-scale free convection induced by buoyancy-driven flow may develop in such fault zones. In larger 2D models at the scale of extensional sedimentary basins, Simms and Garven (2004) also found that steeply dipping extensional faults can provide pathways for vertical fluid flow across large thicknesses of basin sediments, thus modifying the dynamics of thermal convection.

With their 3D studies, Bächler et al. 2003, found that the observed small-scale temperature patterns can be explained only by convection systems within steeply dipping fault zones in the Rhine-Graben. Other studies (López and Smith, 1995, 1996) show that different fluid and heat flow regimes at a vertical fault plane fall in well-defined regions in permeability space.

The importance and need for 3D modelling of heat transfer in fractured crystalline rocks was clearly indicated by Kolditz (1995), who used different parallel fracture models. In these

numerical experiments, the dimensional effect of heat-matrix diffusion and its impact on the thermal performance of a hot dry rock reservoir was quantified by comparison of 2,5D with 3D models. These simulations showed that the reduced dimension models overestimate the thermal drawdown by up to 11% after 20 years of production.

Different approaches exist to model faults, including the discrete fracture network (DFN) and the porous medium, as well as the hybrid approach combining these two.

Several studies focused on flow simulations in 3D discrete fracture networks (e.g. Adler and Thovert, 2009; Cacas, 1990; Erhel et al. 2009; Graf and Therrien, 2008; Herbert, 1996; Müller et al. 2010). The DFN enables modelling the connectivity of the faults and joints that give rise to reservoir scale flow behavior. However, no information on the dynamics of the coupling between the flow occurring in the fracture network and in the surrounding matrix can be achieved by the DFN approach.

As opposed to the DFN, the porous media approach provides information on the dynamics of the coupling between the flow occurring in the fractures and the porous media. In the porous medium approach, any 3D mesh quickly becomes too complex for the fault domain, whereas faults can easily be modelled in two dimensions, including different orientations and intersections.

Here, the hybrid approach is used in which faults are implemented as 2D discrete feature elements in a porous medium. Discrete feature elements can only be implemented as vertical or horizontal elements in a 3D body in commercial software so far (COMSOL, Løtveit, 2009; Pryor, 2011; FEFLOW, Diersch, 2002). Nevertheless, geometrical modelling and mesh generation was the subject of several studies (Blessent et al. 2009; Graf and Therrien, 2008; Kalbacher et al. 2007).

3D flow and heat transport simulation studies with inclined faults are not yet concluded. This study aims to fill this gap by a systematic analysis of a simplified structural setting.

Here, a fault is modelled as an inclined plane (discrete element) in a 3D porous matrix domain. The dipping fault plane approximates more accurately the natural fault geometry than the usual orthogonal fault implementation. Additionally, applying the hybrid approach provides information on the dynamics of the coupling between the flow occurring in the fractures and the surrounding porous media. Therefore, the interaction between discrete flow paths and rock matrix can be specifically addressed.

The goal of this work is to systematically assess the influence of faults on the fluid system and thermal field. In this regard, simulations of the coupled fluid and heat transport are carried out for a synthetic model including one geological layer and one dipping fault. The synthetic finite

element model is constructed and simulated by applying a combination of open source software (pre-processor “MeshIT”, Blöcher et al. 2010a, Cacace et al. 2013, and numerical simulator “OpenGeoSys”, Kolditz et al. 2012a). To evaluate the main impact of the fault on the pressure, velocity and temperature fields, first a background model (no fault implemented) is compared to a reference model (fault integrated). Secondly, sensitivity analyses are conducted to quantify the effects of the fault`s transmissivity in terms of its geometrical width and permeability on the fluid flow and thermal field.

As such, the simulation results provide basic principles of how the fluid and heat transfer is affected by different configurations of an inclined fault. By applying the combination of open-source software, the study furthermore tests the reliability of this method and provides essential basics for future simulations of real case scenarios with more complex fault and fracture systems (Cacace et al. 2013).

2.2 Methodology

2.2.1 Mathematical and physical principles

For the synthetic models used in this study, the input data required are scattered data points (x-, y-, and z-coordinates) outlining the 3D geometry of the system to be simulated (geological units plus faults). Based on this information, consistent, unstructured, boundary-conforming Delaunay tetrahedral meshes are generated by means of a fully automated approach (Blöcher et al. 2010a). Faults are represented as 2D planar (in this study) or not planar discrete structures embedded in the outer boundary volume of the rock matrix. The resulting 3D meshes can be directly imported to existing finite element/volume numerical software to simulate coupled processes in faulted geological systems.

To carry out numerical simulations of coupled fluid and heat transfer, the mesh is imported in the open source software OpenGeoSys (Kolditz et al. 2012a; Kolditz et al. 2012b). OpenGeoSys is a finite element based numerical simulator for coupled thermal, hydraulic, mechanical, and chemical (T-H-M-C) processes for both fractured and non-fractured porous media (Kolditz et al. 2012a; Wang et al. 2011; Watanabe et al. 2010).

The present work focuses on simulating the coupled groundwater fluid dynamics and resulting temperature field (i.e. T-H simulation). The simulation of further couplings, e.g. of mechanical and geochemical processes are beyond the scope of this work. Accordingly, the following description of the numerical aspects of the OpenGeoSys software covers only hydrothermal

processes. A more detailed description taking rock deformation mechanics into account may be found in Watanabe et al. 2010.

To simulate coupled T-H processes in fractured porous media, OpenGeoSys follows a hybrid approach where discrete fractures are superimposed on a continuous volume representing the porous matrix (Kolditz et al. 2012b). This results in a macroscopic (volume averaged) mathematical description of the relevant governing equations, which differ between the two subdomains (fractures and rock matrix) of the fractured porous medium.

The equation describing fluid flow in 3D saturated porous media as implemented in the OpenGeoSys software is given by the following equation balanced over a reference volume (REV):

$$S_s \frac{\partial P}{\partial t} + (\nabla \cdot \mathbf{q}_f) = Q_f \qquad 1$$

where P is the fluid pressure, $S_s = \gamma_w(\beta + \varepsilon\alpha)$ is the specific storage, γ_w being the fluid specific weight, ε being the bulk porosity, β being the bulk aquifer material compressibility, and α the fluid compressibility, $\mathbf{q}_f$ is the fluid (Darcy) flux, and Q_f is the fluid mass source/sink term. Darcy's law is adopted to represent the fluid flow. Accordingly, the flux term $\mathbf{q}_f$ is then given by:

$$\mathbf{q}_f = -\frac{\mathbf{k}}{\mu}\left(\nabla P - \rho_f \mathbf{g} \nabla z\right) \qquad 2$$

where μ is the fluid dynamic viscosity, $\mathbf{g} = (0,0-g)$ is the gravity vector, z the reference depth, and $\mathbf{k}$ is the intrinsic permeability tensor.

Within the 2D fault domain the fluid equation takes the form:

$$b_m S_s \frac{\partial P}{\partial t} + \nabla \cdot \left(b_h \mathbf{q}_f\right) = Q_f \qquad 3$$

with S_s specific storage of the fault (assumed to be fully fluid saturated), and $b = b_m + b_h$ the effective (average) width of the fault comprising both hydraulic (b_h) and mechanical effects (b_m). All other parameters are the same as described as in equation 1.

As in the porous medium case, Darcy's law is assumed to describe groundwater flow within the fault under the widely adopted theoretical assumption of parallel fracture walls, thus resulting in:

$$\mathbf{q}_f = -\frac{\mathbf{k}}{\mu_f}\left(\nabla P - \rho_f \mathbf{g} \nabla z\right) \qquad 4$$

Where μ_f is the fluid dynamic viscosity, $\mathbf{g} = (0,0-g)$ is the gravity vector, z the reference depth, and $\mathbf{k} = \frac{b_h^2}{12}\mathbf{I}$ the permeability tensor with I the unit tensor assuming isotropic permeability along the fault plane. Following Darcy`s law, the study only deals with laminar flow within the fault.

The heat transport (advection plus diffusion) equation for the matrix is given by:

$$(\rho c)_{eff}\frac{\partial T}{\partial t} + \nabla \cdot \mathbf{q}_T = Q_T; \quad \mathbf{q}_T = \phi(c\rho)_f \mathbf{v}T - \lambda_{eff}\nabla T \qquad 5$$

with $(\rho c)_{eff} = \varphi(\rho c)_f + (1-\varphi)(\rho c)_s$ being the specific heat capacity of the system involving a fluid $(\rho c)_f$ and a solid $(\rho c)_s$ phase.

The heat transport equation for the fracture is given by:

$$b_m(c\rho)_f\frac{\partial T}{\partial t} + \nabla \cdot \mathbf{q}_T = Q_T; \quad \mathbf{q}_T = b_h(c\rho)_f \mathbf{v}T - b_m\lambda_f\nabla T \qquad 6$$

In both of the above equations $(\rho c)_{eff} = \phi(c\rho)_f + (1-\phi)(c\rho)_s$ is the heat storage term of the porous medium with φ porosity, c_f specific heat capacity of the fluid, ρ_f fluid density, c_s rock specific heat capacity, and ρ_s rock density. T is the temperature, $\mathbf{q}_T$ is the heat flux taking into account both advective $\varphi(c\rho)_f \mathbf{v}T$ in Eq. 5 and $b_h(c\rho)_f \mathbf{v}T$ in Eq. 6 with $\mathbf{v} = \frac{\mathbf{q}_f}{\varphi}$ being the fluid velocity and dispersive terms $\lambda_{eff}\nabla T$ in Eq. 5 and $b_m\lambda_f\nabla T$ with $\lambda_{eff} = \varphi\lambda_f + (1-\varphi)\lambda_s$ being the heat conductivity of the porous medium. Q_f is the heat source/sink term. In Eq. 6 no mechanical effects on the fracture width are taken into account.

The two sets of equations (fluid flow and heat transport) for the fault and porous medium domain are coupled by means of the Darcy velocity ($\mathbf{v} = \frac{\mathbf{q}_f}{\varphi}$). Additionally, a nonlinear coupling may arise from considering thermal and pressure effects on the fluid density and thermal effects on the fluid viscosity, respectively, in the momentum equation (Eq. 2 and 4), e.g. Kolditz and Diersch, 1993; Magri, 2004). These additional coupling terms generally lead to highly nonlinear systems of partial differential equations that are reflected in usually unstable and therefore error prone numerical simulations. Stabilization techniques by relaxation and preconditioning methods during the matrix assemblage, upwinding and iterative numerical

procedures, as well as proper discretization methods, are the subject of a still open debate within the modeller community (e.g. Diersch and Kolditz, 2002; Kolditz and Diersch, 1993; Simmons et al. 2001).

Within the applied hybrid approach, the two systems of equations (fault and matrix) are numerically solved by standard finite element techniques. The link between matrix and fault flow dynamics is then assured by forcing a continuity condition on the velocity field for the finite elements sharing edges with the boundaries between the two domains. Consequently, the equations governing groundwater and heat transport for the fault are represented as averages on a reference volume by means of the width of the fault zone `WFZ` ($b = b_m + b_h$). This parameter together with the fault permeability (k) uniquely determines the transmissivity of the fault as $T = b \cdot k$ and provides the major constraints on the potential for fluid to flow along the fault plane.

The WFZ defines the width of the area, which is influenced by a zone of different assigned permeability in the area of the determined fault zone.

2.2.2 Model set-up

The geometrical model consists of a single homogeneous and isotropic geological layer extending 200 m x 200 m horizontally, 120 m in the vertical direction and is cut by a NE-SW striking, dipping fault (dip angle 80.5° towards SE) (Fig. 2.1a). The fault dissects the geological layer over a horizontal length of 233 m. To avoid boundary effects, the fault does not extend to the model boundaries. The final 3D mesh used for all numerical simulations consists of approximately 19.000 nodes and 100.000 elements.

To solve the equations governing the coupled fluid and heat transport, physical properties have to be assigned to all domains of the model. Hydraulic and thermal properties as assigned for both the layer and the fault are listed in Table 2.1. Fluid parameters used in the modelling are listed in Table 2.2.

Table 2.1 Hydraulic and thermal properties used in the modelling, after Blöcher et al. 2010a.

Property	Unit	Layer	Fault
Porosity φ	[-]	0.08	0.3
Storage β	[1/Pa]	7.0E-10	4.6E-10
Permeability κ	[m^2]	1.0E-14	1.0E-08
Density ρ_s	[kg/m^3]	2600	1000
Heat Capacity c_s	[J/kgK]	1000	4680
Thermal Conductivity λ	[J/Kms]	3	0.6

Table 2.2 Fluid properties used for modelling.

Fluid parameters	Unit	Layer
Density ρ	[kg/m^3]	1000
Viscosity η	[Ns/m^2]	1.0E-03
Specific thermal conductivity	[W/mK]	0.6
Specific heat capacity	[kJ/kgK]	4.186

2.2.3 Simulations

A total number of 11 coupled fluid and heat transport simulations are carried out. Of these, 6 simulations are shown which are representative for the selected parameters as listed in Table 2.3.

The background model is the model without fault. This model is run to separate the hydraulic and thermal effects induced by the boundary conditions from those related to the fault. The results of the background model are compared to the reference model, on which all other simulations are based on. A high permeability contrast between the fault (K_{fault} = 1e-08 m²) and the layer (K_{layer} = 1e-14 m²) is implemented (Table 2.1) to easily quantify magnitudes and characteristics of the disturbances induced by the fault with respect to the model without fault (background model). The WFZ in the reference model is set to 0.05 m. The assigned porosities are identical in all models and have been chosen such that a pronounced contrast between fault (φ = 0.3) and matrix (φ = 0.08) porosity is considered (Table 2.1).

To investigate the effects of fluid density, an additional simulation for the reference model is carried out. The fluid density is taken into account as a function of temperature with a constant thermal expansion coefficient.

To quantify the impact of the geometry and the permeability of the fault on the coupled fluid and heat transport, two groups of sensitivity analyses are conducted: for the WFZ, model with minimum WFZ and model with maximum WFZ, and for the permeability of the fault, model with minimum permeability and model with maximum permeability (Table 2.3).

Table 2.3 List of all numerical models described in this manuscript. The values of the width of the fault zone (WFZ) and permeability adopted in each of the respective models are also presented.

width of the fault zone b [m]	fault permeability k [m^2]	transmissivity T = b*k [m^3]	model names	
0	0	0	background model	
0.05	1.00E-08	5.00E-10	reference	fault models
0.0005	1.00E-08	5.00E-12	min WFZ	
15	1.00E-08	1.50E-07	max WFZ	
0.05	1.00E-12	5.00E-14	min permeability	
0.05	1.00E-08	5.00E-10	max permeability	

2.2.4 Initial and boundary conditions

In addition to the assigned material properties, the numerical solution depends on the choice of boundary conditions. The boundary conditions prescribed for all models are best illustrated for the case of the background model.

For the fluid pressure, an initial pressure value of 1.75e+06 Pa is set for the total model domain. In addition, pressure boundary conditions are assigned at the northern and southern side of the model (Fig. 2.1a).

The fluid pressure values are chosen to approximate the pore pressure gradient in a free water column that averages to 10 MPa km^{-1} (Eisbacher, 1996). The pressure conditions are chosen to simulate hydrostatic pressure conditions that would correspond to a depth range of 125-225 m and 75-175 m for the northern and southern boundary, respectively.

The values are calculated with $p = \rho*g*z$ with the fluid density $\rho = 1000$ kg/m^3, the gravitational acceleration $g = 10$ m/s^2 and z corresponding to the height of the liquid column.

For the northern boundary of the model, the fluid pressure is interpolated between 1.25e+06 Pa at the top and 2.25E+06 Pa at the bottom which results in an increasing pressure from top to bottom. Analogously, the fluid pressure at the southern boundary of the model increases from 0.75e+06 Pa at the top to 1.75e+06 Pa at the bottom.

Overall, the pressure decreases from the northern to the southern boundary. This pressure gradient (∇p = 0.5e+06 Pa / 200 m = 2500 Pa/m) generates a regional flow field from the north to the south.

As for the pressure, an initial temperature also has to be assigned to the model. An initial temperature value of 60°C is applied for the entire model domain. In addition, temperature boundary conditions are assigned along the northern boundary of the model (Fig. 2.1b). A temperature value of 40°C is set along the NE-edge of the model, whereas a temperature value of 80°C is applied along the NW-edge. The temperature for the area in between is obtained by interpolation of these two temperatures. Therefore, the temperature linearly increases from east to west from 40°C to 80°C along the northern boundary. Accordingly, cold water (40°C) spreads out from the north-eastern part of the model and warm water (80°C) is provided from the north-western part of the model.

These thermal boundary conditions induce a mixture of cold and hot water and facilitate tracing of the fluid flow paths in and around the fault on the basis of the temperature distribution.

Although a variation with depth of the imposed temperature along the northern boundary would have been closer to reality, choosing horizontally varying temperature boundary conditions has some important advantages in terms of visualization and understanding all processes occurring within the simulations.

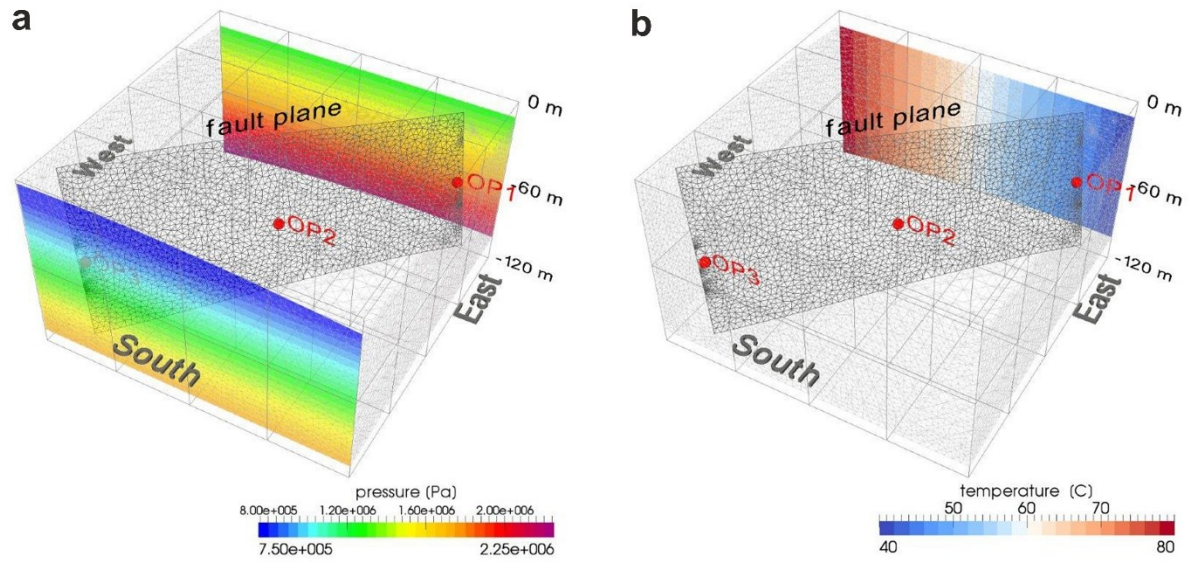

Figure 2.1 Wireframe of the 3D mesh (geological layer + inclined fault) with location the three observation points and pressure (a) as well as temperature (b) boundary conditions applied in all simulations.

2.2.5 Time discretization

To ensure that stable conditions for the pressure, velocity and temperature evolve in the numerical simulations all calculations are carried out for approximately 500 years. The discrete time steps are calculated manually based on a Courant criterion to prevent numerical oscillations.

2.3 Results

2.3.1 Background model

The results of the background model without fault represent the basic pressure, velocity and temperature field induced only by the applied boundary conditions (Figs. 2.2a and 2.2b).

Fluid pressure, fluid velocity and temperature fields

Starting from the initial pressure value of 1.75e+06 Pa in the entire domain, the pressure field evolves according to the applied boundary conditions at the northern and the southern side. The pressure gradient imposed by the boundary conditions generates a regional flow field from the north to the south. Figure 2.2a shows the corresponding pressure drop from the north to the south illustrated by the 3D pressure distribution within the entire model for the final state at approximately 500 years.

The distribution of isobars demonstrates that the pressure linearly decreases from the north to the south. The isobars run continuously through the model, reflecting an undisturbed regional hydrostatic pressure field. The resulting homogenous regional flow field is characterized by Darcy velocities of 3.1e-07 m/s.

Based on the initial temperature of 60°C for the entire model domain, the temperature field starts to develop after starting the simulation due to the temperature and pressure boundary conditions. The stable 3D temperature field of the total domain for the last time step shows the inflow of cold water of 40°C at the north-eastern side and the income of 80°C hot water at the north-western model side (Fig. 2.2b). Accordingly, the 3D isotherms clearly reflect a linear temperature increase from 40°C at the NE-edge to 80°C at the NW-edge of the model induced by the adopted temperature boundary conditions.

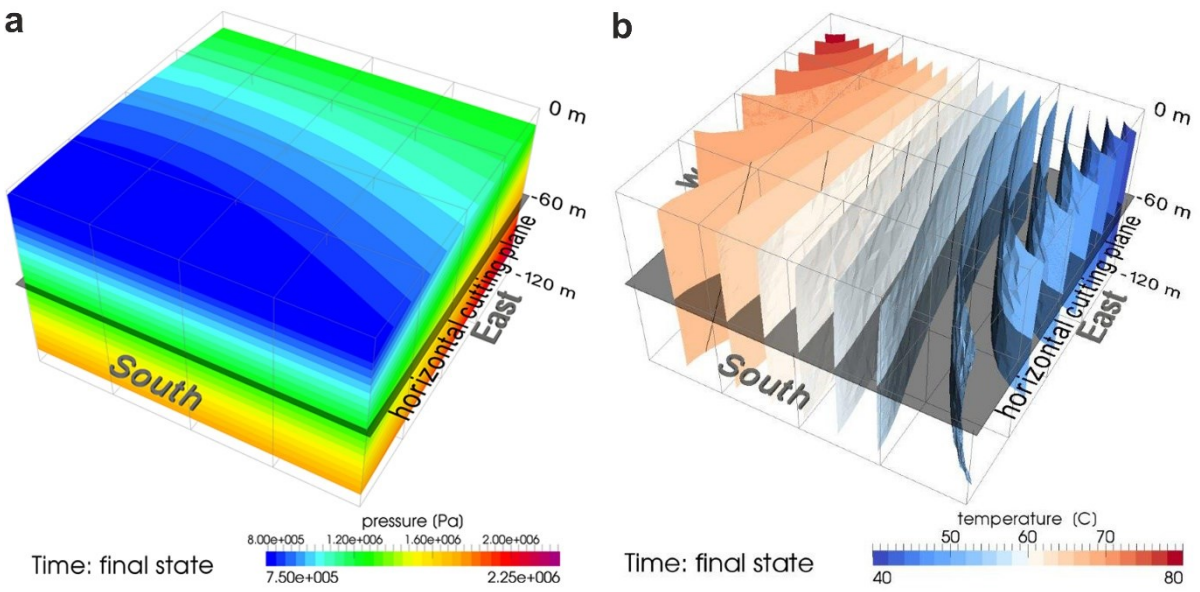

Figure 2.2 3D pressure field (a) and distribution of discrete 3D isotherms (b) for the background model with location of a horizontal cutting plane at -60 m.

2.3.2 Fault model

Early stage pressure, fluid velocity and temperature evolution

All models discussed show a similar early stage evolution characterized by variable pressure and fluid velocity fields during their equilibration phases and a purely diffusive temperature evolution. These aspects are induced by the imposed pressure boundary and initial conditions that require a finite (approximately 1 month) simulation time for the system to equilibrate. During this stage, the temporal behavior of the system is affected only by local and transient hydrostatic pressure gradients with the fault playing no role. For this reason, the main characteristics of this transient phase in the evolution of the system are described only once for the case of the reference model (Table 2.3). It is, however, worth noting that similar conclusions are valid for all other models that include the fault.

The temporal evolution of the pressure field during the entire simulation is illustrated by means of three discrete observation points set at different locations along the fault plane (Figs. 2.1a and 2.1b). The depth of all three points is approximately defined as the average of the model vertical extension (60 metres below the top surface and above the bottom surface).

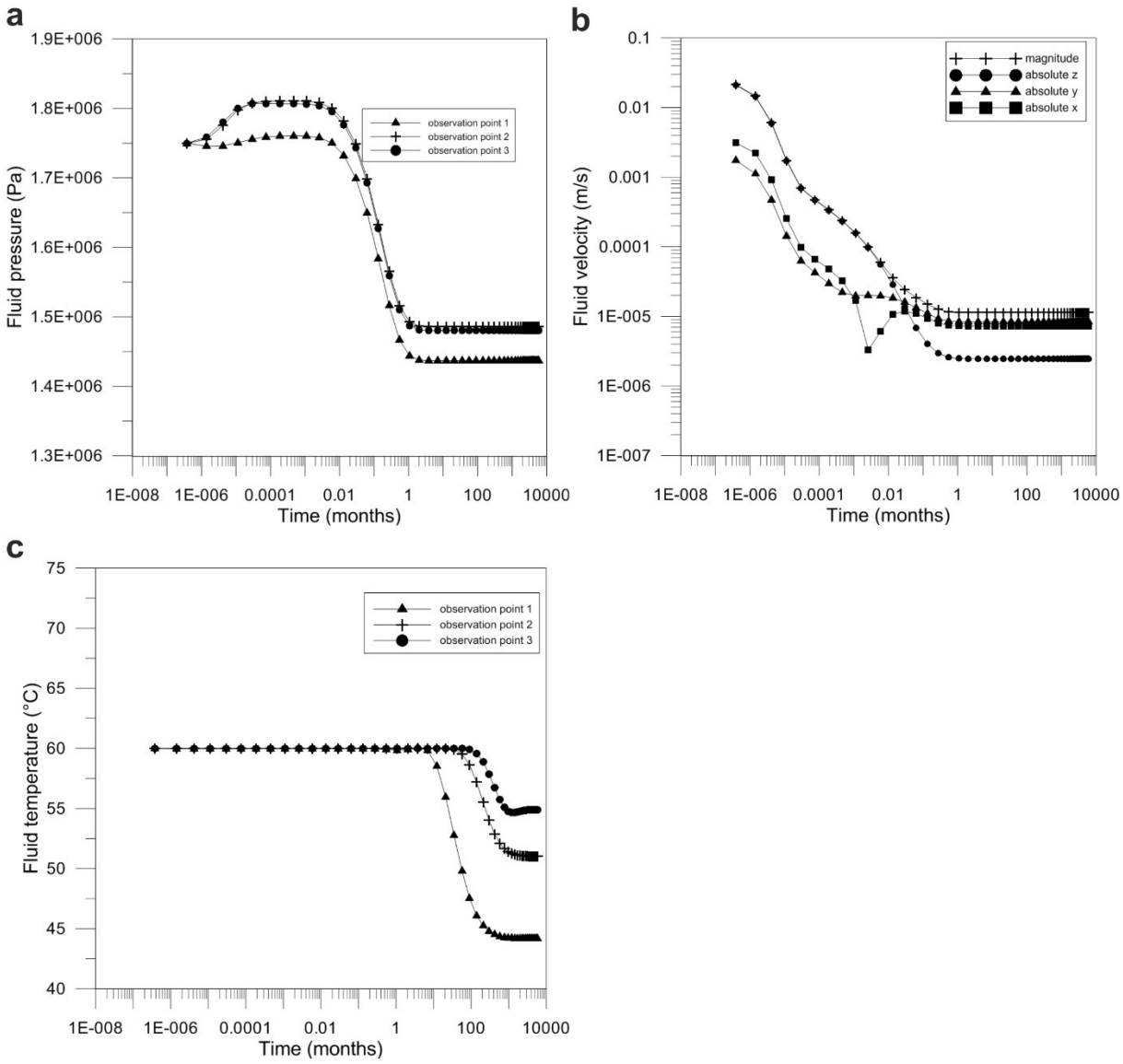

Figure 2.3 Fluid pressure evolution through time at the three observation points (a), fluid velocity evolution for observation point 3 (b) and temperature evolution along the three observation points (c), see Figures 2.1a and 2.1b for their respective location.

The pressure evolution in Figure 2.3a clearly shows an unsteady early stage (up to 1 month of simulation time). During this time period, the pressure first increases and then decreases with time as the regional pressure field is stabilizing according to the assigned pressure boundary and initial conditions. Pressure boundary conditions assigned along the northern and southern boundaries induce a regional horizontal pressure gradient on the model, creating the observed changes in the pressure field initially set constant within the model. Differences in the pressure values between the three observation points are related to their locations with respect to the constant pressure conditions set at the northern and southern boundaries. The transient pressure field behavior is also reflected in a temporally variable field of the fluid flow. Figure 2.3b

illustrates the temporal evolution of the velocity field at observation point 3 (vector components and magnitudes), which is also representative for the other observation points.

The evolution of the fluid velocity is characterized by an initial decrease of all velocity components (until approximately 0.01 month). This correlates with the modelled increase in the pressure field for the same time period. Comparing the computed magnitudes of the velocity vectors with the respective values of their three components, it is clear that during this stage fluid flow is only vertical in the observation point.

Very high fluid velocities (~1e-03 ms^{-1}) are found along the fault plane, showing a consistent vertical downward oriented vector field. In contrast, relatively low (downward) fluid velocities characterize the bounding domain of the porous rock (Fig. 2.4a).

The modelled transient pressure field explains the resulting consistent vertical velocity field. During pressure stabilization, the system is under hydrostatic load conditions with no horizontal pressure gradients, induced by the pressure boundary conditions. Local vertical pressure gradients generate a corresponding vertical flow whose downward orientation is maintained by hydrostatic pressure conditions. Differences in velocities between the fault and the porous medium are only related to the modelled contrast between the high fault transmissivity and the relative low rock permeability.

A change in the overall fluid velocity field is observed approximately after 0.01 month of simulation time. Figure 2.3b indicates that the changes in the velocity magnitudes is coeval with a gradual change in its direction with velocity vectors that start deviating from the vertical direction to orientate on the horizontal (x, y)-plane. These changes in the velocity field are shown in Fig. 2.4b. Within the fault plane, the fluid starts to flow sub-horizontal. Magnitudes of fluid velocities are no longer constant along the fault plane.

Lower velocities (~1e-06 ms^{-1}) are found at the north-eastern tip of the fault where fluid coming from the outer porous medium is driven into the fault by an almost stable regional pressure field. Due to the higher fault permeability, compared to the surrounding porous medium, the fluid becomes faster when entering the fault. Within the fault plane, the fluid further accelerates in the northern part because the pressure distribution provides more inflow than outflow for the fault zone. In contrast, in the southern part the outflow from the fault becomes dominant resulting in a reduction of fluid velocity within the fault. Due to the quasi-steady pressure field, the fluid starts to flow according to the pressure gradient imposed by the boundary conditions within the porous matrix. This is also indicated by the modelled linear north-south increase in fluid velocity in regions removed from the fault.

Figure 2.3c illustrates the temporal evolution of the thermal field for all the three observation points. During pressure stabilization, conduction dominates the active heat transport thus resulting in no changes in the thermal field with respect to the constant initial temperature distribution adopted in the entire model.

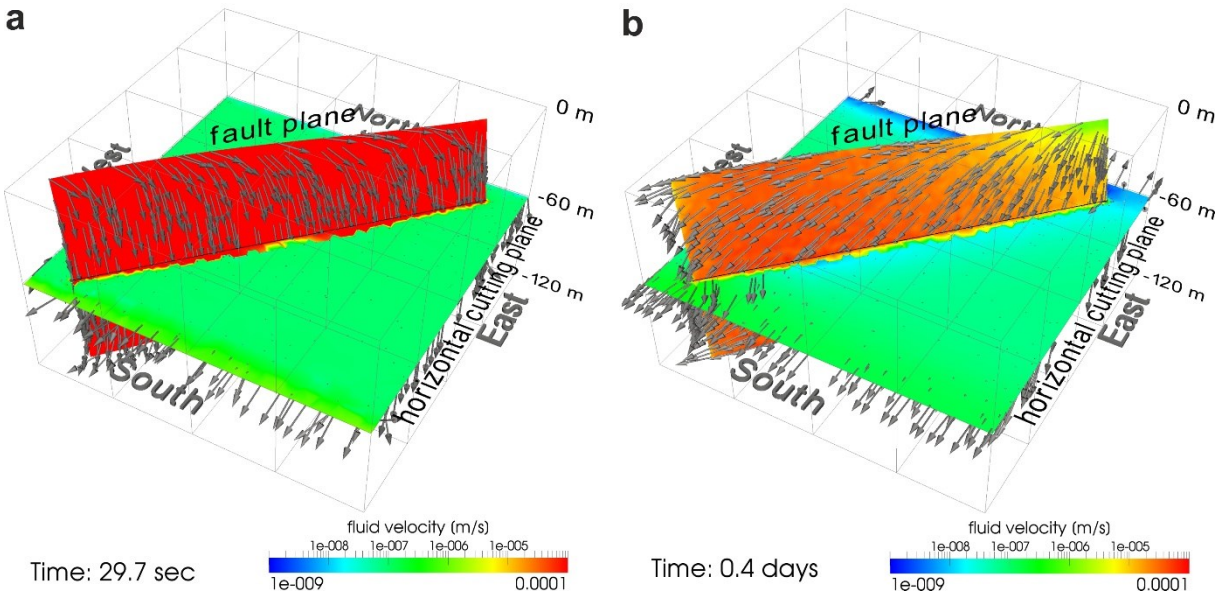

Figure 2.4 Fluid velocity vectors along the whole fault plane as well as along a horizontal plane cutting the model approximately in the central part during (a) the initial stage and (b) after 0.4 days (~0.01 month) of simulation. Non-scaled vectors represent the velocity direction and the background colours map their magnitudes.

Final stage

Reference model

Fluid pressure

After 1 month, stable conditions for the fluid pressure are reached. From this time step onward no changes in the regional pressure field are detected.

The stable pressure field developed in the entire model is illustrated by the 3D pressure distribution for the final stage of the simulation (Fig. 2.5a). The final steady pressure field is strongly influenced by the presence of the fault. This is obvious from the distribution of isobars in the 3D model showing a different spatial pattern with respect to the background model (Fig. 2.2a). Major changes in the pressure field occur in the central parts of the domain where the pressure field is clearly influenced by the presence of the fault. The distribution of isobars on a 2D horizontal slice extracted from the central part of the model shows that the fault-related

effects on the pressure field are largest at the two tips of the fault (Fig. 2.5b). The isobars are converging at the north-eastern edge of the fault where fluid starts to flow into the fault. As the fault is more permeable than the surrounding matrix the pressure decreases faster at the entry point of the fault. The fluid is guided through the fault resulting in a pressure equilibration that is reflected by the almost parallel isobars near the fault in the central part of the model.

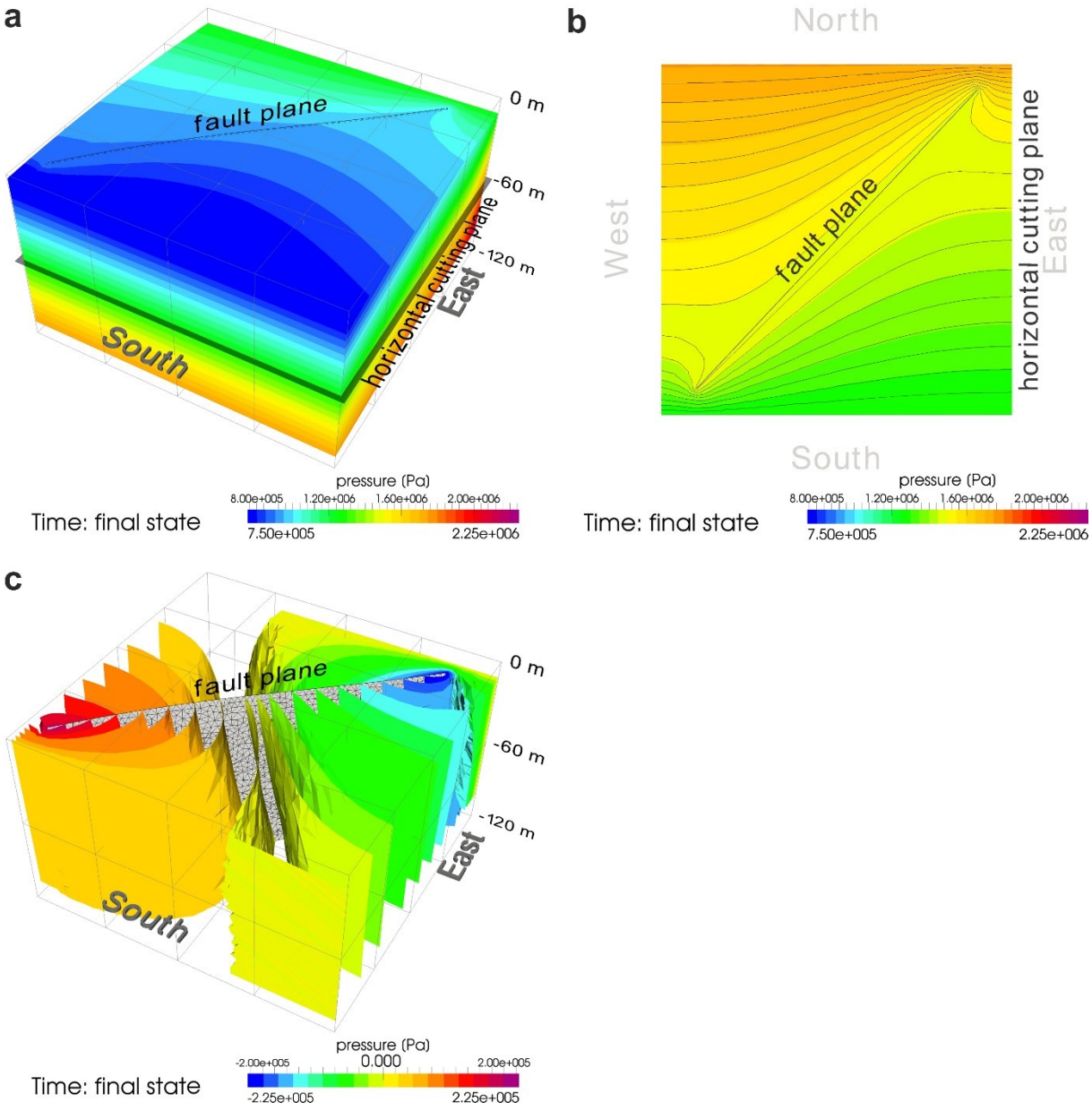

Figure 2.5 Final pressure field for the reference model showing the stable 3D pressure distribution and location of a horizontal cutting plane at -60 m (a), the pressure isobars on the horizontal cutting plane (b) and pressure contours presenting the pressure differences between background model and reference model (c).

The general impact of the fault on the hydrostatic pressure field is also demonstrated by iso-contours of the pressure differences between the background model and the current reference model in Fig. 2.5c. From the central part of the model, the pressure differences gradually increase towards the NE and SW-edges around the fault. Pressure differences are greater near the fault, further demonstrating the significant impact of the fault on the pressure field. The maximum pressure differences of up to ± 0.225 MPa occur directly at both edges of the fault.

Fluid velocity

After ~ 1 month, stable pressure conditions reflect a steady-state fluid velocity field. Due to the regional pressure gradient imposed by the boundary conditions, a consistent north-south directed flow field evolves within the porous matrix domain. Figure 2.6 shows the velocity field within the model domain.

Highest velocity values (ranging between 1e-05 – 1e-04 m/s) are observed within the fault. These high velocities are induced by the higher permeability of the fault compared to the surrounding matrix. Together with the WFZ of 0.05 m, this contrast leads to a higher transmissivity of the fault (5e-10 m^3, Tab. 2.2) and the fault acts as a preferential flow pathway with respect to the matrix area. This causes the destabilization of the hydrostatic pressure field in and around the fault area (cf. Figs. 2.5a and 2.5b). Due to the small WFZ of 0.05 m, the fluid is channelled within the fault, which results in an increased flow velocity there. Figure 2.6 also shows differences in the fluid velocity magnitudes within the fault plane. Minimum fluid velocities (~1e-05 m/s) occur along the boundary contacts between the fault and the porous matrix where fault-matrix interaction, together with 3D dispersive effects, cause the observed decrease in the fluid velocity. In contrast, the fluid velocity increases while moving from the fault's edges into the fault plane reaching maximum values around the central part of the fault. The higher fault permeability induces the observed acceleration of the fluid, an aspect enhanced by the planar nature of the flow within the fault plane.

In contrast, the lowest velocity magnitudes (ranging between 1e-08 and 1e-07 m/s) are observed in the matrix. There, the horizontal flow is also predominant, but, in response to the permeability contrast between matrix (K_{layer} = 1e-14 m^2) and fault (K_{fault} = 1e-08 m^2), it is characterized by lower velocities than in the fault.

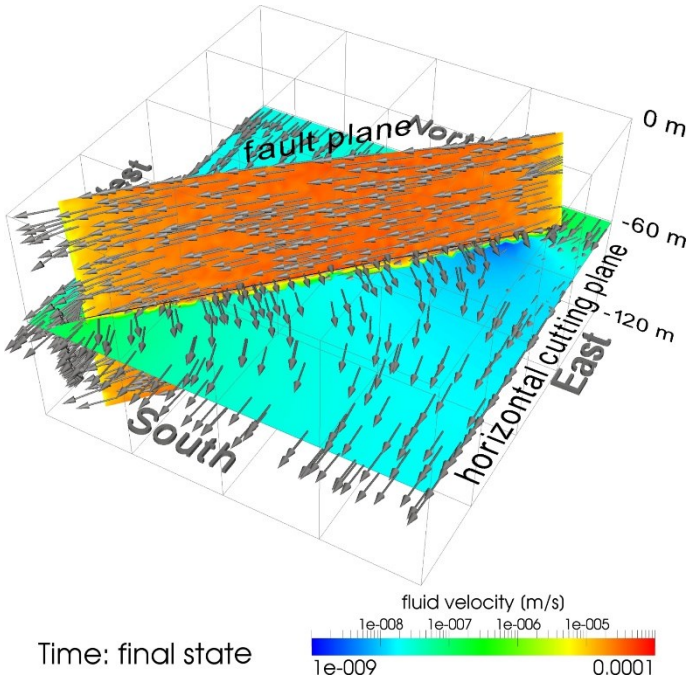

Figure 2.6 Fluid velocity vectors along the fault plane as well as along the horizontal cutting plane of the reference model. Non-scaled vectors represent the velocity direction and the background colours map their magnitudes.

Fluid temperature

The final temperature field for the total domain shows that the evolving temperature reaches values between 65-80°C in the matrix of the north-western part of the model, which is higher than the initial temperature. This increased temperature is induced by the inflow of the warm water front from the north-western boundary of the model.

Cold water is advected into the fault from the north-eastern site of the model (Fig. 2.7a). The cold water front is than led through the highly permeable fault, and the water mixes and equilibrates with the warm water front in the matrix coming from the north-western part of the model. Accordingly, the water cools towards the central part of the model. For the stable field, a two-part temperature system develops with a warmer western and a colder eastern part separated by the fault.

Iso-contours of the temperature differences between the background model without fault and the reference model are shown in Fig. 2.7b. In the north, there are no temperature differences because the fault does not cut this part of the model and has no influence on the temperature distribution. By contrast, the temperature field is strongly influenced in and around the fault. The temperature differences gradually increase up to 12°C towards the south-western part of the model around the fault. These high temperature differences confirm that the fault acts as a

conduit for the fluid. The inflow of cold water through the fault causes a cooling in the SW in the reference model (Fig. 2.7a).

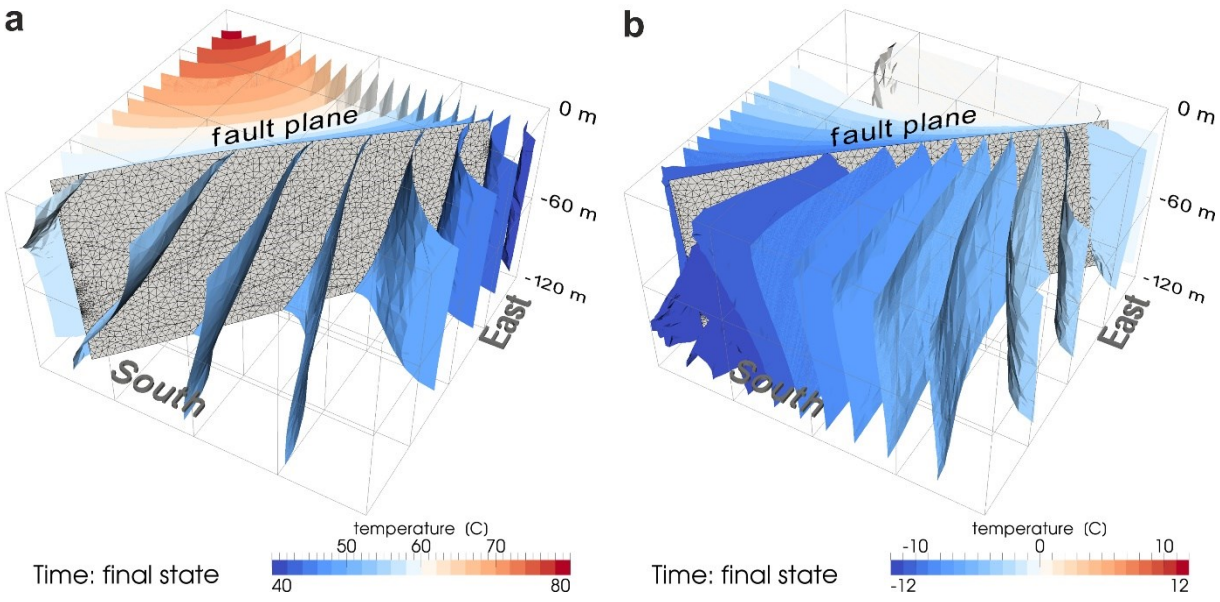

Figure 2.7 Distribution of discrete 3D isotherms as obtained for the reference model (a) and iso-contours of the temperature differences between background model and reference model (b).

Density-dependent flow

Results from a further simulation in which the fluid density is a function of the modelled temperature by means of a constant thermal expansion coefficient reveal no thermal convection (results not shown). Comparing the reference model in which the fluid density effects are not considered results in slight pressure differences ranging from -3541 to +3016 Pa (<1 bar) and temperature variations between -2 and 5°C. The effects on fluid and thermal regimes are within such a small range, that within all the other models presented in the manuscript the fluid density (and viscosity) is considered constant and not as a function of temperature (and pressure).

The little differences observed between the two simulations are expected due to the geometric size of the model as well as the applied initial and boundary conditions. The small model size (200 m x 200 m horizontally and 120 m vertically) inhibits the development of convection cells. Moreover, the pressure gradient (∇p = 0.5e+06 Pa / 200 m = 2500 Pa/m) induced by the boundary conditions forces a horizontal fluid flow throughout the system after reaching the steady-state. The constant initial temperature condition of 60°C and the boundary induced temperature variation from 40°C to 80°C results in temperature differences of maximum 20°C. The according changes in fluid density (from ~ 992 kg/m³ (T_{low} = 40°C) to ~ 983 kg/m³ (T_{ini} =

60°C) to ~ 972 kg/m³ (T_{high} = 80°C)) are too low to induce considerable density dependent effects on the fluid flow.

2.3.3 Sensitivity analysis for fault transmissivities

To quantify the impact of the geometry and main fluid parameters of the fault on the coupled fluid and heat transport, variations of the transmissivity (T) of the fault are assessed by changing first the WFZ (b) and second the permeability of the fault (k) according to the definition of the transmissivity:

$$T = b \cdot k$$

Corresponding values for WFZ and permeability as well as the calculated transmissivity are listed in Table 2.3.

Sensitivity analysis: width of the fault zone (WFZ)

First, the WFZ is step-wise changed. Starting with a minimum value of 0.0005 m, the value is gradually increased by one order of magnitude in each simulation run up to a maximum WFZ of 15 m. The results obtained from models of the two extreme values of the WFZ (model with minimum WFZ and model with maximum WFZ in Table 2.3) are presented and discussed.

Fluid pressure

The final pressure state for model with minimum WFZ reveals that the isobars are influenced by the presence of the fault, despite of its very small width. This influence on the pressure field is caused by the fluid flowing into the fault because of the higher permeability of the fault (K_{fault} = 1e-08 m²) compared to the matrix.

For the model with maximum WFZ the isobars are distinctly curved, comparable to the case for the final pressure state of the reference model (Figs. 2.5a and 2.5b). They are not parallel as in the case where no fault is implemented (Fig. 2.2a). Highest pressure is found at the northern tip of the fault, while the lowest pressure is encountered at the southern end of the fault, -thus resulting in a higher pressure gradient along the fault plane when compared to the previous study case, the model with minimum WFZ.

The fault influences the pressure field more effectively for the maximum WFZ: the isobars are bunched around the edges of the fault, and are oriented sub-parallel to the fault approaching the latter (cf. Fig. 2.5b). The geometry of the modelled isobars reflects a higher amount of fluid

which is driven through the highly transmissive fault, a process causing an almost uniform pressure along the fault. These sub-parallel isobars are not present for the model with minimum WFZ. This is due to the smaller total amount of fluid guided through the narrower and less transmissive fault.

In conclusion, the hydrostatic pressure field is clearly more influenced by the fault with the larger width and obviously, the fault-induced pressure deviation is more effective with increasing WFZ.

In contrast, the pressure gradient along the fault is larger in the model with minimum WFZ (~ 697 Pa/m) than in the model with maximum WFZ (~ 0.05 Pa/m) (cf. Fig. 2.5b). Translating pressure gradients to fluid velocity (Equation 2, chapter 2.2.1), higher velocity magnitudes are expected for the minimum WFZ than for the maximum WFZ model.

Fluid velocity

Figure 2.8 illustrates the final velocity field for the model with minimum WFZ (Fig. 2.8a) and for the model with maximum WFZ (Fig. 2.8b).

The direction of the fluid velocity field along the fault plane and in the porous domain is similar in both cases and closely resembles the velocity field described in the reference model. Accordingly, the modelled direction and orientation of the fluid velocity field are mainly influenced by the imposed pressure boundary conditions. Changing the WFZ has no impact on the direction and orientation of the fluid velocity field. Fluid velocity vectors are aligned parallel to the fault strike in both cases, reflecting a channelized flow field within the fault plane due to the permeability contrast between the fault and the porous domain.

As expected from the pressure results discussed above, main differences between the two models are found in the calculated fluid velocities. Generally, higher velocities are observed in the fault plane of the model with minimum WFZ (Fig. 2.8a), where the velocities approach 1e-04 m/s. Relatively low velocities (~ 1e-07 m/s) are found along the fault plane for the model with the maximum WFZ (Fig. 2.8b). This aspect is in agreement with the results obtained for the pressure fields for the two cases, revealing a higher pressure gradient for the minimum WFZ than for the maximum one.

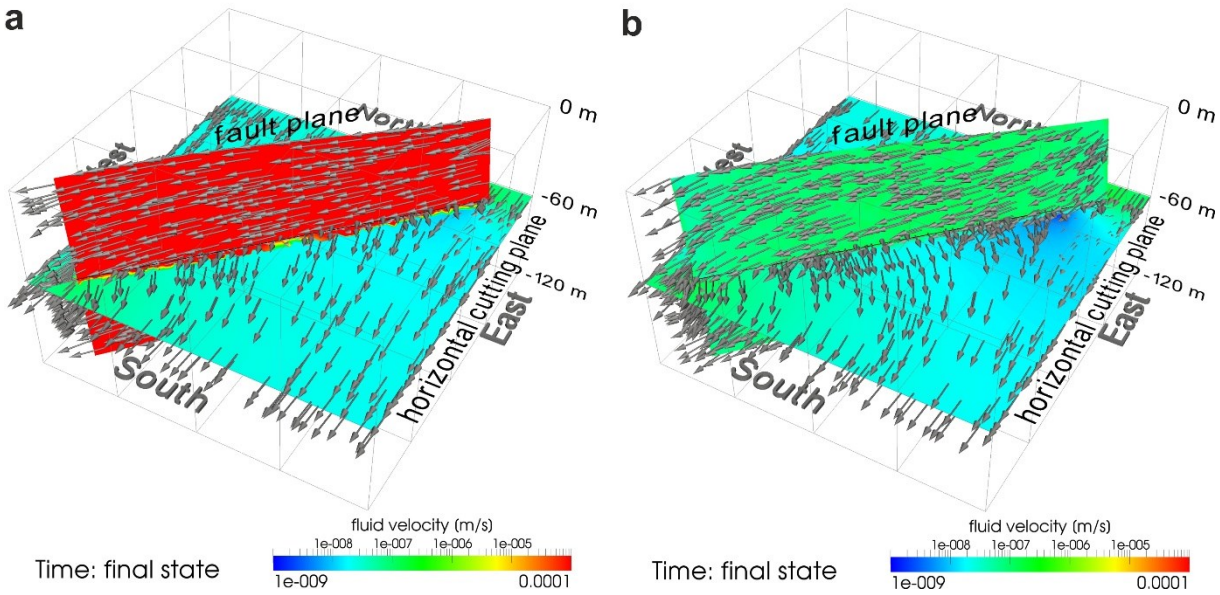

Figure 2.8 Fluid velocity vectors along the fault plane as well as along the horizontal cutting plane for model with minimum WFZ (a) and model with maximum WFZ (b). Non-scaled vectors represent the velocity direction and the background colours map their magnitudes.

In general, a linear relationship is found between WFZ and fluid velocity (Fig. 2.9), indicating that velocities increase with decreasing widths.

Accordingly, the highest velocities occur in the models with the smallest WFZ, as the fluid channelled in the narrower WFZ becomes faster. Increasing the width by one order of magnitude generally reduces the velocity in the fault by one order of magnitude.

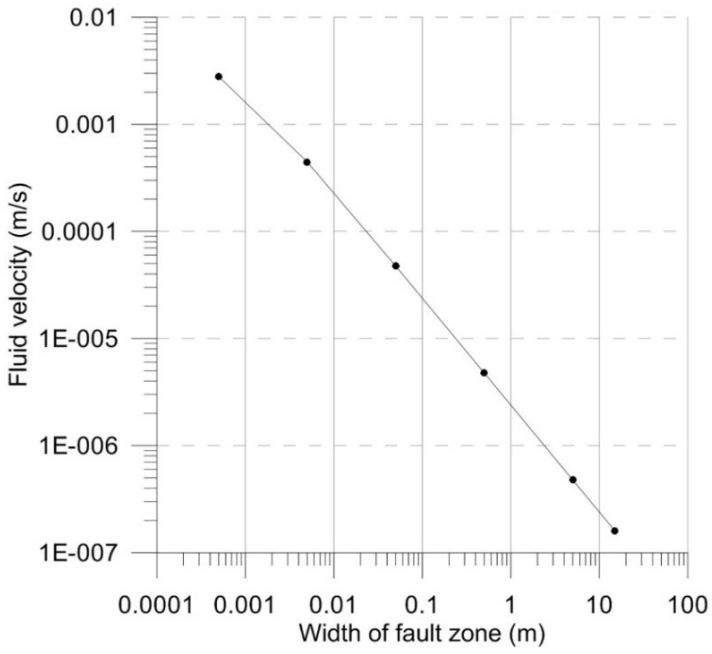

Figure 2.9 Fault zone width vs. fluid velocity (black dots) for all model simulations within the sensitivity study for the WFZ in observation point 2, located in the central part of the fault plane.

Fluid temperature

A similar final thermal state characterizes the two models with minimum WFZ and with maximum WFZ (cf. Fig. 2.7a). In both cases, cold water enters the fault from the north-eastern boundary of the model. This cold water is then driven through the fault and thermally equilibrates on its way with the surrounding warmer water masses in the matrix, resulting in a general cooling trend. At the south-eastern edge, the water leaves the fault and spreads out into the south and south-eastern part of the model in a fan-like pattern indicated by the curved isotherms. The model with minimum WFZ isotherms` in the south-eastern part reach slightly larger values compared to the isotherms in model with maximum WFZ. For model with minimum WFZ, absolute temperatures remain higher as the general cooling trend is not as strong as in the reference model or in model with maximum WFZ. Though the fluid is the fastest in the fault with the smallest WFZ, only a smaller amount of water guided through the fault can thermally equilibrate with the surrounding warmer water in the matrix. This results in a less efficient overall cooling and consequently higher temperatures in the model with minimum WFZ.

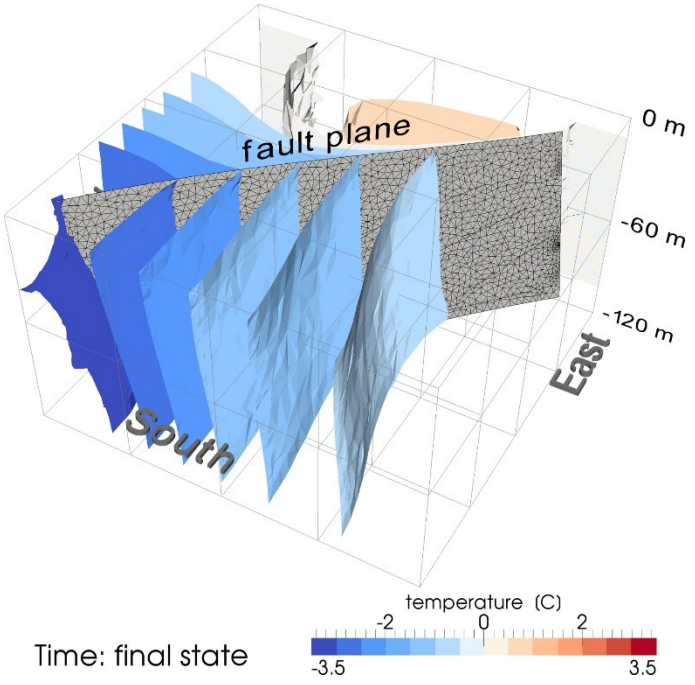

Figure 2.10 Distribution of discrete 3D isotherms of the temperature differences between model with minimum WFZ and model with maximum WFZ.

The temperature differences between these two models are shown in Fig. 2.10. Here, the temperatures start to diverge in the central part of the model. From there, the temperature differences gradually increase towards the end of the fault, reaching up to 3.5°C in the south-western part of the model. The modelled temperature differences clearly reflect that more cool water is led through the entire fault for the maximum WFZ.
This results in a cooling effect in the central and in the SE-part of the model. On the contrary, despite the high fluid velocity, less fluid can be transported through the fault with the minimum WFZ. In this case, the cooling induced by the flow driven through the fault is far smaller.

Sensitivity analysis: permeability

Within the second group of sensitivity analyses, the permeability of the fault is varied between the reference permeability of K_{fault} = 1e-08 m² and K_{fault} = 1e-12 m². Within this range, the fault acts as a preferential pathway for the fluid. The lower end of this range (K_{fault} = 1e-12 m²) represents a flow regime that roughly corresponds to the background model.

Fluid pressure

The regional pressure field in the model with maximum permeability is strongly influenced by the fault (cf. Fig. 2.5a and 2.5b). A very low pressure gradient (~ 11 Pa/m) occurs between the entry and end of the fault, with the isobars running almost parallel to the fault trace in the proximity of the fault. This sub-parallel distribution of isobars reflects the large amount of fluid which is, due to the very high permeability (K_{fault} = 1e-08 m²), able to flow across the fault, causing an almost uniform pressure along the fault. In addition, the highest permeability contrast $\left[\frac{K_{fault}}{K_{layer}}\right]$ = 1e+06 between fault and matrix (K_{layer} = 1e-14 m²) favors the inflow of fluid into the highly permeable fault.
In the model with minimum permeability, the isobars are crossing the model straight from the west to the east. In this case, the pressure field is only induced by the applied pressure boundary conditions. The fault has apparently no influence on the regional pressure field similar to the case when no fault is implemented within the model (Fig. 2.2a).
The distribution of isobars shows very high pressures at the fault entry and low pressures at the end of the fault which results in the highest pressure gradient along the fault of all models (~ 1775 Pa/m). In addition, the permeability contrast is very low $\left[\frac{K_{fault}}{K_{layer}}\right]$ = 1e+02 between fault and matrix which reduces the driving power of the fault on the fluid.

In summary, the regional pressure field is strongly influenced by variations in the permeability of the fault. The results from the model with maximum permeability demonstrate that a relatively high permeability contrast between the fault and the layer (in a range of two to four order of magnitudes) leads to non-hydrostatic pressure conditions. For the model with minimum permeability, the low permeability of the fault, along with the low permeability contrast between layer and fault, leads to no influence of the fault on the pressure field. The regional pressure field is only induced by the applied boundary conditions at the southern and northern boundaries of the model domain.

Fluid velocity

The final velocity field for both permeability models are shown in Fig. 2.11a and Fig. 2.11b, respectively. Velocities found in the model with maximum permeability reach up to 5e-05 m/s along the fault plane. These are caused by the very high permeability in the fault that enables a free fluid flow through the fault.

Overall reduced velocities along the fault plane occur in the model with minimum permeability, indicating that the fluid is slowed down due to the low permeability of the fault. This effect is enhanced by the matrix permeability (K_{layer}= 1e-14 m²), causing reduced fluid velocities within the total model domain.

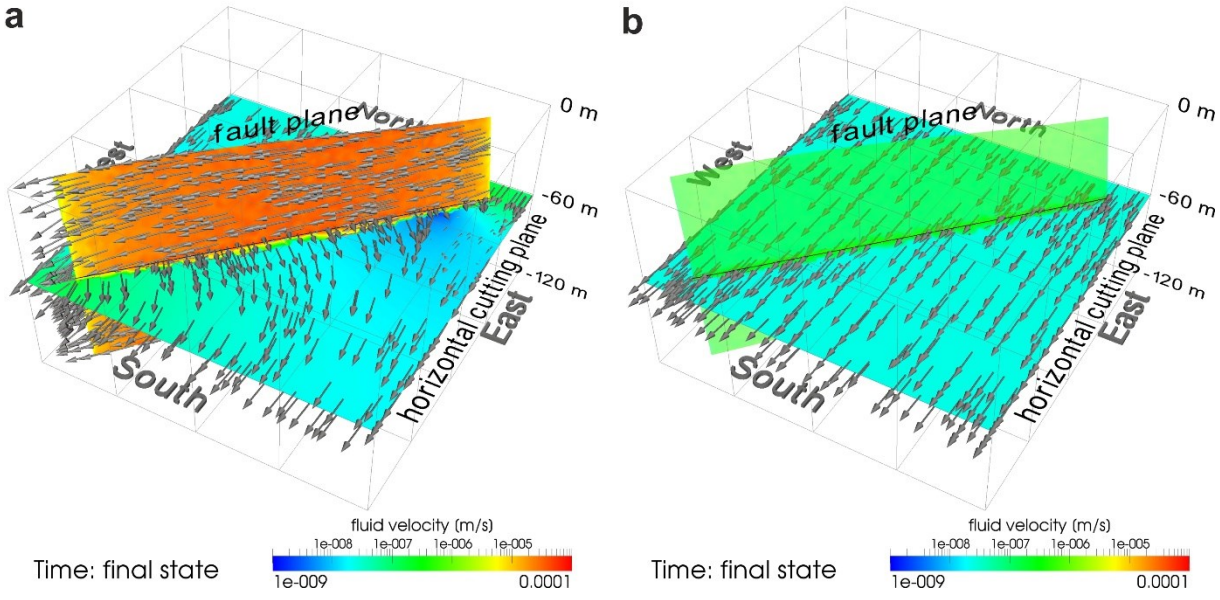

Figure 2.11 Steady-state fluid velocity vectors along the fault plane as well as along the horizontal cutting plane for model with maximum permeability (a) and model with minimum permeability (b). Non-scaled vectors represent the velocity direction and the background colours map their magnitudes.

In conclusion, maximum velocities between 3e-05 m/s and 5e-05 m/s within the central part of the fault occur in the permeability range between K_{fault} = 1e-08 m² to 1e-10 m^2. These maximum velocities are induced by the high permeabilities within the fault. Furthermore, the increased flow rates within the permeable faults are favored by the high contrast between fault and matrix permeability.

Fluid temperature

Fig. 2.12a presents the final temperature field for the model with maximum permeability for the total domain. The cold water front from the north-eastern boundary enters the highly permeable fault, as indicated by the 3D isotherms.

The temperature distribution reveals that the cold water front is led through the highly permeable fault. In the central part of the model, the cold water masses driven inside the fault thermally equilibrate with the warm water front from the north-western part of the model, resulting in a general cooling there.

The temperature field for the total model domain is displayed in Fig. 2.12b for the model with minimum permeability. Because of the low permeability contrast between fault and layer, the fault has no influence on the temperature distribution. In detail, Fig. 2.12b reveals that the temperature field only evolves as a result of the adopted boundary conditions (cf. Figs. 2.1b and 2.2b). The isotherms are running almost straight from the north to the south in the central part of the model.

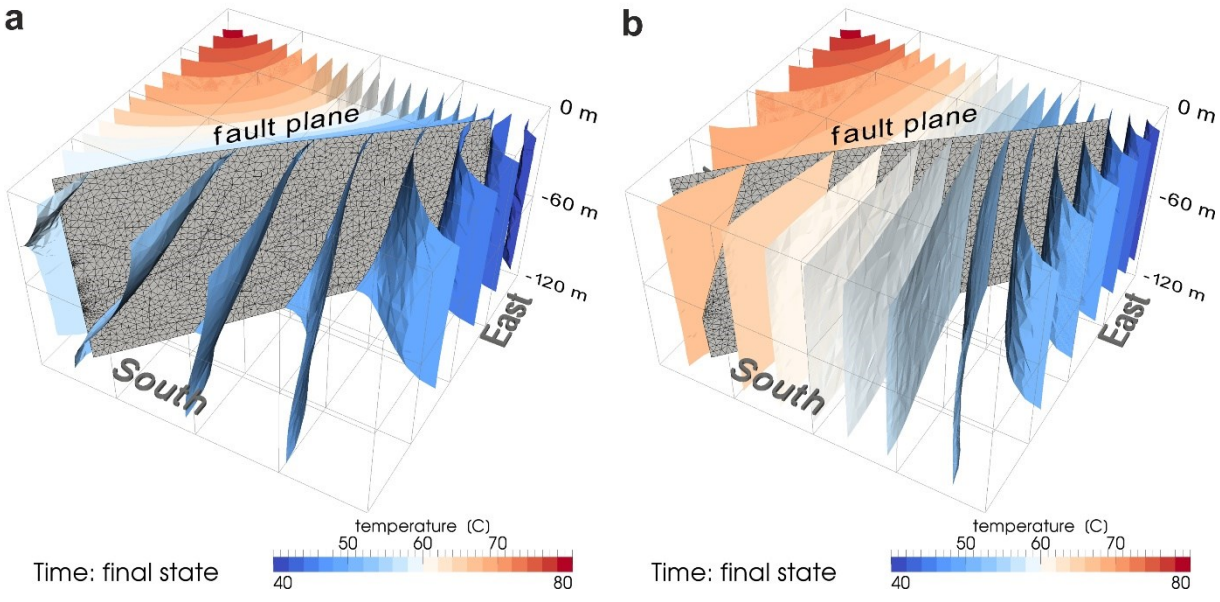

Figure 2.12 Distribution of discrete 3D isotherms for model with maximum permeability (a) and model with minimum permeability (b).

In summary, the temperature field is influenced by highly permeable faults in the range of k_{fault}: 1e-08 m^2 and 1e-10 m^2. Within this range, lower temperatures, especially in the central part of the model, result from large amounts of cold water transported inside the fault.
On the contrary, no fluid appears to enter the fault if the fault permeability is set to K_{fault} = 1e-12 m² due to the decreased permeability contrast of $\left[\frac{K_{fault}}{K_{layer}}\right]$ = 1e+02 between fault and matrix.
The temperature field is not altered by the fault and evolves only in response to the applied boundary conditions.

2.4 Discussion

Simulating coupled processes occurring in fractured geological systems is a challenging task. Difficulties arise not only in properly integrating the real geometry and degree of heterogeneities found in nature in a consistent numerical model, but also in effectively discriminating the influence of all interacting factors in the model results.
Important influencing factors include geometrical parameters like the model structure and mesh configuration, physical parameters comprising initial as well as boundary conditions and the assignment of physical properties (e.g. Ingebritsen and Sanford, 1998; Kaiser et al. 2013a; Noack et al. 2012). Furthermore, the degree of coupling between the governing equations for fluid and heat transport and the coupling between different processes can have a significant influence on the geothermal field (Kolditz and Diersch, 1993; McDermott et al. 2006). Fault characteristics like e.g. surface roughness, orientation to the stress field, geometry and connectivity between each other can also affect the results (e.g. Thompson and Brown, 1991; McDermott et al. 2006).
However, taking into account most of these influencing factors can lead to a superposition of effects that hampers the understanding of individual parameters. Factors like special boundary conditions and a complex heat-source term complicate a dimensional analysis of convection resulting from pressure gradients, potentially leading to physical instability (Kolditz and Diersch, 1993).
Within this work, the geometrical model setting is kept as simple as possible. Important fault characteristics are restricted to the width of the fault zone and permeability. This strategy aims to minimize the high number factors influencing the system, improving the quantitative assessment of each of the parameters impact on the resulting flow regime and temperature

distribution. Consequently, these limitations prevent a confounding of effects from the various factors in the results.

The application of the hybrid approach combining porous media and discrete elements addresses the interaction between discrete flow paths and rock matrix.

The results show that the systematic variation of the fault permeability or of the WFZ affects the entire pressure, velocity and temperature field. The assigned permeability contrast between porous rock matrix and discrete fault zone determines the effect of the fault in controlling the evolving hydrothermal field. Increased flow rates within very permeable faults are favored by a high contrast between fault and matrix permeability. This consequently leads to increased velocities in the fault and high temperature differences between fault and matrix. Contrarily, the driving power of the fault on the fluid is reduced by a low permeability contrast between fault and matrix. This leads to decreased velocities in the fault and no thermal variations between matrix and fault.

The pressure, velocity and temperature evolution depending on the assigned physical properties demonstrates the strong coupling between matrix and fault. This coupling proves that it is important to consider the porous rock matrix and reveals its interaction with the implemented fault. In the discrete fracture network approach, this coupling is not resolved, and the approach is merely applied for dense fracture networks that require the consideration of the flow connectivity between the faults.

The implementation of a dipping fault more closely approximates the natural fault geometry than the usual orthogonal fault implementation. Fig. 2.13 shows the pressure differences between a model with a dipping fault of 60° and a model with a vertical fault. Both models have the same size as the one used in the study, but with shortened fault planes. Maximum pressure differences of up to ± 0.1 MPa occur around the edges of the faults. Also, temperature variations of up to 5°C can be observed when comparing the two models. The pressure and temperature differences clearly indicate the influence of the adopted dipping angle of the faults. Furthermore, they point to the importance of the implementation of an inclined fault and the consequent approximation of the natural fault geometry in the model.

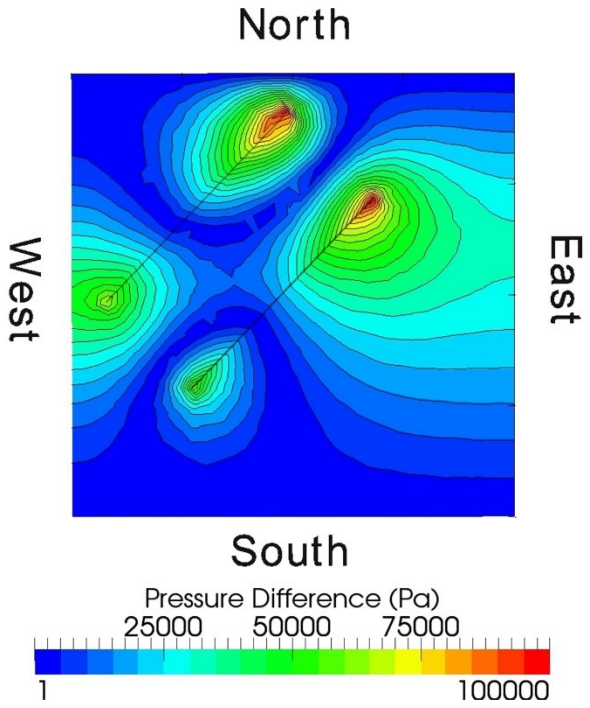

Figure 2.13 Distribution of isobars of the pressure differences between a model with a dipping fault of 60° and a model with a vertical fault on a horizontal cutting plane at -90 m.

2.5 Conclusions

Based on a 3D synthetic model in which an inclined fault is implemented, sensitivity analyses are carried out to quantify the effects of the transmissivity of the fault on the resulting fluid flow and thermal field.

In the absence of the fault (background model), a steady, stable pressure field due to hydrostatic load conditions results in a homogeneous regional velocity field throughout the entire model domain, as driven by the assigned pressure boundary conditions. Heat advection by a constant and isotropic velocity field and heat conduction by the homogenous rock leads to a temporal evolution that closely reflects the boundary setting.

In contrast, a relatively high transmissivity of the fault (reference model) has a significant impact on the fluid and heat flow by locally influencing the hydrostatic pressure field. Maximum absolute pressure differences up to 0.225 MPa are found with respect to the undisturbed background model and the reference model, with the fault acting as a preferential fluid pathway. This reflects variations in the temporal evolution of the thermal field as indicated by temperature differences up to 12°C between the two models. In case of the reference model, the heat is no longer isotropically advected following the applied pressure and thermal boundary conditions. Rather, it tends to concentrate within the fault plane leading to a completely

different final thermal state. Due to the imposed thermal boundary conditions, relatively cold water, channelled and quickly advected in the fault, results in a net cooling process.
Varying either the fault zone width or the fault permeability will result in significant differences in the pressure, velocity and temperature field. The influence of the fault on the pressure field is augmented by relatively large widths of the fault zone. A linear inverse relationship between WFZ and fluid velocity is observed with one order magnitude increase in the width resulting in a decrease of the velocity field of around 1e-01 m/s within the fault.
The evolving temperature distribution is distinctly different for the studied scenarios. In the case of the model with maximum WFZ, a general cooling trend occurs in and around the fault, indicating that a large amount of cold fluid from the north-eastern model side is led through the fault. For the model with the minimum WFZ, a less efficient overall cooling occurs due to a smaller amount of water being transported through the fault.
The pressure field is strongly influenced by high permeabilities in the fault (K_{fault} = 1e-08 to 1e-10 m²), leading to fluid velocities that are larger in the fault compared to the surrounding matrix. Again, the temperature field is affected in that the highly permeable faults (K_{fault} = 1e-08 to 1e-10 m²) cause cooler temperatures especially in the central part of the model. On the contrary, the fault has no considerable influence on the temperature distribution for the model with the permeability K_{fault} = 1e-12 m² because not sufficient cold fluid enters the fault.

The outcomes of this study are necessary for understanding the effects of variable fault parameters on the fluid and heat evolution in a fractured geological system by means of 3D finite element simulations. Quantifying the impact of faults is important for a reliable assessment of the fluid and heat transport needed for geothermal studies. Furthermore, the outcomes provide a solid base for future simulations of real case scenarios with complex fault systems.
Though these results may appear simplistic at first view, they represent a breakthrough in that they treat the fault-influenced transport of fluid and heat in 3D. Moreover, the results reveal a linear relationship between fluid velocity and WFZ. As opposed to 2D, the 3D approach enables a reasonable quantification of the fluid pressure evolution and state. The applied concept for the numerical simulations that integrate the 3D nature of the flow and the consideration of inclined faults in a porous medium as evolving in natural, fractured geological systems thus provides a useful tool for complex geothermal modelling.
Concerning future applications, the next steps should include the gradual increase of complexity within the simulations by extending the model size and the number of faults, taking into account

fluid density and viscosity dependent effects and considering further important fault characteristics. Accordingly, a suitable subject of future work would be the investigation of a real-case study based on a detailed 3D structural model of a geothermal test site in which major faults are integrated and their impact on the hydrothermal regime is studied.

Acknowledgements

We thank Björn Lewerenz for very helpful computational support and Philipp Balling for his contributions to visualization and artwork. We acknowledge valuable advice and support in technical questions concerning OpenGeoSys from Dr. Norihiro Watanabe. Jonathan Banks is thanked for his corrections and editing. Additional thanks go to Dr. Hang Si from the WIAS Institute in Berlin for his help in using his open source meshing software TetGen (Si, 2008). The numerical results are visualized by using the open source postprocessor ParaView. Constructive comments and suggestions for improvement by two anonymous reviewers and Prof. Olaf Kolditz are gratefully acknowledged. This work is part of the project GeoEn and has been funded by the German Federal Ministry of Education and Research in the program ‘‘Spitzenforschung in den neuen Ländern’’ (BMBF Grant 03G0671A/B/C).

3 Controls on the deep thermal field – implications from 3D numerical simulations for the geothermal research site Groß Schönebeck

Abstract

The deep thermal field in sedimentary basins can be affected by convection, conduction or both resulting from the structural inventory, physical properties of geological layers and physical processes taking place therein. For geothermal energy extraction, the controlling factors of the deep thermal field need to be understood to delineate favorable drill sites and exploitation compartments. We use geologically based 3D finite element simulations to figure out the geologic controls on the thermal field of the geothermal research site Groß Schönebeck located in the E part of the North German Basin. Its target reservoir consists of Permian Rotliegend clastics that compose the lower part of a succession of Late Carboniferous to Cenozoic sediments, subdivided into several aquifers and aquicludes.

The sedimentary succession includes a layer of mobilized Upper Permian Zechstein salt which plays a special role for the thermal field due to its high thermal conductivity. Furthermore, the salt is impermeable and due to its rheology decouples the fault systems in the suprasalt units from subsalt layers.

Conductive and coupled fluid and heat transport simulations are carried out to assess the relative impact of different heat transfer mechanisms on the temperature distribution. The measured temperatures in 7 wells are used for model validation and show a better fit with models considering fluid and heat transport than with a purely conductive model. Our results suggest that advective and convective heat transport are important heat transfer processes in the suprasalt sediments. In contrast, thermal conduction mainly controls the subsalt layers.

With a third simulation, we investigate the influence of a major permeable and of three impermeable faults dissecting the subsalt target reservoir and compare the results to the coupled model where no faults are integrated. The permeable fault may have a local, strong impact on the thermal, pressure and velocity fields whereas the impermeable faults only cause deviations of the pressure field.

Published as:

Cherubini Y, Cacace M, Scheck-Wenderoth M, Moeck I, Lewerenz B (2013) Controls on the deep thermal field – implications from 3D numerical simulations for the geothermal research site Groß Schönebeck. Environmental Earth Science 70(8): 3619-3642.

http://link.springer.com/article/10.1007%2Fs12665-013-2519-4. The final publication is available at link.springer.com.

3.1 Introduction

Geothermal energy production utilizes the Earth`s internal heat and potentially provides a renewable energy resource which is increasingly exploited on a commercial scale especially to reduce CO_2 emissions. Hydrothermal energy systems utilize natural formation fluids brought to the surface through wells drilled for that purpose. Where the ratio of temperature and natural production rate is too low to generate energy, the geothermal system is enhanced by stimulation treatments. These anthropogenic geothermal systems are referred to as Enhanced Geothermal Systems (EGS) typically developed by an injection and a production well to circulate thermal water (Huenges, 2011). Any exploitation of geothermal energy, in particular from EGS resources, is affected by the temperature distribution in the subsurface that can vary regionally and over time. Different mechanisms of internal heat transfer – conduction, convection or both control the temperature distribution of the deep thermal field (Verhoogen, 1980). The rate of heat and fluid flow is in turn affected by the composition of the geological layers (Bjørlykke, 2010). Preferential pathways or tight barriers for fluids caused by faults and fractures may in addition significantly influence the fluid circulation and thermal field within the reservoir rocks. Therefore, it is important to investigate the processes that control heat transport in the subsurface. Numerical simulations enable studying the processes over time, taking place in geothermal systems and are therefore useful tools for both, geothermal exploration and reservoir engineering as they can provide necessary information on temperature variations and fluid circulation in greater depths. The positive aspect of numerical simulations is that they incorporate both, the structural setting of the subsurface and the physical processes of coupled fluid and heat transport. With this study, we investigate the geological controls on the deep thermal field by means of 3D simulations in the vicinity of the hydrothermal EGS research site Groß Schönebeck, located 40 km north of Berlin in the North German Basin (Fig. 3.1).

The site is an in situ laboratory exhibited by a well doublet system with one well (EGrSk 3/90) initially drilled for gas exploration and now acting as an injector (Huenges et al. 2002; Moeck et al. 2005). The second well (GtGrSk 4/05) has been drilled as a production well to establish a thermal water loop (Zimmermann et al. 2007). The in situ laboratory recently has been the

target of an increasing number of studies aiming at improving its productivity (Blöcher et al. 2010b; Huenges et al. 2006; Reinicke et al. 2005; Zimmermann et al. 2010; Zimmermann et al. 2011).

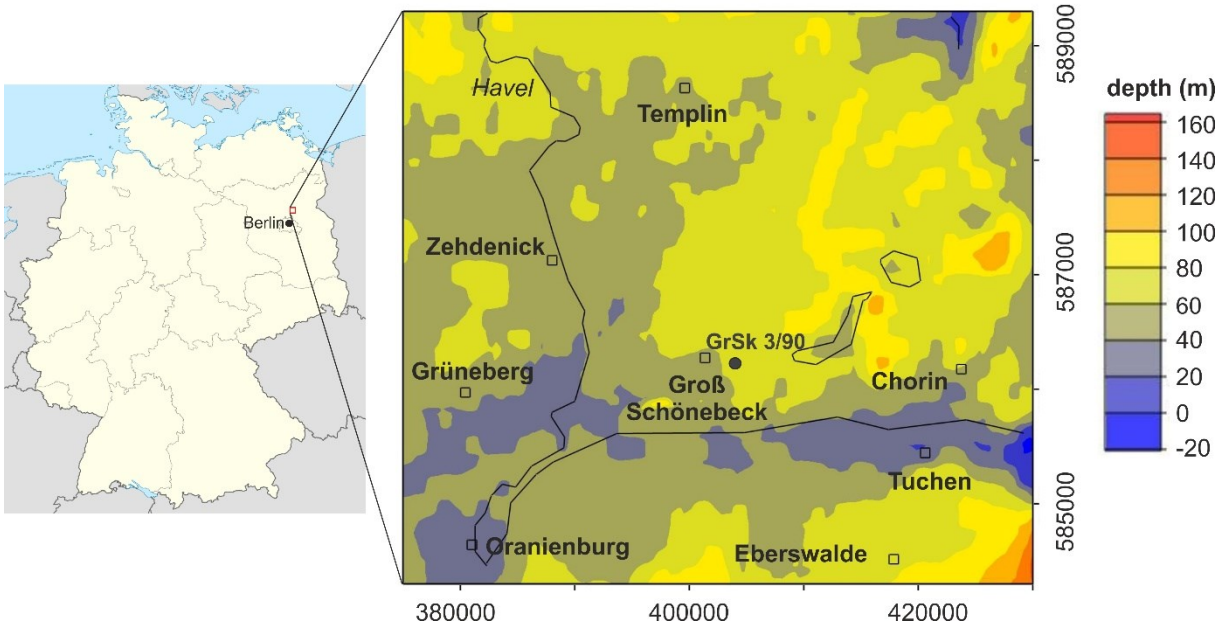

Figure 3.1 a: Map of Germany showing the location the Groß Schönebeck test site. The study area (red rectangle) covers a surface of 50 km in N-S and of 55 km in E-W direction; b: Topography map of the model area in UTM zone 33N with main rivers and lakes (thin black lines) (ETOPO1, after Amante and Eakins, 2009). The well GrSk3/90 (black dot) indicates the position of the hydrothermal EGS research site Groß Schönebeck.

Within the sedimentary succession of the Groß Schönebeck model area a layer of mobilized Upper Permian Zechstein salt (Fig. 3.2a) plays a special role for the thermal field due to its high thermal conductivity and its special configuration. Previous modelling studies on different scales already demonstrated that the different thickness of this salt rock, ranging from few tens of meters to more than several thousand meters, caused by salt tectonics, strongly control the thermal regime in the North German Basin (Bayer et al. 1997; Cacace et al. 2010; Kaiser et al. 2011; Noack et al. 2010; Scheck, 1997). Besides, the sedimentary succession is decoupled into different aquifer systems by several hydrogeological barriers controlling most of the fluid flow in the subsurface. These hydrogeological barriers comprise the Tertiary Rupelian clays, the Triassic Muschelkalk limestones and the Zechstein salt. Due to its specific rheology, the latter also decouples the deformation pattern in the study area into a supra- and a subsalt compartment with specific fault systems each (Fig. 3.2b).

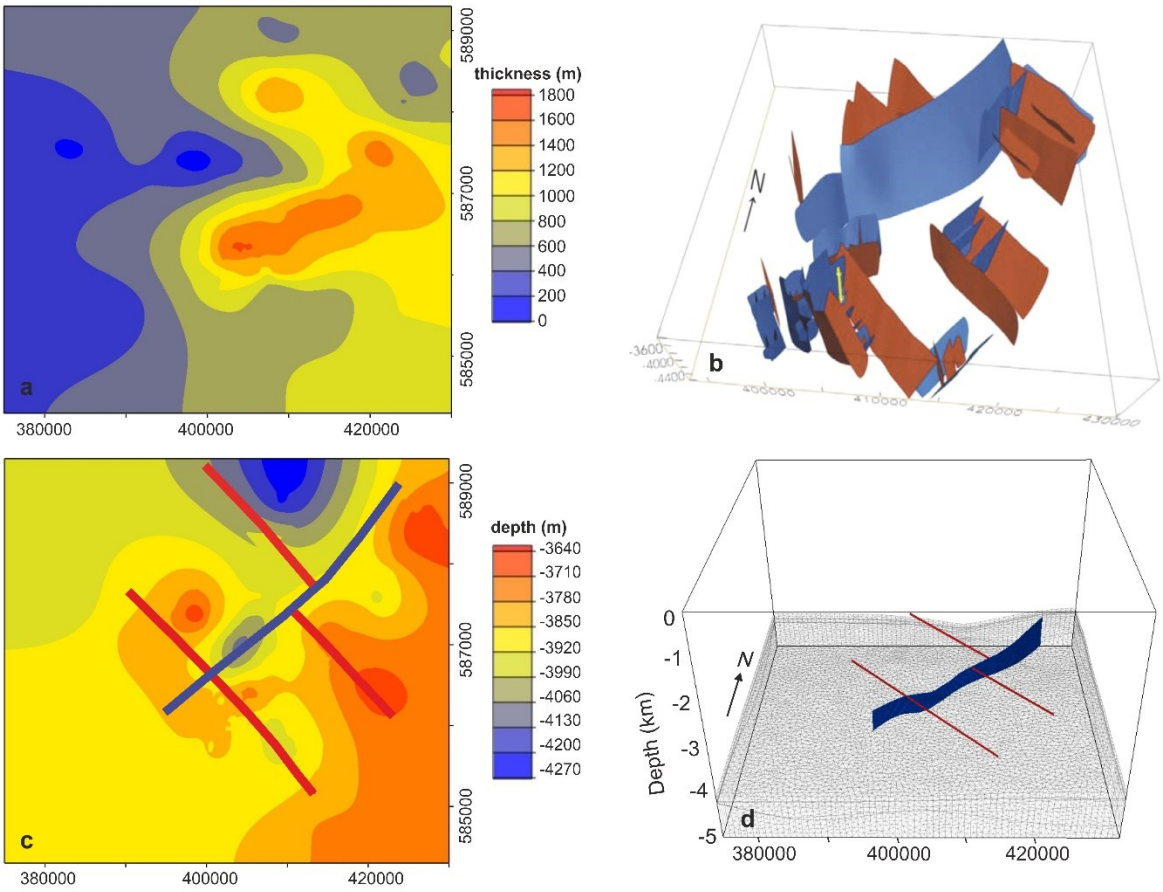

Figure 3.2 a: Thickness map of Permian Zechstein salt which is characterized by two NE and NW trending salt ridges in the centre and NE; b: 3D hydrotectonic model for the Rotliegend reservoir indicating the hydraulic conductivity of the faults with respect to their kinematic behavior within the current in situ stress field (from Moeck et al. 2005). Red faults: acting as seals; Blue faults: serving as conduits; Yellow tube: location of the well GrSk 3/90; c and d: Simplified subsalt fault system representing the major faults in the area Groß Schönebeck at (c) the Top Rotliegend depth map corresponding to the uppermost surface cut by the faults and (d) the implemented faults in the subsalt layers of the 3D finite element model. According to Figure 3.2b, in both subfigures the red NW-SE oriented faults are supposed to act as barriers, the blue NE-SW trending fault as a conduit to fluid flow.

The thermal field of the Groß Schönebeck area has been recently investigated by Ollinger et al. (2010). Their 3D conductive model indicated a thermal regime controlled by heat conduction and spatially variable thermal conductivities in the different geologic layers. Also, the cycle performance of the well doublet system was evaluated by means of a thermohaline finite element simulation including deviated wells and hydraulically induced fractures in the reservoir zone of Groß Schönebeck (Blöcher et al. 2010b). However, the thermal regime of the larger area around Groß Schönebeck and the influence of the natural fault zones have not been addressed up to now.

The present study investigates the controlling factors of the deep thermal field for the larger area of Groß Schönebeck by means of 3D finite element simulations. Conductive and coupled

fluid and heat transport simulations are carried out to assess the relative impact of different heat transfer mechanisms on the temperature distribution with respect to the hydrogeological setting in the study area. Furthermore, the influence of faults affecting the Lower Permian (Rotliegend) geothermal target reservoir is studied by integrating major faults of the subsalt fault system into the numerical model (Figs. 3.2c and 3.2d). The simulation results for the fault model are compared to a scenario where no faults are integrated to quantify the influence of the faults on the temperature and pressure fields and to assess the relevance of theses changes. To validate the models, calculated temperatures of all models are compared with corrected temperatures derived from wells located in the study area (Fig. 3.3a).

3.2 Geological setting and model setup

The structural model of the Groß Schönebeck area covers a surface of 50 km in N-S and of 55 km in E-W direction. It reaches down to – 5 km depth and resolves a succession of Carboniferous to Quaternary age (Fig. 3.3a and Table 3.1). The Permian Zechstein salt layer subdivides the sedimentary succession into a supra- and a subsalt sequence. The dominating structure of the Zechstein is a NE-SW trending salt ridge (rising from ~ - 4180 to - 2160 m) which has been formed by halokinetic processes (Fig. 3.2a)

The 3D model of the Groß Schönebeck area used in this study is based on an earlier structural model (Moeck et al. 2005) that has been now vertically refined by integrating additional layers. This refinement allows differentiating the major hydraulically active layers in the suprasalt succession. Accordingly, the Cenozoic is differentiated into a Quaternary unit and Tertiary units. The Quaternary unit is mainly composed of unconsolidated, clastic sediments and its geometry corresponds to the 3D structural model of Brandenburg in NE Germany (Noack et al. 2010). Deep reaching channels formed by subglacial erosion characterize the structural pattern of the base Quaternary, and are often filled with a variety of porous and permeable sediments (BURVAL WORKING GROUP, 2009). The underlying Tertiary is composed of unconsolidated sands, silts, clay and marly limestones and is subdivided into three sub-units, - the Post-Rupelian, Rupelian and Pre-Rupelian. Of particular hydrogeological interest is the Oligocene Rupelian, mainly composed of clay. A low permeability characterizes this clay unit due to small grain sizes and a highly absorptive capacity. The Rupelian acts as the uppermost hydraulic barrier in the model separating the permeable geological units above (Quaternary and Post-Rupelian) and below (Pre-Rupelian and Mesozoic) (Table 3.1 and Fig. 3.3b). The spatial

distribution of the Rupelian layer is derived from well data provided by the Geological Survey of Brandenburg and adjusted to the geological maps available for the study area (Stackebrandt and Manhenke, 2002).

Below the Tertiary, a succession of moderately consolidated marls, sand-, silt- and mudstones of Cretaceous to Jurassic age follows downward. As these stratigraphic horizons are characterized by similar physical properties, they are combined to a single layer of uniform properties in the model (Table 3.1). Following downward, the Upper and Lower-Middle Keuper (Upper Triassic) formations are likewise merged into one single layer in the model, representing a uniform parameter domain, mainly composed of clays, marls and gypsum. Accordingly, this unit is less permeable than the overlying one.

In a similar way, the Upper-Middle Muschelkalk and Lower Muschelkalk (Middle Triassic) are assembled to form a single Triassic Muschelkalk layer. This stratigraphic unit consists of limestones and calcareous marls and this special lithology leads to a strongly reduced hydraulic activity. Accordingly, the Muschelkalk represents the second hydraulic barrier within the sedimentary succession (Fig. 3.3b).

Sediments like silts with minor sand partition, clays and evaporites are characteristic for the Lower Triassic Buntsandstein unit, which is characterized by a moderate permeability. Following downward, the Upper Permian is considered as one layer predominantly composed of evaporates (mainly salt). Due to its specific mineral lattice and its mechanical properties, the porosity and permeability of the salt are extremely low (cf. Hudec and Jackson, 2007). Consequently, the Zechstein salt is considered as hydraulically impermeable and acts as the third hydraulic barrier in our model (Fig. 3.3b). Moreover, the salt is thermally more conductive than other sediments.

The subsalt sequence includes the Permian Rotliegend deposits, corresponding to the Rotliegend aquifer, and a layer of uppermost Carboniferous. The first represents the target reservoir zone of the geothermal site (Zimmermann et al. 2007). The deposits of the Upper Rotliegend are subdivided into the Hannover Formation with mainly mudstones and fine-grained sandstones and the Dethlingen Formation, which is composed of fine- to coarse-grained sandstones. At the base of the Upper Rotliegend, sandstones and clast-supported conglomerates form the Havel Subgroup (Holl et al. 2005). The Lower Rotliegend consists of volcanic (andesitic) rocks. Foliated, flyschoid sediments form the Carboniferous rocks integrated in the model as the lowermost impermeable layer.

Summarizing, the final structural model as used in the simulations consists of 17 geological layers (Fig. 3.3a) with a horizontal resolution of 220 m x 227 m. The three hydrogeological

barriers, - the Rupelian, the Muschelkalk and the Zechstein separate the stratigraphic succession of the model into different aquifer systems (Fig. 3.3b). Accordingly, four main aquifer systems can be distinguished from top to bottom: (1) the Cenozoic aquifer (from surface to Post-Rupelian); (2) the 'Mesozoic' aquifer (between Rupelian and Muschelkalk) (3) the Buntsandstein aquifer (between Muschelkalk and Zechstein) (4) the Rotliegend reservoir (between Zechstein and Carboniferous basement).

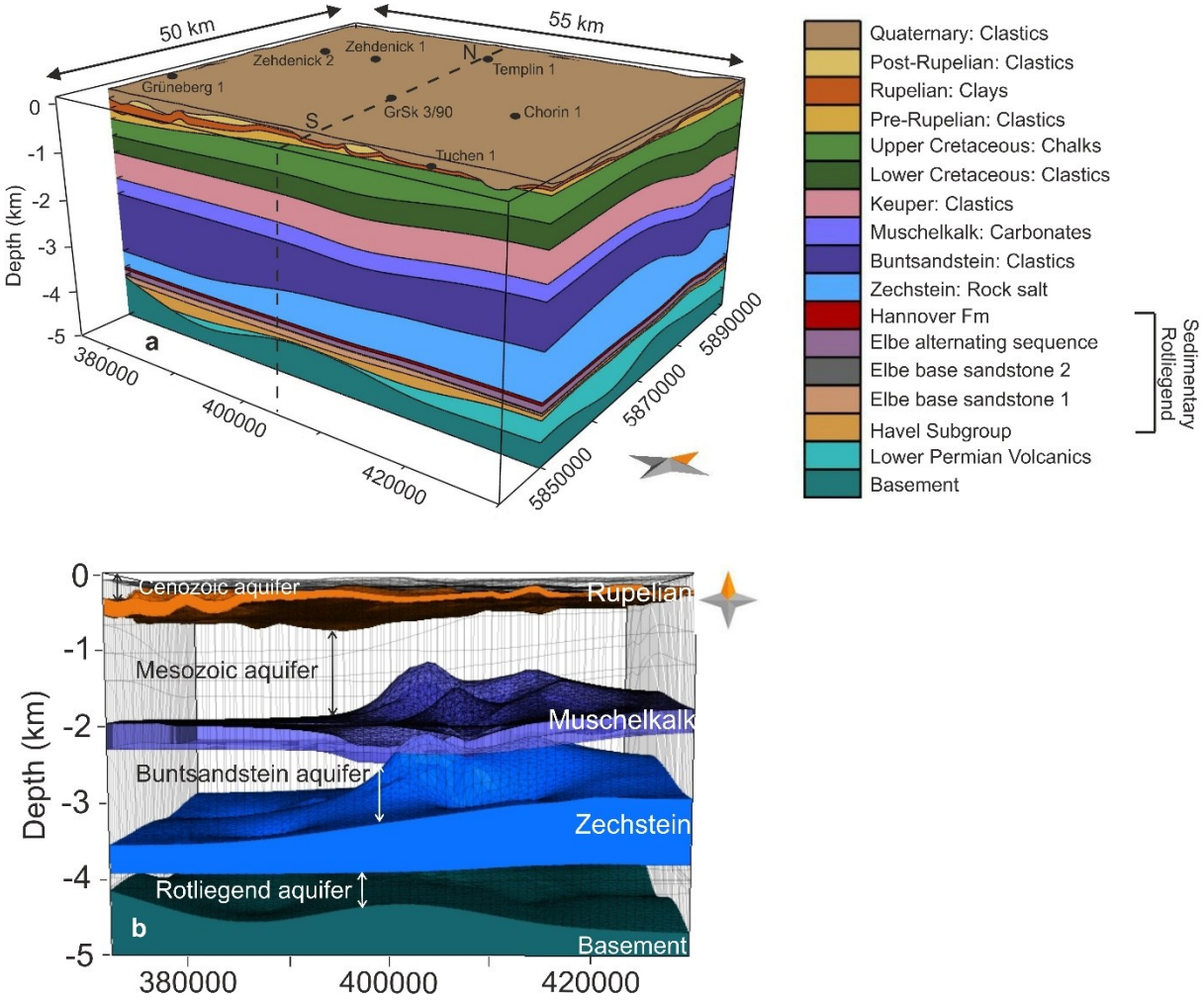

Figure 3.3 a: 3D geological model of Groß Schönebeck with the stratigraphic layers (vertical exaggeration: 7:1). Black points on top indicate the location of the wells in the area Groß Schönebeck for which temperature measurements are available. The dotted black line delineates the location of the vertical cross section from N to S through the research well GrSk3/90 used to illustrate results in Figs. 3.5, 3.7, 3.8. The frontal view displays a vertical profile from W to E through well Tuchen 1. Note the Quaternary channel cutting the Upper Cretaceous layer at shallow depth (up to ~ 200 m) in the SE.
b: Distribution of low permeability aquicludes and high permeability aquifers integrated into the model (vertical exaggeration: 7:1). The quasi-impervious layers are from bottom to top (with average thickness in brackets): basement (540 m), Permian Zechstein (700 m), Triassic Muschelkalk (300 m), Oligocene

Rupelian (120 m). The aquifer systems from bottom to top: Rotliegend aquifer (580 m), Buntsandstein aquifer (940 m), Mesozoic aquifer (1770 m), Cenozoic aquifer (190 m).

3.2.1 Fault system

Seismic data image a fault pattern in the study area which is mechanically decoupled by the Zechstein salt into a suprasalt and a subsalt fault system (Moeck et al. 2009). Due to the impermeability of the salt layer the different fault systems are hydraulically isolated where the salt rock reaches a thickness of tens to thousands of meters. This decoupling allows a separate consideration of the behavior of the two systems.

The suprasalt structure is dominated by the Zechstein morphology of NE-SW trending salt ridges and surrounded by salt rim synclines (Moeck et al. 2009). Major NW-SE and minor NE-SW oriented faults dominate the subsalt fault system in the Rotliegend rocks (Fig. 3.2b). Displacement along the faults indicates normal faulting by hanging wall down movement (Moeck et al. 2009).

A stress regime between normal faulting and a transition to strike-slip faulting is indicated in the Groß Schönebeck Rotliegend reservoir by an integrated approach of 3D structural modeling, 3D fault mapping, stress ratio definition based on frictional constraints, and a slip-tendency analysis (Moeck et al. 2009). Faults with high shear stress are supposed to be hydraulically active (e.g. Ito and Zoback, 2000; Zhang et al. 2002, 2007) and extensional faults may act as fluid-conduits (e.g. Gudmundsson et al. 2002). Therefore, the discrimination of critically stressed faults and extensional faults within the current stress field allows assessing the hydraulic conductivity of faults in the geothermal aquifer, by resolving the amount of shear stress and normal stress on any fault plane (by slip-tendency analysis) (Moeck et al. 2009). Arising thereby, the NNE to NE trending moderately dipping faults bear the highest shear stresses in response to the current stress field and as critically stressed faults, they are supposed to act as preferential pathways for fluid flow (Barton et al. 1995; Moeck et al. 2009). By contrast, the non-critically stressed NW-SE trending faults are expected to serve as barriers to fluid flow (Fig. 3.2b).

As only the subsalt fault system affects the reservoir target zone, we integrate only the latter into the model. Therefore, the fault pattern is simplified-, in that the major faults are integrated as representative fault zones, dissecting the Rotliegend reservoir, from top Hannover Formation to top basement (Fig. 3.2c). According to their hydraulic conductivity with respect to the current in situ stress field (Fig. 3.2b), a major NE-SW trending fault, which has been interpreted from

seismic sections (Moeck et al. 2009),- is supposed to act as a conduit and three minor NW-SE oriented faults are considered as barriers to fluid flow (Figs. 3.2c and 3.2d).

3.3 Method

The coupled fluid and heat transport models are based on the finite element method (FEM) and the simulations are carried out with the commercial software FEFLOW® (Diersch, 2002). FEFLOW® is a software package for modeling fluid flow and transport processes in porous media with variable fluid density effects. The governing partial differential equations of density coupled thermal convection in saturated porous media are based on Darcy`s law, as well as on mass and energy conservation laws (e.g. Bear, 1991; Nield and Bejan, 2006). The description of the equations is given in the Appendix A.

3.3.1 FEM model construction: Spatial discretization and parametrization

As a first step, the geometry of the stratigraphic layers as derived from the structural model described above is transferred into a format applicable for its use in a numerical simulation.
In general, the basic algorithms provided by the software FEFLOW® are two and a half dimensional. A 3D model is generated by vertical superposition of 2D unstructured triangular surfaces, representing internal geological boundaries (i.e. slices of the 3D model). All slices share the same horizontal spatial discretization. The third dimension is entered by vertically connecting nodal points between two confining slices to form a layer of the 3D model. Therefore, the starting point for the finite element model generation is to define a “supermesh” in FEFLOW® which forms the framework for the generation of the finite element mesh and contains all basic geometrical information the mesh generation algorithm needs (Diersch, 2002). By means of this 2D planar geometric object, the outer boundary of the model area is defined. Furthermore, lines representing the geometry of the faults` traces (Fig. 3.2c) are inserted within the supermesh prior to the triangulation phase. By adding those piecewise linear polylines as internal constraints to the triangulation, the trace of the fault could be fully restored within the model. Based on the geometric frame provided by the supermesh, a 2D unstructured triangle mesh is generated. In order to best approximate discrete faults as well as to enforce numerical stability for the simulation, a higher order of element refinement along the fault lines is performed than in the remaining part of the model.

To reproduce the geological structure, the z-coordinates of each geological top and base surface are assigned to each node of the corresponding top and bottom slice. Therefore, the resulting layer thicknesses a priori determine the vertical resolution of the numerical model. To optimize the numerical stability, the vertical resolution of the model is enhanced by subdividing two layers of large thicknesses (the Lower Triassic Buntsandstein and the Permian Zechstein) into two sub-layers of equal thicknesses respectively. A planar slice at a constant depth of -5000 m is integrated, along the base of the model to enforce numerical stability.

The major NE-SW oriented fault (conduit, Figs. 3.2c and 3.2d) is implemented by means of discrete feature elements. The latter represent finite elements of lower dimensionality, which can be inserted at element edges and faces (Diersch, 2002). In principle, FEFLOW® offers several distinct laws of fluid motion for discrete feature elements: Darcy, Hagen-Poiseuille and Manning-Strickler. Here, we use vertical 2D discrete elements and assume Darcy's law to describe fluid flow within the fault. The minor NW-SE trending faults (barriers, Figs. 3.2c and 3.2d) are modeled as equivalent porous media. They are represented by finite element areas for which a very low permeability is assigned along the trace of the fault. The respective areas of mesh refinement are set for 20 m on either side of the faults traces (lateral extent in total 40 m per fault barrier). The final 3D finite element model is composed of 20 slices and accordingly 19 layers. The model consists of approximately five million elements (= triangular prisms).

According to the main lithology of each geological unit, hydraulic and thermal rock properties are assigned constant to each corresponding layer in the numerical model (Table 3.1) and to the faults (Table 3.2). Each layer is considered homogenous and isotropic with respect to its physical properties. Taking into account anisotropic conditions would increase the understanding of the already complex interaction between physical processes and the composition of geological layers, but should be considered in future research as soon as detailed data are available.

Generally, the thermal conductivities increase downward due to compaction. An exception is the high thermal conductivity of the Zechstein salt layer.

Table 3.1 Stratigraphic units with predominant lithologies and corresponding physical properties used for the numerical simulations of the geothermal field for the Groß Schönebeck area. Hydrogeological barriers separating the stratigraphic succession into different aquifer systems are highlighted (bold).
Permeabilities, porosities and heat capacities assigned after Magri, 2005. Permeability, porositiy and heat capacity values for Post-Rupelian, Rupelian, Pre-Rupelian after Magri et al. 2008.
Thermal conductivities and radiogenic heat production after Scheck, 1997. Thermal properties for Post-Rupelian, Rupelian, Pre-Rupelian adapted from Magri et al. 2008. Radiogenic heat production value for the Rupelian after Balling et al. 1981. In brackets another set of properties tested in the numerical

simulations. Permeabilities, porosities and heat capacities for the Cenozoic to the Upper Permian Zechstein and for the Carboniferous after Magri, 2005; Scheck, 1997; for the Upper Rotliegend Formation to Late Carboniferous after Blöcher et al. 2010b; for Post-Rupelian, Rupelian, Pre-Rupelian after Magri et al. 2008. Thermal conductivities and radiogenic heat production for the Cenozoic to Upper Permian Zechstein after Norden and Förster, 2006 and Norden et al. 2008; for Post-Rupelian, Rupelian, Pre-Rupelian after Magri et al. 2008. Radiogenic heat production for the Rupelian after Balling et al. 1981. Thermal conductivities for the Upper Rotliegend Formation to Late Carboniferous after Blöcher et al. 2010b, for Carboniferous after Ollinger et al. 2010.

Stratigraphic Unit (Predominant lithologies)	Permeability $\kappa[m^2]$	Porosity ε[%]	Rock heat capacity c_s [MJ/m^{3}K]	Thermal conductivity λ [W/mK]	Radiogenic heat production Q_T [10^{-7} W/m^3]
Quaternary (Sand, silts)	1E-12 [1E-12]	23 [23]	3.15 [3.15]	1.5 [1.5]	7 [9]
PostRupelian (Sand, silts, clay)	1E-13 [1E-13]	23 [23]	3.15 [3.15]	1.5 [1.5]	7 [9]
Rupelian (Clays)	1E-15 [1E-15]	20 [20]	3.3 [3.3]	1 [1]	4.5 [4.5]
PreRupelian (Sands, silts, marls)	1E-13 [1E-13]	10 [10]	2.4 [2.4]	1.9 [1.9]	3 [6]
Upper Cretaceous (Marls, sandstones, siltstones)	1E-13 [1E-13]	10 [10]	2.4 [2.4]	1.9 [1.9]	3 [6]
Jurassic – Lower Cretaceous (Siltstones, mudstones)	1E-13 [1E-13]	13 [13]	3.19 [3.19]	2 [2]	14 [15]
Keuper (Clays, marls, gypsum)	1E-14 [1E-14]	6 [6]	3.19 [3.19]	2.3 [2.3]	14 [16]
Muschelkalk (Limestones, marls)	1E-18 [1E-18]	0.1 [0.1]	2.4 [2.4]	1.85 [1.85]	3 [10]
Buntsandstein (Silts, sands, evaporites)	1E-14 [1E-14]	4 [4]	3.15 [3.15]	2 [2]	10 [18]
Upper Permian Zechstein (Evaporites, mainly salt)	Impermeable ~ 0 [~0]	~0 [~0]	1.81 [1.81]	3.5 [4.5]	0.9 [4]
Upper Rotliegend – Hannover Fm (Sandstones, mudstones, siltstones)	1E-14 [1E-16]	3 [1]	2.67 [2.4]	1.84 [1.9]	10 [18]
Upper Rotliegend Elbe alternating sequence (Sandstones)	1E-14 [1.61E-15]	3 [3]	2.67 [2.4]	1.84 [1.9]	10 [14]
Upper Rotliegend Elbe base sandstone 2 (Sandstones)	1E-14 [6.44E-14]	3 [8]	2.67 [2.4]	1.84 [2.9]	10 [14]
Upper Rotliegend Elbe base sandstone 1 (Sandstones)	1E-14 [1.29E-14]	3 [15]	2.67 [2.4]	1.84 [2.8]	10 [10]
Upper Rotliegend Havel Subgroup (Sandstones, conglomerates)	1E-14 [2.58E-16]	3 [0.1]	2.67 [2.6]	2.13 [3]	10 [12]
Lower Permian Volcanics (Andesites, rhyolithes)	1E-14 [3.22E-16]	3 [0.5]	2.67 [3.6]	2.5 [2.3]	20 [10]
Carboniferous (Basement rocks)	Impermeable ~ 0 [~0]	~0 [~0]	2.46 [2.7]	2.65 [2.7]	15 [20]

Table 3.2 Table with physical properties assigned for the faults. Porosity, heat capacity, thermal conductivity, radiogenic heat production values for the conduit represent average values of the geological layers (adopted from Bächler et al. 2003; Clauser and Villinger, 1990), whereas for the barriers the same values as for the Sedimentary Rotliegend are used.

Property	$Fault_{Conduit}$	$Fault_{Barrier}$
Porosity φ	0.3	~ 0
Rock heat capacity c_s [MJ/m^{3}K]	2	2.67
Thermal conductivity λ [W/mK]	2	1.84
Permeability κ [m^2]	1.0E-09	Impermeable ~0
Radiogenic heat Q_T [10^{-7} W/m^3]	8	10

3.3.2 Simulations

An overview of all simulations is given in Table 3.3. To evaluate the influence of the dynamic coupling between heat and fluid transport processes, an uncoupled simulation is carried out, in which only the conductive heat transfer is considered (model 1). Within model 2, in addition to the conductive heat transport, the movement of fluid is allowed and fluid density effects are taken into account, resulting in a coupled fluid and heat transport simulation.
To assess the impact of faults on the coupled fluid and heat system, faults are implemented in model 3. The simulation results are compared with model 2, in which no fault is included.

Table 3.3 List of all simulations presented.

models		type of simulation
(No fault) models	1	steady state conductive
	2	transient coupled fluid and heat transport
fault model	3	transient coupled fluid and heat transport

3.3.3 Time discretization

The uncoupled model 1 is performed as a steady-state simulation assuming equilibrium conditions for the conductive heat transfer. The transient coupled fluid flow and heat transport simulations for the models 2 and 3 are carried out for 250 000 years to obtain steady-state conditions. All results are shown for the final simulation state at 250 000 years.

3.3.4 Boundary and initial conditions

For the top flow boundary condition, a fixed hydraulic head equal to the topographic elevation is set. Thereby, the groundwater flow is mainly controlled by gradients in the topography. At the model base, a no-flow boundary condition is assigned to simulate the impermeable nature of the basement.

For the temperature boundary conditions, a fixed constant surface temperature of 8°C is assumed, representing the average surface temperature in NE-Germany (Katzung, 1984). At the model base a basal heat flux Q [mW/m²] is prescribed that allows a variable temperature distribution in -5 km depth (Fig. 3.4). The spatially varying heat flux for the modeled area is extracted from a lithosphere-scale conductive thermal model of Brandenburg (Noack et al. 2012). This model takes into account the thermal effects of the underlying differentiated crust and lithosphere, down to a depth of - 125 km.

The pressure and temperature initial conditions are obtained from steady-state uncoupled flow and heat transport simulations.

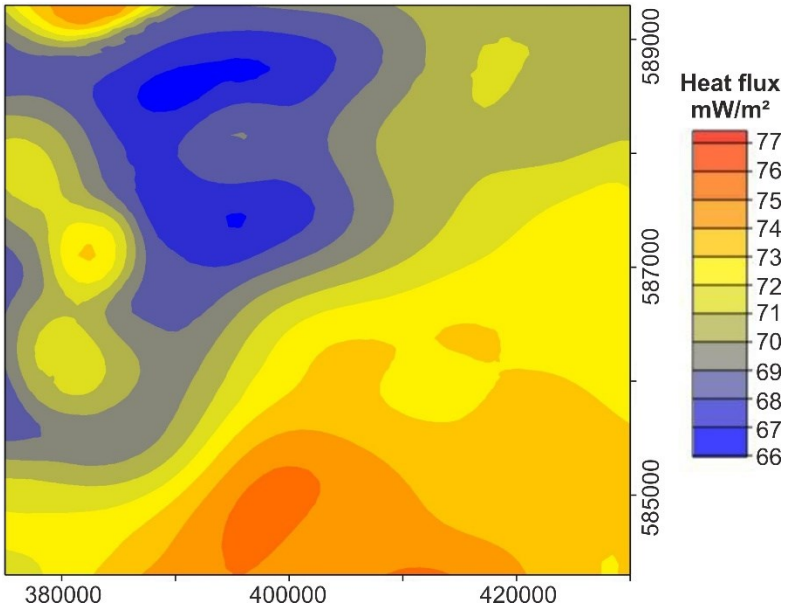

Figure 3.4 Spatially varying heat flux used as lower thermal boundary condition extracted from a lithosphere-scale conductive thermal model of Brandenburg (Noack et al. 2012).

3.4 Results

3.4.1 Conductive model 1

The preliminary investigation of the purely conductive model (1) permits a later comparison with the coupled fluid and heat transport model (2), and allows a clear distinction between conductive heat transfer mechanisms and coupled components. Conductive heat transfer occurs due to rock molecules transmitting their kinetic energy by collision (Turcotte and Schubert, 2002). Fig. 3.5a displays a representative, geological cross section, vertically cutting the model from north to south. The position of the cross section is sketched in the geological model in Fig. 3.3a and cuts the location of the Groß Schönebeck well GrSk 3/90. The profile dissects two major salt pillows in the central and in the northern part of the cross section, bordered by salt rim synclines. Fig. 3.5b shows the corresponding temperature distribution along the cross section for the conductive model 1. The temperature pattern above the Zechstein salt is characterized by almost flat isotherms which reflect the diffusive nature of heat transfer via conduction. Only directly above the major salt pillows, in particular above the thick pillow in the central part, the isotherms are slightly bent convex upward.

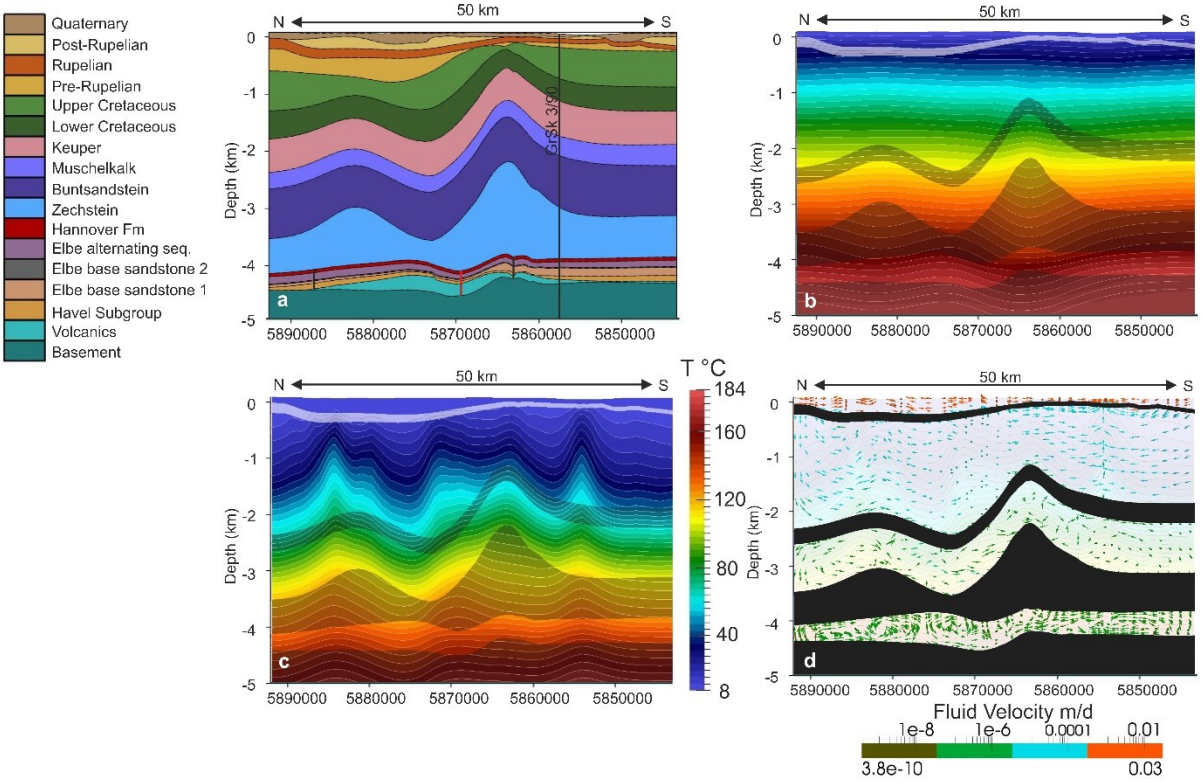

Figure 3.5 a: Vertical geological cross section from N to S through GrSk 3/90 for which the results in subfigures 3.5b, c, d and Figure 3.7 are shown. Position of the well is displayed by the black solid line. The location of the cross section is delineated in Fig. 3.3a by the dotted black line. The location of the permeable fault cutting the central part of the cross section below the salt rim syncline is indicated by

the red solid line. The positions of the two fault barriers dissecting the profile in the N and S parts are displayed by black solid lines. The outlines of the impermeable basement, Zechstein and Muschelkalk layers are grey-shaded and Ruplian is white-shaded in the background of the temperature profiles of Figs. 3.5b, c and 3.7a. In Figs. 3.5d and 3.7c these four layers are black-shaded. Vertical exaggeration: 7:1 for all sections; b: Temperature distribution of the conductive model 1. The conductive thermal field is generally characterized by flat isotherms, which are locally bent in response to the highly conductive Zechstein salt. c: Temperature distribution of the coupled fluid and heat transport model 2. Fluid flow processes alter the thermal regime as displayed by the convex up- and downward shaped isotherms. The development of the coupled fluid system and thermal field is closely related to the distribution of permeable and impermeable sedimentary layers. d: Combination plot of the fluid velocity vectors (length non-scaled) and temperature distribution with reduced intensity in the background. The vectors illustrate the different fluid flow characteristics and changing velocities in the four aquifer systems decoupled from each other.

Throughout the Zechstein salt the temperature pattern is disturbed showing isotherms which are bent convex downward within the two major salt pillows. In the area of the salt rim synclines the isotherms are bent convex upward. This temperature pattern gives rise to a dipole shaped thermal anomaly above and within major salt structures. This thermal anomaly is induced by thermal refraction, as triggered by the sharp contrast in thermal conductivity between the thermally more conductive salt and the less conductive surrounding sediments (Table 3.1).

The temperature pattern observed within the Zechstein salt continues downward throughout the entire pre-salt sequence: below the major salt pillows we find convex downward shaped isotherms indicating cooler temperatures. By contrast, the isotherms are bent convex upward below the salt rim synclines reflecting increased temperatures.

According to Fourier`s law, the energy flow is equal to the thermal conductivity multiplied by the temperature gradient within the rock. Increasing the rock thermal conductivity enhances the energy flow within the system. Therefore, the high thermal conductivity of the salt exerts a strong control on the entire conductive temperature field. This phenomenon is known as the “chimney effect” (cf. Scheck, 1997). Accordingly, salt structures act as chimneys of efficient heat transfer and thus cause higher temperatures above salt structures and lower temperatures in and below the two major salt pillows (Fig. 3.5b).

The higher temperatures in the area of the salt rim synclines are mainly induced by the sediments overlying the salt. Due to their low thermal conductivities, they cause heat storage, i.e. thermal blanketing.

Comparison between modelled and measured temperatures

For validation of our simulation results, the modeled temperatures are compared to observed temperatures from different wells in the vicinity of Groß Schönebeck (Tables 3.4 and 3.5). Observed temperature values available for the different wells are plotted against depth in comparison with the modeled temperature gradients for the respective well (Fig. 3.6a-g).

Table 3.4 Observed temperatures in wells used for the comparison with modeled temperatures of the conductive model 1, the coupled fluid and heat transport model 2 and an additional simulation in which the permeability of the Rupelian clay is decreased to k=1e-18 m² (s. chapter 3.5): Temperature (T) at total depth (TD) of temperature log and corrected temperature (Tcorr.) at TD of log for perturbed logs after Förster (2001).

Well	TD of log/ depth of BHT [m]	T at TD of log [°C]	Tcorr. at TD of log [°C]	T of conductive model 1 [°C]	T of coupled model 2 [°C]	T of additional coupled model [°C]
Chi/Chorin 1/71	3800	144.3	147	144	111	112
Gür/Grüneberg 2/74	4100	157	161	172	152	160
Tl/Templin 1/95	1652	69.3		87	55	58
Tuc/Tuchen 1/74	4250	139.8	147	170	137	138
Zeh/Zehdenick 2/75	3650	139		160	138	138
Zeh/Zehdenick 1/74	4250	159.5	162	174	147	148

Table 3.5 Observed temperatures in wells after Norden et al. (2008), used for the comparison with modeled temperatures of the conductive model 1, the coupled model 2 and an additional model in which the permeability of the Rupelian aquitard is decreased to k=1e-18 m² (s. chapter 3.5).

Well	Depth [m]	Temperature [°C]	Quality	T of conductive model 1 [°C]	T of coupled model 2 [°C]	T of additional coupled model [°C]
GrSk/Groß Schönebeck 3/90	2800	119.9	unperturbed	123	101	113
	3770	135.1	unperturbed	144	124	135
	4230	148.6	unperturbed	161	142	152
	4286	150.8	unperturbed	163	144	154
Chi/Chorin 1/71	2900	126.6	Slightly perturbed	123	87	88
	3650	139.8	Slightly perturbed	139	105	107

The comparison of the well measurements (black rhombs) with the modeled temperatures of the conductive model 1 (red solid line) shows that the temperatures predicted by the conductive model are too hot (mean value of $\Delta T=11°$ K), except for well location Chorin 1/71 where the well data show a very good fit with the modeled values (Fig. 3.6c). This well penetrates the slope of a thick NE-SW trending salt ridge (cf. Fig. 3.2a). Accordingly, the temperatures in well

Chorin 1/71 are measured within the Zechstein (Ollinger et al. 2010), and directly below the salt. Consequently, predominant conductive heat transfer is expected in response to the hydraulic impermeability of the salt. Likewise, the simulated temperatures of the conductive model 1 reveal a good fit with the two uppermost observed temperatures at well GrSk 3/90 throughout the Zechstein salt, also indicating heat transfer via conduction there (Fig. 3.6e). Except for Chorin 1/71 and the two uppermost observed temperatures at GrSk3/90 (Figs. 3.6c and 3.6e), the modeled temperatures of the conductive model 1 do not reproduce the observations. The relatively large misfit between modeled and observed temperatures points toward other heat transfer processes that may influence the thermal field in addition to conduction.

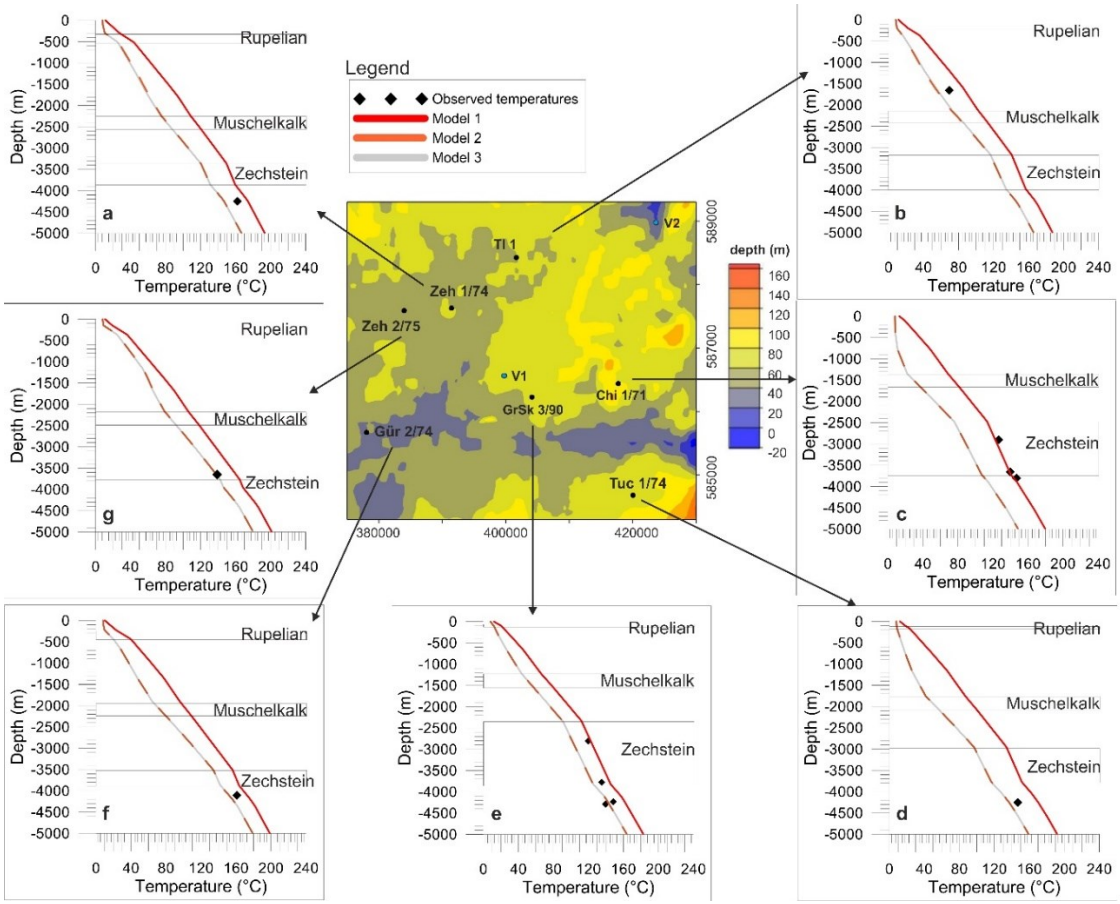

Figure 3.6 Map of the surface topography (defining the hydraulic upper boundary condition) with the locations of the different wells. V1 and V2 display the positions of two virtual wells for which calculated temperatures-depth gradients are plotted in Fig. 3.11. In sub-figures 3.6 a-g, the observed temperature values available for the different wells are plotted against depth in comparison with the modeled temperature gradients for the respective well. Observed temperatures are displayed by black rhombs. The modeled temperatures for conductive model 1 are represented by solid red lines, for the coupled model 2 by dotted orange lines and for the fault model 3 by solid grey lines. The depth position of the Rupelian, the Muschelkalk and the Zechstein layers are outlined by grey lines in the background in each figure.

3.4.2 Coupled fluid and heat transport model 2

Within model 2 we investigate the possible influence of fluid flow processes on the thermal field, as one possible additional mechanism. Fluid density driven convection and advection induced by topography-driven groundwater flow are both taken into account within the simulation. Figure 3.5c shows the temperature distribution and Figure 3.5d the velocity field of the coupled fluid and heat transport model 2 for the same geological cross section (Fig. 3.5a). Compared to the conductive model 1 (Fig. 3.5b), the isotherms are depressed, displaying distinctively lower temperatures (range ~ 20-40°C). This temperature drop is induced by the adopted upper thermal boundary conditions (8°C) generating a permanent cold water inflow at the model surface with highest fluid velocities (0.001-0.03 m/d) (Fig. 3.5d). Except for the Cenozoic aquifer, the isotherms are not flat like in the conductive case (Fig. 3.5b).

In the suprasalt sequence, the isotherms are bent convex upward above thick salt rim synclines, bordered by convex downward shaped isotherms (Fig. 3.5c). The fluid vectors reflect the isotherm distribution and upward movement of the fluid is observed in areas where the isotherms are bent convex upward (Fig. 3.5d). Fluid velocities of 1e-5 – 1e-4 m/d occur within the Mesozoic aquifer and decrease within the Buntsandstein aquifer (~ 1e-6 m/d). Within the latter, the thermal disturbances are also weaker than in the Mesozoic aquifer.

These thermal instabilities are characteristic for thermal density driven convective heat transport which is associated with the circulation of hot fluids. The heat is carried by the fluid movement, originating out of fluid density changes due to temperature variations: the heated fluid from the deeper regions becomes buoyant and rises due to its lower density, forming convection cells (Bundschuh and Arriaga, 2010). Generally, the development of thermal convection is observed in permeable aquifers (Table 3.1, Fig. 3.3b). In these aquifers, the fluid is allowed to circulate in the free void space of the sediments (Fig. 3.5d). However, the development of pronounced convection cells is obviously favored by a larger thickness (cf. Bjørlykke, 2010), which is only the case for the Mesozoic aquifer (Fig. 3.3b).

Hydraulically impermeable layers, like Zechstein, Muschelkalk and Rupelian inhibit fluid movement and thus the progression of convection cells from one aquifer to another. Therefore, the extension of convective flow within the Mesozoic aquifer system is limited by the Muschelkalk and Rupelian aquicludes (Fig. 3.5c).

In the area of the Zechstein salt, convex upward and downward shaped isotherms above and below major salt pillows again reflect the chimney effect triggered by the high thermal conductivity of the salt (Fig. 3.5c).

Throughout the Rotliegend aquifer system, corrugated to flat isotherms are present. Although fluid circulation is observed within this less thick aquifer (Fig. 3.3b) the very low fluid velocities (3.8 – 1e-8 m/d) (Fig. 3.5d) and the flat character of the isotherms points to predominant conductive heat transfer within the aquifer.
However, compared to the conductive model 1, the convex upward shaped isotherms in and below the salt rim synclines are more pronounced. The increased temperatures are, like for the conductive case, due to thermal blanketing, caused by the thermally less conductive, thick post-salt sediments but also additionally triggered by the thermal feedback from the convection cells above. This thermal feedback leads to a more pronounced isotherm deviation than in the conductive model 1 (Fig. 3.5b).

Comparison between modelled and measured temperatures

The comparison of the well measurements (black rhombs) with the modeled temperatures of the coupled model 2 (dotted orange line) reveals a good fit with the observed temperature values in Tuchen 1/74 (Fig. 3.6d), GrSk 3/90 (Fig. 3.6e), Grüneberg 2/74 (Fig. 3.6f), and Zehdenick 2/75 (Fig. 3.6g) (deviations < 10° K). In Zehdenick 1/74 (Fig. 3.6a) and Templin 1/95 (Fig. 3.6b), the temperature deviations are slightly higher (> 10° K). At these locations the observed temperatures are located between the conductive (red solid line) and coupled (dotted orange line) model predictions which complicates a clear distinction between conductive and coupled heat transport processes. However, all modeled temperature curves for the coupled simulation show a very similar trend in each well. With increasing depths, the temperatures increase steadily though the values are smaller than in the conductive model 1 for the same depth. Only in the thickness ranges of the Rupelian, the Muschelkalk and the Zechstein layers, the slope of temperature curves is parallel to the conductive case, confirming the impermeable nature of these layers that hamper cold water inflow from the surface into deeper parts of the model. At locations where the Rupelian is eroded (Chorin 1/74, Fig. 3.6c) strong cooling is observed in shallower depth levels (< - 1500 m) caused by the unhampered cold water inflow from the surface into the Mesozoic aquifer. The enhanced cooling in the shallow part of well location Tuchen 1/74 (Fig. 3.6d) can be explained by the presence of a quaternary channel in lateral offset of the well (cf. Fig. 3.3a). The permeable subglacial channel hydraulically connects the Quaternary with the Mesozoic aquifer providing local pathways for the cold inflow from the surface.

In summary, the modeled temperatures of the coupled model 2 fit the observations better than the temperatures of the conductive model 1. These results suggest that the assumption of a coupled fluid and heat transport system approximates the natural temperature regime observed in the area Groß Schönebeck better than the purely conductive mechanism. Nevertheless, greater temperature deviations are still found between observations and model predictions. Generally, the temperatures of the coupled model 2 are colder than the measured values (Tables 3.4 and 3.5). In Chorin 1/74, large deviations between measured and simulated temperatures of model 2 (33.3-38.6° K) are due to the predominant conductive heat transport throughout the Zechstein salt (Tables 3.4 and 3.5). For the same reason, the uppermost temperature values of the coupled model 2 are too cold (11-18.9° K) compared to the observed temperatures at well GrSk 3/90 throughout the Zechstein salt (Table 3.5). Also, the lowermost temperatures at GrSk 3/90 underestimate the observations (6.6-6.8° K, Table 3.5) as well as the values at Grüneberg 2/74 (5° K), Templin 1/95 (14.3° K), Tuchen 1/74 (2.8° K), Zehdenick 2/75 (1° K) and Zehdenick 1/74 (12.5° K) (Table 3.4). Possible reasons for these deviations could be the choice of physical properties assigned for the geological units, the structural limitations of the model and the choice of boundary conditions (s. chapter: 3.5). Another reason could be related to the impact of faults on the thermal field. To assess the potential influence of faults on the target reservoir of the Groß Schönebeck well (GrSk3/90), we implemented the major faults in this reservoir into a third series of simulations.

3.4.3 Fault model 3

Vertical cross section

In model 3 a major NE-SW oriented permeable fault and three NW-SE oriented impermeable faults are integrated (Fig. 3.2c and 3.2d). The simulation results of fault model 3 are compared with the coupled model 2, in which no faults are included (in the following referred to as no fault model 2). The results of fault model 3 are illustrated in Fig. 3.7a for the same vertical cross section as shown in Fig. 3.5a and which is cut by three faults, including two barriers and one conduit.

The locations of the two fault barriers in the N and S parts of the cross section are framed by dotted black rectangles in Fig. 3.7a. By comparison to the no fault model 2 (Fig. 3.5c) and to the conductive model 1 (Fig. 3.5b), no differences can be traced in the isotherm pattern, indicating that the fault barriers have no remarkable influence on the thermal field. Due to their very low permeability and porosity (Table 3.2), they are almost impermeable and unable to

conduct heat by fluid flow. Therefore, conductive heat transport is likely to persist as the predominant heat transfer mechanism in those areas. Because the thermal properties of the barriers do not differ from the rock matrix of the Sedimentary Rotliegend (Table 3.1), no influence on the isotherm pattern can be identified (Fig. 3.7a).

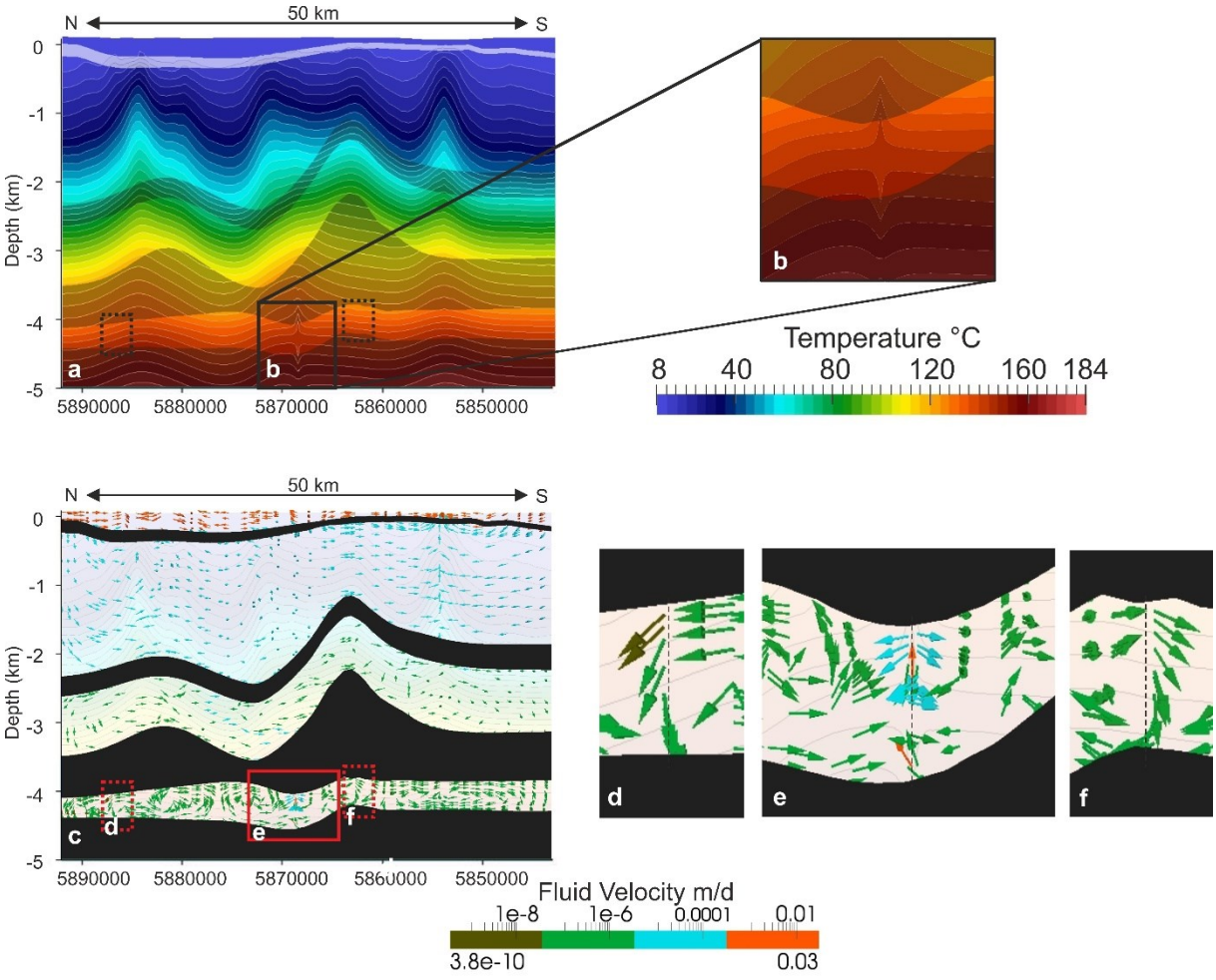

Figure 3.7 a: Temperature distribution of the fault model 3 on the same vertical cross section as Fig. 3.5a. The location of the permeable fault cutting the central part of the cross section below the salt rim syncline is framed by the black rectangle. The locations where the two fault barriers dissect the profile are framed by a dotted black rectangle; b: Zoom on the temperature distribution around the permeable fault as indicated by the black rectangle in Fig. 3.7a. Convex upward shaped isotherms at the faults upper tip and convex downward shaped isotherms at the lower tip form a thermal anomaly induced by the permeable fault; c: Fluid velocity vectors (length non-scaled) and temperature distribution with reduced intensity in the background. The fluid flow in the subsalt sequence is influenced by the three faults dissecting this profile for which d-e display zooms into the fault areas for (d and f) the impermeable faults and for (e) the permeable fault.

The location of the permeable fault, however, can be observed by locally disturbed isotherms directly below the salt rim syncline at the northern flank of the central salt pillow (solid black

rectangle in Fig. 3.7a). A zoom into this fault-induced temperature anomaly reveals that the isotherms are sharply bent convex upward at the upper tip of the fault (Fig. 3.7b). This convex upward isotherm pattern continues upwards and diminishes towards the top of the overlying salt layer. By contrast, the isotherms are shaped convex downward at the lower tip of the fault. This thermal pattern continues downward throughout the underlying basement layer. In the central part of the fault (at its mid-depth), the temperatures are equal to the thermal field adjacent to the fault.

The overall isotherm pattern in the permeable fault displays a relatively uniform temperature distribution (144-148°C) resulting in temperatures that are higher at the top and lower at the bottom of the fault compared to the no fault model (Fig. 3.5c). The fault-induced thermal anomaly indicates that the permeable fault locally impacts on the temperature field of the Rotliegend aquifer, but also on that of the overlying salt and the underlying basement. Within these two layers, the heat from the fault is transferred not by fluids but by conduction due to the impermeable nature of salt and basement.

The appropriate flow field is shown in Fig. 3.7c as a combination plot of fluid velocity vectors and distribution of isotherms for the same vertical cross section (cf. Fig. 3.5a). Figs. 3.7d and 3.7f show zooms into the location of the two fault barriers in the N and S parts of the cross section whereas Fig. 3.7e illustrates a zoom into the permeable fault area in the central part (cf. Fig. 3.7b).

The velocity vectors expose an influence of the faults on the fluid circulation within the Rotliegend aquifer (Fig. 3.7c). Although the isotherm pattern is not affected by the fault barriers, the vectors indicate fluid deviation along these faults (Figs. 3.7d and 3.7f). Along both fault barriers downward flow occurs with decreased velocities (~ 1e-7 – 3.8e-10 m/d) but no fluid flow can be traced in their central parts. This observation indicates a fluid stagnation zone within the fault barriers in which no significant volume of fluid can be transmitted due to the impermeable conditions and confirms that the heat is transmitted by conduction there.

By contrast, the fluid circulation and velocity are significantly influenced within and around the permeable fault (Fig. 3.7e). At mid-depth and at the lower tip, fluid vectors display fluid flow towards the fault from the surrounding sediments. In the fault center, the vectors indicate upward oriented flow with highest velocities up to 0.03 m/d. At the upper tip, the fluid spreads out of the fault and moves laterally and downward along its flanks.

From surrounding sediments towards fault, the fluid advection is induced the by high permeability contrast between these two domains (Tables 3.1 and 3.2) and causes thermal equilibration there. This equilibration leads to the observed relatively uniform temperature

distribution ranging between 144 to 148°C in the permeable fault (Fig. 3.7b). The upward moving fluid finally spreads out at the upper tip of the fault because it cannot enter the overlying impermeable Zechstein salt.

To track the thermal state and fluid movement along the entire permeable fault, the distribution of isotherms with flow vectors are shown along the entire fault plane in Fig. 3.8. The isotherms reveal alternating convex upward and downward shapes with corresponding hotter (140-148°C) and colder (132-140°C) domains. The flow vectors display a vigorous fluid circulation within the permeable fault. The colder domains roughly correspond to downward oriented flow whereas the hotter domains consort with upward oriented flow. At the upper tip, the vectors also indicate horizontal flow along the fault plane.

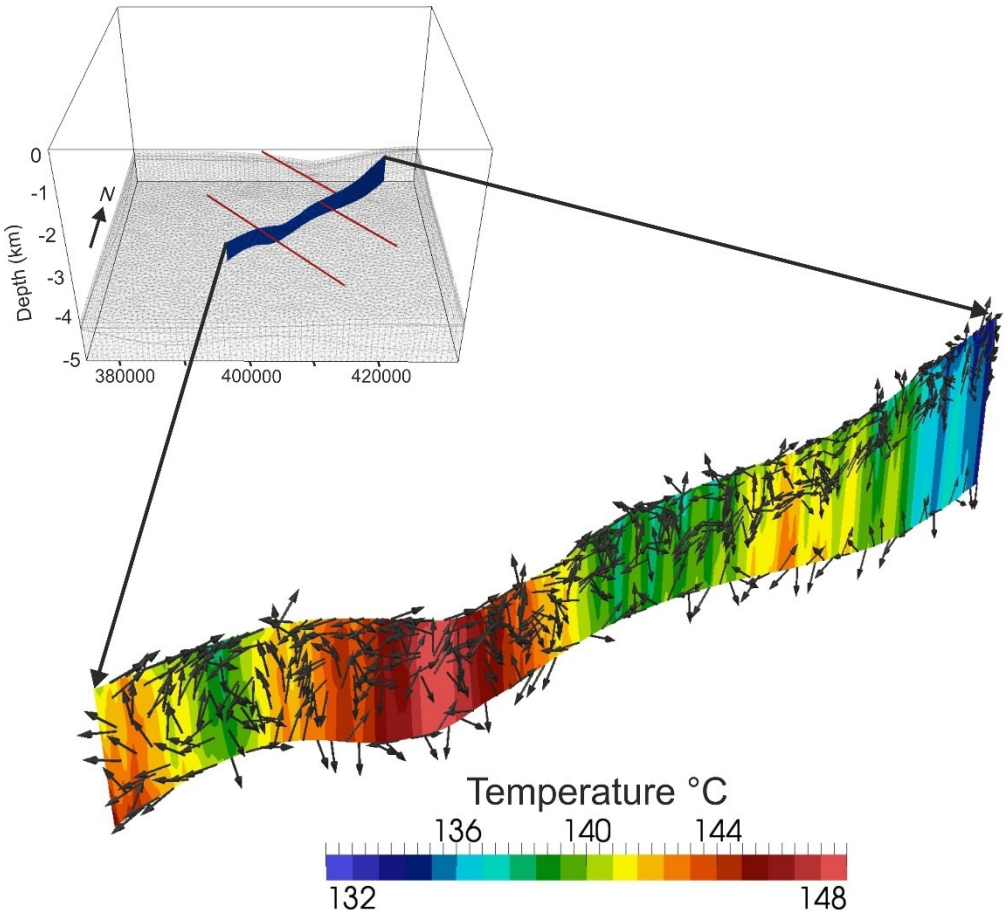

Figure 3.8 Temperature distribution along the entire permeable fault with fluid vectors (length non-scaled). Alternating hotter (140-148°C) and colder domains (132-140°C) with corresponding convex upward and downward shaped isotherms indicate convective heat transport and vigorous fluid flow within the permeable fault.

The higher fault permeability enables up and downward fluid flow with increased velocities as displayed by the vectors in the fault center in Fig. 3.7e. The differently oriented vectors reflect the convex up and downward shaped isotherm pattern which is characteristic for convective flow (cf. Fig. 3.5c and 3.5d). Within the fault heated fluid becomes less dense due to thermal expansion. The buoyant fluid rises, cools and finally flows downward again due to its increased density. The observed horizontal flow at the upper faults tip is induced by the overlying Zechstein salt that acts as a sealing rock. As a consequence the fluid spreads out of the faults top and distributes along both sides of the fault (cf. Fig. 3.7e).

Horizontal temperature distribution

Figs. 3.9a and 3.9b show the temperature distribution on a horizontal slice cutting the no fault model 2 and fault model 3 at a constant depth of -4000 m. A temperature difference map between the two models is shown for -4000 m depth (Fig. 3.9c). At this depth the upper tips of the faults come close to the base of the Zechstein layer.

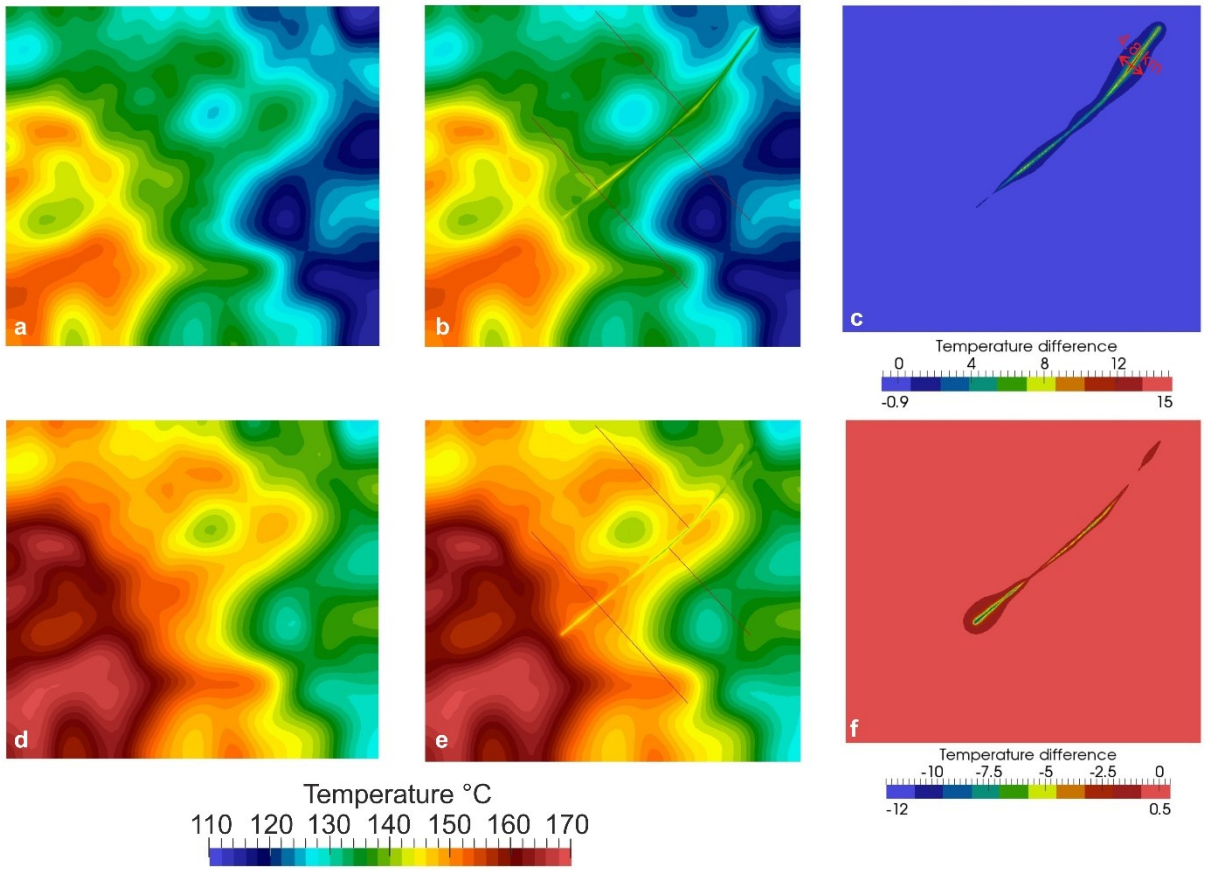

Figure 3.9 Temperature distribution on a horizontal slice in -4000 m depth cutting (a) the no fault model 2 and (b) the fault model 3 whereas (c) displays the corresponding temperature difference map in which the no fault model 2 is subtracted from fault model 3. Positive values indicate higher temperatures in

the fault model and vice versa. The temperature differences are up to 15°C higher in the NE-SW trending permeable fault than in the no fault model 2. Note the area influenced by the latter encompasses ~ 4.8 km at the NE tip of the fault (red arrow); (d-e) Temperature distribution on a horizontal slice in -4400 m depth cutting (d) the no fault model 2 and (e) the fault model 3. Fig. 3.9f shows the temperature difference map in which the no fault model 2 is subtracted from fault model 3. Positive values indicate higher temperatures in the fault model and vice versa. In contrast to -4000 depth, the temperatures in the permeable fault are up to -12 °C cooler than in the no fault model 2.

The temperature patterns for model 2 (Fig. 3.9a) and for model 3 (Fig. 3.9b) correlate with the thickness of the Zechstein layer (Fig. 3.2a): in the SW model area, where the salt has thicknesses close to zero, the temperatures are significantly higher (up to 40°C). On the contrary, in areas with increased salt thicknesses in the central and E parts of the model, we find lower temperatures (range: 112-120°C) below the major NE and NW trending thick salt ridges.

By comparing the temperature distribution of the fault model 3 (Fig. 3.9b) with that of the no fault model 2 (Fig. 3.9a), it can be seen that the permeable NE-SW trending fault influences the temperature field: at the SW tip, isotherms trend towards the fault entry, indicating higher temperatures (~142-144°C) compared to the same area in model 2 (~ 134-138°C). In the central part of the fault, the isotherms display values between 142-146°C decreasing towards the NE tip (132-140°C), where the temperatures in the no fault model 2 range between 110 and 124°C. The varying temperatures in different parts of the permeable fault reflect the alternating hotter and colder domains caused by the convective fluid circulation within the fault (cf. Fig. 3.8).

The corresponding temperature difference map between model 2 and 3 shows that the temperatures in the permeable NE-SW trending fault are up to 15 °C higher than in the no fault model 2 (Fig. 3.9c). The temperature differences are largest in the NE part of the fault. There, also the range of influence of the fault covers a maximum distance of ~ 4.8 km. Though the overall temperature range is limited within the entire fault (132-148°C), larger temperature differences occur below the major salt structures, where the surrounding thermal field is cooler (Fig. 3.9a). With increasing distance from the fault, the temperature differences gradually decrease indicating an equilibration with the matrix thermal field (cf. Figs. 3.7b and 3.7e).

The temperature distribution in -4400 m depth is shown on Fig. 3.9d for the no fault model 2 and in Fig. 3.9e for the fault model 3. The horizontal slice mainly cuts the Lower Rotliegend Volcanics, representing the lowermost unit cut by the faults. Fig. 3.9f depicts the temperature differences between the two models at the same depth. Compared to the temperature field in -4000 m depth (Fig. 3.9a), the temperatures in model 2 are up to 15°C higher at -4400 m depth (Fig. 3.9d). Locally increased temperatures occur in the SE and E, where the salt thickness is close to zero, whereas locally reduced temperatures evolve in the W, below the thickest salt

ridges. Comparing the predicted temperatures for the two models reveals that the temperatures in the fault are cooler than in the no fault model (Fig. 3.9d and 3.9e). Similar to -4000 m depth (Fig. 3.9b), the temperatures range between 142-146°C at the SW tip, between 140-144°C in the central part and decrease towards the NE tip (134-140°C).

The similar temperatures observed at both depths result from fluid advection from surrounding sediments into the fault (cf. Figs. 3.7c and 3.7e).

In contrast to -4000 m depth, the temperature difference map at -4400 m (Fig. 3.9f) indicate temperatures that are up to 12 °C lower in the fault compared to the no fault model 2. The temperature differences are highest in the SW model area, where the temperatures are significantly higher in the matrix thermal field (cf. Fig. 3.9d).

Both temperature difference maps in -4000 m and -4400 m depth demonstrate that the fault barriers have no impact on the thermal field (cf. Fig. 3.7a).

Comparison between modelled and measured temperatures

In all well locations (Fig. 3.6a-g) the modeled temperature curves of the fault model 3 are similar to the no fault model 2 generally fitting well with the observation data. Despite of the fact that the locations of the wells Zehdenick 1/74 and GrSk 3/90 are close to the NW-SE trending fault barriers (Fig. 3.2c), no temperature variations between fault and no fault model are observed. This temperature trend confirms that the thermal field is not influenced by the fault barriers (Figs. 3.7a, 3.9c and 3.9f).

Pressure

The calculated pressure of both the fault and no fault model ranges between ~40 MPa in -4400 m and ~ 44 MPa in -4400 m which corresponds to the observed hydrostatic pressure conditions in the Groß Schönebeck reservoir (Huenges et al. 2001).

In Figs. 3.10a and 3.10b the pressure differences are depicted between the models 2 and 3 at -4000 m and -4400 m depth. In both figures, negative values indicate a lower pressure in the fault model whereas positive values correspond to a higher pressure in the fault model.

In -4000 m depth the pressure differences are in the range of -43 to -15 kPa. Pressure drops (~ -30-35 kPa) develop within the NW-SE trending fault barriers (Fig. 3.10a) and pressure offsets can be observed around them. Likewise, the pressure is reduced in the permeable fault, particularly at its tips (~ -30-43 kPa). This pressure drop correlates with the highest topographic elevation of the permeable fault plane in the NE and SW (cf. Fig. 3.8). Pressure offsets around

the barriers are caused by the high permeability contrast between faults and surrounding Rotliegend sediments (Tables 3.1 and 3.2).

In -4400 m depth the pressure differences range from -7 to 60 kPa (Fig. 3.10b). Here, the pressure is higher in the faults (~ 20-50 kPa) compared to the no fault model 2. Within the impermeable faults, the pressure differences are relatively uniform (~ 40 kPa). In the conduit the pressure increase is more pronounced in areas where the fault reaches greatest depths in the SW parts and in the NE (cf. Fig. 3.8). Similar to -4000 m, pressure offsets develop around the impermeable faults due to the high permeability contrasts between faults and surrounding sediments.

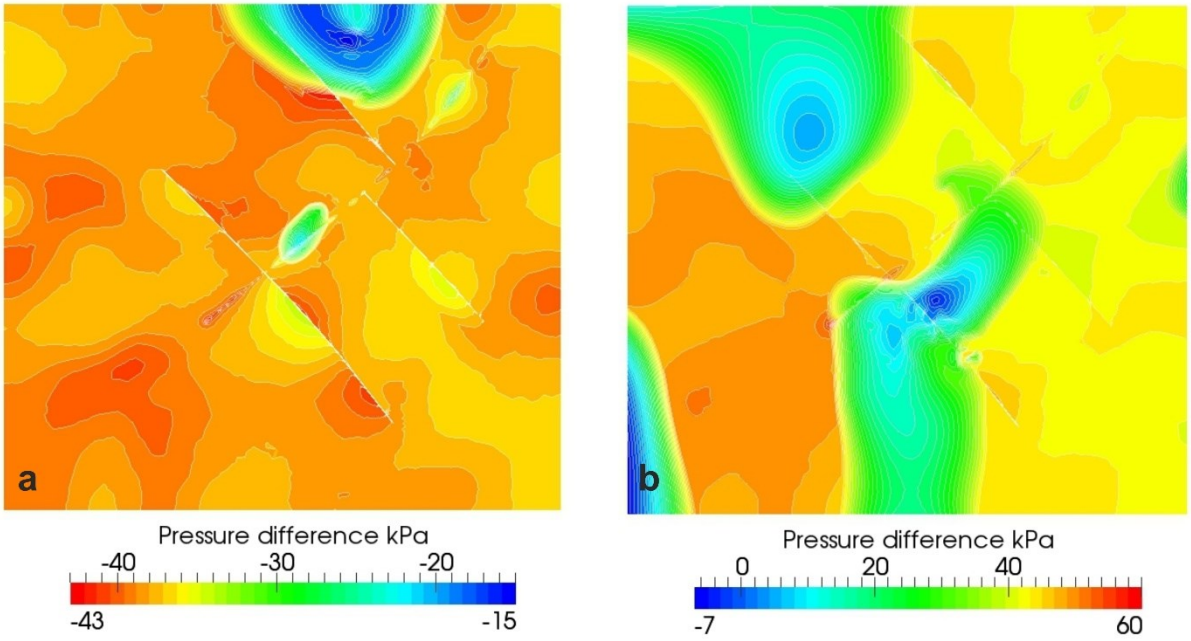

Figure 3.10 Pressure differences between no fault model 2 and fault model 3 (a) at -4000 m depth and (b) at -4400 m depth. Positive values indicate a lower pressure in the fault model whereas negative values correspond to a higher pressure in the fault model. Pressure offsets are visible and most prominent around the NW-SE oriented impermeable faults.

3.5 Discussion and conclusions

The 3D conductive and coupled fluid and heat transport simulations and the integration of faults into the system revealed several specific controlling factors for the thermal field.

Conduction

Assuming thermal conduction as the only heat transport mechanism reproduces the thermal observations in those parts of the model where layers are impermeable. Those layers comprise the Tertiary Rupelian, the Triassic Muschelkalk and the Permian Zechstein and the basement.

There, the contrasts in thermal conductivities decisively shape the temperature distribution. The most obvious effect of this type is the influence of the thermally highly conductive Zechstein salt. This strong impact of the Permian Zechstein salt on the deep thermal field is consistent with results from previous modelling studies in the North German Basin (Bayer et al. 1997; Cacace et al. 2010; Kaiser et al. 2011; Noack et al. 2010; Scheck, 1997; Sippel et al. 2013; Magri, 2005). The salt leads to a focused transfer of heat, amplified in salt structures like diapirs and pillows where the characteristic di-pole shaped thermal anomalies develop.
In our conductive model, the temperatures are too hot compared to the temperature observation from the different wells, apart from well measurements obtained from the Zechstein salt. For the remaining parts of the model, relatively large deviations occur between modeled and observed temperatures suggesting that additional heat transfer processes are active that modify the temperature distribution.

Advection

Accordingly, fluid flow considered in addition to heat transport within a coupled simulation reproduces observed temperatures better in those domains where permeable layers are present. In comparison to the conductive model, suppressed isotherms show that the fluid flow has an overall cooling effect induced by the upper thermal boundary condition. This cooling effect reaches greater depths in areas where the Rupelian is missing because cold water can flow unhampered into the Mesozoic aquifer. Additional local pathways for the cold water inflow are provided by Quaternary channels, hydraulically connecting the Quaternary with the Mesozoic aquifer. The influence of advective cooling through topography-driven fluid flow on the temperature field has been demonstrated previously by 2D flow and heat simulations along the northern Rheingraben (Lampe and Person, 2002). Furthermore, simulation results of 2D thermohaline models of the North German Basin indicate that the inflow of freshwater reaches the Pre-Rupelian aquifer even in areas where the Rupelian is thin and that this inflow is favored by Quaternary channels (Magri et al. 2008). In summary, our results suggest that cooling due to topography-driven fluid flow may reach down to depths of maximum -1800 m if the Rupelian layer provides adequate windows.

Convection

In addition to advective cooling, the overall temperature distribution of the coupled fluid and heat transport model is influenced by convective heat transfer closely linked to the distribution of permeable aquifer systems and impermeable aquicludes.

In the suprasalt sequence, convection cells develop in the Mesozoic aquifer, where the latter is sufficiently thick and permeable. Both, thickness (i.e. water column) and permeability of the sediments are the most critical factors for the Rayleigh number which expresses the conditions required for thermal convection (Bjørlykke, 2010). The underlying thin and low permeable Muschelkalk aquiclude, however, decouples the flow system into the Mesozoic aquifer above and the Buntsandstein aquifer below. Although thermally induced instabilities can be observed within the Buntsandstein aquifer, its thickness is obviously insufficient for the development of convection cells.

In conclusion, the suprasalt unit is predominately influenced by advective heat transport in the Cenozoic and shallow part of the Mesozoic aquifer (up to maximum -1800m depth) counteracted by convective heat transport within the latter.

In contrast, the temperature distribution of the subsalt system appears to be mainly influenced by conduction and by a thermal feedback with the overlying layers. Although there are indications for weak fluid circulation in the permeable sediments of the Rotliegend aquifer, fluid velocities (~ 1e-08-1e-10 m/d) are too slow to cause significant temperature anomalies. This observation leads to the conclusion that conduction outweighs the heat transfer via fluids in the Rotliegend aquifer.

However, the generally good fit between the modeled temperatures of the coupled fluid and heat transport simulation and the observed values suggests that fluid flow processes play an important role in the heat transfer mechanisms controlling the overall thermal field of the Groß Schönebeck area. This finding disagrees with earlier results from a conductive thermal model of the Groß Schönebeck test site (Ollinger et al. 2010) and of the Brandenburg area (Noack et al. 2010) stating that the entire thermal regime in the region is dominated by conduction. However, our results confirm that the moderate permeability of the Rotliegend aquifer, combined with a comparably small thickness, prevents that convection could alter the diffusive thermal regime (cf. Ollinger et al. 2010). We agree with Noack et al. 2012 in that moving fluids in restricted areas may influence the deep thermal field of the Brandenburg area. Furthermore, coupled simulations of fluid and heat as well as mass transport for the E part of the North German Basin confirm that thermally induced convection at the basin scale is feasible though locally restricted (Kaiser et al. 2011; Magri, 2005). In accordance with these results we suggest that induced convective circulation in the shallower aquifers decisively shapes the thermal field in the Groß Schönebeck area, whereas a convective influence in the deep Rotliegend aquifer can be neglected.

Comparison to other models

The comparison of the modeling results with temperatures estimations by Agemar et al. (2012) shows a generally good fit with the coupled model 2 at -4000 m and -4400 m depth (Figs. 3.9a and 3.9d). A similar regional temperature trend can be observed in both maps. At -4000 m depth, highest temperatures (150-155°) characterize the SW model area, while temperatures vary between 145-150° in the W in both cases. In the northern part, minor differences are observed with temperatures ranging between ~138-140° in the coupled model 2, compared to temperatures of ~140-145°C by Agemar et al. (2012). In the central part (around the location of the well GrSk3/90), the temperatures are similar in both maps (135-140°). By following the regional temperature trend (Fig. 3.9a and 3.9d), temperatures gradually decrease towards the S and the E parts in the two cases. In the SE and E model area, however, temperatures of the coupled model 2 are generally ~ 10-15°C colder than the values estimated by Agemar et al. (2012). The cooler temperatures in the SE/E model domain are induced by the location below the major salt ridges. Temperatures are additionally decreased by a thermal feedback from net cooling in the shallow Mesozoic aquifer due to unhampered cold water inflow through the "Rupelian windows" (areas where the clay has been eroded or not deposited). This net cooling may overestimate the impact of cold water advection due to the chosen upper boundary conditions (s. next paragraph).

Model limitations

Despite of the generally nice fit of the fluid and heat transport simulation with well measurements and the temperature estimations by Agemar et al. (2012) some deviations occur between modeled and predicted temperatures.

These deviations could be related to several reasons such as (1) the choice of physical properties assigned for the geological units (2) the structural limitations of the model and (3) the choice of boundary conditions.

(1) Since the hydraulic properties, especially the permeability, are a crucial factor in influencing the fluid and thermal system, the choice of values is important. The hydraulic properties used for the simulations are based on spatially available data (Čermák et al. 1982) which have been averaged to basin-scale (i.e. km) (Magri, 2005; Magri et al. 2008). Using the same properties, a variety of modeling studies established in the E part of the NGB (Cacace et al. 2010; Kaiser et al. 2011; Kaiser et al. 2013a; Noack et al. 2013; Pommer, 2012; Przybycin, 2011) confirm that these values represent effective properties when investigating the controlling physical

processes at basin-scale (i.e. process-oriented modeling) and furthermore benefit from being comparable to each other. Moreover, they proved that these values, comprising thermal and hydraulic properties, match observed temperatures from wells (Noack et al. 2012; Noack et al. 2013). However, the assumption of a uniform distribution of physical properties does not reflect the heterogeneity of the respective layers (Noack et al. 2012). Therefore, a certain degree of uncertainty remains due to the spatial variability of hydraulic properties (Magri, 2005; Magri et al. 2008) and could easily vary an order of magnitude. For this reason, additional simulations are conducted for both the supra- and the subsalt sequence to assess the sensitivity of the model with respect to the physical parameters.

Since in the shallow model domain the Rupelian clay plays an important role in affecting the fluid flow, the permeability of the Rupelian is decreased to k=1e-18 m², representing an appropriate permeability value for plastic clay in an additional simulation. The simulation results generally show higher temperatures, especially in areas where the Rupelian clay is present with highest thicknesses (in the W). The temperature increase is strongest in the shallow Cenozoic and Mesozoic layers (mean range: 0-30°C). In the deeper subsalt sediments the thermal pattern converges, but still slightly higher temperatures (~ 0-15°C) are present, confirming the thermal feedback of the suprasalt on the subsalt model domain. The comparison with the measured temperatures show a better fit than for the coupled model 2, assuming a higher permeability for the Rupelian. A generally good fit is observed for the wells Grüneberg 2/74 (Table 3.4) and GrSk3/90 (Tables 3.5), in the other wells the temperatures are similar or slightly increased compared to the coupled model 2 (Tables 3.4 and 3.5).

Sensitivity analyses for the permeability values in the Cenozoic and Mesozoic layers have been also run by Noack et al. 2013 by 3D coupled fluid and heat transport simulations for the Brandenburg area. Major outcomes from this study were that decreased permeablities for the Pre-Rupelian clay formations lead to rising temperatures values close to the results from conductive modeling and that advective cooling is strongly reduced if a decreased permeability by one order of magnitude is considered for the Quaternary and Tertiary layers.

Overall, the dependence of the permeability on the modelling results and its uncertainty calls for a sensitivity studies for this parameter and is ongoing work.

For the subsalt sequence, we tested other sets of thermal and hydraulic properties for the conductive and coupled models. Focusing on the deviations between modeled and predicted temperatures observed in the subsalt sequence (cf. Fig. 3.6a), an end-member set, listed in Table 3.1 (values in brackets) has been chosen. The reason for this choice is that the properties are

better resolved for the subsalt layers including the Rotliegend (reservoir) aquifer compared to the original set of properties (Table 3.1, values outside brackets). The end-member set contains hydraulic and thermal properties of the Rotliegend aquifer reservoir rocks measured under in situ conditions (Blöcher et al. 2010b). Furthermore, higher values of radiogenic heat production rates for the Cenozoic to Upper Permian Zechstein and a higher thermal conductivity for the Permian Zechstein salt are used (Norden and Förster, 2006; Norden et al. 2008). The temperature trends of these simulations are similar to the model results with the original set of properties (Table 3.1). Temperature differences (in the range: 0-5°C) occur only within the Zechstein salt and its proximity. The temperatures of the model with the end-member property set are higher on top and lower at the bottom of the salt, by comparison. The maximum differences (up to 5°C) are observed in well locations where the salt thickness is largest (Figs. 3.6 c,d,e) whereas in areas with lower salt thickness the differences are very small (0-1°C) (Figs. 3.6 a,b,f,g). The enhanced impact of the salt is caused by its higher thermal conductivity compared to the original set of properties (Table 3.1). From the results of this sensitivity study, we can conclude that the deviations between modeled and predicted temperatures are not primarily linked to the property assignment.

(2) Those components of the misfit that could be related to structural limitations of the model and/or, as already addressed in the previous section, to lithological heterogeneities not considered in the property assignment of the individual geological layers (Fig. 3.6a) are more difficult to assess. Quantifying effects of this type would require a more detailed consideration of structural input data and physical properties.

(3) The misfit in shallower depth (Fig. 3.6b) could be related to the chosen upper boundary conditions triggering a constant inflow of cold water during the simulation. It remains to investigate to which degree this thermal condition influences the overall temperature distribution and thermal evolution within the coupled simulations. This should consider also realistic information on recharge conditions and the coupling with surface water transport.
A further influencing factor which might enlarge the offset of the observed temperatures and especially the conductive thermal model is the spatially varying heat flux used as the lower boundary condition. The basal heat flux is extracted from a conductive thermal model of Brandenburg which is extended down to the Lithosphere-Asthenosphere Boundary (LAB) and takes into account a differentiated crust (Noack et al. 2012). This model generally fits well to observed temperature data from wells. Yet a small degree of uncertainty may persist due to a

partly overestimation of the temperatures. However, the results should be considered as a good approximation given the fact that the model is consistent with temperature, deep seismic and gravity observations. Therefore, it represents a profound base for defining the lower thermal boundary conditions of the smaller-scale Groß Schönebeck model.
Altogether, the relatively small size of the model combined with the laterally closed boundaries for fluid and heat transport may in addition favor a stronger impact of the adopted boundary conditions compared to larger scaled models. Future studies should consider the assignment of lateral boundary conditions extracted from larger scaled fluid and heat transport models.

Fault model

The results of the model in which subsalt major faults are included reveal a local and strong influence of the permeable NE-SW trending fault. The temperature distribution and the velocity vectors indicate convective flow in the fault (~ 0.001 m/d). Lateral fluid advection from surrounding sediments into the fault is induced by the high fault permeability. In the fault, the convective heat transport leads to an equilibration of the temperatures. This results in the observed higher temperatures at the top (-4000 m depth) and lower temperatures at the base (-4400 m depth) compared to the no fault model. Above and below the fault, heat is transferred by conduction due to the impermeability of the underlying basement and the overlying Zechstein salt. Additionally, the salt prevents the fluid to move upwards which causes lateral flow at the upper tip of the fault and downward flow along the fault`s flanks.

Convective flow in permeable faults has also been proposed earlier. Yang (2006) simulated fluid flow and heat transport based on a highly idealized 3D model of the McArthur Basin (Northern Australia) including two subvertical permeable faults. The results demonstrated that significant fluid circulation takes place mainly within the more permeable faults rather than in the host rocks and that both, upwelling and downwelling flow develops within the two faults at different longitudinal distances giving rise to temperature variation along the fault strike direction. Other coupled simulations of fluid flow, heat transfer and reactive mass transport with an idealized 3D section of a vertical fault system showed that finger-like convection can arise in the fault zone (Alt-Epping and Zhao, 2010). Similar to our findings, the results indicated vigorous fluid flow throughout the fault plane that promotes thermal homogenization there.

Additional simulations were carried out to consider the effects of lower permeability values of the fault on the surrounding groundwater and thermal field (not shown). Convective flow has

been observed in the conductive fault even for a lower permeability value in the fault. In general, few quantitative data are available to provide geologically plausible permeability values for faults and fault-like features incorporated in numerical simulations (Evans et al. 1997). Because technology does not allow the acquisition of detailed property distributions from within active faults (Fairley, 2009), most information on fault property distributions in the published literature are derived from studies of exhumed paleofaults (e.g. Antonellini and Aydin, 1994; Caine et al. 1996; Rawling et al. 2001) or borehole testing in active faults (e.g. Barton et al. 1995). Laboratory-determined permeabilities for natural fault core materials show a range of variation of approximately 10 orders of magnitude (1e-12 to 1e-22 ² from Smith et al. 1990) (Caine et al. 1996). Evans et al. 1997 inferred that fault core materials may be characterized by the lower end of the permeability range (about 1e-17 – 1e-18 m²), whereas more heterogeneous damage zone materials may be characterized by the wider range of higher permeabilities (1e-16-1e-11 m²). Most of numerical studies of different geological settings or based on synthetic models use values in the range of k=1e-11 to 1e-14 m² for conductive faults (e.g. Alt-Epping and Zhao, 2010; Bächler et al. 2003; Bense et al. 2008; Cacace et al. 2013; Clauser and Villinger, 1990; Fairley, 2009; Geiger et al. 2004; Lampe and Person, 2002; López and Smith, 1995; Magri et al. 2010; Simms and Garven, 2004; Yang, 2006), whereby the mean value is around k=1e-13 m² and a sufficient permeability contrast between the fault- and the host rock domain is even assured. For this study, mean permeabilities around k=1e-13 m² have been initially used for the conductive fault, due to a lack of information on fault composition and property data. However, no effect was observed on the hydrothermal field, which is ascribed to the (too) low permeability contrast between fault and surrounding sediments (k=1e-14 m², Table 3.1). To ensure a sufficiently high permeability contrast between fault and surrounding sediments, a higher permeability value was set for the conduit (k=1e-9 m², Table 3.2), characterizing the higher end of the permeability range. Furthermore, sensitivity tests have been conducted with lower fault permeabilities. The assumption of a fault permeability in between moderate (k=1e-13 m²) and high permeability (k=1e-09 m²) of k=1e-11 m² shows a more pronounced convective thermal pattern in the fault within a slightly broader temperature range (118°-154°C) with respect to the more permeable fault (131-149°C). As a result of the lower permeability, fluid velocities decrease up to two orders of magnitudes compared to the highly permeable fault of model 3. Despite of these differences, the first order mechanisms that control the fluid and heat transport in the fault remain the same as well as the range of influence on the thermal field.

Although our results indicate a significant impact of the permeable fault on the thermal field, the fault model temperature curves are similar to the no fault model 2 in all well locations and both reproduce the observation data similarly well. This is related to the fact that none of the wells is located adjacent to the NE-SW oriented permeable fault. To quantitatively assess the thermal impact of the permeable fault we plotted the calculated temperatures for the no fault and fault model for two virtual wells (Figs. 3.11a and 3.11b) along the fault (locations in Fig. 3.6).

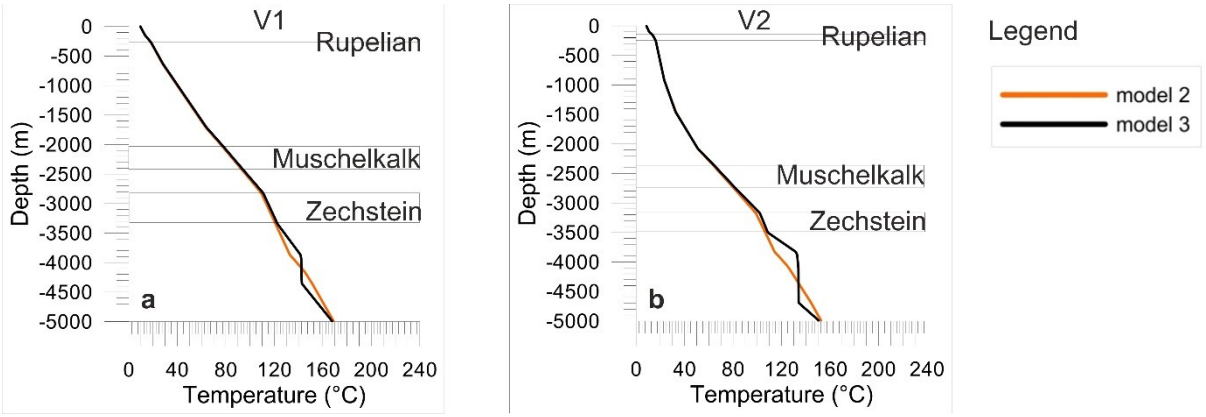

Figure 3.11 Calculated temperatures-depth gradients for two virtual wells in the (a) SW and (b) NE parts of the NE-SW oriented permeable fault. Their locations are displayed in Fig. 3.6 in V1 and V2, respectively. The modeled temperatures for the no fault model 2 are represented by solid orange lines and for the fault model 3 by black solid lines. The depth position of the Rupelian, the Muschelkalk and the Zechstein layers are outlined by grey lines in the background in both figures. Below the Zechstein layer significant temperature differences demonstrate the local impact of the permeable fault on the thermal field.

The plots reveal temperature difference of up to 10°C below the Zechstein layer and confirm a significant impact of the permeable fault on the thermal field along the fault. By contrast, the temperature field is not influenced by the NW-SE trending fault barriers. No significant quantities of fluids can be transmitted due to the impermeable conditions and thus conduction is the predominant heat transport mechanism like in the surrounding sedimentary Rotliegend. Accordingly, no thermal signal is imprinted by the low permeable faults because the thermal properties of the barriers do not differ from sedimentary matrix.

Nevertheless, the fault barriers induce minor deviation of the matrix flow, which is not effective enough to cause temperature variations in the surroundings of the faults. Increasing the spatial extent of the barriers may enhance their impact on fluid circulation and thermal field. However, the fact that the barriers influence the pressure field is obviously independent from their spatial extent. This finding is in agreement with Haneberg (1995) who stated that the effectiveness of

a low-transmissivity fault as a pressure seal is independent of the fault thickness in absence of fault zone discharge.

Conclusions

Our results suggest that different heat transport processes closely linked to the distribution of aquifers and aquicludes mainly control the deep thermal field in the study area. The better fit of the coupled fluid and heat transport model with observed temperatures demonstrates the importance of 3D geologically constrained simulations for assessing the temperature distribution in the subsurface.

Beyond, our results indicate that the consideration of faults, which are more permeable than the host aquifer, is necessary for geothermal exploration because they can exert a strong control on the thermal field and on fluid circulation on a local scale.

The final temperature distribution is the superposed result of all these processes. Conductive, advective and convective heat transport control the temperature field in the suprasalt aquifers providing a thermal feedback superposed on the conductive regime in the subsalt aquifer. The matrix thermal field influences the temperature distribution in the fault, further modified by convective circulation within the latter. The fault itself generates in turn a thermal feedback for the bounding impermeable layers by transferring its locally modified heat to its conductive neighbors.

Assessing the complexity of the different interacting processes represents an important step to understand the specific controlling factors for a complex hydrogeological setting with natural fault zones for an area used for geothermal exploitation.

Acknowledgements

This work is part of the project GeoEn and has been funded by the German Federal Ministry of Education and Research in the programme “Spitzenforschung in den neuen Ländern” (BMBF Grant 03G0671A/B/C).

We thank Vera Noack for her support and for providing the lower thermal boundary condition from the lithosphere-scaled conductive thermal model of Brandenburg (Noack et al. 2012). Björn Kaiser is thanked for helpful computational support and discussion. We gratefully acknowledge the constructive comments and suggestions from two anonymous reviewers and the editorial team. All numerical results are illustrated by ParaView, an open-source, multi-platform and visualization application.

4 Influence of major fault zones on the 3D coupled fluid and heat transport for the area of Brandenburg (NE German Basin)

Abstract

To quantify the influence of major fault zones on the groundwater circulation system and on the thermal field, 3D finite element simulations are carried out. Two fault zones – the Gardelegen and Lausitz Escarpments – have been integrated into an existing 3D structural of the area of Brandenburg in northeast Germany. Different geological scenarios in terms of modeled fault permeability have been considered of which two end member models are discussed in detail. In addition, results from these end member simulations are compared to a reference case in which no faults are considered.

The study provides interesting results with respect to fault-rock matrix interactions and how it affects the regional groundwater circulation system and thermal field.

Impermeable fault zones seem to induce no effects on the resulting temperature distribution, that is, the thermal field is similar to the no fault model. In addition, tight faults have only a local impact on the fluid flow system within a domain of limited spatial extent centred on the fault zone. Fluid flow from the surrounding aquifers is deviated in close proximity of the fault zones acting as hydraulic barriers that prevent lateral fluid inflow into the fault zones.

Permeable fault zones induce a pronounced thermal signature with alternating up- and downward flow along the same structures. Fluid flow along the plane of the faults is principally driven by existing hydraulic head gradients, but may be further enhanced by buoyancy forces. Within recharge domains, fluid advection induces a strong cooling in the fault zones. Discharge domains at shallow depth levels ($\sim<$ -450 m) are instead characterized by the presence of rising warm fluids which results in a locally increase of modelled temperatures which are up to 15°C higher than in the no fault case.

This study is the first attempt to investigate the impact of major fault zones on a 3D basin-scale for the coupled fluid and heat transport in the Brandenburg region. The approach enables a quantification of mechanisms controlling fluid behavior and temperature distribution both within host rocks and fault zones as well as how they dynamically interact. Therefore, the results from the modelling provide useful indications for geothermal energy exploration.

Accepted:

Cherubini Y, Cacace M, Scheck-Wenderoth M, Noack V (2013) Influence of major fault zones on the 3-D coupled fluid and heat transport for the Brandenburg region (NE German Basin). Geothermal Energy Science

[Author`s note: The manuscript underwent modifications during the review process after this document was compiled. Please check the journal for the final version.]

4.1 Introduction

Faults can significantly influence physical processes that control heat transfer and fluid motion in the subsurface. Faults provide permeable pathways for fluids at a variety of scales, from great depth in the crust to flow through fractured groundwater, geothermal and hydrocarbon reservoirs (Barton et al. 1995). Faults are also important because they may offset porous aquifer rocks against shales, rendering permeable rocks a dead-end in terms of fluid flow (Bjørlykke, 2010). To understand the role of faults and their impact on the fluid system and thermal field is also extremely important for geothermal applications. Existing fault zones and fractured domains modify the overall reservoir permeability structure and therefore change the flow dynamics of the reservoir. Apart for an accurate description of the parameter space, to correctly simulate operating scenarios under different working conditions requires a detailed representation of the geometry of the target formations comprising local inhomogeneities characterizing the natural system. Numerical simulations provide a useful tool for analyzing heat and fluid transport processes in complex sedimentary basin systems integrating heterogeneous fault zones.

The focus of this study is to investigate the impact of major fault zones on the fluid and heat transport by 3D numerical simulations. Our study is based on a recently published structural model of the Brandenburg area in the south-eastern part of the Northeast German Basin (NEGB) (Noack et al. 2010). Figure 4.1a and Figure 4.1b outline the location of the study area and its present-day topographic elevation. The dominantly clastic sedimentary succession of the NEGB resolved in the model ranges from the Permian to Cenozoic and reaches up to 8000 m thickness in the central part of the basin (Fig. 4.2a). In response to variations in lithologies, four aquitards of regional extent subdivide the sedimentary succession into different aquifer systems (Fig. 4.2b). These aquitard layers are from top to bottom, the Tertiary Rupelian clays (Fig. 4.3a), the Middle Triassic Muschelkalk limestones (Fig. 4.3b), the Upper Permian Zechstein salt (Fig. 4.3c) and the Permian basement forming the lowermost impermeable layer in the model (Fig. 4.3d). Model detailed information about the hydrogeological configuration of sedimentary layers of interest is given in chapter 4.2.1.

Along the southern margin the basin is dissected by two major fault zones, the Gardelegen and Lausitz Escarpments (Fig. 4.1b), which vertically offset the Pre-Permian basement by several km. As a result, the basement is uplifted by about 5 km coming close to the surface south of the

Gardelegen fault, where it lies next to the Permian-Cenozoic basin fill (Scheck-Wenderoth et al. 2008) (see also Fig. 4.3d).

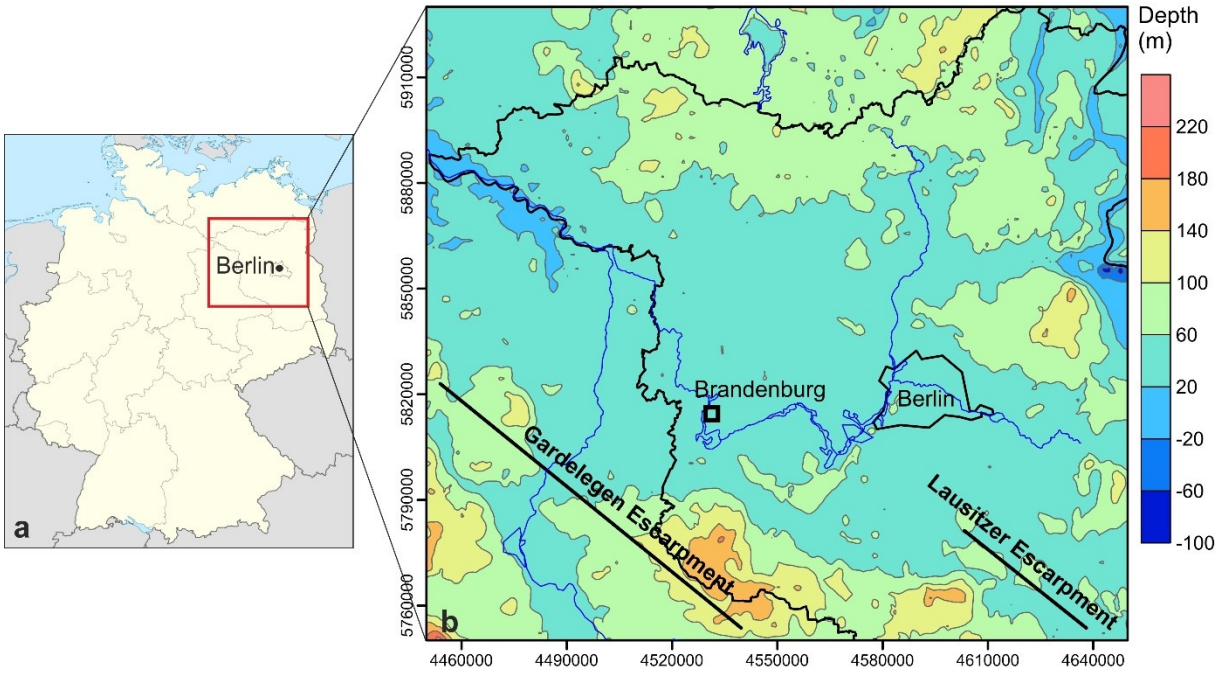

Figure 4.1 (a) Map of Germany showing the outlines of the study area located in the federal state of Brandenburg. The study area (red rectangle) covers a surface of 180 km in N-S and of 200 km in E-W direction.
(b) Topography map (= top of Quaternary) of the model area in UTM zone 33N (ETOPO1, after Amante and Eakins, 2009) with the borderline of Brandenburg (black solid line), main rivers (blue lines) and the location of the Gardelegen and Lausitzer Escarpments being part of the larger Elbe Fault System. The approximated traces of these two major fault zones are given by the straight black solid lines.

The conductive thermal field of the area of Brandenburg has been first calculated by Noack et al. (2010, 2012). Model results were compared with available temperature data and showed a good consistence indicating a predominantly conductive heat transport in the area (Noack et al. 2010). Local deviations between observations and model results were interpreted to be the result of additional fluid related processes. Indeed, more recent 3D coupled fluid and heat transport simulations revealed that the shallow thermal field down to the impervious Muschelkalk is influenced by forced convective processes due to hydraulic gradients (Noack et al. 2013).
These previous studies provided deeper insights in the present-day thermal structure of the area of Brandenburg. However, the impact that major existing fault zones may additionally have on the groundwater system and resulting thermal field has not been investigated so far. Previous 2D numerical studies applied to different geological settings showed that faults may significantly influence the hydrothermal field (e.g. Bense et al. 2008; Garven et al. 2001; Lampe

and Person, 2002; Magri et al. 2010; Simms and Garven, 2004; Yang et al. 2004 a,b). These investigations demonstrated that along-fault convection may be an important heat transport mechanism in permeable faults and may give rise to significant variations in the thermal field. Results from 3D studies seem to confirm these conclusions (Alt-Epping and Zhao, 2010; Bächler et al. 2003; Baietto et al. 2008; Cacace et al. 2013; Cherubini et al. 2013; López and Smith, 1995, 1996; Yang, 2006). However, differences between 2D and 3D studies have been found, due to the fact that the longitudinal fluid flow and heat transport along the strike of the faults are ignored in 2D studies (Yang, 2006).

With the study area, previous attempts to investigate the influence of the Gardelegen fault zone relied on 2D coupled fluid and heat transport simulations. The study revealed a hydraulic interaction between shallow and deep aquifers in which upward convective and downward advective flow through the permeable fault coexist (Pommer, 2012). The present study aims to upgrade the results obtained so far by assessing the influence of major fault zones within a 3D basin-scale model. In the following, the results of the first 3D hydrogeological model of the Brandenburg area that integrates two major fault zones dissecting the southern margin of the NEGB and that couples transient fluid and heat transport in finite element simulations are presented and discussed.

Due to variations in the regional stress field, different geological scenarios with an idealized fault zone representation in terms of their hydraulic behavior have been tested of which we present three end-member models: (1) no faults (model 1), (2) tight fault zones (model 2), (3) highly permeable fault zones (model 3). Model 1 is the reference case. It describes the natural state of the system with respect to the regional groundwater and thermal field. Thereby, the regional thermal field is investigated by considering the interaction of different fluid and heat transport processes with respect to the hydrogeological setting of the study area. In model 2, a very low permeability is assigned for the faults zones, making them effectively impermeable to fluid flow. By contrast, in model 3, fault zones have a high permeability and are therefore supposed to act as hydraulically conductive structures. By means of these two end-member models, the influence of major fault zones on the coupled fluid and heat transport is quantified and the interaction between fault zones and surrounding sediments is addressed.

To assess the respective impact of the different faults on the thermal field and fluid circulation system, the results of all three models are compared to each other and the outcomes are discussed. Despite of the idealized fault zone representation, the simulation outcomes provide useful hints on hydraulic and thermal fault zone behavior that may be beneficial for geothermal energy exploration.

4.2 Data and method

4.2.1 Hydrogeological model

The 3D structural model covers an area of 200 km in E-W and 180 km in N-S direction reaching down to -8000 m depth with a horizontal resolution of 1000 m x 1000 m, corresponding to 210 x 180 grid points. The model integrates 14 geological layers ranging from the Quaternary at the top to the Pre-Permian basement (Fig. 4.2a). In Table 4.1 all stratigraphic units are listed with predominant lithologies and corresponding physical properties adopted for the numerical simulations.

As summarized in Fig. 4.2b, the sedimentary succession is hydraulically decoupled by four regional aquitards (Tertiary Rupelian, Middle Triassic Muschelkalk, Permian Zechstein, Pre-Permian basement) into four main aquifer systems (Cenozoic aquifer, Mesozoic aquifer, Lower Triassic Buntsandstein, Sedimentary Rotliegend). The corresponding thickness maps for all aquitard layers are given in Figure 4.3.

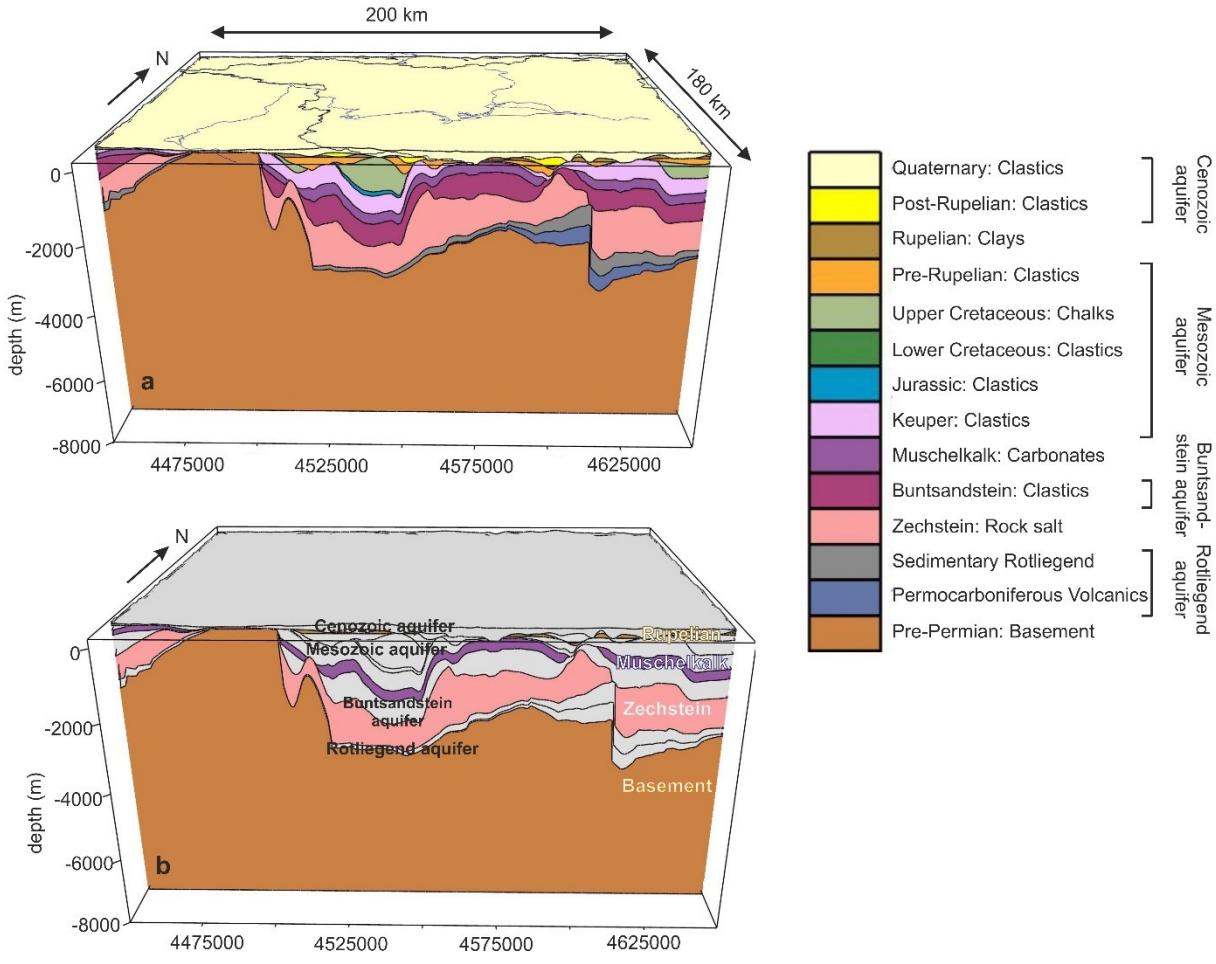

Figure 4.2 (a) 3D geological model of the study area with the stratigraphic layers resolved (vertical exaggeration: 7:1). Note the exposed Pre-Permian basement coming close to the surface at the

southwestern margin and the Permian Zechstein diapirs controlling the structural configuration of the overburden sediments. At the southern basin margin, the Gardelegen and Lausitz Escarpments vertically offset the Pre-Permian basement against the Permian to Cenozoic basin fill by several km.
(b) Distribution of aquitards and aquifers in the 3D geological model (vertical exaggeration: 7:1). Four main layers act as regional barriers to fluid flow comprising the lowermost Pre-Permian basement, the Permian Zechstein, the Middle Triassic Muschelkalk and the Tertiary Rupelian in the shallower part of the model. These aquitards hydraulically decouple the sedimentary succession into four main aquifer systems, from bottom to top: the Rotliegend aquifer, the Lower Triassic Buntsandstein aquifer, the Mesozoic aquifer, the Cenozoic aquifer.

The uppermost Quaternary layer, consisting of unconsolidated, permeable sediments, is followed by the clastic Tertiary which has been resolved into a Post-Rupelian, Rupelian and Pre-Rupelian sub-unit. Of these, the clay-rich Rupelian unit is characterized by a very low permeability (Table 4.1), thus representing the shallowest hydraulic barrier in the sedimentary succession separating the Quaternary and Tertiary complexes from the deeper aquifers (Fig. 4.2b and Fig. 4.3a) (cf. Hebig et al. 2012). Over most parts of the study area, the thickness of the Rupelian clay varies between ~ 0-280 m, only the northwestern part is characterized by a higher thickness up to ~ 520 m (Fig. 4.3a). Areas where the Rupelian clay has not been deposited or eroded, the “Rupelian windows”, hydraulically connect the shallow Cenozoic aquifer complex with the Mesozoic aquifer.
The Cenozoic units are followed downward by the clastic Upper and Lower Cretaceous, Jurassic and Upper Triassic Keuper layers, together forming the Mesozoic aquifer complex. Though limestones are the predominant lithology of the subjacent Middle Triassic Muschelkalk, this layer acts as a second hydraulic barrier in the sedimentary succession, due to alternating anhydrite sequences (Fig. 4.2b and Table 4.1). In the central and northern parts of the study area, the Muschelkalk aquitard reaches down to ~ – 4,000 m depth, whereas it comes close to the surface at the southern margin (Fig. 4.3b). Below, the Lower Triassic Buntsandstein aquifer mainly consists of clastic sediments whereas evaporites, composed mainly of rock salt form the underlying Permian Zechstein layer. The Zechstein salt layer represents the third regional aquitard in the model (Fig. 4.2b). Apart from its impermeable behavior, rock salt has a relatively high thermal conductivity with respect to values for common sedimentary rocks (Table 4.1). Due to its thermal and fluid properties as well as its high level of geological structuration with up to 4500 thick salt diapirs locally piercing the overburden (Fig. 4.3c), this layer exerts a primary role in controlling the deeper groundwater circulation patterns and the thermal field. Below the salt, the clastic Sedimentary Rotliegend represents a prominent target horizon for geothermal exploration (e.g. Zimmermann et al. 2007). It is followed downward by the Permocarboniferous Volcanics. The lowermost, highly-compacted Pre-Permian represents

the basement layer which is assumed to be hydraulically impermeable due to its burial depth acting as the fourth major aquitard in the model (Fig. 4.2b and Table 4.1). The basement thickness gradually increases from north-west to south-east revealing up to ~ 7000-8000 m thickness across the southern margin ("Flechtingen High") (Fig. 4.3d).

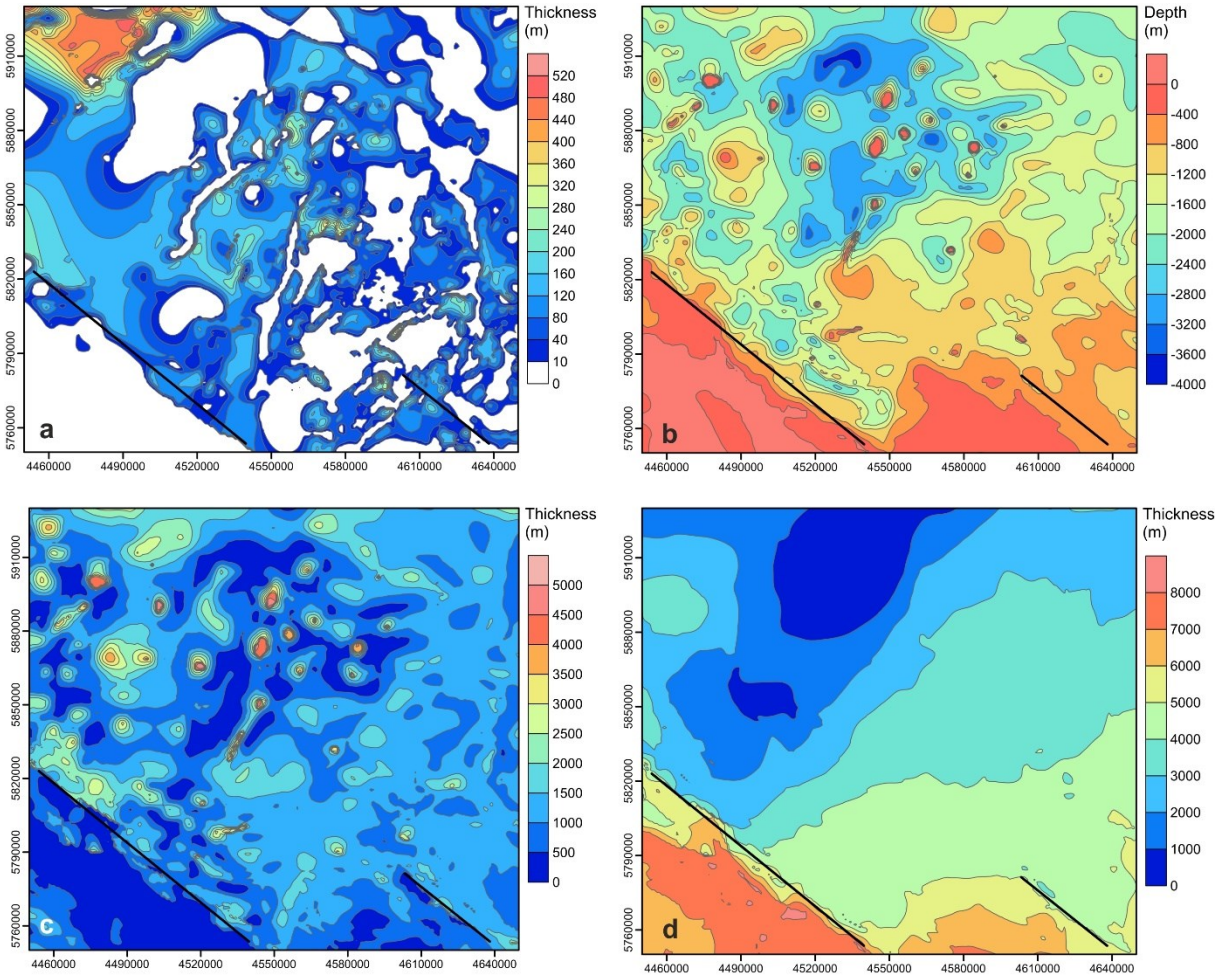

Figure 4.3 (a) Thickness map of the Tertiary Rupelian aquitard revealing large geological windows where this clay-rich layer was not deposited or has been eroded. Location of the Gardelegen and Lausitzer Escarpments are given by the solid black lines (also in the following subfigures).
(b) Depth of the top Middle Triassic Muschelkalk. This layer represents the lower limit of the Mesozoic aquifer. (c) Map showing the highly variable thickness distribution of the Permian Zechstein, characterized by numerous salt pillows that can reach locally thicknesses of up to 4500 m. Around the salt structures (salt rim synclines), reduced thicknesses indicate areas where the overburden Mesozoic and Cenozoic clastics reach their maximum thicknesses.
(d) Thickness map of the impermeable Pre-Permian basement delineating the inverted southern margin where up to ~ 8000 m thick basement comes close to the surface ("Flechtingen High"). The basement thickness thins abruptly near the large Gardelegen and Lausitz Escarpments and gradually decreases north of these faults towards the basin centre.

4.2.2 Fault system

The Gardelegen and Lausitz Escarpments are two major WNW-ESE-striking structures of the larger Elbe fault system (EFS). The EFS encompasses an approximately 800 km long, WNW-ESE-striking zone extending from the southeastern North Sea to southwestern Poland along the present southern margin of the North German and Polish Basins (Scheck et al. 2002). During a Late Cretaceous – early Cenozoic compressional event induced by the Alpine convergence and by the opening of the North Atlantic ocean individual faults of the EFS in north Germany were reactivated to a certain extent as thrust or transpressional faults. Along these faults vertical offsets may reach several kilometers (Scheck et al. 2002). As part of these reactivated structures, the Gardelegen and Lausitz fault zones sub-vertically cut through all sedimentary layers in the structural model and offset the uplifted Pre-Permian basement ("Flechtingen high") across the southern margin by up to 4 km against the Permian to Cenozoic sedimentary succession of the basin north of the faults.

Faults orientation within the present-day stress field is a primary factor controlling their hydraulic behavior with critically stressed faults acting as highly permeable hydraulic conduits and non-critically stressed faults acting as hydraulic barriers (Barton et al. 1995). Therefore, a characterization of hydraulic properties of the faults integrated in the model could be achieved via a previous knowledge of the present-day in situ stress field.

The present-day regional stress field in Germany and surrounding regions as summarized by the most recent release of the World Stress Map shows a broad-scale NW–SE direction of the maximum horizontal stress S_{Hmax} in the western part with a rotation toward NE–SW in the easternmost part of the region (World stress map, 2000 and references therein). Borehole stress data show a different orientation of S_{Hmax} in the suprasalt and subsalt complexes (Roth and Fleckenstein, 2001). Subsalt in situ stress data show a more uniform S_{Hmax} orientation with an approximate N-S direction opening to a more NE-SW direction in the eastern parts of the basin (Marotta et al. 2002; Cacace et al. 2008). In contrast, the stress field in the suprasalt is highly inhomogeneous and shows no dominant direction of the maximum component (Röckel and Lempp, 2003).

From what stated above, no simple relationship between in situ stress field and fault pattern can be obtained. In order to represent the different possible stress-states, various geological scenarios have been tested of which two end-member models are represented: (1) fault zones are considered as barriers to fluid flow because they are non-critically stressed (model 2), and (2) fault zones are supposed to act as hydraulically conductive structures because they are critically stressed (model 3). In addition, a simulation in which no faults are included is also

presented (model 1). Simulation results of the two fault models (model 2 and model 3) are then compared to the no fault case (model 1) to quantify their respective impact on the coupled fluid and heat transport system.

4.2.3 Set-up of the numerical model

3D coupled fluid and heat transport simulations are carried out with the numerical simulator FEFLOW® (Diersch, 2002). This commercial software package is based on the finite element method (FEM) and enables the modeling of coupled fluid flow and transport processes in variably saturated porous media. The governing equations of density coupled thermal convection in saturated porous media are given in the Appendix A.

Within coupled simulations, different fluid and heat transfer processes are taken into account including conduction, convection and advection.

Conductive heat transfer occurs due to an existing temperature gradient through rock molecules transmitting their kinetic energy by collision (Turcotte and Schubert, 2002). The flow of heat is directly proportional to the existing temperature gradient via the medium bulk thermal conductivity (see Eq. 3, Appendix A).

Heat transport by moving fluids includes convection and advection. Convective heat transport is a form of buoyant flow due to differences in fluid temperature (or salinity) whereas advection is triggered by gradients in the hydraulic head inducing flow from higher to lower hydraulic potentials (Bjørlykke, 2010). For the present study, only temperature-induced density changes of the fluid are considered and the influence of salinity of the fluid is neglected within the simulations. Mixed convection is the result of all these different fluid and heat transfer processes acting on the same geological system.

4.2.4 FEM model construction

For building the finite element model, the outlines of the study area (180 km x 200 km) need to be defined as a “superelement” in FEFLOW®. To integrate the faults into the model, two lines representing the approximated traces of the fault zones are implemented into the superelement. Within its frame, a 2D unstructured triangle mesh is then generated, referred to as a “reference slice”. To build up a 3D model, copies of the reference slice (all with the same horizontal mesh resolution) are vertically connected at each nodal point of the mesh. One geological layer is represented by the 3D body between a top and a bottom slice. According to the number of 14 geological layers, 15 slices are required to construct the 3D model. To reproduce the geological

subsurface structure, the geometry of the stratigraphic layers is derived from the structural model (Fig. 4.2a). The extracted z-coordinates (elevations) of each geological top and base surface are assigned to each node of the corresponding top and bottom slice in the numerical model. Therefore, the resulting layer thicknesses a priori determine the vertical resolution of the numerical model. To guarantee numerical stability, the vertical resolution of the model is refined by subdividing all layers into two sub-layers respectively. The model is closed along its base by inserting a planar slice at a constant depth of -8,000 m.

According to the main lithology of each geological unit, hydraulic and thermal rock properties are assigned to each corresponding layer in the numerical model (Table 4.1). Each layer is considered homogenous and isotropic with respect to its physical properties.

Permeable fault zones are implemented as a combination of discrete feature elements and equivalent porous media. Discrete feature elements are finite elements of lower dimensionality, which can be inserted at element edges and faces (Diersch, 2002). We use vertical 2D discrete elements and assume Darcy's law as governing law of fluid motion within the fault elements as well. A highly permeable (permeability equal to that of the discrete fault) domain extending for 500 m on either side of the fault trace has been additional integrated. This domain surrounding the discrete fault elements has been locally refined to ensure a stable calculation of the simulated physical processes. Mesh resolution within this domain is approximately 100 m. Impermeable faults are modeled as equivalent porous media having a lateral extent of 1 km, that is, equal to the permeable fault zones case.

The final 3D finite element model consists of 28 layers (accordingly 29 slices) with approximately 3,5 million elements (= triangulated prisms).

Table 4.2 summarizes the fault properties adopted in the two model realizations.

Table 4.1 Stratigraphic units with predominant lithologies and corresponding physical properties used for the numerical simulations. Hydrogeological barriers separating the stratigraphic succession into different aquifer systems are highlighted (bold).
Porosity and heat capacity after Magri, 2005. Permeability values assigned for the Cenozoic (Post-Rupelian, Rupelian, Pre-Rupelian and Quaternary) after Noack et al. 2013, for the Mesozoic and Palaeozoic after Magri, 2005.
Thermal conductivity and radiogenic heat production used for numerical simulations of the thermal field for the Brandenburg area; thermal conductivities and radiogenic heat production after Bayer et al. 1997, thermal properties for Post-Rupelian, Rupelian and Pre-Rupelian after Noack et al. 2013, Radiogenic heat production of Rupelian after Balling et al. 1981.

Stratigraphic Unit (Predominant lithologies)	Permeability $\kappa[m^2]$	Porosity $\varepsilon[\%]$	Rock heat capacity c_s [MJ/m^{3}K]	Thermal conductivity λ [W/mK]	Radiogenic heat production Q_T [10^{-7} W/m^3]
Quaternary (Sand, silt, clay)	1.00E-13	23	3.15	1.5	7
Post-Rupelian (Sand, silt, clay)	1.00E-14	23	3.15	1.5	7
Rupelian (Clay)	1.00E-16	20	3.3	1	4.5
Pre-Rupelian (Sand, silt, clay)	1.00E-14	10	2.4	1.9	3
Upper Cretaceous (limestone (chalk))	1.00E-13	10	2.4	1.9	3
Lower Cretaceous (Clays with sand and silt)	1.00E-13	13	3.19	2	14
Jurassic (Clays with sand, silt, marl)	1.00E-13	13	3.19	2	14
Keuper (Clays with marl & gypsum)	1.00E-14	6	3.19	2.3	14
Muschelkalk (Limestone)	1.00E-18	0.1	2.4	1.85	3
Buntsandstein (Silts with sand, clay, evaporite)	1.00E-14	4	3.15	2	10
Zechstein (Evaporites)	Impermeable ~0	~0	1.81	3.5	0.9
Sedimentary Rotliegend (Clay-, silt,- and sandstone)	1.00E-14	0.3	2.67	2.16	10
Permo-Carboniferous Volcanics (Rhyolithe and andesite)	1.00E-14	0.3	2.67	2.5	20
Pre-Permian basement (Granites, strongly compacted clastics)	Impermeable ~0	~0	2.46	2.65	15

Table 4.2 Thermal and hydraulic properties used for the fault modeling.
°values after Pommer (2012);
* mean values of the geological layers averaged by their thicknesses;

Properties	Faults permeable	Faults impermeable
Porosity Ɛ[%]	30°	~0
Rock heat capacity c_s [MJ/m^{3}K]	2.49°	2.6*
Thermal conductivity λ [W/mK]	2.63°	2.4*
Permeability κ[m^2]	1E-12°	~0
Radiogenic heat production Q_T [10^{-7} W/m^3]	0.89°	0.9*

4.2.5 Time discretization

Though the present study aims to address the present-day state, coupled simulations for all models are run in transient for 250 000 years. This is done to let the system equilibrate thus obtaining pseudo steady-state conditions. Given the goal of the study, results are shown only for the final simulation state at 250 000 years.

4.2.6 Boundary and initial conditions

A fixed hydraulic head equal to the topographic elevation is assigned at the top of the model. Due to this upper flow boundary condition, groundwater flow is predominantly controlled by gradients in the topography. No-flow boundary conditions are set along the bottom and lateral boundaries of the model.

As upper thermal boundary condition, we assume a fixed constant surface temperature of 8°C, according to the average surface temperature in NE-Germany (Katzung, 1984). At the model base (-8000 m depth), a variable temperature distribution is defined which has been extracted from a lithosphere-scale conductive thermal model of Brandenburg taking into account the thermal effects of the underlying differentiated crust and lithosphere, down to a depth of - 125 km (Noack et al. 2012). Figure 4.4 illustrates the variations imposed to the bottom thermal

boundary. Highest temperatures (~260-285°C) characterize the southern and eastern area. Furthermore, temperatures increase up to ~275°C along the western margin. By contrast, lowest temperatures are present at the southern margin (down to 220°C) and in the northern and northwestern model area. The regional temperature field at this depth is predominantly controlled by the thickness distribution of the underlying upper crust (characterized by higher values of thermal conductivity and radiogenic heat production) and of the low conductive post-salt deposits (Noack et al. 2012).

Initial pressure and temperature conditions are derived from steady-state uncoupled flow and heat transport simulations respectively.

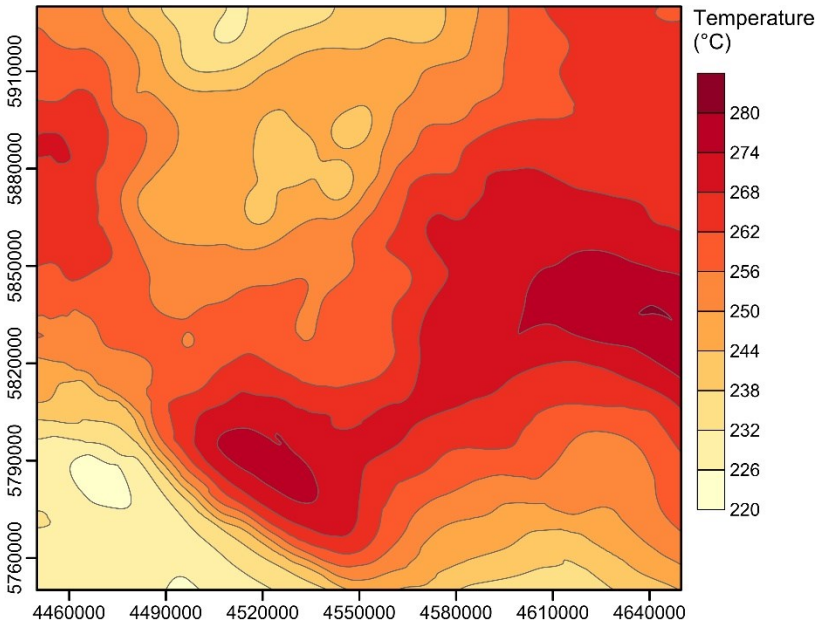

Figure 4.4 Laterally variable temperature distribution at -8,000 m depth used as lower thermal boundary condition for all numerical simulations presented in the manuscript. It has been extracted from a lithosphere-scale conductive thermal model of Brandenburg by Noack et al. (2012).

4.3 Modelling results

4.3.1 Regional thermal field

A preliminary investigation of the regional thermal field at different depth levels enables to carry out a first assessment of the temperature distribution with respect to the regional hydrogeological setting. This evaluation is necessary to more completely quantify the influence of the fault configurations on the fluid and thermal regime.

Figures 4.5a displays the horizontal temperature distribution at -1,000 m depth for model 1 (no faults). The results for model 2 (impermeable fault zones) and model 3 (permeable fault zones)

are shown in Fig. 4.5b and Fig. 4.5c respectively. The depth level of -1,000 m is located below the Tertiary Rupelian aquitard and cuts through the Pre-Rupelian Mesozoic aquifer as well as the Pre-Permian basement along the southern margin of the basin (Fig. 4.2b and 4.3d). The temperature maps at -3,000 m depth of model 1 (Fig. 4.5d), model 2 (Fig. 4.5e) and model 3 (Fig. 4.5f) cut through the Mesozoic sediments, major Permian salt diapirs and the Pre-Permian basement at the southern margin (cf. Figs. 4.3c and 4.3d).

4.3.2 Horizontal temperature distribution: -1,000 m depth

At -1,000 m depth, temperatures range between ~ 30 and 50 °C in wide parts of the study area. Local spots of higher temperatures (up to 80°C) are also visible in the western and central domains (Fig. 4.5a). Across the southern margin of the basin, temperatures are sensitively lower (~ 22-34°C) and are even colder in larger parts of the north and northeastern model area (10-20°C).

The regional temperature pattern can be correlated to the thickness of the overlying Rupelian aquitard (Fig. 4.3a). Locations where the Rupelian clay is missing ("Rupelian windows") correspond to areas of strongly reduced temperatures. The reason of the observed cooling trend should be related to cold water inflow from the top surface (set to 8°C) which penetrates unhampered into deeper parts of the model thus leading to the modeled cooling within the Mesozoic aquifer (cf. Fig. 4.2b). Higher topographic elevations (recharge areas) above these Rupelian windows (cf. Fig. 4.1b) enhance cold water advection and hence the observed cooling. On the contrary, local spots of distinctly higher temperatures in the western and central domains can be correlated to areas with an increased thickness of the Rupelian aquitard which prevents cold water inflow from the surface to reach this depth levels (cf. Fig. 4.3a). As a consequence significantly higher temperatures are generated below the Rupelian. At these locations, temperatures additionally increase in the vicinity of major Zechstein salt diapirs (Fig. 4.3c) due to the thermal blanketing effect by thick and low conductive Mesozoic sediments. Across the southern margin, larger areas of lower temperatures correspond to domains in which the Pre-Permian basement reaches almost the surface ("Flechtingen High") (Fig. 4.3d). The thick impermeable and thermally highly conductive basement leads to a very efficient conductive heat transport towards the surface. Due to the absence of overlying sediments heat cannot be stored by thermal blanketing and gets lost at the surface thus explaining the observed thermal trend along the margin of the basin (cf. Fig. 4.2a).

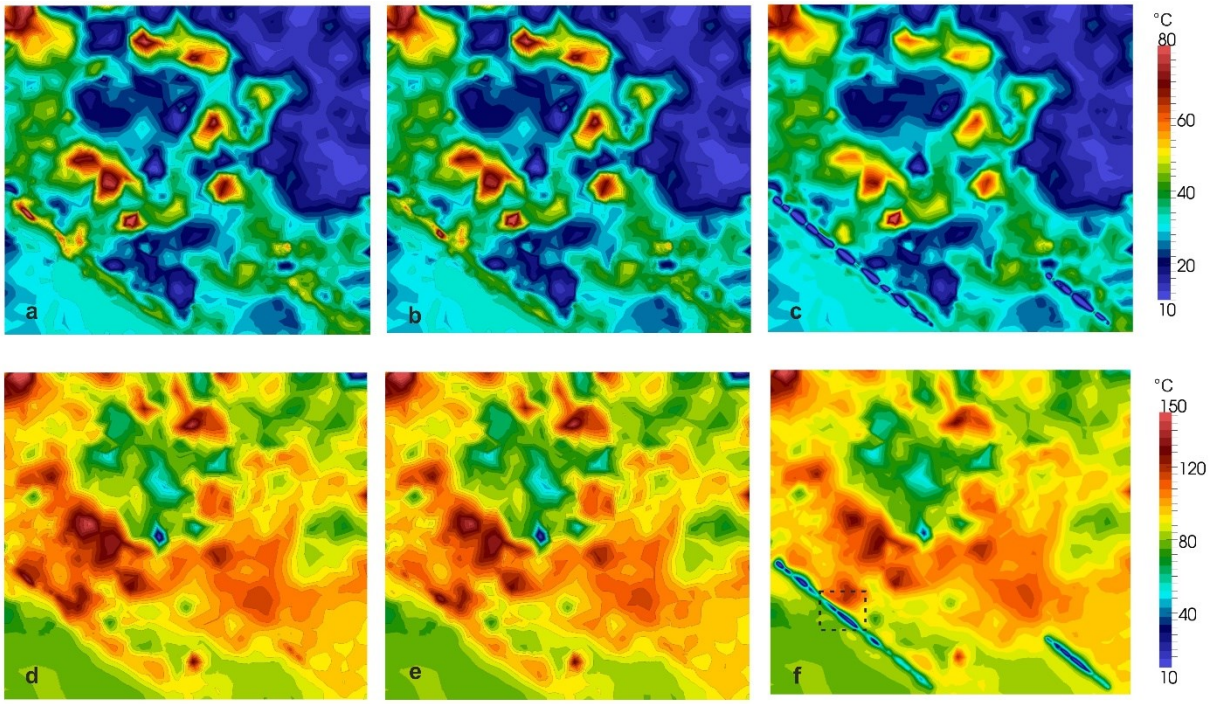

Figure 4.5 (a-c) Temperature distribution along a horizontal slice at -1,000 m depth cutting the (a) no fault model (model 1), (b) impermeable fault model (model 2) and (c) permeable fault model (model 3). (d-f) Temperature distribution along a horizontal slice at -3,000 m depth cutting the (d) no fault model (model 1), (e) impermeable fault model (model 2) and (f) permeable fault model (model 3). In (e) the black rectangle displays the position of the map view in Fig. 4.9b. Note the significant difference in the modeled temperatures in the proximity of the faults for model 3 compared to the very similar model 1 and model 2.

4.3.3 Horizontal temperature distribution: -3,000 m depth

At -3,000 m depth the thermal field shows a wider range of variations with respect to the shallower temperature distribution described above. At this depth level modeled temperatures vary between minima of approximately 10°C and maxima of up to 150°C (Fig. 4.5d). Local spots of reduced temperatures (~44-52°C) occur in the central and northwestern parts. As already observed at -1,000 m depth, the southern margin is characterized by relatively lower temperatures with respect to the central domains (~80°C). Higher temperatures of up to 150 °C, however, occur in the western, northwestern, east and in the central parts. These positive thermal anomalies show both short-wavelength ("spot-like anomalies") and long-wavelength ("elongated anomalies") characteristic geometries.

The occurrence of local negative thermal anomalies in the central and northwestern domains can be structurally linked to the topology of the Rupelian aquitard and of the Middle Triassic Muschelkalk aquitard, the latter limiting the Mesozoic aquifer at its base (Fig. 4.3b). Indeed, cooler temperatures are present in areas where the Mesozoic aquifer reaches deeper than -3,000

m beneath major hydrogeological windows in the Rupelian thickness distribution (cf. Figs. 4.3a and 4.3b). Therefore, cold water from the top surface can flow downward and penetrate to greater depths.

The long term spatial distribution of modeled temperatures in the remaining part of the study area is mainly controlled by the geometry and thickness of the Pre-Permian basement (Fig. 4.3d). Reduced temperatures are present across the southern margin where the basement reaches its highest thickness and shallowest depths. Similar to the thermal pattern at -1,000 m depth, heat loss is caused by the lack of insulating cover sediments. By contrast, domains of increased temperatures in the basin center evolve beneath a thick basement overlain by a thick sequence of Mesozoic sediments that act as a thermal blanket.

Additionally, temperatures rise in the vicinity of major salt diapirs ("spot-like anomalies"). These are locations where low conductive Mesozoic and Cenozoic sediments reach their highest thicknesses and hence where their thermal blanketing effect is most effective.

From the results described above it can be concluded that the temperature distribution is the result of superposed thermal effects generated by the complex interaction between the hydrodynamics induced by the boundary settings and the hydrogeological configuration of the basin comprising different sediment types as (a) the permeable but thermally insulating Mesozoic sediments, (b) the intercalated but partially discontinuous aquitards (Rupelian and Middle Triassic Muschelkalk), (c) the impermeable but thermally conductive Zechstein salt and (d) the Pre-Permian basement.

Modeled temperature distributions for model 2 (impermeable faults) show a striking resemblance with those obtained for the reference model 1 (no faults) both, at -1,000 m and -3,000 m depth (Fig. 4.5b and Fig. 4.5e). The similarity to the no faults scenario indicates that the impermeable fault zones have no remarkable influence on the thermal field.

At -1,000m depth, model 3 (highly permeable faults) shows distinctly cooler temperatures (10-30°C) along both fault zones with an alternating thermal signature (Fig. 4.5c). In the central part of the fault zones, temperatures as low as 10°C are present (compared to around 40°C in previous models), increasing to ~ 20°C at the margins and changing alternately reaching local maxima of ~30°C. The total range of influence of the permeable Lausitz fault zone varies between ~3.5 and 7.4 km and for the Gardelegen fault zone between ~2.4 and 8.8 km.

These variations are due to the different type of geological layers adjacent to the fault zones. The range of influence is decreased in areas where the fault zone is bordered by the Pre-Permian, Zechstein and Muschelkalk aquitards. Due to their hydraulically impermeable setting, heat is transferred only by diffusion within these layers, thus leading to a less effective

propagation of thermal anomalies far from the fault domains. By contrast, the range of influence is increased in those areas where the fault zones are next to aquifers because the heated fluid can spread out into the permeable sediments, reaching to greater distances within the layers.
Differences in the local thermal field can also be observed at -3,000 m depth between model 3 and models 1 and 2 (Fig. 4.5f). Along the fault planes isotherms are arranged in an alternating pattern, displaying values between 10-56°C. Therefore, at these locations the temperatures are about 35-45° lower than those obtained from the previous model realizations. At this depth, the total range of influence varies between ~6 and 10 km for the Lausitz fault zone and between ~6.5 km to 12 km for the Gardelegen fault zone.

4.3.4 Temperature distribution in the fault zones

To understand the pronounced thermal signature within both permeable faults (model 3), a more detailed analysis of the thermal state along the entire fault zones is carried out.
Figure 4.6a displays the temperature distribution along the Gardelegen and Lausitz fault zones. Temperatures range between 8°C and 75°C along both faults. Convex upward shaped isotherms (corresponding to temperatures as high as 35-75°C) alternate with isotherms that are bent convex downward (indicating temperatures as low as 8-30°C). This alternating temperature pattern reflects thermal anomalies already described in the regional thermal field at -1,000 m and -3,000 m depth along the permeable fault zones (Figs. 4.5c and 4.5f).
A combination plot of isotherms and fluid velocity vectors along the Gardelegen fault (similar conclusions are also valid for the Lausitz fault zone) shows that convex downward shaped isotherms (cold domains) correspond to relatively fast downward groundwater flow (~1e-02 – 3e-02 m/d) (Fig. 4.6b). By contrast, convex upward bent isotherms conform to mainly upward groundwater flow of lower fluid velocities (~1e-04 – 1e-01 m/d).

The temperature distribution and corresponding fluid dynamics within both faults can be spatially correlated with the topographic elevation along the fault zones (Fig. 4.6b). At areas of high topographic elevation, the recharge areas, cold water (8°C) is forced to enter from the surface of the model due to the hydraulic boundary conditions imposed. According to Darcy's law (see Eq. 2 in the Appendix) steep hydraulic head gradients result in higher flow velocities of infiltrating water. Due to the higher permeability of the fault zone (Table 4.2), fluid can easily flow downwards being fast enough to result in the observed cooling. Reaching deeper parts of the fault zone, the fluid is heated by thermal equilibration with the surrounding matrix system (its velocity diminishes with depth) and will rise upwards at specific areas following the

distribution of the hydraulic head gradients. These hotter domains within the fault mainly correspond to areas of lower topographic elevation, the discharge areas.

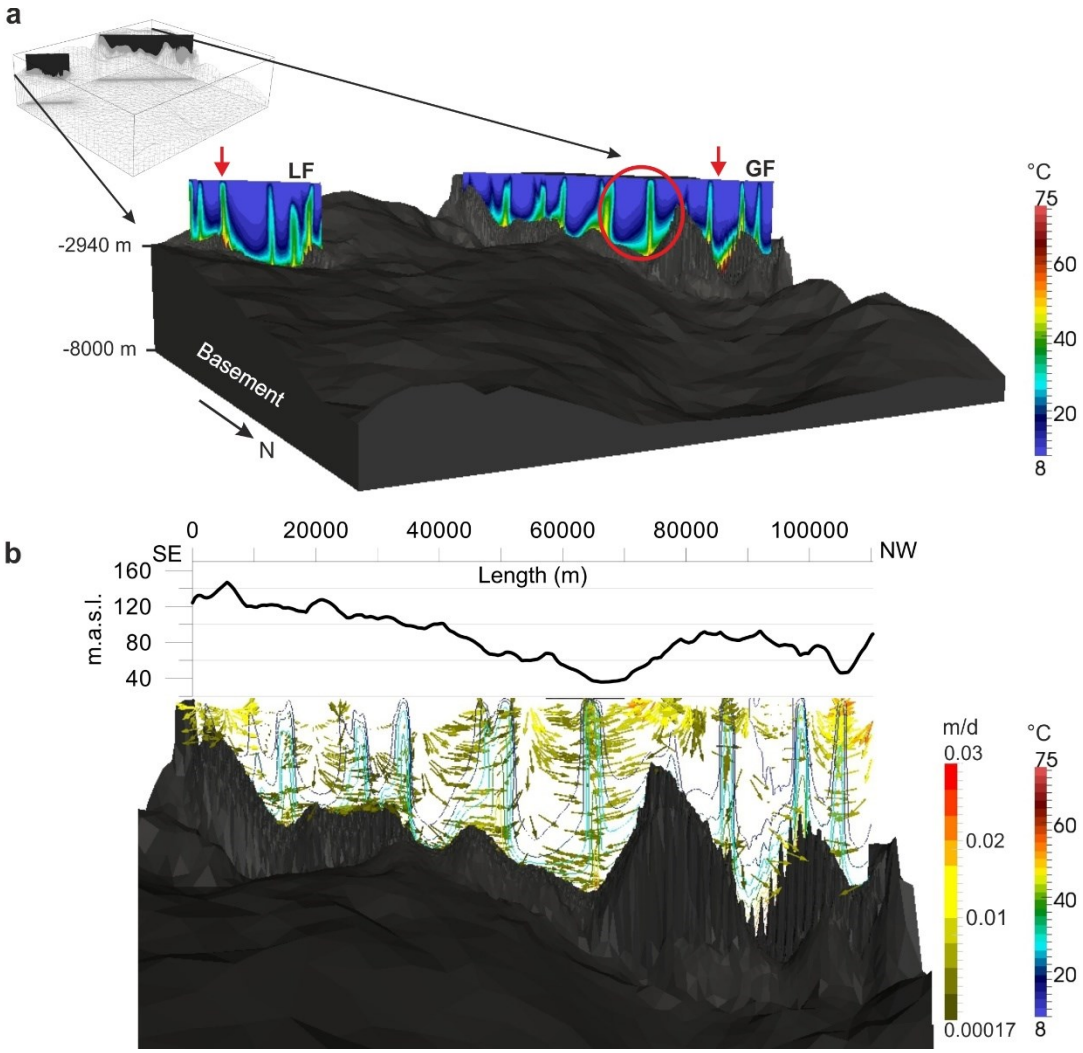

Figure 4.6 (a) Temperature distribution along the fault planes in strike direction of the permeable Gardelegen (GF) and Lausitz faults (LF). Alternating hotter and colder domains characterize the thermal state within both fault zones. The red arrows indicate the location of two vertical cross sections shown in Figs. 4.7 and 4.8. The cross sections cut through the faults zones parallel to the N-S-axis. The red circle shows the location of the zoom of Fig. 4.9 (vertical exaggeration: 7:1).
(b) Combination plot of fluid velocity vectors (length of vectors are not scaled) and isotherms along the entire length of the Gardelegen fault assumed permeable (model 3). On top, the topographic elevation used as a proxy for hydraulic head boundary condition at the surface is delineated along the trace of the fault zone. Down- and upward oriented flow are initiated by hydraulic head gradients but may be enhanced by a convective fluid flow component.

In conclusion, fluid motion within the fault is driven principally by fluid advection due to hydraulic head gradients imposed along the top boundary. Depending on the pressure and temperature conditions at depth, local upward movement of the fluid may be locally enhanced by buoyancy forces. However, thermal buoyant forces exert only a secondary contribution to the fluid movement thus having a little, if any, impact on the resulting thermal field.

4.3.5 Interaction between fault zones and surrounding sediments

To analyze the temperature field and fluid behavior along the fault zones and to understand the interaction between fault zones and surrounding sediments, two representative vertical profiles are chosen. The first profile cuts through a recharge zone at the Gardelegen fault (GE), whereas the second profile dissects a discharge area at the Lausitz fault zone (LE) (Fig. 4.6a). Based on these two profiles, the results are visualized by focusing only on the fault zone areas. For both sections temperature distribution and flow field are illustrated for models 1, model 2 and model 3, respectively (Fig. 4.7a-f and 4.8a-f). These profiles should be considered as representative for the other parts of the fault zones characterized by similar hydraulic conditions.

Recharge area – Gardelegen fault zone

Model 1

A first consideration of the temperature distribution for model 1 reveals relatively flat isotherms in the area of the Pre-Permian basement, displaying somewhat cooler temperatures in the south (Fig. 4.7a). Convex upward shaped isotherms characterize the central part of the profile in the narrow transition zone between the deep and the shallow Rotliegend aquifer within a transition region extending between the Pre-Permian basement and the Permian Zechstein. Within the Permian Zechstein layer, the isotherms distinctively bend upwards. This thermal anomaly indicates locally higher temperatures in the salt decreasing in the surrounding sediments.

Flat isotherms in the area of the Pre-Permian basement reflect conductive heat transfer through this hydraulically impermeable layer. In addition, its higher thermal conductivity leads to an efficient heat transfer towards the surface. In the south, the basement is nearly exposed at the surface and it is not covered by insulating sediments. Due to its special geological setting, reduced temperatures are observed. This cooling trend reflects the thermal signature already observed in the regional thermal field along the southern margin of the study area (Figs. 4.5a and 4.5d).

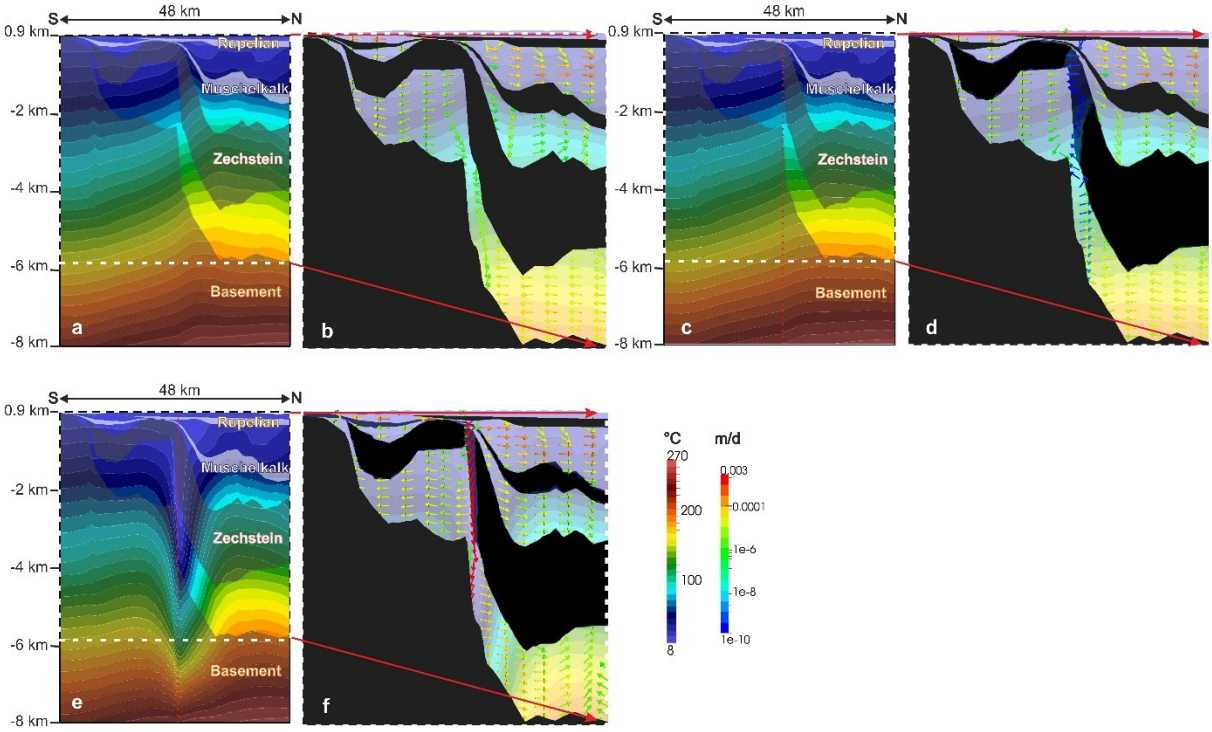

Figure 4.7 N-S cross-section through the southwestern part of the Gardelegen fault (GF) plane (the location of the cross section is outlined in Fig. 4.6a by the red arrow on the right-hand side). In the combination plots of temperature distribution and fluid velocity vectors (subfigures 4.7b, d, f), the lengths of the fluid velocity vectors are non-scaled and the temperature distribution is shown with reduced intensity in the background. (a) Temperature distribution for model 1 in which no faults are integrated. The almost flat character of the isotherms reflects the diffusive nature of conductive heat transfer throughout the impermeable Pre-Permian basement. Isotherm deflection is only present where the conductive Zechstein salt is thick. (b) Fluid velocity vectors and temperature distribution for the no fault model 1 indicating horizontal flow in the upper aquifers. Predominantly upward directed flow only occurs where a hydraulic connection exists between the shallow and the deep Rotliegend aquifer.
(c) Temperature distribution for the model 2 in which the fault zones are integrated as impermeable structures. The position of the fault zone is displayed by the dotted red line. Only a slight temperature increase is observed at the offset between shallow and deep Rotliegend aquifer when compared to the no fault model. (d) Fluid velocity vectors and temperature distribution for the impermeable fault model 2. Very low fluid velocities are evident along the fault and the communication of shallow and deep Rotliegend aquifers is inhibited. Apart from that, within the surrounding aquifer sediments, fluid direction and fluid velocities are similar to the no fault model 1.
(e) Temperature distribution for the permeable fault model 3. A strong cooling is induced by the permeable fault zone cutting through the central part of the profile (indicated by the dotted red line). (f) Fluid velocity vectors and temperature distribution for fault model 3 displaying a fast downward oriented flow inside the permeable fault zone and a lateral outflow into the surrounding aquifer sediments.

The observed thermal anomaly throughout the Permian Zechstein salt is caused by thermal refraction, triggered by the sharp contrast between the thermally highly conductive salt and the low thermal conductivity of the surrounding sediments. Because the salt acts as a heat chimney,

conductively transferring the heat towards the surface, it results in higher temperatures in the salt than within the surrounding less conductive sediments.

So far, the results demonstrate that conductive heat transfer decisively shapes the local thermal field through the thick Pre-Permian basement and the Permian Zechstein, both impermeable to fluid flow and thermally more conductive than the surrounding sediments (Table 4.1).

In the shallow Cenozoic, Mesozoic and Buntsandstein aquifers, fluid velocity vectors indicate a diverging regional flow at the vertical offset in the central part of the profile (marking the position of the Gardelegen fault) (Fig. 4.7b). This flow pattern results from the location of the profile beneath a major recharge area where cold water enters in the model and flows into the shallow aquifer sediments following the regional groundwater flow.

In the Rotliegend aquifer, fluid velocity vectors indicate regional flow from north to south. They also display a hydraulic connection of reduced velocities (~ 1e-06 m/d) within the narrow transition domain between the deep and shallow Rotliegend aquifer. Due to the adjacent impermeable basement, fluid flows upward following the geometry of the basement and flanking Zechstein salt layer. Upward flow of heated fluid leads to the observed upward bent isotherms across this transition domain (Fig. 4.7a). By entering the shallow Rotliegend aquifer, fluid locally mixes with the regional flow.

Model 2

The thermal field for model 2 shows only weak disturbances in the fault zone area with respect to the case previously described (Fig. 4.7c). Compared to the thermal field of the no fault model 1 (Fig. 4.7a), only a slight temperature increase (max. 6°C) can be distinguished in the domain of the hydraulic connection between the shallow and deep Rotliegend aquifer.

Moving to the fluid velocity results (Fig. 4.7d), the results nicely show that fluid cannot enter the fault zone. Instead, fluid flow is redirected along the impermeable structure with very low fluid velocities (~ 1e-10 m/d) and flows laterally into the aquifers with increased velocities (~1e-08 – 1e-06 m/d). Generally, fluid flow direction and fluid velocities are similar to the flow field of the no fault model 1 within the aquifer systems (cf. Fig. 4.7b).

The presence of a tight fault has only a minor influence on the flow dynamics. Indeed, neither the fluid velocity in the surrounding sedimentary layers nor the fluid direction appears to change in the vicinity of the fault zone when compared to the no fault model 1 (Fig. 4.7b).

Very low fluid velocities along the fault-matrix boundary and spatially limited influence of the fault zone result in no remarkable influence on the thermal field. A minor temperature

difference between the two models results from the locally disturbed fluid flow at the fault offset which marks the transition between shallow and deep Rotliegend aquifer.

Model 3

Considering the fault zone as more permeable than the neighboring sedimentary layers significantly changes both the thermal field (Fig. 4.7e) and the fluid circulation pattern (Fig. 4.7f), in comparison to the no fault case (Figs. 4.7a and 4.7b). A negative thermal anomaly characterizes the thermal state in which the isotherms are sharply bent downward indicating a strong cooling in the central domain of the fault plane. This pattern continues to greater depth but weakens towards the Pre-Permian basement. Along both sides of the fault zone, a step-wise increase in modelled temperatures is visible at a distance of approximately 3 km from the fault plane.

The corresponding fluid velocity vectors display a fast downward oriented flow (of up to 0.003 m/d) in the central part of the fault zone (Fig. 4.7f). Along the fault flanks velocity vectors indicate a lateral fluid outflow from the fault zone into the permeable sediments of the different aquifer systems. While this lateral flow direction is maintained throughout the aquifer systems, the fluid velocity gradually decreases with increasing distance from the fault zone.

The observed fast downward oriented flow in the fault zone explains the strong cooling observed at the same location. The relatively strong temperature drop is induced by the surface water inflow (8°C) from the upper tip of the fault zone located beneath a major recharge area (cf. Fig. 4.6b). The higher permeability of the fault zone translates in high fluid velocities and downward oriented flow through the fault zone. Reaching the lower tip of the fault, fluid cannot penetrate the impermeable Pre-Permian basement. Within this layer, heat is transferred only by conduction. This transition between heat transfer processes is displayed by the weakening of downward bent isotherms throughout the Pre-Permian basement layer.

As a possible further consequence of the fast downward flow in the fault zone, fluid penetration occurs from the fault zone into the surrounding aquifers. The gradual decrease of the fluid velocities with increasing distance from the fault mainly results from the differences in the permeability of the fault and of the surrounding aquifers, the permeability decreases from the fault zone to the sedimentary layers (Tables 4.1 and 4.2). Accordingly, velocity of modelled lateral flow may vary within each aquifer.

The induced lateral outflow from the fault zones into the surrounding aquifers is also reflected by an increased range of influence of the permeable fault zones in the regional temperature distribution at 1,000 m and 3,000 m depth as described previously (cf. Figs. 4.5c and 4.5f).

The shallow and deep Rotliegend aquifers are still hydraulically connected though offset by the presence of the permeable fault which considerably changes fluid pathways and fluid velocities. Most significantly, direction of fluid flow is reversed along the offset, changing from slowly upward flow in the no fault case (Fig. 4.7b) to fast downward oriented flow in the permeable fault zone (Fig. 4.7f). As a further consequence of the downward flow in the fault, fluid flow direction is inverted within the deep Rotliegend aquifer sediments.

In summary, when located beneath a major recharge area, the highly permeable fault is characterized by downward oriented fluid flow, which induces net cooling in the permeable fault zone. In the adjacent aquifers, fluid flow is directed away from the fault zone and varies in magnitudes in relation to the specific permeability values of the individual sedimentary layers.

Discharge area – Lausitz fault zone

Model 1

In the no fault model 1, flat and almost horizontal parallel isotherms characterize the area of the thick Pre-Permian basement whereas slightly disturbed isotherms can be observed within the Zechstein salt (Fig. 4.8a). In the Mesozoic aquifer, the isotherms indicate slightly decreased temperatures below the Rupelian windows in the northern part of the profile.

The geometric distribution of the isotherms within the basement points to conductive heat transfer through this impermeable layer. Thermal refraction is reflected by the pattern of modeled isotherms throughout the Zechstein salt and surrounding sediments. Cooler temperatures in the Cenozoic and Mesozoic aquifers are induced by the inflow of cold surface water through the Rupelian windows.

Beneath the latter hydrogeological window, fluid velocity vectors indicate vigorous fluid flow (Fig. 4.8b). In the deeper Buntsandstein and Rotliegend aquifers, a predominant lateral fluid flow direction from north to south is displayed by the fluid velocity vectors. This regional trend is only disturbed at the narrow transition between deep and shallow Buntsandstein and Rotliegend aquifers (marking the location of the Lausitz fault zone) where the basement and Zechstein salt are closest.

The regional flow direction from north to south is induced by the location of the profile at a discharge area, adjacent to a major recharge zone in the north (cf. Fig. 4.1b). Due the steep hydraulic head gradient (connecting the discharge with the recharge area), enhanced fluid inflow occurs from the north and results in the regional north-south directed flow pattern. At

the narrow hydraulic connection between deep and shallow Buntsandstein and Rotliegend aquifers, fluid flows upwards by following the relief of the impermeable basement and Zechstein salt layers. By reaching the shallow parts of the Buntsandstein and Rotliegend aquifers, fluid mixes with the shallow aquifer fluids.

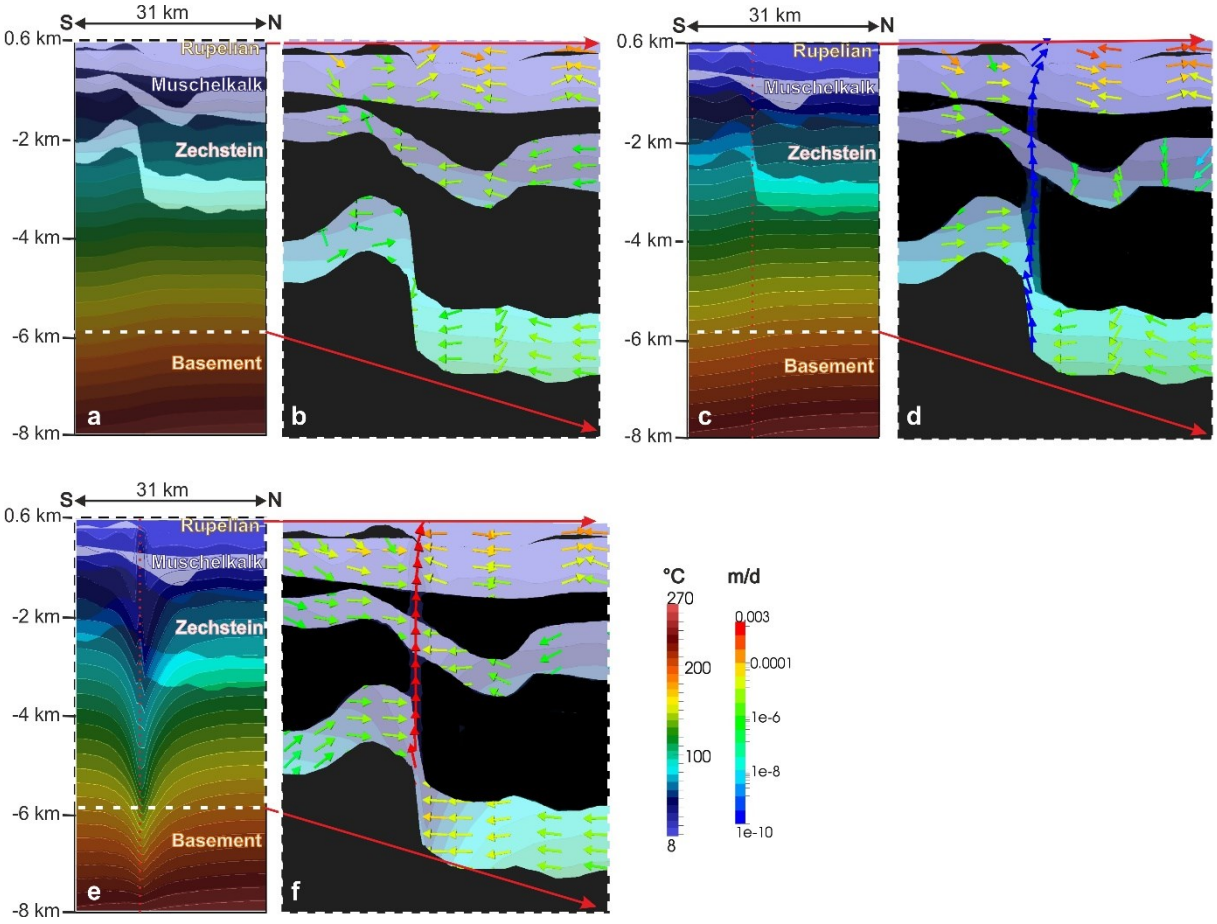

Figure 4.8 N-S cross-section through the southeastern part of the Lausitz fault (LF) plane (the location of the cross section is outlined in Fig. 4.6a by the red arrow on the left-hand side).
In the combination plots of temperature distribution and fluid velocity vectors (subfigures 4.8b, d, f), the lengths of the fluid velocity vectors are non-scaled and the temperature distribution is shown with reduced intensity in the background.
(a) Temperature distribution for model 1 in which no faults are implemented. The isotherms indicate a net cooling effect in the shallow Cenozoic and Mesozoic aquifers, induced by unhampered cold water inflow through the Rupelian windows in the northern part of the profile.
(b) Fluid velocity vectors and temperature distribution for the no fault model 1. The regional flow direction is from north to south. At the offset, where the basement, Zechstein and Buntsandstein layers are in close contact, fluid mixing occurs within the aquifers.
(c) Temperature distribution for the impermeable fault model 2. The position of the fault zone is displayed by the dotted red line. The isotherm pattern closely resembles the thermal field for the no fault model 2.
(d) Fluid velocity vectors and temperature distribution for model 2. Because the fault zone is acts as a fluid flow barrier, no hydraulic connection exists between deep and shallow aquifers at the offset.

(e) Temperature distribution for the permeable fault model 3. The isotherms are bent upwards inside the fault zone indicating a temperature increase there.
(f) Fluid velocity vectors and temperature distribution for the permeable fault model 3. Fast upward oriented flow characterizes the central part of the fault zone whereas lateral fluid advection is observed from surrounding sediments towards the fault with reduced fluid velocities.

Model 2

The isotherm pattern for model 2 (Fig. 4.8c) is very similar to the thermal field of the no fault model 1 (Fig. 4.8a) and confirms previous conclusions made on the regional temperature field (Figs. 4.5b, 4e) and on the temperature distribution around the Gardelegen fault zone (Fig. 4.7c). In the shallow Cenozoic and Mesozoic aquifers, fluid velocity vectors resemble the regional trend as observed in no fault model 1 (Fig. 4.8d). Along the fault zone, fluid is characterized by very low fluid velocities (~ 1e-10 m/d). Fluid flow is locally disturbed and redirected north of the fault zone within the deeper part of the Buntsandstein aquifer. Throughout the deeper part of the Rotliegend aquifer, the regional north-south flow pattern is dominant. Compared to the no fault model 1, fluid flows from the shallow Buntsandstein and Rotliegend sediments towards the fault zone and no fluid mixing can be observed at the narrow transition.
Along the fault zone, fluid flow is characterized by very low fluid velocities due to impermeable conditions of the latter. Because fluid cannot discharge into the fault zone, it is redirected in the adjacent aquifer sediments. No hydraulic connection exists between the shallow and deep Bundsandstein and Rotliegend aquifer domains. Therefore, no mixing occurs between the shallow and deep aquifer. But fluid flows laterally from the shallow Buntsandstein and Rotliegend sediments towards the impermeable fault zone.
In conclusion, the results for model 2 confirm a spatially limited impact of a tight fault zone which leads to an almost unchanged temperature field when compared to the no fault scenario. The effects of the impermeable fault zone are only local and results in a disturbance of the flow field nearby the fault zone which inhibits any hydraulic communication between shallow and deep aquifers which are offset at depths by the fault (Buntsandstein and Rotliegend).

Model 3

In case of a permeable fault zone (model 3), significant differences can be observed in the thermal field compared to the models 1 and 2 (Fig. 4.8e). In the central part of the fault zone, the isotherms are bent upwards revealing locally increased temperatures which gradually decrease within the underlying Pre-Permian basement.
Fluid velocity vectors display a fast upward directed flow at the same location (max. 1e-4 m/d) (Fig. 4.8f). Similar to model 1, fluid velocity vectors display vigorous fluid flow below the

Rupelian windows within the shallow Cenozoic and Mesozoic aquifers and a regional flow from north to south in the deeper Buntsandstein and Rotliegend aquifers north of the permeable fault zone. In general, fluid inflow occurs from all surrounding aquifer sediments into the fault zone (~1e-06-1e-04 m/d).

Fast upward oriented flow reflects a local temperature increase within the fault zone (Fig. 4.8e). Within the Pre-Permian basement, fluid flow is impeded and the heat is transferred by conduction only. Lateral inflow from the aquifer into the fault zone is induced the by high permeability contrast between fault and surrounding sediments (Tables 4.1 and 4.2). Within the fault zone, fluid flows upwards following the hydraulic head potential (cf. Fig. 4.6b).

In conclusion, upward oriented fluid flow induces higher temperatures in the permeable fault zone. Fluid inflow is observed from the less permeable surrounding aquifers into the permeable Lausitz fault zone located beneath a major discharge area.

3D sections

To get a final overview of the fluid behavior around both fault zones, 3D close-up views are shown for the two fault models (model 2 and model 3).

Fig. 4.9a shows a zoomed plot of the flow field in the sedimentary layers above the Zechstein salt layer around the permeable Gardelegen fault zone (model 3). The temperature field along the strike direction of the Gardelegen fault zone is shown in the background.

Velocity vectors indicate increased fluid inflow from the top of the section into the Cenozoic aquifer with highest velocities (4e-04 – 8e-04 m/d) down to the depth level of the Rupelian aquitard. Throughout the Mesozoic aquifer, fluid velocities are reduced (~ 2e-04 – 4e-04 m/d) compared to the shallow Cenozoic aquifer. Below the Muschelkalk aquitard, fluid velocities further decrease down to ~1e-09 m/d within the Buntsandstein aquifer.

While fluid velocities gradually drop with depth due to decreasing permeabilities of the aquifers (Table 4.1) and aquitards, modelled fluid flow shows a consistent direction within the whole aquifer systems. A downward oriented flow is displayed in the shallow Cenozoic aquifer. Downward flow occurs in areas where cooler temperatures (~ 8-25°C) characterize the internal part of the fault zone (in the background, Fig. 4.9a). Fluid is then redirected towards the fault zone in all aquifers due to the high permeability of the latter. Finally, upward oriented flow can be seen in areas where higher temperatures (~ 25-50 °C) are present in the fault zone.

Looking from top of the 3D image in map view, we can conclude that the fault zone influences the fluid movement and the temperature field in the surrounding sediments at -3,000 m depth within an influence radius of ~ 5 km (Fig. 4.9b; cf. Figs. 4.5c and f).

Figs. 4.9c and 4.9d show top views for the same 3D block section as in Fig. 4.9a for the permeable fault model 3 and for the impermeable fault model 2, respectively. Fluid velocity vectors clearly reflect enhanced fluid advection from the surrounding sediments towards the permeable fault zone (Fig. 4.9c). By contrast, fluid cannot enter the impermeable fault zone (Fig. 4.9d). Furthermore, overall reduced fluid velocities characterize the flow in close proximity to the fault zone (~ 1e-9 – 4e-4 m/d) where the fluid flow is deviated along the same structure. The range of influence is restricted to a distance of ~ 1 km on each side of the fault.

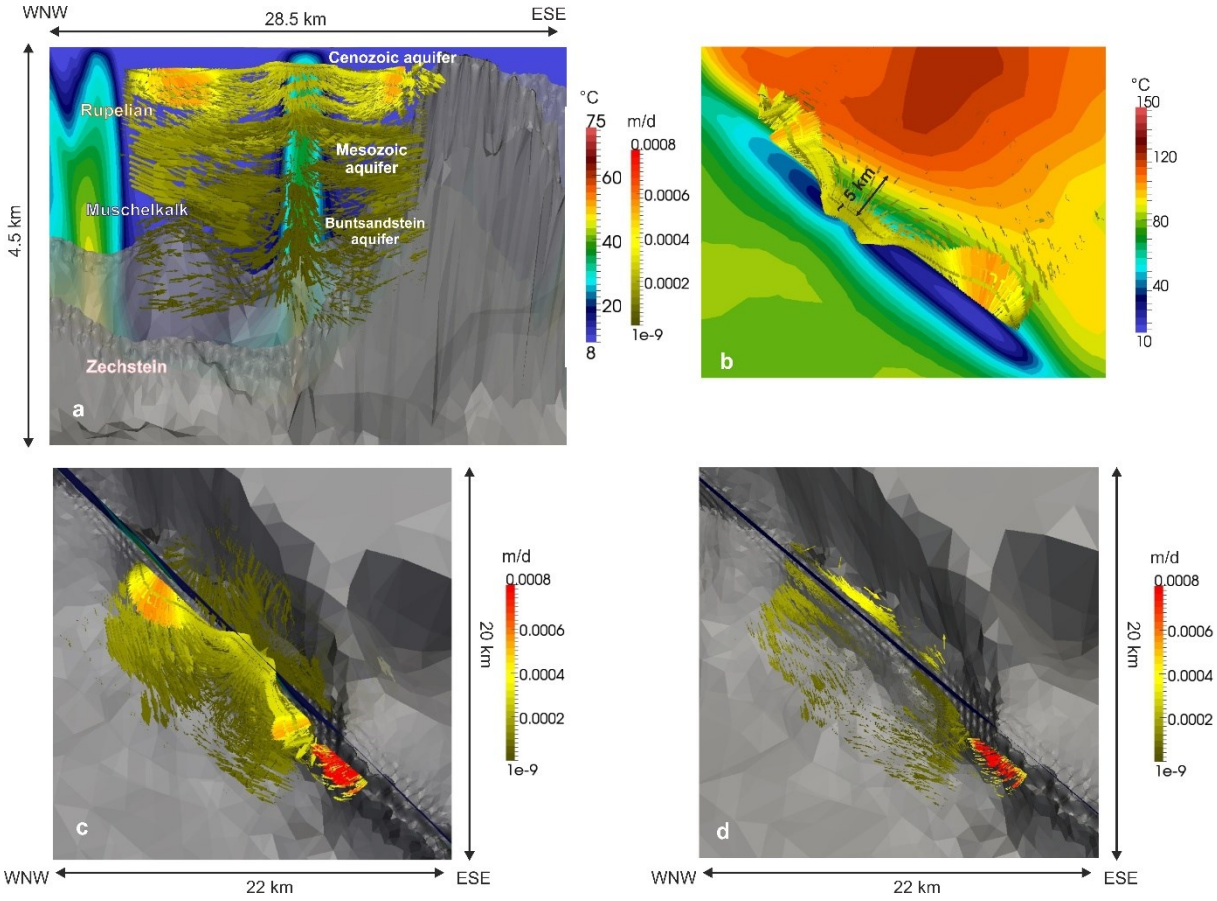

Figure 4.9 (a) Zoom into the 3D flow field around the permeable fault zone (model 3) above the Permian Zechstein layer (grey-shaded). The temperature distribution along the strike of the Gardelegen fault zone is displayed in the background. Location of the zoom is delineated in Fig. 4.6a by the red circle. The velocity vectors clearly indicate flow from the surrounding aquifers towards the permeable fault zone. The lengths of the fluid velocity vectors are non-scaled.
(b) Top view of Fig. 4.9a zooming on the temperature distribution at -3,000 m depth (position is outlined in Fig. 4.5f by a black rectangle) indicating the range of influence of the fault on the flow and thermal field.

(c) Top view on the 3D flow field around the permeable fault zone (model 3) for the same location as in Fig. 4.9a and b. Fluid advection towards the fault zone is displayed by the vectors which is induced by the high permeability contrast between fault and neighboring sedimentary layers.
(d) Top view on the 3D flow field around the impermeable fault zone (model 2) for the same location as in the previous subfigures. Fluid flow in the surrounding sediments is redirected parallel to the fault zone due to the impermeable nature of the fault.

4.4 Discussion and conclusions

The investigation of fault zones with varying permeability by 3D coupled fluid and heat transport simulations reveals a distinct local influence on the regional thermal field and fluid system for the different permeability configurations considered.

Regional thermal field without faults

The regional temperature distribution at different depth levels is the result of superposed thermal effects generated by the complex interaction between aquifers and aquitards of varying thickness and different fluid and heat transport active processes, that is, advection, buoyant flow and heat conduction.

Advective processes strongly affect the shallow thermal field in the Cenozoic and Mesozoic aquifers down to maximum penetration depth of approximately -3,000 m. Where the Rupelian clay is missing (hydrogeological windows), inflow of cold water from the top surface, as triggered by the upper boundary conditions, induces a pronounced cooling in the Mesozoic aquifer. 3D models of coupled fluid and heat transport of the NEGB have already shown that pressure forces triggered by local topographic gradients may be strong enough to induce a net cooling on the shallow aquifer system, whereby higher permeability of the corresponding layers promotes greater penetration depths of cold water (Kaiser et al. 2011).

Indications for convective flow in the shallower Mesozoic aquifer play an additional, though secondary role, in areas confined by a thick sequence of Rupelian clay, preventing inflow of cold water from the Cenozoic aquifer and shielding the influence of superficial hydraulic head gradients on the underlying Mesozoic aquifer (Noack et al. 2013).

Heat conduction through the thick Pre-Permian basement and the Permian Zechstein (both impermeable to fluid flow but thermally higher conductive than the surrounding sediments), decisively shapes the local thermal field across the southern margin and in the vicinity of salt diapirs in the central basin.

Influence of impermeable fault zones

When implementing fault zones as low permeable structures, the temperature distribution strongly resembles the regional thermal field modeled when no faults have been considered. The influence of impermeable faults on the flow field is local, limited to the fault zones itself and their close proximity. Fluid flow, both direction and magnitudes of fluid velocity, within the surrounding sediments is unaffected by the presence of tight faults. At the fault zones, fluid flow is deviated from the sediments with very low velocities. Acting as hydraulic barriers, fault zones prevent a lateral fluid inflow. As a consequence, fluid cannot be transmitted through the fault zones resulting in very low fluid velocities, thus leaving again conduction as the dominant heat transport process. Therefore, due to low fluid velocities and a spatially limited influence of the fault, no remarkable influence on the thermal field can be observed.

Influence of permeable fault zones

Highly permeable fault zones (model 3) may locally exert a considerable influence on the thermal field. Along both permeable fault zones distinctly cooler temperatures than in its surroundings characterize the thermal field, expressed by an alternating thermal signature. The range of influence of the permeable fault zones extends over a distance of ~ 2.4-8.8 km in -1,000 m depth and ~6-12 km in -3,000 m depth.

Inside the fault zones, a net cooling effect is induced by relatively fast downward oriented flow. Triggered by fluid advection due to hydraulic head gradients and enhanced by the high permeability of the fault zones, cold water can easily flow downwards generating the observed cooling.

The observed cooling in the fault zones alternate with higher thermal anomalies through upward directed flow. Below discharge areas upward oriented flow occurs which may be locally enhanced by buoyancy forces having a secondary effect on both the hydrodynamics and thermal field.

Interaction between fault zones and surrounding sediments

The fluid behavior in the sediments surrounding both fault zones is principally controlled by existing hydraulic head gradients and by the permeability of the fault zones. Modelled fluid flow and thermal field within the surrounding sediments are locally influenced by the presence of permeable fault zones along their strike direction. Across these fault zones, the thermal field and fluid flow are affected by the thickness and permeability of the sedimentary layers adjacent to the faults.

Below recharge areas and adjacent steep hydraulic gradients, downward oriented flow inside the fault zones in turn affects the temperature and flow field in the surrounding sediments. Fast downward flow impresses a lateral fluid discharge into the surrounding aquifers. Below discharge areas, the regional flow pattern induced by topographic gradients in combination with the higher fault permeability, leads to lateral fluid inflow from the aquifers towards the fault zones.

Both, the lateral outflow from faults into the aquifers below recharge areas and the lateral inflow from aquifers into the faults below discharge areas clearly demonstrate the dynamic interaction between host rocks and fault zones.

Outside the range of influence of the fault zones, the temperature distribution is mainly controlled by different heat transport processes, closely linked to the distribution of the aquifers and aquitards.

Inferences for geothermal applications

The fault model outcomes provide valuable inferences on fault zone behavior and their impact on the surrounding groundwater circulation system and thermal field which might be useful for geothermal energy exploration.

The study has highlighted two major implications for geothermal applications.

Impermeable fault zones has little effect for the thermal field and very locally deviate the flow field in the sediments next to the faults. Therefore, this setting would be an unfavourable place to drill a geothermal well.

Drilling a geothermal well into or in close proximity to a permeable fault zone would be more prospective in the shallow part of the model domain (up to ~ 450 m depth) where rising warm fluids are in concert with high permeability of the faults. These spots of rising warm water are locally restricted but temperatures are increased (up to 15°C compared to the thermal field without faults). By contrast, domains of colder temperatures next to permeable sediments are the most unfavourable areas for geothermal utilization.

In summary, the best place to drill a prospective geothermal well would need to be chosen with care as two conditions should to be fulfilled: (1) enhanced inflow of warm and deep water into the fault and (2) rising branch of heated fluid within the fault zone.

Model limitations and outlook for future studies

Some limitations of the study presented include (1) the structural resolution of the model, (2) the physical fault zone representation, (3) the choice of hydraulic boundary conditions adopted along the top boundary of the model.

(1) The structural resolution of the model especially concerns the distribution of sedimentary layers in the proximity of the fault zones, as we concluded that the fluid flow in the surrounding sediments may locally contribute to the fluid behavior of the permeable fault. As the current study revealed that fault zones locally influence the thermal and fluid system, in a subsequent step, a higher resolution of the model could be achieved by a structural refinement and by focussing only on the areas around the fault zones by decreasing the model size considerably. This step, however, would also assume better constraints on physical rock properties for both the sedimentary and the fault zones (see also point 2 below).

(2) As the two fault zones are represented as idealized permeable/impermeable zones of a finite width, further studies may consider a more heterogeneous composition of the fault zone, possibly consisting of a damage zone and a fault core. However, more detailed data would be required on the structure and composition of the Gardelegen and Lausitz fault zones. These could be beneficial for future studies aiming at a more quantitative assessment of their impact on the resulting thermal and groundwater field. Local reservoir scale models integrating higher resolved structural data, information derived from boreholes and in situ measurements may provide better constraints for the characterization of fault zones (e.g. Cacace et al. 2013; Blöcher et al. 2010b). However, up-scaling from reservoir to basin-scale may lead to non-realistic model settings. Better constraints on hydraulic behavior of fault zones may be provided by prospective integrated geophysical methods (e.g. Magnetotellurics) that could provide a more sound base to discriminate between different end-member models. At present, a direct assessment of the hydraulic behavior of faults by the determination of their orientation within the present-day stress field was not possible. This was reflected in the modelling approach followed in the present study in which different end-member stress states have been tested. Given the state of the art of available information, the study presented in this manuscript represents so far the best quantitative approach to characterize the thermal and hydraulic behavior of major fault zones in the basin-scale model.

(3) The cooling observed in the permeable fault zone and in the Mesozoic aquifer may overestimate the influence of forced convection processes in the model due to the crude boundary setting adopted throughout the models. Future studies are needed which should

integrate more realistic information on recharge rates in the study area and may additionally be improved by a dynamic coupling with surface water transport modelling.

This study is the first attempt to investigate the impact of major fault zones on a 3D basin-scale for the coupled fluid and heat transport in the Brandenburg region. The finite element simulation outcomes provide new insights on the dynamic processes and mechanisms that control the fluid behavior and thermal evolution of fault zones with varying permeability in the context of a complex hydrogeological setting. While the lateral influence of a 1 km wide fault zone is rather limited with respect to the neighboring sediments, temperature variations within the fault zone may be significant, thus having interesting application for issues related to geothermal exploration.

Acknowledgements

This work is part of the project GeoEn and has been funded by the German Federal Ministry of Education and Research in the program “Spitzenforschung in den neuen Ländern” (BMBF Grant 03G0671A/B/C).

Björn Lewerenz and Björn Kaiser are thanked for helpful computational support and Peter Klitzke for his contributions to visualization. All numerical results are illustrated by ParaView, an open-source, multi-platform and visualization application.

5 Discussion, outlook and conclusions

5.1 Discussion

As the objective of this thesis was to study the influence of faults on the coupled fluid and heat transport in the subsurface, 3D numerical simulations were carried out for different geological settings on the local,- regional- and basin-scale. By following the main research questions (chapter 1.1), new methodological and scientific insights arose for 3D geothermal fault modelling which are discussed in detail within the following subchapters.

5.1.1 Numerical approach

To address the objective of this thesis, 3D simulations of the coupled fluid and heat transport needed to be carry out in which faults are integrated as structural discontinuities within the numerical models. To answer the question whether and how it is possible to implement inclined faults in 3D numerical models, different numerical approaches have been initially tested. The software evaluation as well as the consequent simulations carried out led to new methodological insights for 3D finite element based geothermal fault modelling. Though the implementation of structural discontinuities in three-dimensional models represented a major challenge, the results demonstrate that it is possible to simulate coupled processes (fluid and heat) for 3D finite element models with integrated fault structures. Furthermore, they indicate the importance of carrying out fully 3D simulations that consider faults since determining thermal patterns and rates of fluid flow in these distinct discontinuities is a three-dimensional problem (cf. Caine and Forster, 1999).
The outcomes provide an effective workflow for the implementation of faults in 3D finite element models, which can be used for simulating coupled physical processes. As such, this workflow may provide a generic guideline for any fault-related geothermal modelling studies on different scales, including small-scale (synthetic) as well as complex regional-, and basin-scale geological settings.

Within the 3D finite element models used for the numerical simulations, the geological structure of stratigraphic layers and the architecture of faults have to be geometrically reproduced by the finite element mesh. The goal was to approximate the faults architecture within the mesh as realistic as possible, thereby taking length and dipping angle of the individual structures into account.

For the simulations, first different kinds of open-source and commercial software were evaluated and tested to figure out which tool is (a) able to reproduce dipping and non-planar (and intersecting) faults in a 3D numerical model, (b) at the same time capable of simulating coupled thermal and hydraulic processes in porous media, and (c) include a complex geology on the basin scale.

In general, different approaches exist to model structural discontinuities, including the discrete fracture network (DFN) and the porous medium, as well as the hybrid approach combining these two (cf. chapter 2.1). Since the DFN does not account for porous media, this approach was ineligible for the purpose of this thesis.

In the porous medium approach, faults are implicitly taken into account by a permeability assignment of the equivalent porous medium (EPM). However, any mesh quickly becomes too complex for the fault domains, when implementing dipping structures in a 3D mesh, because a fine horizontal as well as vertical discretization is required for the fault domain, which is determined by the length and dipping angle of the fault. In more detail, this means that the greater the penetration depth of the fault, the higher the vertical refinement and the smaller the dipping angle of the fault structures, the greater the area of horizontal mesh refinement must be to produce meaningful results. If the geological structure described by the finite element model is already complex (like in regional-scale models,- in our case the Groß Schönebeck and Brandenburg models), the implementation of just very few inclined faults would lead to an inapplicable and too complex model with far too many elements. Accordingly, the simulations would become too time expensive to be useful.

In the hybrid approach, the porous medium approach is combined with discrete feature elements, which are finite elements of lower dimensionality, to be inserted at element edges and faces (Diersch, 2002). Contrary to the EPM, this approach needs only limited mesh refinement next to the fault domains and is therefore an adequate methodological approach that enabled to study the objective of this thesis.

In the course of evaluating different software, the numerical simulator “OpenGeoSys” has been chosen first. “OpenGeoSys” is an open-source software able to calculate coupled thermo-hydraulic processes for 3D faulted geological systems in porous media, by following the hybrid approach (Kolditz et al. 2012a). During this stage, a fully automated approach has been developed, which is able to create consistent, unstructured, boundary-conforming Delaunay tetrahedral meshes (pre-processor “MeshIt”; Blöcher et al. 2010a; Cacace et al. 2013) to be directly imported into finite element/volume numerical software. Faults are represented as 2D planar or non-planar discrete structures embedded in the 3D finite element mesh. By means of

the combination of the open-source pre-processor and “OpenGeoSys”, the investigation has been started with synthetic models based on a simple structure (one geological layer cut by a fault), to capture basic principles on hydraulic and thermal fault behavior (chapter 2). Keeping the model simple and changing only one parameter (fault width, permeability) within the simulations enabled a quantitative assessment of the influence of each parameter on flow regime and temperature distribution.

However, generating finite element meshes for the more complex geological setting of Groß Schönebeck (regional scale), could not be achieved by the available pre-processor at that time. Therefore, the commercial software FEFLOW® (Diersch, 2002) has been chosen to simulate 3D coupled fluid and heat transport processes for the subsequently studied regional-scale models. Within FEFLOW®, faults can be modelled as vertical 2D discrete feature elements for which different fluid motion laws can be applied (chapter 3.3.1). The application of discrete feature elements, however, is restricted to structural discontinuities that have a higher permeability than the surrounding (matrix) domain. This is because the permeability of the discrete element is added to the permeability of the background (matrix) domain. Therefore, discrete feature elements cannot be applied for modelled tight faults. Instead, faults with a lower permeability than the matrix domain can only be modeled as equivalent porous media. As such, they are represented by finite element areas for which a very low permeability is assigned along the trace of the discontinuity. Since faults are vertically implemented, considerably less horizontal mesh refinement is required, compared to the (EPM) setting with inclined faults. Thus the approach is suited for steeply dipping faults.

For permeable fault zones with a larger width (1 km, Brandenburg model), a combination of vertical discrete feature elements and equivalent porous media was used (chapter 4.2.4). Thereby, a refined permeable domain with a permeability equal to that of the discrete fault is assigned on either side of the fault trace. Since the fault implementation is vertical and the mesh refinement is restricted to the fault domains, again, considerably less horizontal mesh refinement is required, compared to the EPM for dipping structures.

However, even with a vertical fault implementation, the overall structure of the finite element models is still complex enough to complicate significantly the numerical stability during the simulations of coupled physical processes. Stabilization as well as simulations of such complex models are very time-consuming. Therefore, these factors should be implicitly taken into account in advance of 3D fault modelling of coupled physical processes for complex regional- and basin-scale geological settings.

5.1.2 Heat transfer mechanisms

To study the influence of faults on the coupled fluid and heat transport requires an understanding of the different heat transport processes that may evolve in these structural discontinuities as they control the resulting fluid flow and temperature distribution, both necessary to assess for geothermal exploration. If the results are compared where faults act as barriers or conduits, it becomes clear that along tight structures heat transfer by conduction dominates. Contrarily, in case of faults serving as conduits for fluids, buoyancy-, and topography-driven fluid flow may evolve.

Conduction

Conductive heat transport occurs in tight faults. As these structural discontinuities act as hydraulic barriers, a lateral fluid inflow from the surrounding host sediments is inhibited. Consequently, fluid cannot be transmitted through the faults, resulting in very low fluid velocities there, leaving conduction the dominant heat transfer process. However, hydraulic communication between different aquifers may be disrupted by the presence of tight faults.

As a result, hydraulic effects of tight faults are local, restricted to the faults itself and its close proximity. Although spatially limited, the presence of impermeable faults induce very low fluid velocities inside as well as nearby these structures (~ 3e-13 m/a). Moreover, fluid flow is redirected along the same faults. These results agree with very low flow rates in and along tight faults found by simulations in other settings. Examples include simulations of coupled fluid and heat transport for a cross-section of the Rhine Graben in the order of 1e-5 m/a (Lampe and Person, 2002) and fluid velocities smaller than 1.3e-13 m/s in a synthetic model (López and Smith, 1995).

The observed low flow rates in combination with a spatially limited influence of tight faults result in no remarkable influence on the thermal field. Nevertheless, their consideration is important because they locally deviate the pressure field at depth along their trace. Despite our results showed no fault-induced thermal variations, tight structures may cause local changes of temperatures, if, according to a special internal composition (e.g. quartz-cementation or salt rock infill), they have a higher thermal conductivity than the surrounding sediments. This may cause thermal refraction, similar to phenomena demonstrated for thermally highly conductive rock salt in the NEGB (e.g. Bayer et al. 1997; Scheck, 1997). Such focused enhancement of heat transport may lead to locally increased temperatures inside tight fault structures, and lower temperatures along the fault-host domain boundaries. Of course, the spatial extent of such positive temperature anomalies will primarily depend on the width of the fault zones.

Free thermal convection

Under specific conditions, buoyancy-driven flow may evolve in highly permeable faults. These conditions are met within a specific geological setting, in which the upper tip of the fault is not bounded by the topographic surface, but instead bordered by hydraulically impermeable aquitard sediments. The aquitard on top of the fault shields the underlying sedimentary layers and the fault from the direct influence of surface fluid advection driven by hydraulic head gradients. In this specific case, free convection can control the fluid and heat flow inside the structural discontinuity. Numerical experiments and sensitivity analyses approved that faults with strong initial heat input, due to their depth of penetration or magmatic activity, are the most likely candidates to carry discharge fluids associated with hydrothermal free convection to the sites of metal precipitation (Yang et al. 2004a).

Alt-Epping and Zhao (2010) also proposed that a high permeability contrast between fault and host domain promotes focused convective flow within the fault zone. Their observation was based on coupled fluid, heat and mass transfer simulations of a synthetic model including a vertical fault zone.

In line with this hypothesis, this thesis made a step forward in providing an accurate value for the permeability contrast, which is required for the development of thermal convection within faults. For the Groß Schönebeck model, our sensitivity analysis for fault permeabilities revealed that free convection evolves only in faults, which are at least three orders of magnitude more permeable than the surrounding sediments (cf. chapter 3.5). Otherwise, the fault will not have an effect on the fluid system and thermal field. Similarly, López and Smith, 1995 showed that convection dominates within a fault zone at host rock permeability lower than ~ 1e-15 m² and fault permeabilities higher than ~1e-13 m² within coupled fluid and heat transport simulations of a synthetic model.

Another aspect is that the permeability contrast promotes lateral fluid advection from surrounding sediments into the structural discontinuity. Inside the fault, convective heat transport leads to an equilibration of temperatures with time. At the specific geothermal site of Groß Schönebeck, this thermal equilibration results in up to 15°C higher temperatures at the top of the fault (~ -4000 m depth) and up to 12°C lower temperatures at its base (~ -4400 m depth) within the geothermal reservoir, when compared to a setting where no faults are considered. Though strongly depth-dependent, these positive thermal anomalies may provide good targets for geothermal applications. However, it should be kept in mind, that the temperature distribution within the specific reservoir is the result of the interaction of different kinds of heat transport mechanisms, closely linked to the distribution of aquifers and aquitards,

which in turn affects the temperature differences between fault and surrounding sediments. Both, the temperature distribution in the fault and adjacent sedimentary layers in combination with the fault width controls the range of influence of the fault on the thermal field, covering a maximum distance of ~ 4.8 km in -4000 m depth in the specific case of Groß Schönebeck.

Forced convection

Forced convection is the predominant heat transport mechanism in permeable faults, if these geological structures are close to or reach up the surface. In this specific setting, fluid motion inside a highly permeable fault is principally driven by fluid advection due to existing hydraulic head gradients. Below major recharge areas and adjacent steep hydraulic gradients, fast downward oriented flow is generated inducing a net cooling of groundwater in the permeable fault. If the fault reaches greater depth (down to the basement), the fluid may be heated by thermal equilibration with the surrounding sedimentary system. At the same time, the fluid velocity in the fault diminishes with depth. The heated fluid will then tend to rise upwards beneath major discharge areas inducing higher temperatures at shallow depth. This upward flow may be locally enhanced by buoyancy forces, having a secondary effect on the hydrothermal field. Fernàndez and Banda (1990) confirm that forced convection will generate thermal anomalies only when faults reach deep enough to allow rapid ascent of water and whereas fluid flow is slow in its descent. In fact, forced convection was the only mechanism found in their modelling study to explain thermal anomalies observed along master faults in the Valles-Penedes Graben.

In general, topographic relief appears to be the dominant controlling factor for groundwater flow in continental land masses, both in the shallow and deep subsurface (e.g. Freeze and Witherspoon, 1967; Tóth, 1962). Topography-driven fluid flow in faults has been observed in 2D numerical models of a transect across the Rhinegraben, with groundwater recharging along deep basement faults at topographic highs and discharging fault systems at topographic lows (Lampe and Person, 2002).

This thesis furthermore provides information on fluid behavior in the sediments surrounding permeable faults. The latter is controlled principally by existing hydraulic head gradients and by the fault permeability. Below recharge areas, fast downward flow inside the fault impresses a lateral fluid discharge into the surrounding aquifers. By contrast, the regional flow pattern induced by topographic gradients in combination with the higher fault permeability, leads to lateral fluid inflow from the surrounding aquifer sediments into the fault below major discharge areas. This dynamic interaction between fault and surroundings shows that across the fault, the

composition, thickness and permeability of the adjacent sedimentary layers mainly affect fluid and heat flow patterns.

All in all, the range of influence of permeable fault zones on the flow system and thermal field is locally restricted depending on the width of the fault. Fernàndez and Banda (1990) suggest that high thermal anomalies are commonly very limited in lateral extent (few square meters), because fractures play a major role in focusing groundwater discharge. The results of this thesis confirm this rather limited lateral influence. More specifically, the range of influence of major fault zones located in the Brandenburg area extends over a distance of ~ 2.4-8.8 km in -1,000 m depth and ~6-12 km in -3,000 m depth. Within these ranges, the most prospective places for geothermal utilization are below major discharge areas where rising warm fluids occur in concert with a high permeability of the fault. In the Brandenburg area, at these spots temperatures are up to 15°C higher compared to the thermal field without faults, but are restricted to the shallow part of the model domain (down to ~ 450 m depth). By contrast, domains of colder temperatures below major recharge areas are the most unfavourable areas to drill a geothermal well.

In summary, the results illustrate that faults exert a local effect on the geothermal field, regardless if conduction, free or forced convection is the predominant heat transfer mechanism.

5.1.3 Controlling factors

A major question addressed in this thesis was which factors mainly control the development of different kinds of heat transport mechanisms in faults and their resulting influence on the geothermal field. By considering the first part of the question, the modelling results showed that the development of different kinds of heat transport mechanisms in faults mainly depends on the permeability of the fault and the distribution of permeabilities in the surrounding sediments. Altogether, the model outcomes clearly indicated that the permeability contrast between structural discontinuities and host domain plays a crucial role in influencing the fluid and heat flow. A further decisive factor in controlling the development of different kinds of heat transport processes in faults turned out to be the specific geological setting. Addressing the second part of the question,- which factors control the respective influence of faults on the geothermal field-, primary depends on both, fault width and temperature distribution within the surrounding sediments.

Permeability

Generally, the orientation and distribution of permeable domains (including faults) determines to a large extent the flow pattern of fluid flow in sedimentary basins (Bjørlykke, 2010).

The results of all our modelling studies demonstrated that permeability is a crucial factor in influencing the coupled fluid and heat transport. This concerns both, the permeability of faults and of the surrounding domain, i.e. the permeability contrast between fault and surrounding domain. Permeability directly controls fluid flow and velocity (s. Darcy equation 2, Appendix A), and consequently, also the heat transport processes and associated thermal effects of fluid flow inside faults as well as surrounding areas.

As in situ observations in active fault zones are generally difficult, field studies, based on geochemical examinations give important insights of fluid flow in various geological settings such as fault zones (e.g. Gébelin et al. 2011; Mulch et al. 2007; Pili et al. 2002). Indeed, isotope studies of North-American core complexes indicated that circulating fluid flow in the brittle upper crust is primarily controlled by large-scale fault zone architecture (Gottardi et al. 2013). Associated numerical simulations accordingly showed that fluid migration to mid- to lower-crustal levels is fault controlled, depending primarily on the permeability contrast between fault zone and crustal rocks. As also stated by Caine and Forster (1999), permeability contrasts between components such as fault core and surrounding damage zone is identified as one of the major controlling factors in fault-related fluid flow. Likewise, recent numerical modelling results confirm that fluid migration and thermal patterns in faults and sedimentary basins are highly sensitive to permeability (e.g. Alt-Epping and Zhao, 2010; Lampe and Person, 2002; Luijendijk, 2012; Yang et al. 2004a).

Although the modeling results depend on the choice of permeability values, in general, the transport of heat and fluid in fault-controlled hydrothermal systems is difficult to model realistically, since data or observations are sparse to constrain the distribution of hydraulic properties within faults (Fairley, 2009) (cf. chapters 3.5 and 4.4). However, our results indicate that the first order behavior of heat transport mechanisms and the related range of influence of permeable faults does not change within a well-defined range of permeability values (s. chapter 3.5). In case of the Groß Schönebeck model, this is, however, only valid if a sufficiently high permeability contrast by three orders of magnitude is present between fault and host domain. (cf. chapters 3.5 and 5.1.2).

Geological setting on different scales

A further decisive factor in controlling the evolving different heat transport processes in faults is the geological setting, comprising the specific configuration of the sedimentary layers. This includes the fault`s position relative to the surrounding geological layers and the penetration depth of these structures. Depending on the geological setting, primarily characterized by the thickness distribution and, again, the permeabilities of the individual geological layers, different kinds of heat transport processes may evolve in faults (chapter 5.1.2). In terms of transferability, this dependence shows that it is necessary to consider the specific geological setting, including the geometry of aquitards and aquifers, the fault position and depth, prior to modelling 3D complex faulted systems.

Common to all models is that faults exert a local, though significant influence on the regional geothermal field. Despite this aspect, the results from each model presented in this thesis indicate that different heat transfer mechanisms may evolve depending on the specific hydrogeological configuration and scale. These findings prevent any generic upscaling between different settings. Indeed, each setting needs to be considered individually with respect to its configuration and scale dimension.

Fault width

The respective influence of faults on the geothermal field depends on fault width and temperature distribution within the surrounding sediments, resulting, in turn, from the interaction of different kinds of heat transport mechanisms, closely linked to the distribution of aquifers and aquicludes.

A general outcome was that the range of influence of faults increases with the width of the faults. Regardless of whether the fault zone width is decreased or increased, however, the first order behavior of heat transport processes remain the same and the resulting thermal distribution is similar in all cases. Moreover, sensitivity analyses based on the fault width for the small-scale synthetic model showed a linear inverse relationship between fluid velocity and fault zone width (chapter 2.3.3). This relationship indicates that increasing the width by one order of magnitude generally reduces the velocity in the fault by one order of magnitude. Not surprisingly, the higher fluid amount that can be guided through a wider fault, increases the thermal effect in and around the fault.

5.2 Outlook for future studies

Besides of the main factors controlling fluid and heat transport in faults, including permeability, related geological setting and fault width, also other factors affect the calculated geothermal field. These influencing factors include specific boundary and initial conditions (chapters 2.4, 3.5, 4.4 and B.5), the choice of physical properties (chapters 3.5, 4.4, B.5), model structure,- scale,- and resolution (chapters 3.5, 4.4) and degree of coupling between all these components. As the results of the Groß Schönebeck and Brandenburg studies revealed, the temperatures in the shallow model domains are especially sensitive to the hydraulic and thermal boundary conditions set at the surface of the models. In these simulations, the hydraulic upper boundary condition prescribed is a fixed hydraulic head equal to the topographic elevation. As the upper thermal boundary condition, a fixed constant surface temperature of 8°C is applied. In response to these chosen upper boundary conditions (chapters 3.3.4, 4.2.6), a constant inflow of cold water is generated during the simulations. Consequently, a net cooling is induced in the shallow level, which may be, however, generally overestimated. In particular, hydraulic head distributions that deviate from the topographic relief may occur. Therefore, future studies should integrate more realistic information on recharge rates and may additionally be improved by a dynamic coupling with surface water transport modelling. Further improvement could be achieved by an assignment of lateral boundary conditions extracted from larger-scaled fluid and heat transport models.

Equally important is the choice of physical properties within faults and geological layers, especially the permeability, as already discussed within chapter 5.1.3. More sound and detailed physical as well as structural input data are required to refine the geological model and to consider a more heterogeneous composition of faults. Specifically, the effect of anisotropic permeabilities could be addressed within future studies. A lower vertical permeability may decrease the extent of topography-driven flow and reduce thermal convection in the geological system. Moreover, anisotropic conditions in faults (vertical > horizontal permeability) may cause the faults to act as combined conduit-barrier systems (e.g. Bense et al. 2008).

Concerning the degree of coupling, in future research, the impact of viscosity on the fluid and heat transport might be addressed in addition to fluid density. In the fault modelling studies carried out for this thesis, fluid viscosity has been considered constant. However, fluid viscosity may specifically influence convective heat transport as this temperature-dependent parameter characterizes the internal friction of the fluid, which offers resistance to the flow.

A further aspect worth addressing in future work is the coupling with salinity, since there is evidence for saline water close to the surface in the NEGB (e.g. Grube et al. 2000;

Schirrmeister, 1996). 3D and 2D thermohaline simulations of the NEGB indicated that hydrostatically driven fluid flow and thermohaline convection can be considered among the major mechanisms currently affecting parts of the NEGB (Kaiser et al. 2013b; Magri, 2005). However, the interaction between shallow and deep aquifers in relation to salty groundwater flow are not fully understood (Magi, 2005; Magri et al. 2009). Faults may play an important role in driving (salty) water from deep aquifers to shallow levels. By connecting deep and shallow aquifer systems, faults can provide preferential pathways for (saline) fluid flow. Furthermore, they may modify the dynamics of thermal convection in that they constrain the size and locations of convection cells (Simms and Garven, 2004). Therefore, 3D thermohaline simulations may be an additional option for future research as fluid salinity is important for buoyancy and viscosity effects and therefore additionally influences the hydrothermal behavior of faults.

Altogether, the improvement suggestions bear further challenges in the numerical realization of 3D coupled simulations, once again complicated by the consideration of faults. In terms of the numerical approach (chapter 5.1.1), meanwhile, progress has been achieved in the development of the pre-processor “MeshIt” (Blöcher et al. 2010a; Cacace et al. 2013). It is now possible to implement various dipping faults in 3D finite element meshes on the regional scale. By implication, faults can be approximated more realistically. This opens new possibilities for future 3D finite element based simulations for coupled (thermo-hydraulic) processes, by applying the aforementioned combination of open source software (“MeshIt” and “OpenGeoSys”) (chapter 5.1.1).

5.3 Conclusions

The thesis showed that the consideration of faults in 3D finite element models for coupled fluid and heat transport simulations is feasible and, in fact, necessary for geothermal energy exploration. Depending primarily on the permeability of the fault and the surrounding domain, the individual geological setting and configuration, and the heat transport mechanisms such as conduction, free and forced convection, control the coupled fluid and heat transport in faults. According to the heat transport mechanism, and determined by fault width and temperature distribution of the surrounding domain, faults can locally exert a strong control on fluid circulation and cause significant temperature anomalies in the subsurface. In particular, this work shows that:

- The influence of faults on the coupled fluid and heat transport is local but significant, depending on the hydraulic conductivity of fault and surrounding domain
- The results from the small-, regional- and basin-scale models show that the outcomes cannot be transferred by upscaling and that it is necessary to consider each specific geological setting separately
- Faults acting as hydraulic barriers have no remarkable influence on the thermal field but cause fluid flow deviation in their close proximity
- Hydraulically conductive faults locally affect the fluid circulation and induce significant temperature changes in the subsurface
- The geological setting characterized by the distribution of aquifers and aquitards surrounding the faults determines the hydrodynamic interaction between these two domains and affects the influence of the faults on the coupled fluid and heat transport
- Regardless whether the faults act as hydraulic barriers or conduits, the hydrogeothermal field inside the range of influence of the faults needs to be considered when drilling a geothermal well
- The implementation of vertical faults in 3D regional-, and basin-scale finite element models and the simulation of coupled fluid and heat transport is possible
- The implementation of dipping faults in 3D regional-, and basin-scale models is still a methodological challenge
- The simulation results match both field observations and numerical results from other areas and at the same time may valuably complement field- and laboratory based investigations

References

Adler PM, Thovert JF, Mourzenko VV (2009) Percolation, and Faults and Fractures in Rock. Springer Encyclopedia of Complexity and Systems Science: 6504-6518

Agemar T, Schellschmidt R, Schulz R (2012) Subsurface temperature distribution in Germany. Geothermics 44: 65-77

Alt-Epping P, Zhao C (2010) Reactive mass transport modelling of a three-dimensional vertical fault zone with a finger-like convective flow regime. J Geochem Explor 106: 8-23

Amante C, Eakins BW (2009) ETOPO1 1 Arc-Minute Global Relief Model: Procedures, Data Sources and Analysis. NOAA Technical Memorandum NESDIS NGDC-24, pp. 1-19

Antonellini M, Aydin A (1994) Effect of faulting on fluid flow in porous sandstones: petrophysical properties. AAPG Bulletin 78(3): 355-377

Aydin A (2000) Fractures, faults, and hydrocarbon entrapment, migration and flow. Mar Pertol Geol 17: 797-814

Bächler D, Kohl T, Rybach L (2003) Impact of graben-parallel faults on hydrothermal convection - Rhine Graben case study. Phys Chem Earth 28: 431-441

Baietto A, Cadoppi P, Martinotti G, Perello P, Perrochet P, Vuataz F-D (2008) Assessment of thermal circulations in strike-slip fault systems: the Terme di Valdieri case (Italian western Alps). Geol Soc London, Special Publications 299: 317-339. doi:310.1144/SP1299.1119

Balling N, Kristiansen JI, Breiner N, Poulsen KD, Rasmussen R, Saxov S (1981) Geothermal measurements and subsurface temperature modelling in Denmark. Techn. Ber. GeoSkrifter, No. 16, Department of Geology, Aarhus University

Barton CA, Zoback MD, Moos D (1995) Fluid flow along potentially active faults in crystalline rock. Geol 23(8): 683-686

Bayer U, Scheck M, Koehler M (1997) Modeling of the 3D thermal field in the northeast German Basin. Geolog Rundsch 86: 241-251

Bayer U, Scheck M, Rabbel W, Krawczyk CM, Götze H-J, Stiller M, Beilecke Th, Marotta A-M, Barrio-Alvers L, Kuder J (1999) An integrated study of the NE German Basin. Tectonophysics 314: 285-307

Bear J (1991) Modeling transport phenomena in porous media. Convective Heat and Mass Transfer in Porous Media: 7-69

Bedrosian PA, Unsworth KJ, Egbert GD, Thurber CH (2004) Geophysical images of the creeping segment of the San Andreas fault: implications for the role of crustal fluids in the earthquake process. Tectonophysics 385: 137-158

Beer H (1996) Temperaturmessungen in Tiefbohrungen - Repräsentanz und Möglichkeit einer näherungsweisen Korrektur. Brandenburg geowiss Beitr 1/96: 28-34

Benek R, Kramer W, McCann T, Scheck M, Negendank JFW, Korich D, Huebscher H, Bayer U (1996) Permo-Carboniferous magmatism and related subsidence of the NE German Basin. Tectonophysics 266: 379-404

Bense VF, Person MA, Chaudhary K, You Y, Cremer N, Simon S (2008). Thermal anomalies indicate preferential flow along faults in unconsolidated sedimentary aquifers. Geophys Res Lett 35(L24406). doi:10.1029/2008GL036017

Bjørlykke K (2010) Subsurface water and fluid flow in sedimentary basins. Petroleum Geoscience: From Sedimentary Environments to Rock Physics. 259–279, Springer, Heidelberg. doi:10.1007/978-3-642-02332-3_10

Blessent D, Therrien R, MacQuarrie K (2009) Coupling geological and numerical models to simulate groundwater flow and contaminant transport in fractured media. Comput Geosci 35: 1897-1906

Blöcher MG, Cacace M, Lewerenz B, Zimmermann, G (2010a) Three dimensional modelling of fractured and faulted reservoirs: Techniques and Application. Chem Erde 70 (S3): 145-153

Blöcher MG, Zimmermann G, Moeck I, Brandt W, Hassanzadegan A, Magri F (2010b) 3D Numerical Modeling of Hydrothermal Processes during the Lifetime of a Deep Geothermal Reservoir. Geofluids 10 (3): 406-421

Bundschuh J, Arriaga M (2010) Introduction to the Numerical Modeling of Groundwater and Geothermal Systems. Fundamentals of Mass, Energy and Solute Transport in Poroelastic Rocks, Taylor & Francis

BURVAL WORKING GROUP (2009) Buried Quaternary valleys - a geophysical approach. Zeitschrift der Deutschen Gesellschaft für Geowissenschaften 160 (3): 237-247

Cacace M, Bayer U, Marotta AM (2008) Strain localization due to structural in-homogeneities in the Central European Basin. Int J Earth Sci (Geol Rundsch) 97: 899-913

Cacace M, Kaiser BO, Lewerenz B, Scheck-Wenderoth M (2010) Geothermal Energy: What we can learn from regional numerical models. Chem Erde 70 (S3): 33-46

Cacace M, Blöcher G, Watanabe N, Moeck I, Börsing N, Scheck-Wenderoth M, Kolditz O, Huenges E (2013) Modelling of Fractured Carbonate Reservoirs – Outline of a novel technique via a case study from the Molasse Basin, southern Bavaria (Germany). Environ Earth Sci. doi:10.1007/s12665-013-2402-3

Cacas MC, Ledoux E, de Marsily G, Tillie B (1990) Modelling fracture flow with a stochastic discrete fracture network: calibration and validation 1. The flow model. Water Resour Res. 26 (3): 479-489

Caine JS, Evans PE, Forster CB (1996) Fault zone architecture and permeability structure. Geol 24(11): 1025-1028

Caine JS, Forster CB (1999) Faults and Subsurface Fluid Flow in the Shallow Crust. Geophysical Monograph 113: 101-127

Cappa F (2009) Modelling fluid transfer and slip in a fault zone when integrating heterogeneous hydromechanical characteristics in its internal structure. Geophys J Int 178: 1357-1362

Čermák V, Huckenholz H-G, Rybach L, Schmid R, Schopper JR, Schuch M, Stöffler D, Wohlenberg J (1982) Physical Properties of Rocks, Volume 1, Subvolume a. In Angenheister G (ed) – Landolt-Börnstein, New Series, V/1a: Geophysics and Space Research, Springer, Berlin Heidelberg New York, pp. 1-373

Cherubini Y, Cacace M, Scheck-Wenderoth M, Moeck I, Lewerenz B (2013) Controls on the deep thermal field – implications from 3D numerical simulations for the geothermal research site Groß Schönebeck. Environ Earth Sci 70(8): 3619-3642, doi: 10.1007/s12665-013-2519-4

Clauser C, Villinger H (1990) Analysis of conductive and convective heat transfer in a sedimentary basin, demonstrated for the Rheingraben. Geophys J Int 100 (3): 393-414

DEKORP-BASIN Research Group (1999) Deep crustal structure of the Northeast German basin: New DEKORP-BASIN ’96 deep-profiling results. Geol 27 (1): 55–58

Diersch H-JG (2002) FEFLOW finite-element subsurface flow and transport simulation system. User's Manual/Reference Manual/ White Papers, Release 5.0. WASY GmbH, Berlin

Diersch H-JG, Kolditz O (2002) Variable-density flow and transport in porous media: approaches and challenges. Adv Water Resour 25: 899-944

Eisbacher GH (1996) Einführung in die Tektonik. Enke, Stuttgart

Erhel J, de Dreuzy J-R, Poirriez, B (2009) Flow simulation in three-dimensional discrete fracture networks. SIAM J Sci Comput 31 (4): 2688-2705

Evans JP, Forster CB, Goddard JV (1997) Permeability of fault-related rocks, and implications for hydraulic structure of fault zones. J Struct Geol 19(11): 1393-1404

Fairley JP (2009) Modeling fluid flow in a heterogeneous, fault-controlled hydrothermal system. Geofluids 2009(9): 153 – 166

Faulkner DR, Jackson CAL, Lunn RJ, Schlische RW , Shipton ZK, Wibberly CAJ, Withjack MO (2010). A review of recent developments concerning the structure, mechanics and fluid flow properties of fault zones. J Struct Geol 32: 1557-1575

Fernàndez M, Banda E (1990) Geothermal anomalies in the Valles-Penedes Graben master fault: convection through the horst as a possible mechanism. J Geophys Res 95(B4): 4887-4894

Fleming CG, Couples GD, Haszeldine RS (1998) Thermal effects of fluid flow in steep fault zones. In Jones G, Fisher QJ, Knipe RJ (eds) Faulting, Fault Sealing and Fluid Flow in Hydrocarbon Reservoirs. Geological Society, London, Special Publications 147: 217-229

Förster A (1997) Bewertung der geothermischen Bedingungen im Ostteil des Norddeutschen Beckens. In Hoth P, Seibt A, Kellner T, Huenges E (eds) Geothermie Report 97-1: Geowissenschaftliche Bewertungsgrundlagen zur Nutzung hydrogeothermaler Ressourcen in Norddeutschland. Scientific Technical Report STR97/15, GeoForschungsZentrum Potsdam, pp. 20-41

Förster A (2001) Analysis of borehole temperature data in the Northeast German Basin: continuous logs versus bottom-hole temperatures. Petrol Geosci 7: 241-254

Freeze RA, Witherspoon PA (1967) Theoretical analysis of regional groundwater flow. 2. Effect of water-table configuration and subsurface permeability variation. Water Resour Res 3(2): 623-634

Garven G, Bull SW, Large RR (2001) Hydrothermal fluid flow models of stratiform ore genesis in the McArthur Basin, Northern Territory, Australia. Geofluids 1: 289-311

Gébelin A, Mulch A, Teyssier C, Heizler M, Vennemann T, Seaton NCA (2011) Oligo-Miocene extensional tectonics and fluid flow across the Northern Snake Range detachment system, Nevada.Tectonics 30(TC5010). doi:10.1029/2010TC002797

Geiger S, Roberts S, Matthai K, Zoppou C, Burri A (2004) Combining finite element and finite volume methods for eggicient multiphase flow simulations in highly heterogeneous and structurally complex geologic media. Geofluids 4: 284-299

Gottardi R, Kao P-H, Saar M O, Teyssier C (2013) Effects of permeability fields on fluid, heat, and oxygen isotope transport in extensional detachment systems. Geochem Geophys Geosyst 14(5): 1493-1522, doi:10.1002/ggge.20100

Graf T, Therrien R (2008) A method to discretize non-planar fractures for 3D subsurface flow and transport simulations. Int J Num Methods Fluid 56 (11): 2069-2090

Grube A, Wichman K, Hahn J, Nachtigall K (2000) Geogene Grundwasserversalzung in den Porengrundwasserleitern Norddeutschlands und ihre Bedeutung für die Wasserwirtschaft. Technologiezentrum Wasser Karlsruhe (TZW), Karlsruhe, pp. 1–203

Gudmundsson A (2011) Rock fractures in geological processes. New York, Cambridge University Press, pp. 1-592

Gudmundsson A, Fjeldskaar I, Brenner SL (2002) Propagation pathways and fluid transport in jointed and layered rocks in geothermal fields. J Volcanol Geotherm Res 116: 257–278

Haneberg WC (1995) Steady state groundwater flow across idealized faults. Water Resour Res 31 (7): 1815-1820

Harcouët-Menou V, Guillou-Frottier L, Bonneville A, Adler PM, Mourzenko V (2009) Hydrothermal convection in and around mineralized fault zones: insights from two- and three-dimensional numerical modeling applied to the Ashanti belt, Ghana. Geofluids 9: 116-137

Hebig KH, Ito N, Scheytt T, Marui A (2012) Review: Deep groundwater research with focus on Germany. Hydrogeol J 20: 227-243. doi:210.1007/s10040-10011-10815-10041

Herbert AW (1996) Modelling approaches for discrete fracture network flow analysis. Developments Geotech Engineering 79: 213-229

Holl H-G, Moeck I, Schandelmeier H (2005) Characterisation of the tectono-sedimentary evolution of a geothermal reservoir - implications of exploitation (Southern Permian Basin, NE Germany). Proceedings World Geothermal Congress 2005, Antalya, Turkey, pp. 5

Hoth K, Rusbült J, Zagora K, Beer H, Hartmann O (1993) Die tiefen Bohrungen im Zentralabschnitt der Mitteleuropäischen Senke - Dokumentation für den Zeitabschnitt 1962 - 1990. Schriftenreihe f Geowiss 2, Gesell f Geowiss, Berlin, pp. 1-145

Hudec MR, Jackson MPA (2007) Terra firma: Understanding salt tectonics. Earth-Sci Rev 82: 1-28

Huenges E, Poser M, Schrötter J (2001) Formationsdruck in der Bohrung Groß Schönebeck – Ableitung aus Pegelmonitoring nach Abschluss des Primärtestes. STR02/14, Geothermie Report 02-1, pp. 1-190

Huenges E, Hurter S, Saadat A, Köhler S, Trautwein U (2002) The in-situ geothermal laboratory Groß Schönebeck – learning to use low permeability aquifers for geothermal power. PROCEEDINGS, Twenty-Seventh Workshop on Geothermal Reservoir Engineering Stanford University, Stanford, California, January 28-30, 2002

Huenges E, Trautwein U, Legarth B, Zimmermann G (2006) Fluid Pressure Variation in a Sedimentary Geothermal Reservoir in the North German Basin: Case Study Groß Schönebeck. Pure Appl Geophys 163: 2141-2152

Huenges E, Ed (2011) Geothermal Energy Systems: Exploration, Development, and Utilization. WILEY-VCH Verlag, pp. 1-463

Hurter S, Haenel R (2002) Atlas of Geothermal Resources in Europe. EC Publication Nr. EUR17811, Luxemburg, pp. 1-93

Hurtig E, Čermak V, Haenel R, Zui V (1992) Geothermal Atlas of Europe. H Haack Verlagsgesellschaft, Gotha, pp. 1-156

Ingebritsen SE, Sanford WE (1998) Groundwater in Geologic Processes. Cambridge University Press, UK

Ito T, Zoback MD (2000) Fracture permeability and in situ stress to 7 km depth in the KTB scientific drillhole. Geophys Res Lett 27: 1045–1048

Kaiser BO, Cacace M, Scheck-Wenderoth M, Lewerenz B (2011) Characterization of main heat transport processes in the Northeast German Basin: Constraints from 3D numerical models. Geochem Geophys Geosyst 12: Q07011. doi:07010.01029/02011GC003535

Kaiser BO, Cacace M, Scheck-Wenderoth M (2013a) 3D coupled fluid and heat transport simulations of the Northeast German Basin and their sensitivity to the spatial discretization: Different sensitivities for different mechanisms of heat transport. Environ Earth Sci. doi:10.1007/s12665-013-2249-7

Kaiser BO, Cacace M, Scheck-Wenderoth M (2013b) Quaternary channels within the Northeast German Basin and their relevance on Double Diffusive Convective transport processes: Constraints from 3D thermohaline numerical simulations. Geochem Geophys Geosyst. doi:10.1002/ggge.20192

Kalbacher T, Mettier R, McDermott C, Wang W, Kosakowski G, Taniguchi T, Kolditz O, (2007) Geometric modelling and object-oriented software concepts applied to a heterogeneous fractured network from the Grimsel rock laboratory. Comput Geosci 11: 9-26

Katzung G (ed) after Kaiser et al (1984) Geothermie-Atlas der Deutschen Demokratischen Republik, Zentrales Geologisches Institut (ZGI)

Knipe RJ (1993) The influence of fault zone processes and diagenesis on fluid flow. In Horbury AD, Robinson AG (eds) Diagenesis and Basin Development. AAPG Sudies in Geology 36: 135-148

Kolditz O (1995) Modelling flow and heat transfer in fractured rocks: dimensional effect of matrix diffusion. Geothermics 24 (3): 421-437

Kolditz O, Diersch H-J (1993) Quasi-steady-state strategy for numerical simulation of geothermal circulation in hot dry rock fractures. Int J Non-Linear Mech 28 (4): 467-481

Kolditz O, Bauer S, Bilke L, Böttcher N, Delfs JO, Fischer T, Görke UJ, Kalbacher T, Kosakowski G, McDermott CI, Park CH, Radu F, Rink K, Shao H, Shao HB, Sun F, Sun YY, Singh AK, Taron J, Walther M, Wang W, Watanabe N, Wu Y, Xie M, Xu W, Zehner B (2012a) OpenGeoSys: an open-source initiative for numerical simulation of thermo-hydro-mechanical/chemical (THM/C) processes in porous media. Environ Earth Sci 67: 589-599. doi: 10.1007/s12665-012-1546-x

Kolditz O, Shao H, Görke U-J, Wang W (eds) (2012b) Thermo-hydro-mechanical-chemical processes in fractured porous media. Lecture Notes in Computational Science and Engineering, Vol 86, Springer, Heidelberg. doi: 10.1007/978-3-642-27177-9

Kühn M, Dobert F, Gessner K (2006) Numerical investigation of the effect of heterogeneous permeability distributions on free convection in the hydrothermal system at Mount Isa, Australia. Earth Planet Sci Lett 244: 655-671

Kühn M, Liebscher A, Martens S, Möller F, Kempka T, Streibel M (2012) Sicherer Betrieb geologischer CO_2-Speicher am Beispiel des Pilotstandortes Ketzin. In Kuckshinrichs W, Hake J-F (eds) CO_2-Abscheidung, -Speicherung und -Nutzung: Wirtschaftliche, umweltseitige und gesellschaftliche Perspektive. Schriften des Forschungszentrums Jülich, Reihe Energie & Umwelt, Advances in Systems Analysis 2: 131 - 148

Landesamt für Umwelt, Natur und Geologie Mecklenburg-Vorpommern (2002) Lage der Quartärbasis, basierend auf der Übersichtskarte 1:500.000 - Präquartär und Quartärbasis, Güstrow

Landesamt für Geologie und Bergwesen Sachsen-Anhalt (2009) Landesbohrdatenbank
URL http://www.sachsen-anhalt.de/LPSA/index.php?id=bohrdatenbank

Lampe C, Person M (2002) Advective cooling within sedimentary rift basins - application to the Upper Rhinegraben (Germany). Mar Petrol Geol 19: 361-375

Liebscher A, Martens S, Möller F, Lüth S, Schmidt-Hattenberger C, Kempka Th, Szizybalski A, Kühn M (2012) Überwachung und Modellierung der geologischen CO_2-Speicherung - Erfahrungen vom Pilotstandort Ketzin, Brandenburg (Deutschland). Geotechnik 35(3): 177-186. doi: 10.1002/gete.201200005

Littke R, Scheck-Wenderoth M, Brix MR, Nelskamp S (2008) Subsidence, inversion and evolution of the thermal field. In Littke R, Gajewski U, Bayer U, Nelskamp S (eds) Dynamics

of Complex Intracontinental Basins: The Central European Basin System. Springer Verlag, Berlin Heidelberg, pp. 125-153

López DL, Smith L (1995) Fluid flow in fault zones: Analysis of the interplay of convective circulation and topographically driven groundwater flow. Water Resour Res 31 (6): 1489 - 1503

López DL, Smith L (1996) Fluid flow in fault zones: Influence of hydraulic anisotropy and heterogeneity on the fluid flow and heat transfer regime. Water Resour Res 32 (10): 3227-3235

Løtveit IF (2009) Analytical and numerical studies of fluid reservoirs and fracture development in heterogeneous rocks. Dissertation, University of Bergen, pp.1-183

Luijendijk E (2012) The role of fluid flow in the thermal history of sedimentary basins: Inferences from thermochronology and numerical modeling in the Roer Valley Graben, southern Netherlands. PhD thesis, VU University Amsterdam, pp. 1-198

Magri F (2004) Derivation of the coefficients of thermal expansion and compressibility for use in FEFLOW. WASY White papers 3: 13-23

Magri F (2005) Mechanismus und Fluiddynamik der Salzwasserzirkulation im Norddeutschen Becken: Ergebnisse thermohaliner numerischer Simulationen (Dissertation Thesis, Freie Universität Berlin). Scientific Technical Report STR05/12, GeoForschungsZentrum Potsdam, pp. 1-131

Magri F, Bayer U, Tesmer M, Möller P, Pekdeger A (2008) Salinization problems in the NEGB: results from thermohaline simulations. Int J Earth Sci (Geol Rundsch) 97: 1075-1085

Magri F, Bayer U, Pekdeger A, Otto R, Thomsen C, Maiwald U (2009) Salty groundwater flow in the shallow and deep aquifer systems of the Schleswig-Holstein area (North German Basin). Tectonophysics 470: 183-194

Magri F, Akar T, Gemici U, Pekdeker A (2010) Deep geothermal groundwater flow in the Seferihisar-Balçova area, Turkey: results from transient numerical simulations of coupled fluid flow and heat transport processes. Geofluids 10: 388-405

Marotta AM, Bayer U, Thybo H, Scheck M (2002) Origin of the regional stress in the North German basin: results from numerical modeling. Tectonophysics 360: 245-264

Maystrenko Y, Bayer U, Scheck-Wenderoth M (2010) Structure and Evolution of the Central European Basin System according to 3D modeling. DGMK Research Report 577-2/2-1

McCann T (1996) Pre-Permian of the north-east German Basin. Geol J 31:159-177

McCann T (1998) Lower Palaeozoic evolution of the NE German Basin/Baltica borderland. Geol Mag 135: 129-142

McDermott CI, Randriamanjatosoa ARL, Tenzer H, Kolditz O (2006) Simulation of heat extraction from crystalline rocks: The influence of coupled processes on differential reservoir cooling. Geothermics 35: 321-344

McKenna JR, Blackwell DD (2004) Numerical modeling of transient Basin and Range extensional geothermal systems. Geothermics 33: 457-476

Moeck I, Holl H-G, Schandelmeier H (2005) 3D Lithofacies Model Building of the Rotliegend Sediments of the NE German Basin. AAPG International Conference & Exhibition (Paris France 2005), CD-ROM, paper #98619

Moeck I, Schandelmeier H, Holl H-G (2009) The stress regime in a Rotliegend reservoir of the Northeast German Basin. Int J Earth Sci (Geol Rundsch) 98: 1643-1654

Müller C, Siegesmund S, Blum P (2010) Evaluation of the representative elementary volume (REV) of a fractured geothermal sandstone reservoir. Environ Earth Sci 61: 1713-1724

Mulch A, Teyssier C, Cosca MA, Chamberlain CP (2007) Stable isotope paleoaltimetry of Eocene core complexes in the North American Cordillera. Tectonics 26 (TC4001). doi:10.1029/2006TC001995

National Research Council (US) Committee on Fracture Characterization and Fluid Flow. (1996) Rock fractures and fluid flow: contemporary understanding and applications. National Academies Press

Nativ R, Adar E M, Becker A (1999) Designing a Monitoring Network for Contaminated Ground Water in Fratcured Chalk. Ground Water 37(1): 38-47

Nield D A, Bejan A (eds) (2006) Convection in porous media. Springer, New York, pp. 1-640

Noack V, Cherubini Y, Scheck-Wenderoth M, Lewerenz B, Höding T, Simon A, Moeck I (2010) Assessment of the present-day thermal field (NE German Basin) - Inferences from 3D modelling. Chem Erde 70 (S3): 47-62

Noack V, Scheck-Wenderoth M, Cacace M (2012) Sensitivity of 3D thermal models to the choice of boundary conditions and thermal properties – a case study for the area of Brandenburg (NE German Basin). Environ Earth Sci 67: 1695-1711

Noack V, Scheck-Wenderoth M, Cacace M, Schneider M (2013) Influence of moving fluids on the regional thermal field: results from 3D numerical modelling for the area of Brandenburg (North German Basin). Environ Earth Sci. doi:10.1007/s12665-013-2438-4

Norden B, Förster A (2006) Thermal conductivity and radiogenic heat production of sedimentary and magmatic rocks in the Northeast German Basin. AAPG Bulletin 90 (6): 939-962

Norden B, Förster A, Balling N (2008) Heat flow and lithospheric thermal regime in the Northeast German Basin. Tectonophysics 460: 215-229

Ollinger D, Baujard C, Kohl T, Moeck I (2010) Distribution of thermal conductivities in the Groß Schönebeck (Germany) test site based on 3D inversion of deep well data. Geothermics 39: 46-58

Ondrak R, Wenderoth F, Scheck M, Bayer U (1998) Integrated geothermal modeling on different scales in the Northeast German Basin. Geolog Rundsch 87: 32-42

Person M, Raffensperger JP, Ge S, Garven G (1996) Basin-scale hydrogeologic modeling. Rev Geophys 34(1): 61-87

Pili É, Poitrasson F, Gratier J-P (2002) Carbon–oxygen isotope and trace element constraints on how fluids percolate faulted limestones from the San Andreas Fault system: partitioning of fluid sources and pathways. Chem Geol 190: 231-250

Pommer H (2012) The control of faults on the thermal field in Northern Germany—Constraints from 2D coupled numerical simulations. Department of Earth Sciences, Freie Universität Berlin, pp. 1-69

Press F, Siever R (1995) Allgemeine Geologie. Spektrum Akademischer Verlag, Heidelberg

Pryor RW (2011) Multiphysics Modeling Using COMSOL®: A First Principles Approach. Jones and Bartlett Publishers, LLC

Przybycin A (2011) Sensitivity study on mesh dependence for 3D coupled fluid- and heat-trasnport-simulations - an example from the North East German Basin. Department of Earth Sciences, Freie Universität Berlin, pp. 1-83

Rawling GC, Goodwin LB, Wilson JL (2001) Internal significance of contrasting fault-zone types. Geol 29: 43-46

Reinicke A, Zimmermann G, Huenges E, Burkhardt H (2005) Estimation of hydraulic parameters after stimulation experiments in the geothermal reservoir Groß Schönebeck 3/90 (Norh-German Basin). Int J Rock Mech Min Sci 42: 1082-1087

Reyer D, Bauer JF, Philipp SL (2012) Fracture systems in normal fault zones crosscutting sedimentary rocks, Northwest German Basin. J Struct Geol 45: 38-51

Röckel T, Lempp C (2003) Spannungszustand im Norddeutschen Becken. Erdöl Erdgas Kohle 119(2): 73-80

Roth F, Fleckenstein P (2001) Stress orientations found in the NE Germany differ from the West-European trend. Terra Nova 13: 289-296

Scheck M (1997) Dreidimensionale Struckturmodellierung des Nordostdeutschen Beckens unter Einbeziehung von Krustenmodellen (Dissertation Thesis, Freie Universität Berlin). Scientific Technical Report STR97/10, GeoForschungsZentrum Potsdam, pp. 1-126

Scheck M, Bayer U (1999) Evolution of the Northeast German Basin - inferences from a 3D structural model and subsidence analysis. Tectonophysics 313: 145-169

Scheck M, Bayer U, Otto V, Lamarche J, Banka D, Pharaoh T (2002) The Elbe Fault System in North Central Europe—a basement controlled zone of crustal weakness. Tectonophysics 360: 281-299

Scheck M, Bayer U, Lewerenz B (2003a) Salt movements in the Northeast German Basin and its relation to major post-Permian tectonic phases - results from 3D structural modelling, backstripping and reflection seismic data. Tectonophysics 361: 277-299

Scheck M, Bayer U, Lewerenz B (2003b) Salt redistribution during extension and inversion inferred from 3D backstripping. Tectonophysics 373(1-4): 55-73

Scheck-Wenderoth M, Lamarche J (2005) Crustal memory and basin evolution in the Central European Basin System - new insights from a 3D structural model. Tectonophysics 397: 132-165

Scheck-Wenderoth M, Krzywiec P, Zühlke R, Maystrenko Y, Froitzheim N (2008a) Permian to Cretaceous tectonics. In: McCann T (ed) - The geology of Central Europe, London, Geological society of London, 2, Mesozoic and Cenozoic, pp. 999-1030

Scheck-Wenderoth M, Maystrenko Y, Hübscher C, Hansen M, Mazur S (2008b) Dynamics of salt basins. In Littke R, Gajewski U, Bayer U, Nelskamp S (eds) Dynamics of Complex Intracontinental Basins: The Central European Basin System. Springer Verlag, Berlin Heidelberg, pp. 307-322

Schellschmidt R, Hägedorn F, Fesche H-W (1999) Das Temperaturfeld in Norddeutschland - neue Messungen, neue Karten, neue Interpretationen. Bericht Archiv-Nr 119 563, Institut für Geowissenschaftliche Gemeinschaftsaufgaben, Hannover

Schellschmidt R, Clauser C, Sanner B (2000) Geothermal energy use in Germany at the turn of the millennium. Proceedings World Geothermal Congress 2000, Kyushu - Tohoku, Japan, pp. 427-432

Schilling O, Sheldon HA, Reid LB, Corbel S (2013) Hydrothermal models of the Perth metropolitan area, Western Australia: implications for geothermal energy. Hydrogeol J, doi: 10.1007/s10040-10012-10945-10040

Schirrmeister W (1996) Aus der Literatur überlieferte Angaben über natürliche Salzwasseraustritte an der Grundwasseroberfläche/Geländeoberfläche in Brandenburg. Brandenburgische Geowissenschaftliche Beiträge 3:94–96

Schneider J, Gebhardt U (1993) Litho- und Biofaziesmuster in intra- und extramontanen Senken des Rotliegend (Perm Nord- und Ostdeutschland). Geol Jb A131: 57-98

Schwab G (1985) Paläomobilität der Norddeutsch-Polnischen Senke, Akademie der Wissenschaften der DDR, Dissertation, Berlin, pp. 1-196

Seibt P, Kellner T (2003) Pratical experience in the reinjection of cooled thermal waters back into sandstone reservoirs. Geothermics 32:733-741

Si H (2008) Three dimensional boundary conforming Delauney mesh generation. Dissertation, Technische Universität, Berlin

Sibson R H (1990) Conditions for fault-valve behaviour. In Knipe RJ and Rutter EH (eds) Deformation Mechanisms, Rheology and Tectonics. Geological Society Special Publication 54: 15-28

Simmons CT, Fenstemaker TR, Sharp Jr. JM (2001) Variable-density groundwater flow and solute transport in heterogeneous porous media: approaches, resolutions and future challenges. J Contam Hydrol 52: 245-275

Simms MA, Garven G (2004) Thermal convection in faulted extensional sedimentary basins: theoretical results from finite element modeling. Geofluids 4: 109–130

Siniscalchi A, Tripaldi S, Neri M, Giammanco S, Piscitelli S, Balsaco M, Behncke B, Magrì C, Naudet V, Rizzo E (2010) Insights into fluid circulation across the Pernicana Fault (Mt. Etna, Italy) and implications for flank instability. J Volcanol Geotherm Res 193: 137-142

Sippel J, Fuchs S, Cacace M, Kastner O, Huenges E, Scheck-Wenderoth M (2013) Deep 3D thermal modelling for the city of Berlin (Germany). Environ Earth Sci. doi:10.1007/s12665-013-2679-2

Smith L, Forster CB, Evans JP (1990) Interaction between fault zones, fluid flow and heat transfer at the basin scale, in: Hydrogeology of low Permeability environments: International Association of Hydrological Sciences selected papers in Hydrogeology, v. 2: 41-67

Stackebrandt W, Ludwig AO, Ataficzuk S (2001) Base of Quaternary deposits of the Baltic Sea depression and adjacent areas (map 2). Brandenburgische geowiss Beitr 8(1): 13-19

Stackebrandt W, Manhenke V (eds) (2002) Atlas zur Geologie von Brandenburg im Maßstab 1:1 000 000. Landesamt für Geowissenschaften und Rohstoffe, Kleinmachnow

Stackebrandt W (2009) Subglacial channels of Northern Germany - a brief review. Zeitschrift der Deutschen Gesellschaft für Geowissenschaften 160 (Heft 3): 203-210

Thompson ME, Brown SR (1991) The effect of anisotropic surface roughness on flow and transport in fractures. J Geophys Res 96 (B13): 21923-21932

Tóth J (1962) A theory of groundwater motion in small drainage basins in central Alberta, Canada. J Geophys Res 67(11): 4375-4387

Turcotte D L, Schubert G (2002) Geodynamics. Cambridge University Press, New York

Verhoogen J (1980) Energetics of the Earth. National Academy of Sciences, Washington, D.C.

Wang W, Rutqvist J, Görke U-J, Birkholzer JT, Kolditz O (2011) Non-isothermal flow in low permeable porous media: A comparison of unsaturated and two-phase flow approaches. Environ Earth Sci 62(6): 1197-1207

Watanabe N, Wang W, McDermott CI, Taniguchi T, Kolditz O, (2010) Uncertainty analysis of thermo-hydro-mechanical coupled processes in heterogeneous porous media. Comput Mech 45 (4): 263-280

Wisian KW, Blackwell DD (2004) Numerical modeling of Basin and Range geothermal systems. Geothermics 33: 713-741

World Stress Map, http://www-wsm.physik.uni-karlsruhe.de/, 2000

Yang J, Large R, Bull S (2004a) Factors controlling free thermal convection in faults in sedimentary basins: implications for the formation of zinc–lead mineral deposits. Geofluids 4: 1–11

Yang J, Bull S, Large R (2004b) Numerical investigation of salinity in controlling ore-forming fluid transport in sedimentary basins: example of the HYC deposit, Northern Australia. Miner Deposita 39: 622–631

Yang J (2006) Full 3D numerical simulation of hydrothermal field flow in faulted sedimentary basins: Example of the McArthur Basin, Northern Australia. J Geochem Explor 89: 440-444

Zhang X, Sanderson DJ, Barker AJ (2002) Numerical study of fluid flow of deforming fractured rocks using dual porosity permeability model. Geophys J Int 151(2): 452–468

Zhang X, Koutsabeloulis N, Heffer K (2007) Hydromechanical modeling of critically stressed and faulted reservoirs. AAPG Bull 91(1): 31–50

Ziegler P A (1990) Geological Atlas of Western and Central Europe. Shell Internationale Petroleum Maatschappij B V, New York, pp. 1-239

Zimmermann G, Reinicke A, Blöcher G, Milsch H, Gehrke D, Holl H-G, Moeck I, Brandt W, Saadat A, Huenges E (2007) Well path design and stimulation treatments at the geothermal research well GtGrSk4/05 in Groß Schönebeck. PROCEEDINGS, Thirty-Second Workshop on Geothermal Reservoir Engineering. Stanford University, Stanford, California, January 22-24, 2007, SGP-TR-183, pp. 1-6

Zimmermann G, Moeck I, Blöcher G (2010) Cyclic waterfrac stimulation to develop an enhances geothermal system (EGS)-Conceptual design and experimental results. Geothermics 39 (1): 59-69

Zimmermann G, Blöcher G, Reinicke A, Brandt W (2011) Rock specific hydraulic fracturing and matrix acidizing to enhance a geothermal system - Concepts and field results. Tectonophysics 503 (1-2): 146-154

Appendix A: Governing equations

The system of equations with variable fluid density (ρ^f) and viscosity (μ^f) is given by the mass conservation of the fluid:

$$\frac{\partial(\varepsilon\rho^f)}{\partial t} + \nabla \cdot (\rho^f \mathbf{q}^f) = \varepsilon Q_\rho \quad (1)$$

with

ε = porosity [-]

ρ^f = mass density of the fluid [$kg\ m^{-3}$]

$\mathbf{q}^f$ = specific discharge (Darcy's velocity) [m^{-s}]

Q_ρ = the sink/source mass term [$kg\ m^{-3}s^{-1}$]

and by the generalized Darcy's law:

$$\mathbf{q}^f = -\mathbf{K}\left(\nabla h + \frac{\rho^f - \rho_0^f}{\rho_0^f}\frac{\mathbf{g}}{|g|}\right) \quad (2)$$

where $\mathbf{K}$ is the hydraulic conductivity tensor of the porous media given by $\mathbf{K} = \frac{\rho_0^f g}{\mu^f}\mathbf{k}$, with $\mathbf{k}$ being the permeability tensor, and g, the gravity acceleration.

Equation 2 is written in terms of hydraulic head rather than pressure as primary variable to conform to the mathematical formulation used in FEFLOW®. Assuming thermal equilibrium between the porous medium and the fluid (i.e. Tf=T=Ts) and if density gradients are neglected, applying the law of energy conservation the following heat transfer equation results:

$$(\rho c)_{fs}\frac{\partial T}{\partial t} + \rho^f c^f \nabla \cdot (\mathbf{q}^f \mathrm{T}) - \nabla \cdot (\boldsymbol{\lambda} \nabla \mathrm{T}) = Q_\mathrm{T} \quad (3)$$

with $(\rho c)_{fs}$ being the bulk specific heat capacity of the fluid (*f*) plus solid (*s*) phase system, defined as

$$(\rho c)_{fs} = \left[\varepsilon\rho^f c^f + (1-\varepsilon)\rho^s c^s\right] \quad (4)$$

Q_T is a heat source-sink function. $\boldsymbol{\lambda}$ is the equivalent thermal conductivity tensor of the fluid and the porous medium. It takes both conductive (Fourier`s) and thermodispersive (mixing) effects into account. Accordingly, the equivalent thermal conductivity may be subdivided into its two components as:

$$\lambda = \lambda_{\mathrm{DISP}} + \lambda_{\mathrm{COND}} \quad (5)$$

where the first term on the right hand side of Equation (5) is the thermodispersive term

$$\lambda_{\mathrm{DISP}} = \rho^f c^f \left[\alpha_T \sqrt{\left(q_i^f q_i^f\right)}\, \mathbf{I} + (\alpha_L - \alpha_T)\frac{q_i^f q_i^f}{\sqrt{(q_i^f q_i^f)}}\right] \quad (6)$$

and the second term is the conductive one:

$$\lambda_{\mathrm{COND}} = \varepsilon\lambda^f + (1-\varepsilon)\lambda^s \quad (7)$$

In Equation (6), α_L and α_T are respectively the longitudinal and transversal dispersion lengths, while λ^f and λ^s appearing in Equation (7) represent the thermal conductivity of the fluid and solid phase, and $\mathbf{I}$ is the unit matrix.

The set of these balance equations are coupled by proper equations of state establishing the dependence of the fluid density and viscosity on the set of primary variables.

In FEFLOW® the fluid density is expressed as a linear polynomial function of temperature and pressure as:

$$\rho^f = \rho_0^f \left[1 - \bar{\beta}\left(T - T_0\right) + \bar{\gamma}\left(h - h_0\right)\right] \tag{8}$$

where $\bar{\beta} = \frac{1}{\rho^f}\frac{\partial \rho^f}{\partial T}\Big|_p$ is the thermal expansion coefficient at constant pressure condition, and $\bar{\gamma} = \frac{1}{\rho^f}\frac{\partial \rho^f}{\partial h}\Big|T$ is the coefficient of fluid compressibility at constant temperature condition.

Taking into account both coefficients $\bar{\beta}$ and $\bar{\gamma}$ constant may become inappropriate for geothermal applications where a larger temperature range has to be considered. To improve the relationship (Eq. 8) a 6th order polynomial $\rho = \rho(T)$ was introduced into FEFLOW® defining β as a nonlinear variable thermal expansion $\beta = \beta(T)$ (Diersch, 2002) valid for temperatures from 0 to 100 °C.

Considering wider ranges of pressure and temperatures require variable thermal fluid expansion $\bar{\beta}$ and fluid compressibility $\bar{\gamma}$ within the state of equation of density (8). In order to reproduce the fluid density for this wider range both coefficients has been approximated for $\rho_{sat} < \rho \leq 100$ MPa and for temperature $0 \leq T \leq 350$ °C by Magri (2004), for fractures and faults by Blöcher et al. (2010b).

The dependence of the fluid dynamic viscosity on the temperature as implemented in FEFLOW® follows the empirical polynomial expression (Diersch, 2002):

$$\mu^f = \frac{1 + 0.7063\varsigma - 0.04832\varsigma^3}{\mu_0} \tag{9}$$

with $\varsigma = \frac{(T - 150)}{100}$, and μ_0 the reference viscosity obtained from Eq. 6 when $T = T_0 = 150$°C.

Within the two-dimensional fault domain the fluid equation takes the form:

$$b_m S_s \frac{\partial P}{\partial t} + \nabla \cdot \left(b_h \mathbf{q}_f \right) = Q_f \tag{10}$$

with S_s specific storage of the fault (assumed to be fully fluid saturated), and $b = b_m + b_h$ the effective (average) width of the fault comprising both hydraulic (b_h) and mechanical effects (b_m). P is the fluid pressure, $\mathbf{q}_f$ the fluid (Darcy) flux, and Q_f is the fluid mass source/sink term.

As in the porous medium case, Darcy's law is assumed to describe groundwater flow within the fault under the widely adopted theoretical assumption of parallel fracture walls, thus resulting in:

$$\mathbf{q}_f = -\frac{\mathbf{k}}{\mu_f} \left(\nabla P - \rho_f \mathbf{g} \nabla z \right) \tag{11}$$

Where μ_f is the fluid dynamic viscosity, $\mathbf{g} = (0,0-g)$ is the gravity vector, z the reference depth, and and $\mathbf{k} = \frac{b_h^2}{12}\mathbf{I}$ the permeability tensor with I the unit tensor assuming isotropic permeability along the fault plane. Following Darcy`s law, the study only deals with laminar flow within the fault.

The heat transport (advection plus diffusion) equation for the matrix is given by:

$$(\rho c)_{eff} \frac{\partial T}{\partial t} + \nabla \cdot \mathbf{q}_T = Q_T ; \quad \mathbf{q}_T = \phi (c\rho)_f \mathbf{v} T - \lambda_{eff} \nabla T \tag{12}$$

with $(\rho c)_{eff} = \varphi (\rho c)_f + (1-\varphi)(\rho c)_s$ being the specific heat capacity of the system involving a fluid $(\rho c)_f$ and a solid $(\rho c)_s$ phase.

The heat transport equation for the fracture is given by:

$$b_m (c\rho)_f \frac{\partial T}{\partial t} + \nabla \cdot \mathbf{q}_T = Q_T ; \quad \mathbf{q}_T = b_h (c\rho)_f \mathbf{v} T - b_m \lambda_f \nabla T \tag{13}$$

In both of the above equations $(\rho c)_{eff} = \phi (c\rho)_f + (1-\phi)(c\rho)_s$ is the heat storage term of the porous medium with φ porosity, c_f specific heat capacity of the fluid, ρ_f fluid density, c_s rock specific heat capacity, and ρ_s rock density. T is the temperature, $\mathbf{q}_T$ is the heat flux taking into

account both advective $\varphi(c\rho)_f \mathbf{v}T$ in Eq. 12 and $b_h(c\rho)_f \mathbf{v}T$ in Eq. 13 with $\mathbf{v} = \frac{\mathbf{q}_f}{\varphi}$ being the fluid velocity) and dispersive terms ($\lambda_{eff}\nabla T$ in Eq. 12 and $b_m\lambda_f \nabla T$ with $\lambda_{eff} = \varphi\lambda_f + (1-\varphi)\lambda_s$ being the heat conductivity of the porous medium). Q_f is the heat source/sink term. In Eq. 13 no mechanical effects on the fracture width are taken into account.

The two sets of equations (fluid flow and heat transport) for the fault and porous medium domain are coupled by means of the Darcy velocity ($\mathbf{v} = \frac{\mathbf{q}_f}{\varphi}$).

Appendix B: Assessment of the present-day thermal field (NE German Basin) – inferences from 3D modelling

Abstract

We use a refined 3D structural model based on an updated set of observations to assess the thermal field of Brandenburg. The crustal-scale model covers an area of about 250 km (E-W) times 210 km (N-S) located in the Northeast German Basin (NEGB). It integrates an improved representation of the salt structures and is used for detailed calculations of the 3D conductive thermal field with the finite element method (FEM).

A thick layer of mobilised salt (Zechstein, Upper Permian) controls the structural setting of the area. As salt has a considerably higher thermal conductivity than other sediments, it strongly influences heat transport and accordingly temperature distribution in the subsurface.

The modelled temperature distribution with depth shows strong lateral variations. The lowest temperatures at each modelled depth level occur in the area of the southern basin margin, where a highly conductive crystalline crust comes close to the surface. In general, the highest temperatures are predicted in the north-western part of the model close to the basin centre, where rim syncline deposits around the salt domes cause insulating effects. The pattern of temperature distribution changes with depth. Closely beneath the salt, the temperature distribution shows a complementary pattern to the salt cover as cold spots reflect the cooling effect of highly conductive salt structures. The predicted temperatures at depths beneath 8 km suggest that the influence of the salt is not evident any more. Similar to the temperature distribution, the calculated surface heat flow shows strong lateral variations. Also with depth the variations in thermal properties due to lithology-dependent lateral heterogeneities provoke changing pattern of the heat flow.

A comparison with published heat flow and temperature data shows that the model predictions are largely consistent with observations and indicates that conductive heat transport is the dominant mechanism of heat transfer. Local deviations between modelled and observed temperatures are in the range of ± 10° K and may be due to the convective heat transport.

To assess the potential influence of convective heat transport we zoom in on a specific location of Brandenburg corresponding to the in situ geothermal laboratory *Groß Schönebeck*. This local model is used to carry out 3D numerical simulations of coupled fluid flow and heat transfer processes. Our coupled models indicate that conduction is the dominant heat transfer mechanism below Middle Triassic strata. Above the Triassic Muschelkalk, the more than 3000

m of sediments with higher hydraulic conductivity promote the formation of convection cells. Here, especially high degrees of coupling result in remarkable convective heat transport.

Published as:
Noack V, Cherubini Y, Scheck-Wenderoth M, Lewerenz B, Höding T, Simon A, Moeck I (2010) Assessment of the present-day thermal field (NE German Basin) - Inferences from 3D modelling. Chemie der Erde 70 (S3): 47-62

B.1 Introduction

Being able to predict temperature distribution with depth in more detail is particularly relevant in the view of global climate change which requires exploration of geothermal energy as a timely strategy.

As direct temperature information with depth can be obtained only by expensive drilling, which, in turn, provides only local information, methods to predict the temperature at different depths are needed. Numerical models considering both the structural setting of the subsurface as well as the physical processes controlling heat transfer are an option to assess and predict lateral and vertical variations of temperature distribution. Here we present new results from numerical modelling of the thermal field in the subsurface of Brandenburg, a federal state in north-eastern Germany. The modelled area comprises the southern part of the Northeast German Basin (NEGB, Scheck and Bayer, 1999) a sub-basin of the Central European Basin System (CEBS), extending from the Southern North Sea to Poland (Littke et al. 2008).

In the north, the study area encompasses a part of the basin centre of the NEGB whereas to the south, the present-day south-eastern basin margin of the NEGB is enclosed. There, the Permian to Cenozoic basin fill has been uplifted and partially eroded along the Elbe-Fault-System (Fig. B.1). The Permian to Cenozoic basin fill of the NEGB is up to 8000 m thick and consists of Rotliegend clastics (Permian), a thick layer of strongly mobilised Zechstein salt (Permian) overlain by Mesozoic and Cenozoic sediments (Schwab, 1985; Bayer et al. 1997; Scheck, 1997). These overburden deposits are morphologically influenced by numerous salt structures which have developed since Early Triassic times in response to changing regional stress fields and differential loading (Scheck-Wenderoth et al. 2008b).

Published temperature maps of Europe for different depths and maps of the surface heat flow density (Hurtig et al. 1992, Schellschmidt et al. 1999, Hurter and Haenel, 2002) provided large-scale concepts for the heat flow pattern. For the study area of Brandenburg, Beer (1996) presented temperature measurements in deep wells and introduced a tentative empirical correction for temperature logs. However, Förster (1997) pointed out that measured borehole temperature data are often recorded shortly after drilling has ceased. Thus, these data do not reflect the equilibrium temperature and the corresponding values may be biased. Using a method to reliably correct borehole temperature data, Förster (2001) as well as Norden and Förster (2006) derived a new thermal database for the NEGB including measured temperatures and radiogenic heat production values measured on drill cores but also lithology-dependent thermal properties such as thermal conductivities. This led to new values of surface heat flow (Norden et al. 2008). Also the relationship between structural setting and thermal field within

the NEGB has been addressed in the last decade based on 3D simulations using finite element methods. Models of the regional, crustal-scale 3D conductive thermal field of the NEGB have been compared with classical one-dimensional extrapolations (Bayer et al. 1997; Scheck, 1997). These works assessed the influence of different lower boundary conditions and concluded that assuming a constant heat flow between 25 mW/m² and 30 mW/m² at the level of the crust-mantle boundary (Moho) reproduces the observed heat flow trends best. Moreover, these models described the decoupling effect of the Zechstein salt between a pre-Zechstein and post-Zechstein succession in the NEGB. This decoupling effect controls both, the structural setting of the overlying layers as well as temperature distribution and fluid flow. Ondrak et al. (1998) showed that regional crustal-scale thermal models can provide reasonable boundary conditions for local high resolution models as commonly used for the assessment of geothermal production sites. In addition to processes related to conductive heat transfer, the impact of heat transport by convection has been addressed mainly with 2D models of coupled heat and fluid transport (Magri, 2005; Magri et al. 2008).

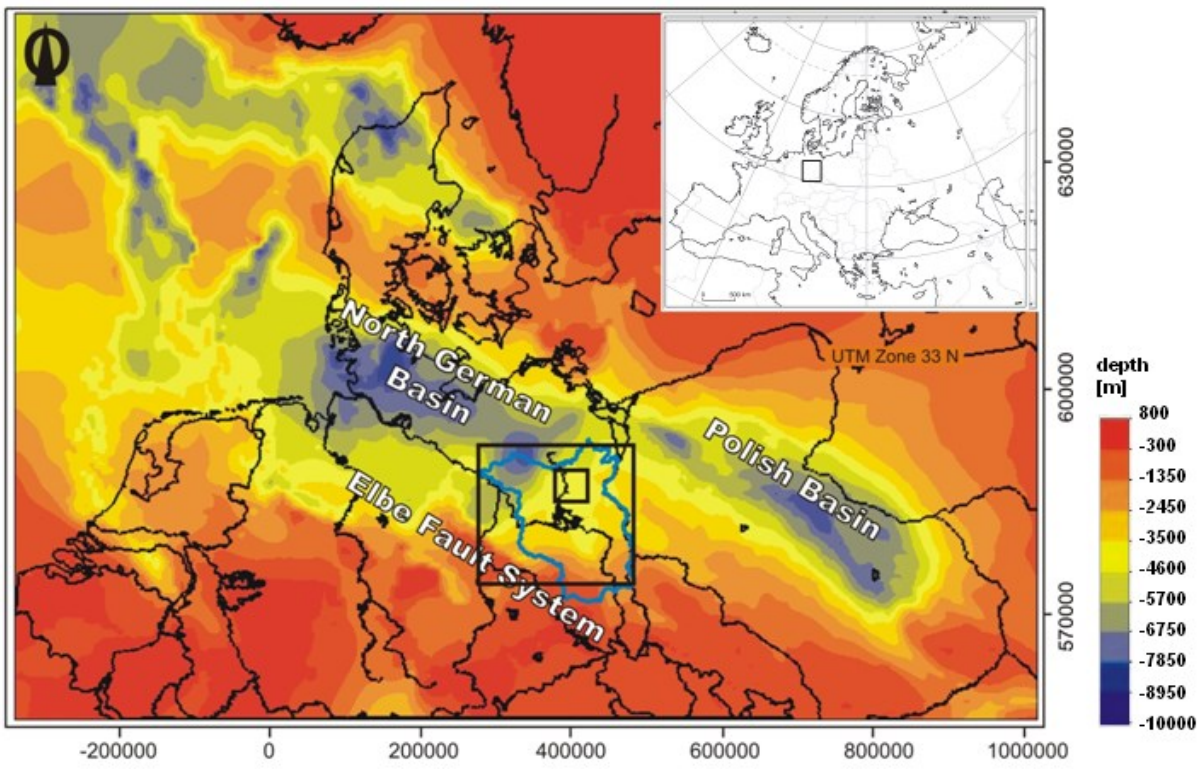

Figure B.1 Location of study area in the south-eastern part of the Central European Basin System; depth to top pre-Permian (modified after Scheck-Wenderoth and Lamarche, 2005). Large rectangle encloses the area covered by the 3D structural and thermal model of Brandenburg, small rectangle indicates the location of the model of the geothermal in situ laboratory Groß Schönebeck, blue line – border of Brandenburg.

Previous studies were based on simplified model assumptions in terms of structural resolution so that they were able to reproduce the general pattern of the thermal field of the Northeast German Basin (Bayer et al. 1997; Ondrak et al. 1998; Norden et al. 2008). To describe dominant mechanisms of heat transport (Magri et al. 2008), their significance with respect to local anomalies such as required for geothermal drilling remained limited. New data concerning both, the structural setting and thus also the spatial distribution of thermal properties, are meanwhile available for the area of Brandenburg and provide the opportunity to build a refined 3D structural model of the area as a base for more detailed temperature calculations. Accordingly, we present a new 3D structural model of the subsurface of Brandenburg characterized by an improved structural resolution compared to earlier models as it is based on a larger data base. For this model we calculate the crustal-scale 3D conductive thermal field and compare our results with available temperature data and published temperature depth maps.

Finally, we zoom in at a specific location in Brandenburg, where currently active experiments related to geothermal energy production are carried out. It corresponds to the in situ geothermal laboratory Groß Schönebeck (Fig. B.1) located 40 km north of Berlin and is one of the key sites of geothermal exploration studies in the North German Basin. The in situ laboratory is installed in a former gas exploration well and is utilized for the development of geothermal technologies necessary for electric power generation. For this geothermal site we present first attempts to model potential influences of convective heat transport in addition to conduction.

B.2 The 3D structural model of Brandenburg

B.2.1 Database

Several published datasets are available for the construction of a refined 3D structural model of Brandenburg (Tab. B.1). The primary database consists of several depth and thickness maps as well as fault maps provided by the geological survey of Brandenburg (Landesamt für Bergbau, Geologie und Rohstoffe Brandenburg - LBGR) that partially are published in the Geological Atlas of Brandenburg (Stackebrandt and Manhenke, 2002). In addition, data from former regional models were used to complement the marginal parts of the rectangular area covered by the model and to avoid boundary effects. Also for those units not differentiated further in the Geological Atlas of Brandenburg, data from previous models have been integrated. These previous models include a model of the Northeast German Basin with a horizontal resolution of 4 km (NEGB: Scheck and Bayer, 1999), an earlier model of the entire Central European Basin System with a horizontal resolution of 8 km (CEBS1: Scheck-Wenderoth and Lamarche,

2005) and a more recent model of the Central European Basin System with a horizontal resolution of 4 km (CEBS2: Maystrenko et al. 2010). These datasets have been complemented by data from published deep wells (Hoth et al. 1993) and by well data provided by the Geological Survey of Sachsen-Anhalt (Landesamt für Geologie und Bergwesen Sachsen-Anhalt - LAGB, 2009).

Table B.1 Input data for 3D structural modelling of Brandenburg: NEGB: 3D structural model of the Northeast German Basin (Scheck and Bayer, 1999); CEBS1: 3D structural model of the Central European Basin System (Scheck-Wenderoth and Lamarche, 2005); CEBS2: 3D structural model of the Central European Basin System (Maystrenko et al. 2010).

Stratigraphic Unit	Type of data	Horizontal resolution/scale	Reference
Topography	grid data	1 Arc-Minute	ETOPO1, Amante and Eakins, 2009
Quaternary	scattered data	1:1.000.000	Stackebrandt and Manhenke, 2002
	scattered data	1: 500.000	Landesamt für Umwelt, Naturschutz und Geologie Mecklenburg-Vorpommern
Tertiary	grid data	NEGB: 4 km	Scheck and Bayer, 1999
	grid data	CEBS1: 8 km	Scheck-Wenderoth & Lamarche, 2005
Upper Cretaceous	scattered data	1:1.000.000	Stackebrandt and Manhenke, 2002
	grid data	NEGB: 4 km	Scheck and Bayer, 1999
	grid data	CEBS1: 8 km	Scheck-Wenderoth & Lamarche, 2005
Lower Cretaceous	grid data	NEGB 4 km	Scheck and Bayer, 1999
Jurassic	grid data	CEBS2: 4 km	Maystrenko et al. 2010
	grid data	NEGB 4 km	Scheck and Bayer, 1999
Keuper	grid data	NEGB 4 km	Scheck and Bayer, 1999
Muschelkalk	scattered data	1:1.000.000	Stackebrandt and Manhenke, 2002
	grid data	NEGB 4 km	Scheck and Bayer, 1999
Buntsandstein	grid data	NEGB 4 km	Scheck and Bayer, 1999
Zechstein	scattered data	1:1.000.000	Stackebrandt and Manhenke, 2002
	grid data	NEGB 4 km	Scheck and Bayer, 1999
	grid data	CEBS1: 8 km	Scheck-Wenderoth & Lamarche, 2005
	grid data	CEBS2: 4 km	Maystrenko et al, 2010
Sedimentary Rotliegend	scattered data	1:1.000.000	Stackebrandt and Manhenke, 2002
	grid data	CEBS2: 4 km	Maystrenko et al. 2010
Permo-Carboniferous Volcanics	scattered data	1:1.000.000	Stackebrandt and Manhenke, 2002
	grid data	CEBS2: 4 km	Maystrenko et al. 2010

B.2.2 Model construction

The first step in modelling is the interpolation of the compiled datasets into 2D grids using a minimum tension gridding technique and considering the trace of faults as interpolation barriers (Earth Vision, Dynamic Graphics Ltd., Version 8.0). Both depth and thickness data are interpolated to obtain the following stratigraphic units composing the 3D model from top to bottom: Quaternary, Tertiary, Upper Cretaceous, Lower Cretaceous, Jurassic, Triassic Keuper,

Triassic Muschelkalk, Triassic Buntsandstein, Permian Zechstein, Permian Rotliegend and Permo-Carboniferous Volcanics (Fig. B.2a).

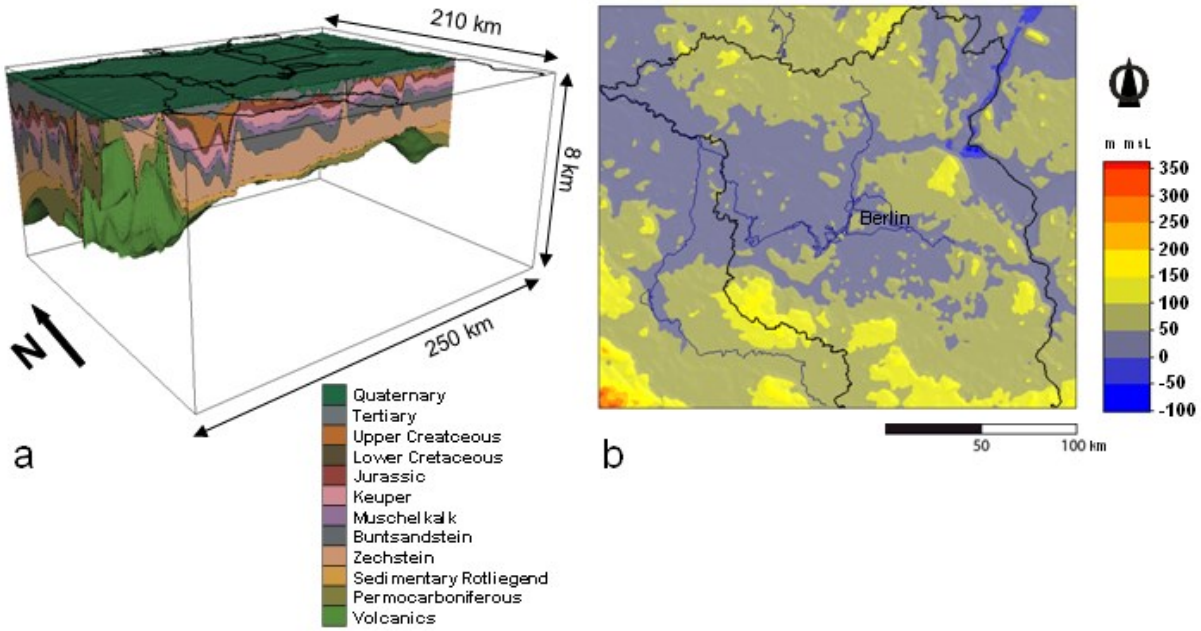

Figure B.2 a: 3D view on the structural model of Brandenburg with colour key for the stratigraphic units differentiated in the model. The model is based on Gauss Krüger zone 4 coordinates. b: present topography of the area; black line – border of Brandenburg, blue line – rivers.

Subsequently, the 2D grids are integrated in a 3D structural model with the software Geological Modelling System (GMS developed at GFZ Potsdam). This part of the task proved to be more complex than expected, as numerous intersections and inconsistencies between the 2D grids have been encountered. These inconsistencies result from 2D interpolation and extrapolation of the available data to areas not covered by observations. The base of Quaternary and the base of Zechstein are chosen as reference levels for the construction of the model as both horizons are very well-constrained by data. To create a model consistent in 3D that also integrates all available observation we follow a twofold strategy. In a first step the model is built from the topography downward to the base of the Lower Triassic Buntsandstein which also represents the top of the Upper Permian Zechstein salt, by calculating the thickness of each horizon resulting from the available datasets. Beginning with the first horizon, the Quaternary thickness is calculated as the difference between its two confining depth levels, the present topography (Fig. B.2b) and the base Quaternary. This procedure is repeated for the other stratigraphic units of the model down to the Triassic Buntsandstein.

In a second step we calculate the configuration for the Sedimentary Rotliegend and for the Permo-Carboniferous Volcanics by subtracting the respective thicknesses from the Base

Zechstein, which also represents the top of the Rotliegend, downwards. The thickness of the Zechstein salt layer corresponds to the difference between the top Zechstein and the base Zechstein horizon. Finally, we complete the model downward adding a layer of pre-Permian crust obtained as the difference between the base of Permo-Carboniferous Volcanics and the depth of the crust-mantle boundary as compiled by Scheck-Wenderoth and Lamarche (2005). Spatially, the final model covers an area of 250 km in E-W direction and 210 km in N-S direction with a horizontal resolution of 1 km and a vertical resolution corresponding to the number of 11 layers resolved in the model (Fig. B.2a).
The detailed configuration of the 3D structural model is illustrated by isopach maps and maps of the base of each horizon (Figs. B.3, B.4 and B.5).

B.2.3 Structural setting

The lowermost unit of the basin fill consists of the Permo-Carboniferous Volcanics. In north-western Brandenburg the base of the Permo-Carboniferous Volcanics reaches depths of more than 8000 m (Fig. B.3a), while in the east the base rises to about 3000 m depth below sea level. In the south, along the inverted southern margin of the basin, this surface is even partially above sea-level. The deepest part of this surface correlates with the location of the largest thicknesses of the Permo-Carboniferous Volcanics (Fig. B.3b). Five zones of increased thickness are present in the northern domain of the model area (Fig. B.3b) with largest values of up to 2000 m along a NE-SW oriented zone in north-western Brandenburg. Thicknesses of up to 1500 m are found in the north-eastern sector of the model domain. In the south of Brandenburg volcanics are absent (Stackebrandt and Manhenke, 2002). Though, the composition of the volcanics varies, as rhyolites, andesites, ignimbrites and basalts were drilled (Hoth et al. 1993), the dominant lithology encountered is rhyolitic.
The base of the next-higher unit - the Sedimentary Rotliegend (Fig. B.3c) - displays a deep structural low in the north-western part of Brandenburg where the respective surface descends with a smooth gradient to depths of more than 7000 m. In contrast, the geometry of this surface shows little change with respect to the underlying layer at the southern margin. Accordingly, the thickest Rotliegend deposits of up to 2000 m (Fig. B.3d) are present in the north-western part of the model close to the basin centre whereas the Rotliegend thickness decreases to the south and east.

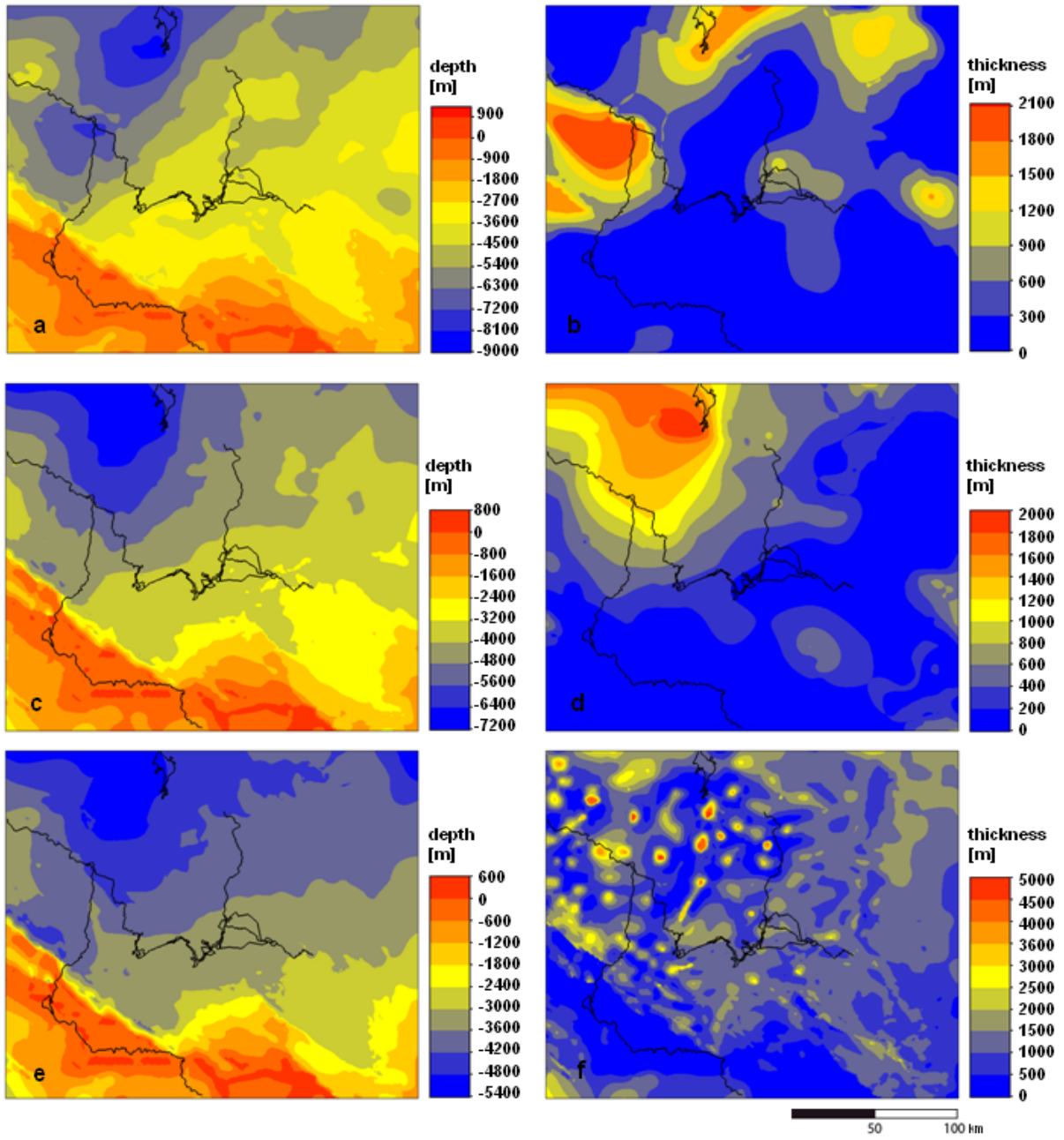

Figure B.3 Isopachs and depths to the base of successive stratigraphic units in the 3D model: a: base of Permo-Carboniferous volcanics; b: isopachs of Permo-Carboniferous volcanics; c: base of Permian Sedimentary Rotliegend; d: isopachs of Permian Sedimentary Rotliegend; e: base of Permian Zechstein salt; f: isopachs of Permian Zechstein salt.

In terms of lithology this layer consists predominantly of non-marine clastics and includes the major aquifer target for deep geothermal exploration at the in situ laboratory Groß Schönebeck. Above the Sedimentary Rotliegend, the base of the Permian Zechstein salt shows a similar structural pattern as the base Rotliegend, though in its deepest parts this surface reaches only about 5000 m (Fig. B.3e). In contrast to the smooth pattern of the base Zechstein, the isopachs of this unit (Fig. B.3f) display a highly differentiated structure. Accordingly, the structural pattern of the Zechstein thickness is characterized by numerous salt pillows and salt diapirs.

The latter are piercing their cover layers to different levels and can reach vertical amplitudes of up to 4000 m.

Complementary, large areas are present where the post-depositional mobilisation results in almost complete removal of the salt. This is expressed by areas of close-to zero present-day thickness of the Zechstein in the north-western part of the study area. As this unit is mainly composed of rock salt, the impact of its structural setting on the lateral and vertical variations in temperature is huge because of its high thermal conductivity.

Basin reconstructions (Scheck et al. 2003b) indicate that the salt thickness distribution is following a similar pattern as the Permian Rotliegend and traces of this trend are visible in the general increase in thickness towards the north-west. Nevertheless, the dominant features of the present salt distribution are very steep thickness gradients. Present day salt structures are aligned along two types of structural axes: NNE-SSW trending axes in the central part of the model and NW-SE trending axes parallel to the Elbe Fault System near the southern margin.

This highly variable thickness distribution of the Zechstein salt causes corresponding gradients in the geometry of all cover layers. Accordingly, the base of the Triassic Buntsandstein (= Top Zechstein, Fig. B.4a) mimics the pattern seen in the Zechstein isopachs - a phenomenon that is repeated in all depth maps of the layers above the salt.

The deepest parts of the Base of the Triassic Buntsandstein reach down to 3600 and 4200 m and, in the north-western part of the study area, where the underlying salt has been completely removed (cf. with salt thickness in Fig. B.3f), even down to 5000 m. A further consequence of salt movement is the overprinted thickness distribution of the cover layers where piercing by salt diapirs causes holes of zero thickness. This post-depositional piercing is obvious in the isopach map of the Buntsandstein (Fig. B.4b), a unit dominantly composed of sandstones and siltstones. Similar to the thickness pattern observed for the Sedimentary Rotliegend, a general increase in thickness towards the north-western part of the model is visible with up to 1200 m of Buntsandstein. In the southern and eastern parts of Brandenburg, the Buntsandstein thickness decreases gradually to less than 200 m. Most of the thickness minima (blue spots of zero thickness) intersect this regional pattern without much local variations around salt diapirs, thus indicating post-depositional piercing.

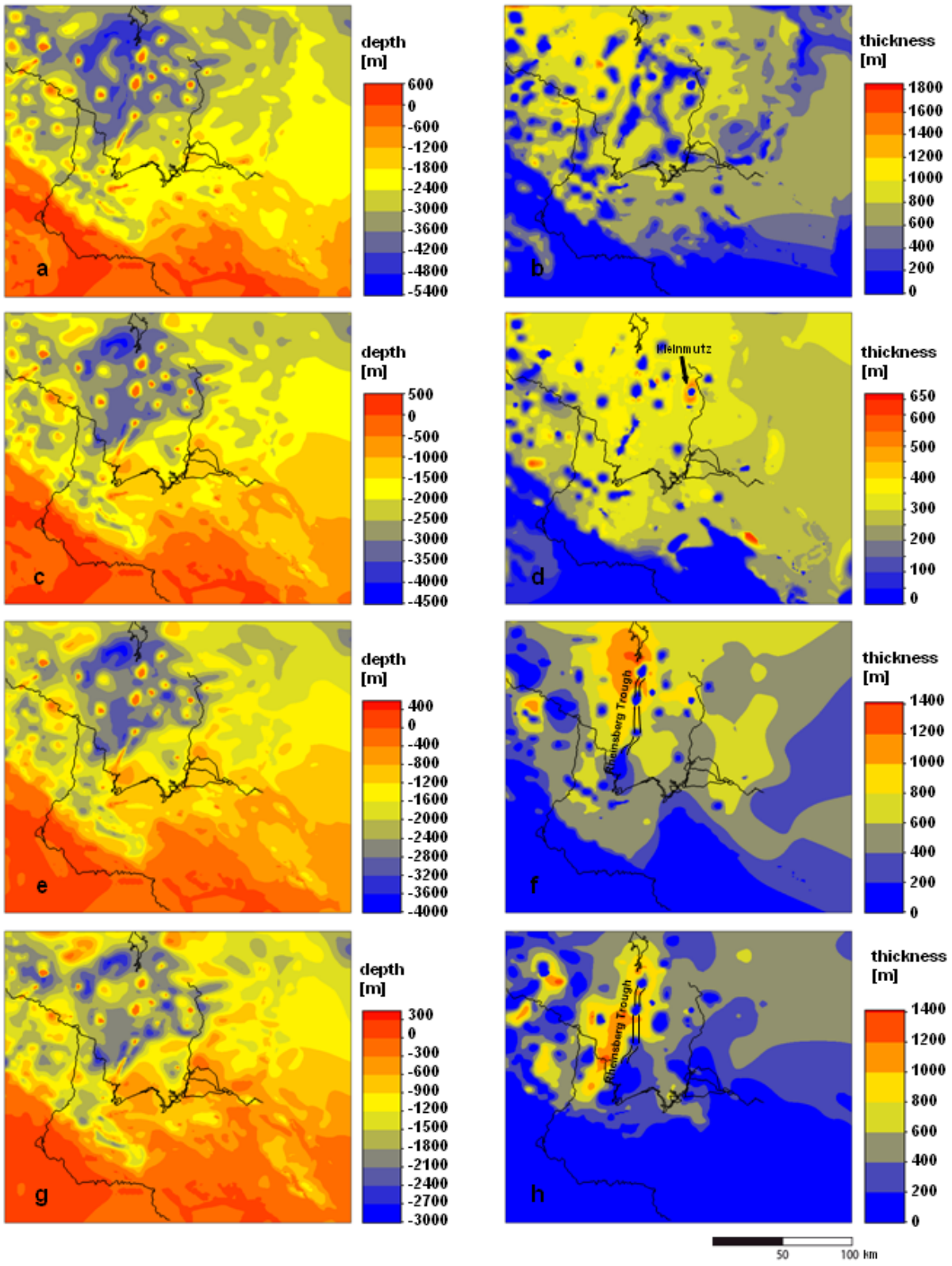

Figure B.4 Isopachs and depths to the base of successive stratigraphic units in the 3D model: a: base of Triassic Buntsandstein; b: isopachs of Triassic Buntsandstein; c: base of Triassic Muschelkalk; d: isopachs of Triassic Muschelkalk; e: base of Triassic Keuper; f: isopach of Triassic Keuper; g: base of Jurassic; h: isopachs of Jurassic.

The base of the Triassic Muschelkalk again mimics the topography of the Zechstein salt and, apart from salt structures, is located at depths between 3000 and 3500 m (Fig. B.4c). As for the Buntsandstein, a long-wavelength pattern of continuously increasing thickness towards the north-western part of the model can be discerned, though the variation in thickness (Fig. B.4d) covers a far smaller range between 300 and 400 m. In addition to the post-depositional thickness minima also local short-wavelength thickness maxima are present. An example of this phenomenon is a local thickness anomaly of more than 500 m in the proximity of the salt diapir Kleinmutz north of Berlin, that indicates syn-depositonal halokinetic movements resulting in salt withdrawal and early formation of a primary salt rim syncline.

The depth to the base of Triassic Keuper shows again a pattern similar to the top Zechstein and is located between 2800 and 3200 m (Fig. B.4e). Contrarily, the thickness map of the Keuper (Fig. B.4f) reveals a change in the location of the main depocentre compared to the underlying layers. In the NNE-SSW oriented Rheinsberg Trough the thickness of this unit mainly composed of continental clastics, locally attains up to 1400 m, whereas it decreases to less than 500 m in the other parts of the model. Seismic data (Scheck et al. 2003a) as well as reconstructions of the salt movements (Scheck et al. 2003b) indicate that the Rheinsberg Trough developed in response to salt withdrawal as a large elongated rim syncline perpendicular to regional E-W extension. Also, local smaller thickness maxima near salt structures point to syn-depositional formation of salt rim-synclines.

The base of the Jurassic (Fig. B.4g) is modelled at depths between 900 and 3000 m with the deepest part in the Rheinsberg Trough. There, also the thickness of the Jurassic (Fig. B.4h) is locally increased to up to 1400 m along a NNE-SSW trending axis. Beside this elongated thickness maximum also smaller thickness maxima attest the formation of syn-depositional Jurassic rim synclines in response to coeval salt withdrawal.

The base of the Lower Cretaceous is up to 2400 m deep and, in contrast to the depth maps of the underlying horizons, is characterized by additional structural depressions indicating coeval formation of salt rim synclines (Fig. B.5a). This is also exposed by the circular shape of thickness maxima of Lower Cretaceous deposits preserved only in the north-western part of Brandenburg and in the southern part of Mecklenburg (Fig. B.5b). There, Lower Cretaceous clastic sediments attain a maximum thickness of up to 1000 m.

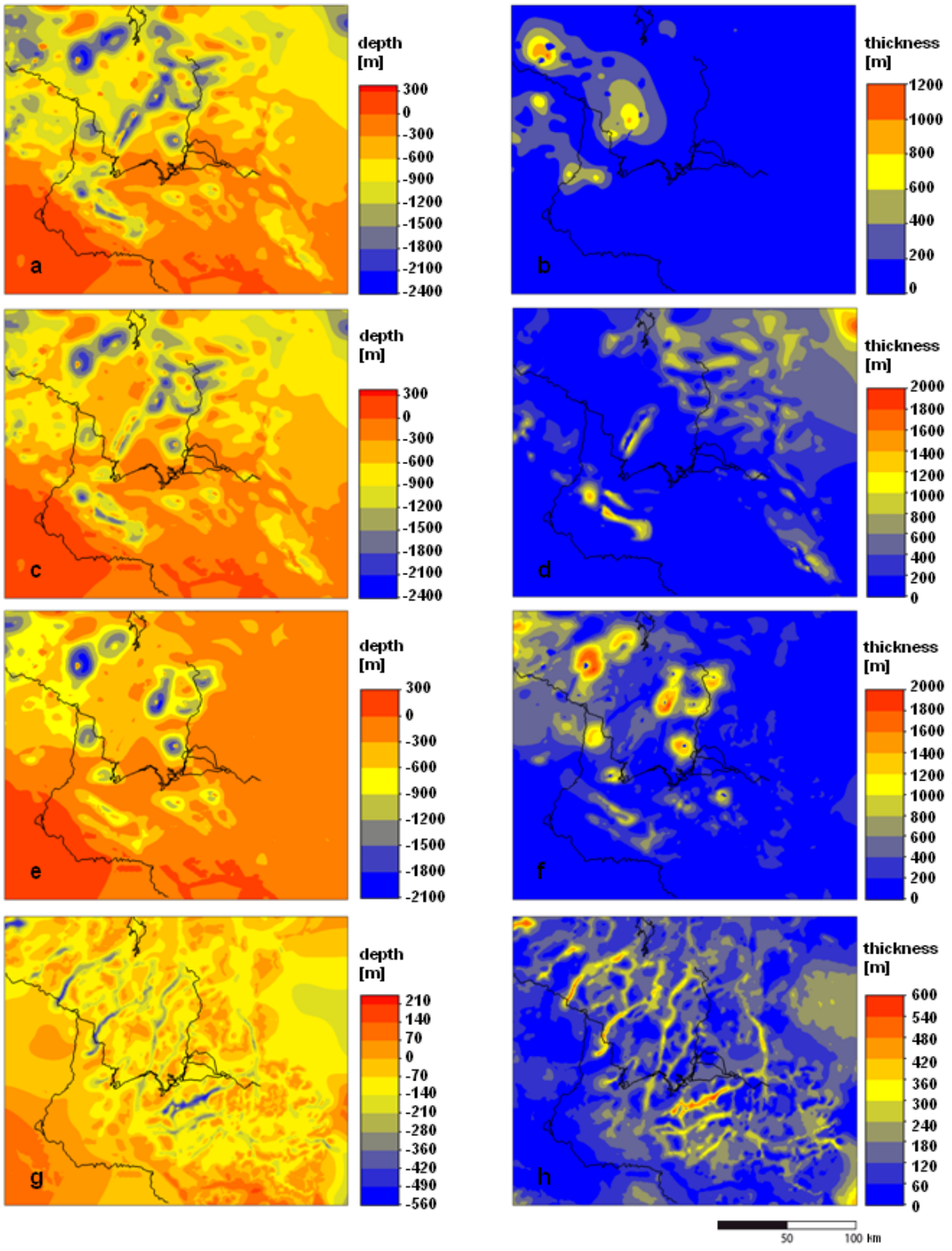

Figure B.5 a: Base of Lower Cretaceous; b: isopachs of Lower Cretaceous; c: base of Upper Cretaceous; d: isopachs of Upper Cretaceous; e: base of Tertiary; f: isopachs of Tertiary; g: base of Quaternary; h: isopachs of Quaternary.

The base of the Upper Cretaceous reaches depths of more than 2000 m (Fig. B.5c) and is generally similar to the base of the Lower Cretaceous. In contrast, the thickness distribution of

the Upper Cretaceous chalk deposits (Fig. B.5d) shows a pattern very different from the underlying layers. Localised maxima of up to 1400 m are present near salt structures of parallel orientation, both characterized by NW-SE oriented axes. Over the largest part of the model area no Upper Cretaceous is preserved, partially in consequence of post-depositional uplift and erosion in the Latest Cretaceous-Early Tertiary (Schwab, 1985; Ziegler, 1990; Scheck-Wenderoth et al. 2008a).

This erosional event is expressed as a regional unconformity in the sediment fill of the area, representing the base of the Tertiary clastic sediments. The depth to base Tertiary additionally bears the imprints of Cenozoic subsidence that had resumed after the phase of erosion (Scheck, 1997). Within Cenozoic salt rim synclines, the base Tertiary is located at up to 2000 m depth (Fig. B.5e) and rises to about 600 m depth in the areas apart from rim synclines. The isopach map of the Tertiary (Fig. B.5f) displays a typical pattern of local salt rim synclines indicated by several circular thickness maxima of up to 2000 m near salt structures. Reduced sediment thicknesses (200 to 400 m) are identified in the south and the east of Brandenburg, some of which have been related to postdepositional erosion by subglacial channels (Stackebrandt et al. 2001).

The uppermost and youngest layer in the model is the Quaternary, the base of which (Fig. B.5g) is structurally controlled by a number of northerly oriented and equally distributed subglacial channels (buried valleys) that locally may reach depths of more than 500 m. These channels were formed by subglacial erosion at the base of the inland ice where the advance caused hydrostatic overpressure in the area of water saturated sediments (Stackebrandt, 2009). They are often filled with a variety of porous and permeable sediments and represent important water reservoirs (BURVAL WORKING GROUP, 2009). The thickness map of the Quaternary (Fig. B.5h) shows that up to 600 m sediments are present in these northerly trending channels whereas the Quaternary is less than 300 m thick outside the channels.

B.3 The 3D conductive thermal model of Brandenburg

To assess the regional thermal field we calculate the steady-state 3D temperature distribution assuming heat conduction as the dominant transport mechanism.

Therefore, we solve the three-dimensional steady-state heat conduction equation:

$$\mathrm{div}\,(\lambda\,\mathrm{grad}\,T) = -S \qquad (1)$$

with λ - thermal conductivity, T - temperature, S - radioactive heat production, numerically using a 3D FEM (Bayer et al. 1997). The solution of equation (1) depends on the thermal

properties (λ and S) and on the choice of boundary conditions. A fixed temperature of 8°C, corresponding to the average surface temperature in the area, has been implemented as upper boundary condition. For the lower boundary, we choose a constant heat flow of 30 mW/m² at the Moho, following results of earlier work (Bayer et al. 1997). The lateral boundaries are considered closed.

For temperature calculation, lithology-dependent physical properties are assigned to each stratigraphic unit of the model. According to equation (1) values for the thermal conductivities and for the heat production are the parameters required for the calculation of the 3D conductive thermal field. These are assigned to each layer assuming a uniform dominant lithology for each layer as detailed in Table B.2.

Table B.2 Input thermal properties for geothermal modelling after Bayer et al. (1997).

Stratigraphic Unit	Lithology	Heat conductivity [W/mK]	Radiogenic heat production [W/m^3]
Quaternary	Sand & Silt & Clay	1.5	7.0E-07
Tertiary	Sand & Silt & Clay	1.5	7.0E-07
Upper Cretaceous	Limestone (Chalk)	1.9	3.0E-07
Lower Cretaceous	Clays with Sand & Silt	2	1.4E-06
Jurassic	Clays with Sand & Silt & Marl	2	1.4E-06
Keuper	Clays with Marl & Gypsum	2.3	1.4E-06
Muschelkalk	Limestone	1.85	3.0E-07
Buntsandstein	Silts with Sand & Clay & Evaporite	2	1.0E-06
Zechstein	Rock salt	3.5	9.0E-08
Sedimentary Rotliegend	Clay-, Silt- & Sandstone	2.16	1.0E-06
Permo-Carboniferous Volcanics	Rhyolithe & Andesite	2.5	2.0E-06
Crust	Granite to Granodiorite	2.55	1.5E-06
Mantle	Peridotite	2.3	3.0E-07

B.3.1 Modelled temperatures

The 3D structural model is illustrated along an E-W cross-section (Fig. B.6a) down to 5000 m depth. As can be seen on the figure, one salt diapir pierces the up to 4000 m thick overburden. This diapir is bounded by salt rim synclines. Fig. B.6b shows exemplarily the impact of the

high thermal conductivity within the salt diapir on the temperature distribution down to 5000 m depth. The isotherms are bent convex upward above the diapir and convex downward below the structure. Highest temperatures are predicted below the salt rim synclines and correlate with the thickness maxima of the overburden sediments.

Figure B.6c-f shows the calculated temperature distribution for selected depth levels. A feature common to all temperature depth maps is the strong lateral variation of predicted temperatures for a certain constant depth level. The temperature map at 2000 m depth (Fig. B.6c) cuts Cenozoic sediments and salt structures within the model. The respective pattern of temperature distribution shows a strong spatial correlation with the thickness distribution of the Zechstein salt layer and the topography of the top salt surface (cf. Figs. B.3f and B.4a). In general, calculated temperatures are higher above salt diapirs but lower within and below salt structures or areas of thick salt. This "chimney effect" is the result of the high thermal conductivity of the salt causing increased heat transfer and therefore enhanced cooling within the salt structure. In contrast, the surrounding low-conductive sediments have an insulating effect and cause heat storage. Therefore, higher temperatures are modelled where the low-conductive units are thick. Accordingly, the highest calculated temperatures at 2000 m depth vary between 90 °C and 100 °C, where the low-conductive sediments of Tertiary salt rim synclines attain their largest thickness in the north-western domain of the model area. In contrast, lower temperatures are predicted in areas where salt diapirs reach structural levels close to the surface and the cooling effect is most pronounced. In areas without prominent salt structures, temperatures generally attain 80 °C to 90 °C. The lowest temperatures of about 60 °C are calculated for the basin margin in the south.

The temperature distribution at 4000 m depth (Fig. B.6d) shows highest temperatures between 145 °C and 160 °C in the northern domain of the model. This map cuts the model along a plane intersecting several salt structures in the western part of the study area where the highest temperatures are calculated. Increasing temperatures are predicted around salt domes due to the insulating effect of the surrounding rim syncline deposits. There, the enhanced lateral heat transfer from the salt structure is "captured" by the low-conductive sediments of the rim syncline. In the eastern part, this map cuts the model below the salt. Accordingly, the calculated temperatures are lower there and vary between 130 °C and 150 °C. The lowest temperatures of up to 100 °C have been calculated at the southern basin margin. This is related to the shallow position of the highly conductive crystalline crust in this domain, also causing a chimney effect.

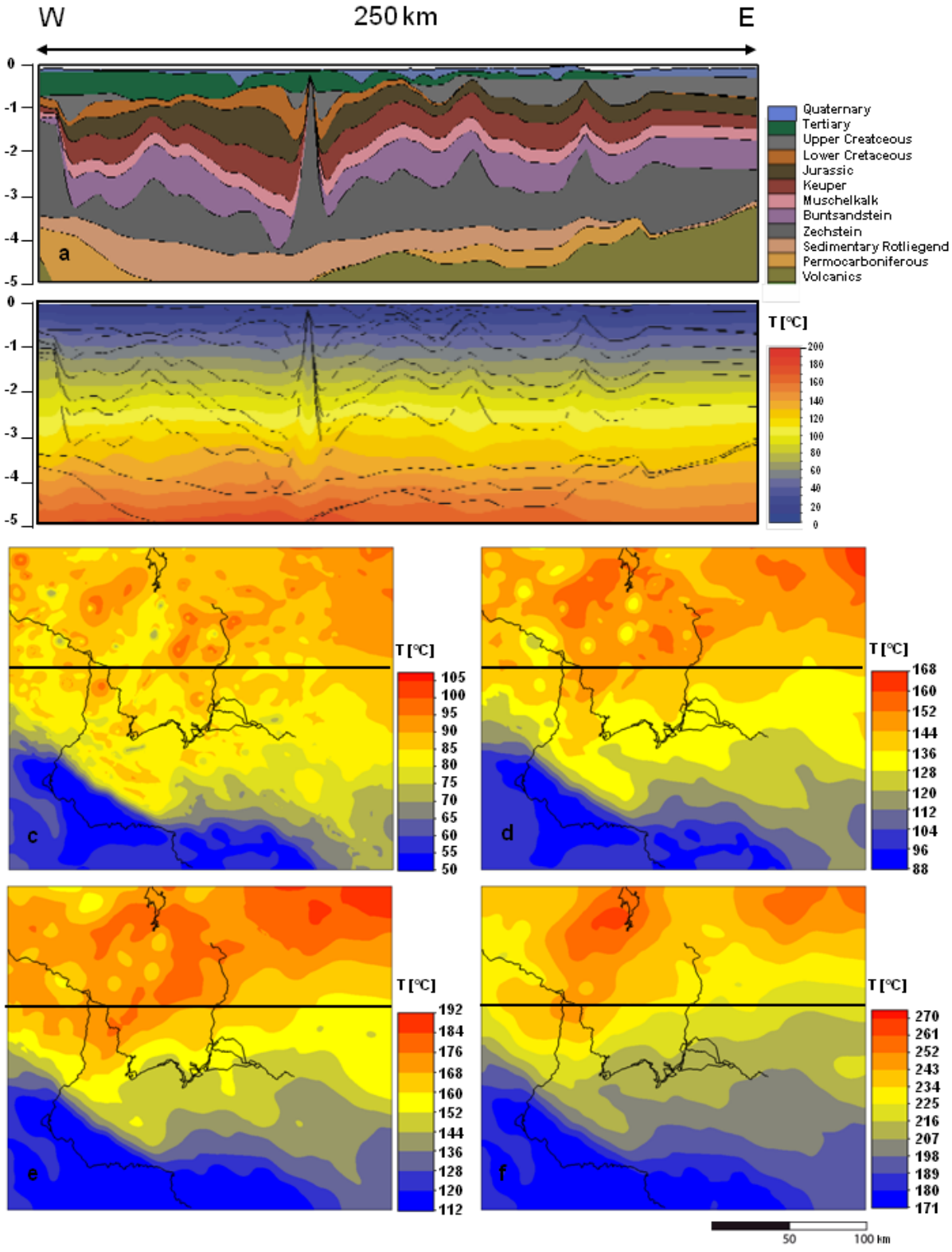

Figure B.6 a: Cross section of the 3D structural model; b: cross section of the 3D thermal model, vertical exaggeration 1:10; c-f: Predicted temperature in °C extracted from the 3D conductive thermal model at the depth of c: 2000 m; d: 4000 m; e: 5000 m; f: 8000 m.

The pattern of temperature distribution changes with depth. At 5000 m depth (Fig. B.6e) the spatial correlation between the pattern of temperature distribution and the salt thickness is only weekly expressed as circular cold spots beneath salt diapirs in the north-western part of the model. The long-wavelength trend of increasing temperatures from the southern margin (~110°C) towards the basin centre (up to 190°C) rather correlates with the cumulative thickness distribution of the post-salt deposits and reflects the blanketing effect and related heat storage due to the low conductivity of these layers.

At the depth of 8000 m (Fig. B.6f) the temperature distribution shows only smooth, long wavelength variations. Domains of elevated temperatures between 230 °C and 270 °C correlate spatially with the superposed thickness maxima of the Permian Rotliegend sediments and the Permo-Carboniferous Volcanics (cf. Figs. B.3b and B.3d). This indicates that these elevated temperatures are caused by the blanketing effect of the respective layers. In contrast, lower temperatures ranging between 170 °C and 200 °C, are calculated for areas where this surface cuts through the highly-conductive pre-Permian crust with the lowest values again occurring at the southern basin margin.

Like for the temperatures, also the lateral variations of heat flow predicted by the model are considerable. The calculated surface heat flow ranges between 80 mW/m² and 125 mW/m² close to salt domes and at the southern basin margin due to the enhanced heat transfer by the geological units with high thermal conductivities. Apart from salt structures predicted values of surface heat flow are lower and vary between 55 mW/m² and 75 mW/m². Likewise, calculated values of heat flow at deeper levels reflect the structural heterogeneities in the model. At 5000 metres depth, values of heat flow are generally lower, reaching 60 mW/m² to 90 mW/m² in the north-western, salt-influenced domain. Reduced heat flow values of 40 mW/m² to 50 mW/m² are characteristic for areas without large salt structures at this depth level.

Both, the predicted temperature range as well as the modelled surface heat flow are consistent with published data, as for example depth-temperature maps derived from 2D extrapolation of borehole measurements (Stackebrandt and Manhenke, 2002) and the map of surface heat flow (Hurtig et al. 1992). However, the added value of the model consists in the predictions considering physical principles as well as lateral variations due to the structural characteristics and lateral heterogeneity of physical properties.

B.3.2 Comparison with published data

Both, the predicted temperature range as well as the modelled surface heat flow are consistent with the general trend of published data, as for example depth-temperature maps derived from 2D intratrapolation of borehole measurements (Stackebrandt and Manhenke, 2002) and the map of surface heat flow (Hurtig et al. 1992). In response to the improved structural resolution of our model concerning the distribution of the highly conductive Zechstein salt, we obtain a more pronounced lateral variation in predicted temperatures compared to published maps. The latter are mainly obtained by interpolation between data points of temperatures measured in wells and may not consistently consider the effects of single salt structures. To assess the consistence with the real measurements a local comparison is therefore required. This comparison is, however hampered by the small amount of published temperature measurements. Comparison between model results and measured temperatures available from literature (Förster, 2001) shows that model predictions deviate from measured values by about 10° K. This deviation is in the same range as the standard deviation of corrected Bottom Hole Temperatures and temperature logs (Förster, 2001). Possible reasons for the difference between predicted and measured temperatures could be related to both, (1) errors related to the observations or (2) oversimplifications in the model.

(1) The measured BHT – temperatures may not represent equilibrium temperatures. This is indicated by the comparison of uncorrected and corrected BHT values. For corrected values the difference is smaller up to 5° K. Moreover, the difference between modelled and measured temperatures is in the same range as the difference between uncorrected and corrected temperatures (Förster, 2001).

(2) The model resolution on one hand and the assumption of laterally constant thermal properties in each layer may not correctly consider the local lithologies.

Future work therefore will focus on the sensitivity of the modelling results with respect to these effects. However, the added value of the model consists in the predictions considering physical principles as well as lateral variations due to the structural characteristics and lateral heterogeneity of physical properties.

B.4 The geothermal in-situ laboratory Groß Schönebeck

To investigate the geothermal field and fluid regime at the Groß Schönebeck site three dimensional coupled fluid and heat transport simulations are carried out. These models enable to quantify the interaction of the different thermal rock properties and their feedback on the

temperature and heat flow distribution related to the geological structures on a local scale. The Zechstein salt is of particular interest in this context because of its strong impact on the local geothermal field due to the high thermal conductivity of the salt. Furthermore, the quasi-impervious salt decouples the overburden strata from the pre-Zechstein layers. In this regard, we present first results from numerical simulations of the coupled heat and fluid transport for the Groß Schönebeck site, discuss the implications for the dominating processes affecting heat transport and the fluid regime but also the limits of smaller scale models.

For the 3D coupled heat and fluid transport simulations a 3D structural model of the area Groß Schönebeck was available (Moeck et al. 2005) based on data from 15 wells with final depths greater than 4000 m and on six seismic profiles from former gas exploration (Ollinger et al. 2010). The site Groß Schönebeck is located at a NE-SW trending salt ridge which rises from -4180 to - 2160 m (Fig. B.7b) and has an average thickness of 700 m. This salt layer divides the sedimentary succession into a supra- and a subsalinar sequence.

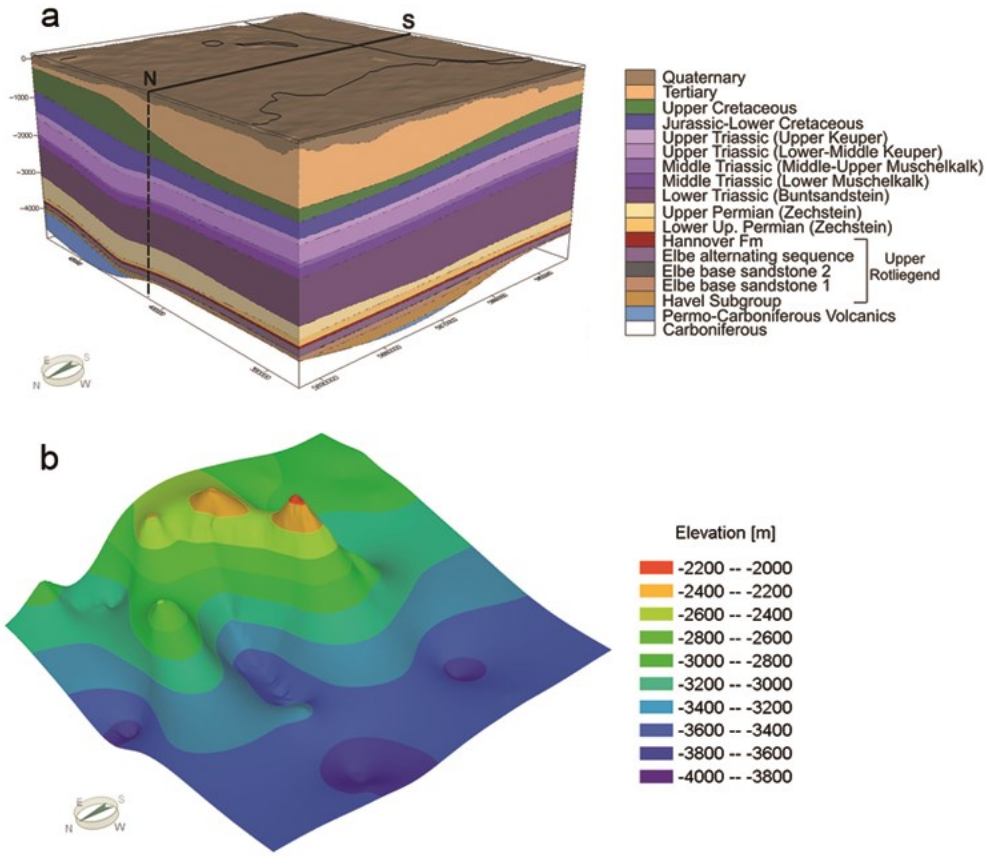

Figure B.7 a: 3D geological model of the Groß Schönebeck site consisting of 18 layers from the Carboniferous to the Quaternary. The solid and dotted lines indicate the location of a representative cross-section which cuts the model from north to south. b: Relief of the Top Zechstein salt.

From top to bottom, the suprasalinar sequence includes Cenozoic unconsolidated sands, clay and marly limestones, weakly consolidated sand- and siltstone of Cretaceous to Jurassic age, silt- and limestones of Triassic age and Upper Permian evaporites (Ollinger et al. 2010). The latter consist mainly of rock salt as well as of minor anhydrites and carbonates.
The sequence below the salt includes the Permian Upper Rotliegend deposits as well as Permo-Carboniferous Volcanics and Carboniferous rocks. Due to its role as the reservoir target zone, the Permian Upper Rotliegend is well characterized. Accordingly, the deposits are subdivided into the Hannover Formation with mainly mudstones and the Dethlingen Formation which is composed of fine- to coarse-grained sandstones. The Havel Subgroup contains sandstones and clast-supported conglomerates (Holl et al. 2005). Below, the layers consist of volcanic (andesitic) rocks of Late Carboniferous and Early Permian and Carboniferous foliated flyschoid sediments.

B.4.1 Method

For carrying out three-dimensional coupled heat and fluid transport simulations the finite element method (FEM) is used. As a first step the geometry of the layers from the structural model (Moeck et al. 2005) is extracted and transferred into a format applicable for using the FEM. Additionally, the Cenozoic layer has been differentiated into a Quaternary and a Tertiary unit. Thus, the final geological model for the FEM simulations consists of 18 layers (Fig. B.7a). For solving the coupled fluid flow and heat transport equations we use the commercial software FEFLOW®. FEFLOW® is a software package for modelling fluid flow and transport processes in natural porous media based on the finite element technique. The governing three partial differential equations of thermal convection in a saturated porous media are based on Darcy`s law, energy and mass conservation laws, e.g. Nield and Bejan (2006). A detailed description of the equations can be found in Appendix A.
The study area covers a surface of 55 km in E-W and 50 km in N-S direction. This square defines the horizontal extension of the finite element mesh and marks the superelement of the 3D model in FEFLOW®. Within the superelement, a grid resolution of 250 x 220 grid points is assigned for constructing the finite element mesh representing a horizontal mesh resolution of 220 x 227 meters. The discretised superelement is a 2D surface slice, which is multiplied according to the number of geological layers within the model. Each slice has the same mesh discretisation and consists of 54531 (249 x 219) rectangular elements.

To reproduce the geological structure, the z-elevations of the geological layers extracted from the structural model were assigned for each node of the 2D surface in a three dimensional space. The third dimension is entered by vertically connecting the nodes of corresponding elements within two slices. Accordingly, the vertical resolution of the constructed 3D model is therefore a priori determined by the individual thickness of each geological layer. To avoid numerical instabilities, layers of large thickness have been subdivided into sub-layers of identical physical properties. The Lower Triassic Buntsandstein and the Upper Permian Zechstein are in each case subdivided into three layers of equal thicknesses whereas the Quaternary layer is differentiated into two units of equal thicknesses. At the base of the model a plane is integrated at a constant depth of 5000 m. As a result, the final model consists of 23 layers which results in approximately one and a half million elements in total.

Physical parameters depending on the lithology of the respective geological unit are assigned for each layer. From the equations summarized in Appendix A, it is obvious, that relevant physical properties influencing the results of simulation are thermal conductivities and radiogenic heat production rates as well as volumetric heat capacities, porosities and permeabilites (Tab. B.3). Likewise, the results are depending on the applied initial and boundary conditions. We use a flow boundary condition equal to the topographic elevation to investigate the influence of the topography on the fluid system. A fixed constant temperature of 8 °C is assigned for the top thermal boundary representing the average surface air temperature in north-eastern Germany. For the bottom, a basal heat flux of 50 mWm^{-2} is applied. This value has been extracted from the large-scale thermal model of Brandenburg (chapter B.3) for the area in the vicinity of Groß Schönebeck. The lateral boundaries are closed to fluid and heat flow. As a starting point the initial temperature and pressure conditions are obtained from uncoupled steady-state heat transport and fluid flow simulations, respectively.

Table B.3 Thermal conductivities and radiogenic heat production used for the numerical simulations of the geothermal field for the Groß Schönebeck site; Thermal conductivities and radiogenic heat production for the Cenozoic to Upper Permian Zechstein after Norden and Förster (2006) and Norden et al. (2008); Data used for the Upper Rotliegend Formation to Late Carboniferous for thermal conductivities after Blöcher et al. 2010b, for Carboniferous after Ollinger et al. (2010); Values for the radiogenic heat production of the Upper Rotliegend Formation to Carboniferous after Ollinger et al. (2010).

Permeabilities, porosities and heat capacities assigned for the coupled heat and fluid transport simulations. Values for the Cenozoic to the Upper Permian Zechstein and for the Carboniferous after Magri et al. (2005); Scheck (1997). Data used for the Upper Rotliegend Formation to Late Carboniferous after Blöcher et al. 2010b.

Stratigraphic Unit	Permeability $\kappa[m^2]$	Porosity $\varepsilon[\%]$	Rock heat capacity c_s [MJ/m^{3}K]	Thermal conductivity λ [W/mK]	Radiogenic heat production Q_T [10^{-7} W/m^3]
Quaternary	1.00E-12	23	3.15	1.5	9
Tertiary	1.00E-12	23	3.15	1.5	9
Upper Cretaceous	1.00E-13	10	2.4	1.9	6
Jurassic – Lower Cretaceous	1.00E-13	13	3.19	2	15
Upper Triassic (Upper Keuper)	1.00E-14	6	3.19	2.3	16
Upper Triassic (Middle – Upper Keuper)	1.00E-14	6	3.19	2.3	16
Middle Triassic (Middle – Upper Muschelkalk)	1.00E-18	~0	2.4	1.85	10
Middle Triassic (Lower Muschelkalk)	1.00E-18	~0	2.4	1.85	10
Lower Triassic (Buntsandstein)	1.00E-14	4	3.15	2	18
Upper Permian (Zechstein)	Impervious ~ 0	~0	1.81	4.5	4
Lower Up. Permian (Zechstein)	Impervious ~ 0	~0	1.81	4.5	4
Upper Rotliegend (Hannover Formation)	1.61E-16	1	2.4	1.9	18
Upper Rotliegend (Elbe alternating sequence)	6.44E-16	3	2.4	1.9	14
Upper Rotliegend (Elbe base sandstone 2)	1.29E-14	8	2.4	2.9	14
Upper Rotliegend (Elbe base sandstone 1)	2.58E-14	15	2.4	2.8	10
Upper Rotliegend (Havel Subgroup)	3.22E-16	0.1	2.6	3	12
Permo – Carboniferous Volcanics	3.22E-16	0.5	3.6	2.3	10
Carboniferous	Impervious ~ 0	~0	2.7	2.7	20

B.4.2 Results from simulations of coupled heat and fluid transfer

Several fluid and heat transport simulations for the Groß Schönebeck model are carried out for 250000 years of simulation time to achieve stable numerical results. The main outcome of our simulations are illustrated along a representative cross-section (Fig. B.8a) that straightly cuts the model from north to south and shows the impact of the salt structures on the thermal field more in detail.

Starting from less coupled simulations, the degree of coupling is step-wise increased during the procedure of modelling. First, the simplest case means a purely conductive model, is calculated to assess the interaction between the different thermal properties and their feedback on the temperature field (Fig. B.8b).

For this case, the temperature field displays in general nearly flat isotherms. This characteristic pattern reflects the diffusive nature of the conductive heat transfer where molecules transmit their kinetic energy by collision and no motion of the medium is involved. The isotherms are significantly disturbed only in the area of the Zechstein salt. Concave isotherms occur within the salt pillows whereas the isotherms above the salt show less pronounced convex shapes. These thermal anomalies are triggered by the high thermal conductivity of the salt compared to the surrounding sediments. Slightly higher temperatures can be observed where the thickness of the suprasalt sediments increases to 3500 m. There, the low thermal conductivities result in insulating effects and an accumulation of heat.

Next, a simulation with one more degree of coupling was carried out in which the fluid density is taken into account as a function of temperature with a constant thermal expansion coefficient (Fig. B.8c). The higher degree of coupling between the governing equations causes convection to take over a major role as a heat transfer mechanism. Convective heat transport is associated with the motion of a medium. When a fluid is heated, its density generally decreases because of thermal expansion and the heated fluid becomes buoyant compared to neighboring areas of lower fluid temperatures. This leads to upward movement of the heated fluid and thus induces convection. In our model, convection can be observed above the calcareous Middle Triassic Muschelkalk. This unit acts like a quasi-impervious layer with much lower hydraulic permeabilities compared to the overburden sediments. As a consequence, the Muschelkalk layer hydraulically decouples the Lower Triassic Buntsandstein unit from younger strata which leads to the development of two aquifer systems with different hydro-dynamical characteristics.

In the system above the Triassic Muschelkalk, the sediments with higher hydraulic conductivity promote the formation of convection cells. Heated fluids tend to rise easier through the permeable sediments of the post-Muschelkalk succession. Furthermore, convective processes

are additionally favoured by the large thickness (up to 3000 m) for the post-Muschelkalk deposits. On the contrary, conduction remains the dominant heat transfer mechanism below the Muschelkalk as indicated by rather flat isotherms of a shape similar to the conductive case. The temperature distribution above the salt domes displays the “chimney effect” which carries away the heat upwards due to the high thermal conductivity of the salt.

One higher degree of coupling between the governing equations involves the fluid density as a function of temperature with a variable thermal expansion coefficient β. In FEFLOW® this relationship is approximated by a 6th order polynomial, meaning that β takes the role of a function being dependent on the temperature which defines a non-linear variable thermal expansion valid for 0-100 °C (Diersch, 2002). For increasing the coupling both variable thermal fluid expansion and fluid compressibility within the state equation of density (see Eq. 8, Appendix A) are considered by means of approximated coefficients for a wide range of pressures ρ_{sat} with $\rho_{sat}<\rho\leq100$ MPa and for temperatures below 350 °C ($0\leq T\leq350$°C) (Magri, 2005). Applying these two approaches for the thermal expansion coefficient during the simulation caused only small variations in the temperature distribution compared to the less coupled model assuming a constant thermal expansion coefficient (Fig. B.8c).

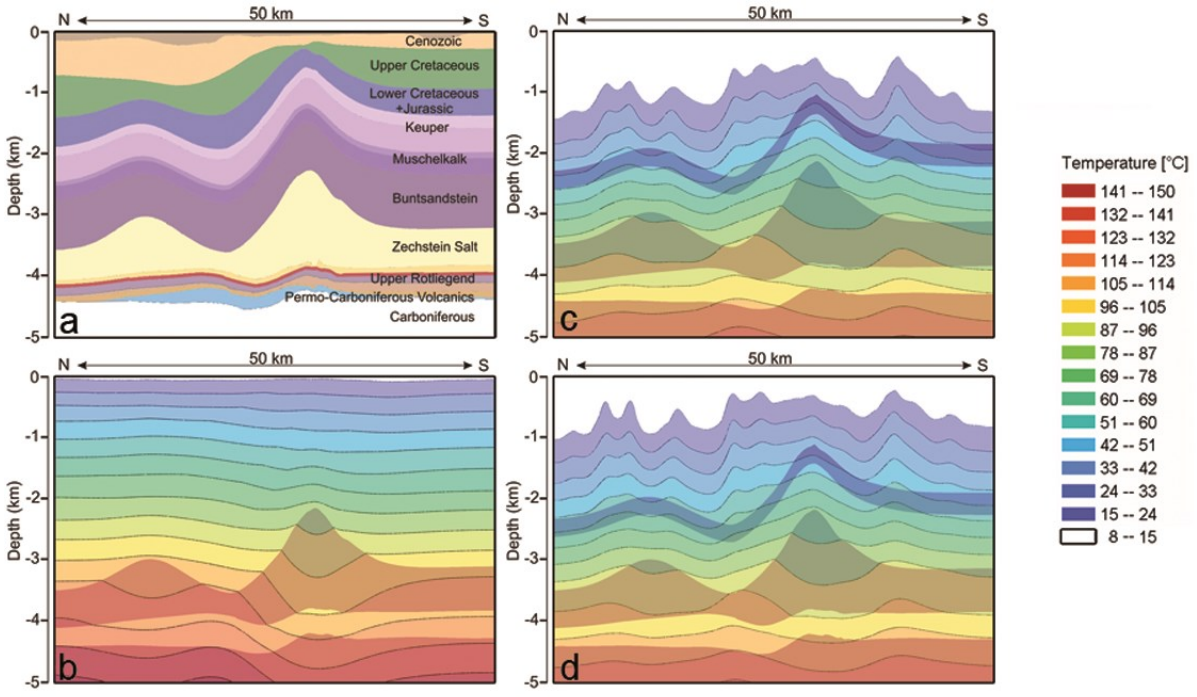

Figure B.8 N-S cross-section illustrating simulation results, vertical exaggeration 1:7. a: Representative cross-section cutting the model from north to south with focus on the Zechstein Salt structure. b-d: Temperature distributions along the cross-section (a) after 250000 years of simulation time: for b: the purely conductive model, c: model in which the fluid density with a constant thermal expansion coefficient is included, d: model in which the fluid viscosity taken as function of temperature is considered in addition to fluid density effects with a non-linear variable thermal expansion.

Significant differences are observed for the temperature field only if fluid viscosity effects are additionally taken into account (Fig. B.8d). These results refer to calculations adopting the highest grade of coupling presented where the fluid viscosity taken as function of temperature is considered in addition to fluid density effects with a non-linear variable thermal expansion. A general increase in temperature leads to a decrease in viscosity which subsequently enforces the convective flow. As a result the convection cells above the Muschelkalk unit are clearly more pronounced and reach higher up to the Quaternary layer. In greater depths conduction is again the dominant heat transfer process. The salt induces curved long-wavelength isotherms within the Buntsandstein which reflect the conductive heat regime in this area.

In summary, the 3D numerical simulations of coupled fluid flow and heat transfer processes of the Groß Schönebeck site confirm the strong impact of the Upper Permian Zechstein salt. The latter disturbs the regional temperature field as indicated by strongly curved isotherms within and above the salt structures. Rather flat isotherms show that heat tends to be dominantly transferred by conduction below the impermeable Middle Triassic Muschelkalk deposits. Though the Buntsandstein and the different Rotliegend units are characterized by reasonable permeabilities, their thickness is obviously too small to allow the development of convection cells. Consequently, the coupled models suggest that conduction is an important heat transfer mechanism in regions below the Middle Triassic strata in the subsurface of northern Germany. In contrast, convection affects heat transport within the up to 3000 m thick, permeable sediments above the Muschelkalk. The integration of fluid density effects causes the formation of convection cells providing a heat transfer mechanism at shallower levels. Considering a variable expansion coefficient, however, does not influence the heat and fluid transport processes strongly. By contrast, temperature dependencies of the fluid viscosity considerably affect the geothermal field. The minor influence of a variable thermal expansion coefficient on the heat and fluid transport could be related to the fact that the absolute temperatures are still too low to cause sufficient thermal expansion in the individual post-Muschelkalk layers.
As a final word of caution we would like to include remarks concerning the limitations of the method. Sources of uncertainty that may be quantified in future studies include: (1) the chosen lateral boundary conditions for the fluid flow and heat transport and (2) the ratio between the vertical to the lateral extent of the model.

B.5 Conclusions

The refined 3D structural model of Brandenburg visualizes the 3D configuration of the subsurface including an improved representation of the salt structures. This model can be evaluated to assess the structural heterogeneities and their relevance for the thermal field in the area but also to analyse changes in subsidence dynamics and related halokinetic processes. The 3D distribution of dominant physical properties assigned in the model can be used as a base for process-oriented modelling of subsurface heat transport. Our preliminary models indicate considerable lateral variations of both temperature and heat flow for any depth level which implies two major conclusions:
(1) Geothermal exploration can take advantage of such models that provide a cheap and rapid method aiding in the selection of a drilling location, and (2) the assumption of a constant heat flow or a constant temperature at the base of local, reservoir-scale thermal models may not be appropriate in areas where short wavelength variations of these parameters are present. These results are, however, preliminary and need to go through further testing. In particular, geological units in nature are not laterally uniform as simplified in our approach. Therefore, the sensitivity of the results with respect to laterally changing lithologies and associated physical properties needs to be studied to evaluate the potential thermal effects of these variations.

Our results further demonstrate that combining large-scale regional models with local-scale models of a geothermal production site is useful. For the Groß Schönebeck site the 3D numerical simulations of coupled fluid flow and heat transfer processes confirm the strong impact of the Upper Permian Zechstein salt. The outcomes indicate a relevant influence of convective heat transport in the upper 3000 m, where a critical thickness of permeable sediments is achieved. Increasing the degree of coupling has little effect on the temperature range in the upper 3000 m as temperature induced density-differences are too small to impose buoyancy of the fluid. Stronger differences in the temperature distribution are only observed when considering the temperature-dependence of fluid viscosity. However, sources of uncertainty may also be given by the ratio between the vertical and the lateral extent of the model and the chosen lateral boundary conditions for fluid flow and heat transport. Our studies suggest that especially high degrees of coupling result in remarkable convective heat transport. How far this result is valid for other geothermal sites remains uncertain. To assess the sensitivity of the results, further studies are required.

Acknowledgements

We thank our colleagues from the geological surveys of Landesamt für Bergbau, Geologie und Rohstoffe Brandenburg, Landesamt für Geologie und Bergwesen Sachsen-Anhalt and Landesamt für Umwelt, Naturschutz und Geologie Mecklenburg-Vorpommern for providing additional well data and for helpful discussions. Mauro Cacace supported us with valuable advices about the physical principles behind the applied simulation methods. The project received financial support from the project GeoEn of BMBF and from Helmholtz Centre Potsdam GFZ German Research Centre for Geosciences. This paper was greatly improved by the comments of three reviewers: R. Kirsch, S. Mazur and K. Obst.

Danksagung

Diese Arbeit entstand in einer Kooperation der Universität Potsdam und dem GeoForschungsZentrum Potsdam innerhalb der Verbundprojektes GeoEn. Die Durchführung des Projektes war dank der Förderung des Bundesministeriums für Bildung und Forschung möglich.

Zuallererst möchte ich mich bei meinen Betreuern Prof. Dr. Magdalena Scheck-Wenderoth und Prof. Dr. Manfred Strecker bedanken. Leni, vielen Dank für Deine großartige Unterstützung während meiner gesamten Doktorandenzeit. Deine engagierte Betreuung, fachliche Kompetenz, Dein offenes Ohr für Probleme jeglicher Art und Deine persönliche Unterstützung haben es mir erst möglich gemacht, diese Arbeit erfolgreich abzuschließen, herzlichen Dank für Alles! Mein besonderer Dank geht an Prof. Dr. Manfred Strecker, der diese Arbeit offiziell von Seiten der Universität Potsdam betreut und begutachtet hat. Ich bedanke mich herzlich bei Dr. Mauro Cacace für seine engagierte Betreuung dieser Arbeit. Danke, Mauro, für Deine ganze Unterstützung, für die vielen hilfreichen und wertvollen Ratschläge und Ideen, fachlichen Erklärungen, die konstruktive Kritik und aufschlussreichen Diskussionen, die entscheidend zum Erfolg dieser Arbeit beigetragen haben.

Für die gute sektionsübergreifende Zusammenarbeit am GFZ möchte ich vor allem Dr. Inga Moeck und Dr. Guido Blöcher danken. Inga danke ich für die lehrreichen Diskussionen, konstruktiven Vorschläge zu meiner Arbeit und die Bereitstellung von Daten zum Störungssystem von Groß Schönebeck. Vielen Dank an Guido für die „numerische“ Unterstützung, die fachlichen Erklärungen, Tipps und die gute Zusammenarbeit.

Vielen Dank für die tolle Zusammenarbeit mit Prof. Dr. Olaf Kolditz und Dr. Norihiro Watanabe am UFZ in Leipzig. Herzlichen Dank an Olaf für die konstruktiven Verbesserungsvorschläge, die Unterstützung als Editor und mit OGS, sowie vor allem die Ermutigungen, die sehr viel bei mir bewirkt haben und meiner Arbeit zu einem wichtigen Durchbruch verholfen haben. Bei Norihiro bedanke ich mich sehr für die wertvolle Hilfe bei OGS und seine Zeit und Geduld, die er für dafür aufgebracht hat.

Bei Dr. Olivier Lacombe und Dr. Dirk Nieuwland möchte ich mich herzlich für die fruchtbaren Diskussionen in Albanien bedanken.

Dr. Frank Wenderoth und Dr. Fabien Magri danke ich für ihre hilfreichen und nützlichen FEFLOW-Tipps.

Bei allen Reviewern und Editoren möchte ich mich für ihren wichtigen Beitrag bedanken, die Qualität der Publikationen zu verbessern.

Mein besonderer Dank geht an die gesamte Sektion 4.4! Es hat sehr Spaß gemacht mit Euch zu arbeiten und auf Konferenzen zu fahren. Besonders der Zusammenhalt und die gute Zusammenarbeit in dieser Sektion haben es mir von Anfang an leicht gemacht, mich am GFZ wohlzufühlen. Für all das Danke an: Anna, Alex, Bo, Christina, Hannes, Ingo, Katja, Jessica, Judith, Julia, Lew, Mauro, Max, Michaela, Peter, Philipp, Vera und Yuriy. Für die technische Unterstützung und die damit entgegengebrachte Geduld danke ich insbesondere Lew sowie Bo und Mauro. Wie oft waren wir mit diversen Herausforderungen softwaretechnischer und numerischer Natur konfrontiert, für die wir letztendlich immer eine Lösung finden konnten. Herzlichen Dank, Alex, für Deine persönliche und organisatorische Unterstützung. Die Gespräche mit Dir haben mir immer sehr geholfen und zum Erfolg dieser Arbeit beigetragen. Ohne Bo und Vera wäre meine Zeit am GFZ nur halb so schön gewesen. Es war super mit Euch zusammenzuarbeiten, und Freud und Leid des Doktorandendaseins zu teilen. Ich danke euch vielmals für die gemeinsame Zeit.

Zuletzt möchte ich mich ganz herzlich bei meinen Eltern, meiner Schwester, meiner ganzen Familie und meinen Freunden bedanken. Danke für Eure liebevolle Unterstützung, Euer Verständnis und Euren Zuspruch während der gesamten Zeit meiner Promotion. Markus, danke für Deine Ermutigungen, Deine Inspiration und dafür, dass Du mich immer zum Lachen bringst!

Erklärung

Hiermit erkläre ich gemäß § 9 Abs. 7 der Promotionsordnung der Mathematisch-Naturwissenschaftlichen Fakultät der Universität Potsdam, dass ich die von mir vorgelegte Dissertation mit dem Titel

Influence of faults on the 3D coupled fluid and heat transport

selbstständig angefertigt, die benutzten Quellen und Hilfsmittel vollständig angegeben und wörtliche und sinngemäße Zitate als solche gekennzeichnet habe sowie Tabellen, Karten und Abbildungen, die anderen Werken in Wortlaut oder dem Sinn nach entnommen sind, in jedem Einzelfall als Entlehnung kenntlich gemacht habe. Ich erkläre außerdem, dass diese Dissertation noch keiner anderen Fakultät oder Hochschule zur Prüfung vorgelegen hat; dass sie, abgesehen von unten angegebenen Teilpublikationen, noch nicht veröffentlicht worden ist sowie, dass ich eine solche Veröffentlichung vor Abschluss des Promotionsverfahrens nicht vornehmen werde. Die Bestimmungen der Promotionsordnung sind mir bekannt.